BEARING WORLD

www.bearingworld.org

Journal

Volume 1_2016, Proceedings of the Bearing World Conference

12-13 April 2016,
Hanover/Germany

Editors: G. Poll _ A. Grunau _ B. Hagemann

Published by
FVA Forschungsvereinigung Antriebstechnik e.V.
VDMA Verlag

Imprint

Bearing World Journal
Volume 1, December 2016

Published by:
Forschungsvereinigung Antriebstechnik e.V.
Lyoner Straße 18
60528 Frankfurt am Main
Germany
www.fva-net.de

VDMA Verlag GmbH
Lyoner Straße 18
60528 Frankfurt am Main
Germany
www.vdma-verlag.com

ISBN 978-3-8163-0705-1

Volume 1_2016, Proceedings of the Bearing World Conference
12-13 April 2016,
Hanover/Germany

Dear reader,

Globalisation of industry increasingly requires international networking of research and development work. With BEARING WORLD, the German Research Association for Drive Technology, FVA, has initiated an international dialogue in which researchers and developers from universities and bearing manufacturers come together with users and experts from the industry. The first international Bearing World Conference, initiated and organised by FVA, took place in April 2016. More than 200 experts from 11 countries met in Hanover to share the latest research findings in the world of bearings.

With Bearing World Journal, our aim is to continue this exchange among international experts by regularly publishing high-quality scientific reports related to rolling and plain bearings. We want to offer the international research community a new international publication platform for cutting-edge research in the field of bearings.

The high quality of Bearing World Journal is ensured by the peer review process, which is carried out by the Bearing World Scientific Board.

This first volume of Bearing World Journal includes the best contributions from the first FVA Bearing World Conference - BEARING WORLD 2016 in Hannover. In the future, high-quality scientific publications from the world of bearings will be published in the Journal, independent of the conference. Please send us your contributions.

We would like to thank all of the authors for their interesting contributions to the first issue of Bearing World Journal.

_ **Prof. Dr.-Ing. Gerhard Poll,** Initiator, Head of international Scientific Board
_ **Dr.-Ing. Arbogast Grunau,** President of the FVA Management Board
_ **Bernhard Hagemann,** Editor-in-chief

Please send your paper via e-mail as Word document to FVA (**submission@bearingworld.org**).
In addition please attach a PDF document.

Bearing World Scientific Board

Scott Bair, Georgia Institute of Technology, USA
Prof. Harry Bhadeshia, University of Cambrigde, Great Britain
Prof. Stefan Björklund, KTH Royal Institute of Technology, Stockholm, Sweden
Prof. Benyebka Bou-Said, Institut National Des Sciences Appliquées (INSA) Lyon, France
Prof. Ludger Deters, TU Magdeburg, Germany
Prof. Duncan Dowson, University of Leeds, Great Britain
Prof. Rob Dwyer-Joyce, University of Sheffield, Great Britain
Prof. Michel Fillon, Université de Poitiers, France
Prof. Sergei Glavastkih, KTH Royal Institute of Technology, Stockholm, Sweden
Prof. Irina Goryacheva, Russian Academy of Sciences, Russia
Prof. Feng Guo, Qingdao Technological University, China
Prof. Martin Hartl, Brno University of Technology, Czech Republic
Prof. Stathis Ioannides, Imperial College London, Great Britain
Prof. Georg Jacobs, RWTH Aachen University, Germany
Prof. Motohiro Kaneta, Brno University of Technology, Czech Republic
Prof. Michael M. Khonsari, Louisiana State University, USA
Prof. Ivan Krupka, Brno University of Technology, Czech Republic
Prof. Roland Larsson, Luleå University of Technology, Sweden
Prof. Antonius Lubrecht, Institut National Des Sciences Appliquées (INSA) Lyon, France
Prof. Piet Lugt, SKF Nieuwegin; University of Twente, Enschede, Netherlands
Prof. Jianbin Luo, State Key Laboratory of Tribology, Tsinghua University, China
Prof. Guillermo Morales-Espejel, INSA Lyon, France
Prof. Anne Neville, University of Leeds, Great Britain
Prof. Hiroyuki Ohta, Nagaoka University of Technology, Japan
Prof. Gerhard Poll, Leibniz University Hanover, Germany
Prof. Martin Priest, University of Bradford, Great Britain
Prof. Farshid Sadeghi, Purdue University, Lafayette, Indiana, USA
Prof. Richard Salant, Georgia Institute of Technology, USA
Prof. Bernd Sauer, TU Kaiserslautern, Germany
Prof. Ian Sherrington, University of Central Lancashire, Great Britain
Prof. Hugh Spikes, Imperial College London, Great Britain
Prof. Gwidon Stachowiak, Curtin University Australia, Australia
Prof. Kees Venner, University of Twente, Enschede, Netherlands
Prof. Philippe Vergne, Institut National Des Sciences Appliquées (INSA) Lyon, France
Prof. Fabrice Ville, Institut National Des Sciences Appliquées (INSA) Lyon, France
Prof. Sandro Wartzack, Friedrich-Alexander-University Erlangen-Nürnberg, Germany
Prof. John A. Williams, University of Cambridge, Great Britain
Prof. Hans-Werner Zoch, IWT Stiftung Institut für Werkstofftechnik, Bremen, Germany

Contents

Noise elimination for vibration-based rolling bearing fault diagnosis

Hamdullah Merdane [a], Reza Golafshan [a], Kenan Y. Sanliturk [b]

[a] ORS Bearings Inc., R&D Center;
[b] Istanbul Technical University, Mechanical Engineering Department

Abstract

Rolling bearings remain one of the most crucial components in industrial machines and due to their critical role, it is of great importance to monitor their conditions under operation. However, due to the background noise in acquired signals, it is not always possible to identify probable faults. This incapability in identifying the faults makes the de-noising process one of the most essential steps in the field of Condition Monitoring (CM) and fault detection. In this context, Singular Value Decomposition (SVD) method can be considered as a reliable and powerful method for noise elimination purposes. In the present study, the proposed SVD-based de-noising method is reviewed and revised in both time and frequency domains for rolling bearing vibration signals. The test case conducted using measured vibration signal for a localized defected rolling bearing demonstrates the effectiveness of the SVD-based de-noising method for the vibration-based bearing fault detection.

1. Introduction

Rolling bearings are one of the most common and important components in many mechanical engineering applications. It is well-known that rolling bearings have a very significant role on the global vibrations of a rotating machinery. Therefore, vibration-based fault detection and diagnosis of the rolling bearings have become a vigorous area of work and have appealed more and more attention in the literature [1,2,3]. When a localized defect occurs on rolling bearing surfaces, a series of impulses are created in vibration signal of a ball bearing. These impulses excite the resonances of the system with a certain repetition frequency. These resonance frequencies generally exceed 1.5 kHz; however, they are usually not of interest since they do not contain any explicit diagnostic information. A desirable and successful diagnostic method should be able to detect the corresponding repetition frequency of the impulse train created by bearing fault(s) [4]. Recently, some of the rolling bearing diagnosis research works are focused on the non-stationary conditions due to variable load and rotating speed, such as during machine run-up and run-down [5,6]. This is a key factor in particular in wind turbine applications. Due to the unavoidable noise in measured data, however, it is not always possible to identify probable faults and this could be the case in many rolling bearing vibration analyses [7,8]. In particular, in industrial environments, vibration signals can be covered with heavy background noise originating from measurement system as well as due to misalignment, unbalance, crack(s) on the rotating shaft, looseness, and distortions [9]. Consequently, noise elimination process appears to be one of the most important steps in the field of Condition Monitoring (CM) and fault detection based on vibration analyses [10].

Among a wide range of de-noising and signal enhancing methods available in the literature [11], noise elimination algorithms based on Singular Values Decomposition (SVD) can yield very reliable results [10,12]. Although, it appears that the SVD-based methods are mostly used in order to extract statistical parameters which can be used for characterizing the captured vibration signals from rolling bearings [13,14,15], relatively few studies are dedicated to signal de-noising and enhancing with the help of SVD. Jiang et al. in [12] have employed SVD for the coefficient matrix of the Reassignment Continuous Wavelet Transform (RCWT) to obtain the de-noised and sharper time-frequency representation of the vibration signal. Chen and Zhang in [16] have formed the input matrix in SVD process based on a series of experiments so that each row is formed by repeating the tests using the same ball bearings. However, the major difficulty with this method is that it requires conducting so many experiments which is a key factor to yield successful results. Golafshan and Sanliturk in [10] have proposed the used of SVD and Hankel matrix for rolling bearing vibration signals for both time and frequency domains. The proposed SVD-based noise elimination method can be performed in five main steps as: 1) converting the measured vibration signal – either in time or frequency domain – into the matrix form using the Hankel matrix formulation, 2) obtaining the corresponding singular values using SVD method, 3) hard thresholding the singular values, which replace the non-significant singular values by zeros, 4) obtaining the revised matrix by modified singular values, and 5) reconstructing the de-noised signal. However, it is worth mentioning that, hard thresholding of non-significant singular values, which replace all the non-significant singular values by zeros, may lead to ignoring some valuable information.

In the present study, as an extension to the previous studies in [10,17], weighting of the non-significant singular values as an alternative to hard thresholding is investigated. The remainder of this paper is organized as follows. First, the formulations and theoretical basis of the SVD-based de-noising method are given in section 2. The fundamental principles of SVD method is presented in Section 3. Then description of the test rig and implementation of the SVD-based de-noising method in both frequency and time domains are presented in sections 4 and 5, respectively. Finally, section 6 is dedicated to some concluding remarks.

2. Methodology

SVD is a numerical method which states that a matrix [A] of rank L can be decomposed into the product of three matrices, [U] (an orthogonal matrix), [S] (a diagonal matrix), and $[V]^T$ (the transpose of an orthogonal matrix [V]). This method is usually presented as [18]

$$[\mathrm{A}]_{\mathrm{m}\times\mathrm{n}} = [\mathrm{U}]_{\mathrm{m}\times\mathrm{m}}[\mathrm{S}]_{\mathrm{m}\times\mathrm{n}}[\mathrm{V}]^{\mathrm{T}}_{\mathrm{n}\times\mathrm{n}} \tag{1}$$

where $U^TU = I$ and $V^TV = I$; S is a diagonal matrix containing the square roots of eigenvalues of A^TA, which can be expressed as $S = \mathrm{diag}(\sigma_1, \sigma_2, \ldots, \sigma_L)$, where $L = \min(m,n)$. These σ_i ($i = 1, 2, \ldots, L$) are called the singular values of the matrix [A].

When the matrix [A] contains measured time domain signal (or its frequency domain counterpart) contaminated with noise, it can reasonably be assumed that the limit for the rank of [A] will be due to noise and other errors in the measured data. According to the previous studies in [10,17], there exists a m×n matrix $[\bar{A}]$ of rank $l \leq L$, which minimizes the sum of the squared error between the elements of the matrix [A] and the corresponding elements of the matrix $[\bar{A}]$ which can be formed as

$$[\bar{\mathrm{A}}] = [\mathrm{U}_l][\mathrm{S}_l][\mathrm{V}_l]^{\mathrm{T}} \tag{2}$$

where $[\bar{A}]$ is the reconstructed matrix using only the largest significant l number of singular values. The same studies suggest that the rest of the singular values can be replaced by zero such that

$$\begin{aligned} \sigma_{\mathrm{i}} &> \varepsilon, \quad \mathrm{i} = 1, \ldots, l \\ \sigma_{\mathrm{i}} &\leq \varepsilon, \quad \mathrm{i} = l+1, \ldots, \mathrm{L} \end{aligned} \tag{3}$$

where ε is a threshold.

To perform the SVD-based noise elimination method, it is necessary to present the measured signals in matrix form. To do so, the Hankel matrix for an input discrete time domain vibration signal, x_i ($i = 1, 2, \ldots, N$) can be obtained as [19]

$$[\mathrm{A}] = \begin{bmatrix} \mathrm{x}_1 & \mathrm{x}_2 & \cdots & \mathrm{x}_\mathrm{n} \\ \mathrm{x}_2 & \mathrm{x}_3 & \cdots & \mathrm{x}_{\mathrm{n}+1} \\ \vdots & \vdots & \ddots & \vdots \\ \mathrm{x}_\mathrm{m} & \mathrm{x}_{\mathrm{m}+1} & \cdots & \mathrm{x}_\mathrm{N} \end{bmatrix} \tag{4}$$

where $\mathrm{m} + \mathrm{n} - 1 = \mathrm{N}$.

Similarly, the Hankel matrix can also be constructed using frequency domain signals. In this case, the Hankel matrix is formed based on spectrum vector which is obtained by Discrete Fourier Transform (DFT). Fourier Transform of the discrete vibration signal, x_i, is expressed as

$$X_k = \frac{1}{N}\sum_{i=1}^{N} x_i e^{-j2\pi ki/N} \tag{5}$$

Then the Hankel matrix for the spectrum vector can also be constructed similarly to Eq. (4) as

$$[A] = \begin{bmatrix} X_1 & X_2 & \dots & X_n \\ X_2 & X_3 & \cdots & X_{n+1} \\ \vdots & \vdots & \ddots & \vdots \\ X_m & X_{m+1} & \cdots & X_N \end{bmatrix} \tag{6}$$

where the same relationship as before holds here, i.e. $m + n - 1 = N$.

After the matrix $[\bar{A}]$ is obtained using the modified singular values, it must be converted back to the vector form. However, it should be noted that the matrix $[\bar{A}]$ is of non-Hankel form. The reconstruction procedure is done by arithmetic averaging along the anti-diagonals of the matrix $[\bar{A}]$ and can be expressed as [20,21]

$$\bar{x}_i = \frac{1}{\beta - \alpha + 1}\sum_{j=\alpha}^{\beta} \bar{A}_{i-j+1,j} \tag{7}$$

where $\alpha = \max(1, i - m + 1)$ and $\beta = \min(n, i)$. The vector, $\bar{x}$, is the de-noised signal.

For the purpose of demonstrating the concept of SVD-based de-noising method, suppose the matrix [A] either by Eq. (4) or Eq. (6). It comprises two parts: uncontaminated data, which contains fault diagnosis information and unwanted part, which represents noise. From Eq. (1) and (2), the following equation can also be derived

$$[A] = [\bar{A}] + [N] = [U_l \quad U_0]\begin{bmatrix} S_l & 0 \\ 0 & S_0 \end{bmatrix}\begin{bmatrix} V_l^T \\ V_0^T \end{bmatrix} \tag{8}$$

where $[\bar{A}]$ and [N] are correspond to uncontaminated part and unwanted part, respectively. Also S_l contains significant singular values σ_i ($i = 1, 2, \dots, l$), which are used to construct the uncontaminated data and S_0 contains non-significant singular values, σ_i ($i = l + 1, \dots, L$).

As a summary, Figure 1 illustrates the schema of SVD-based de-noising method for rolling bearing fault diagnosis. As described earlier, the noise elimination process can be done either in time domain or frequency domain. After constructing the matrix [A] and then performing the SVD process, as mentioned earlier, by hard thresholding of singular values (i.e. ignoring singular values lower than a threshold), the modified matrix [S] is obtained. Then the matrix $[\bar{A}]$ is obtained using the modified matrix [S]. Finally, the de-noised vibration signal in vector form is reconstructed based on matrix $[\bar{A}]$. It is worth mentioning that Golafshan and Sanliturk in [10] have shown that the SVD-based de-noised spectrum can be considered as a reliable alternative to envelope spectrum.

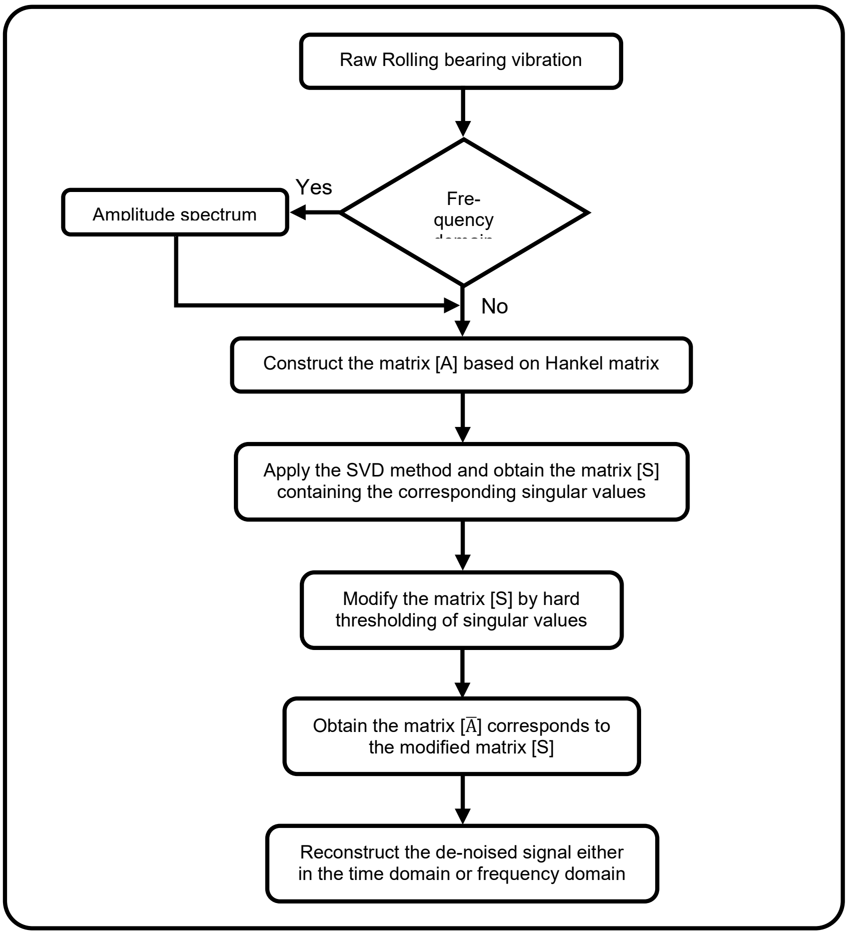

Figure 1: Schema of SVD-based noise elimination method for rolling bearing vibration signals.

3. Principles of The SVD-based Noise Elimination

The purpose of this section is to review and investigate the key principles associated with the use SVD-based noise elimination method in rolling bearing fault diagnosis.

3.1 The size of Hankel matrix

The major issue with the use of SVD in signal processing is determining the size of matrix [A]. Ideally, for any given data with a sample number of N, a square or a nearly square Hankel matrix can be constructed. However, constructing a square Hankel for a measured rolling bearing vibration signal may require excessive CPU-time for further processing. However, it is neither necessary nor desirable to construct a square or nearly square Hankel matrix for de-noising applications. Instead, a rectangular matrix with appropriate selection of the smaller dimension can be used effectively, provided that the smaller dimension, i.e. the maximum possible rank, is large enough to represent the system behavior including the effect of noise. In other words, for choosing the m value in Eq. (4) and Eq. (6) there is a trade-off between speed and de-noising capability. Earlier works on SVD-based de-noising method applied for rolling bearing fault detection in [10,17] have used a Hankel matrix with 1000 row (m=1000) to produce, in total, 1000 singular values. This methodology may be even more effective by employing a smaller Hankel matrix hence achieving a faster algorithm. In the present study, in order to achieve a fast SVD-based de-noising algorithm, a Hankel matrix with 500 rows is used in noise elimination process.

3.2 Threshold selection

The noise threshold, ε, to separate the unwanted and uncontaminated parts of the data is crucial factor in reliability of SVD method noise elimination. One way to determine the noise threshold and the first l singular values in Eq. (8) is to plot the normalized singular values and to choose the appropriate rank when the normalized singular values approach to an asymptote [22]. In addition, as faulty rolling bearing vibration signals have high impulsive nature, the reliable threshold may also be chosen based on quantifying the output signal kurtosis value.

3.3 Thresholding

The so-called Hard thresholding of the singular values, which replaces the non-significant singular values by zeros, may lead to ignoring some valuable fault diagnosis information. To overcome this problem and as a reliable alternative, a weighting function (i.e. exponential function) can be applied to the non-significant singular values rather than hard thresholding. The exponential function is expressed as

$$\mathrm{f(x)} = \mathrm{e}^{-\alpha_\mathrm{i}\,\mathrm{x}} \tag{9}$$

where α is defined as the decay rate of exponential function, f(x). Note that, various weighting functions for non-significant singular values may be obtained based on various decay rates in Eq. (9). In this study, six different values for decay rate, $\alpha_1 = 0.01$, $\alpha_2 = 0.02$, $\alpha_3 = 0.04$, $\alpha_4 = 0.06$, $\alpha_5 = 0.08$, and $\alpha_6 = 0.1$ corresponding, respectively, to the six functions in Figure 2 (Exponential function # 1 to 6), are used to investigate the effects of weighting of the singular values lower than the threshold, ε, in signal enhancing/de-noising in both frequency domain and time domain. Figure 2 illustrates the exponential functions having various decay rates as well as Hard thresholding function.

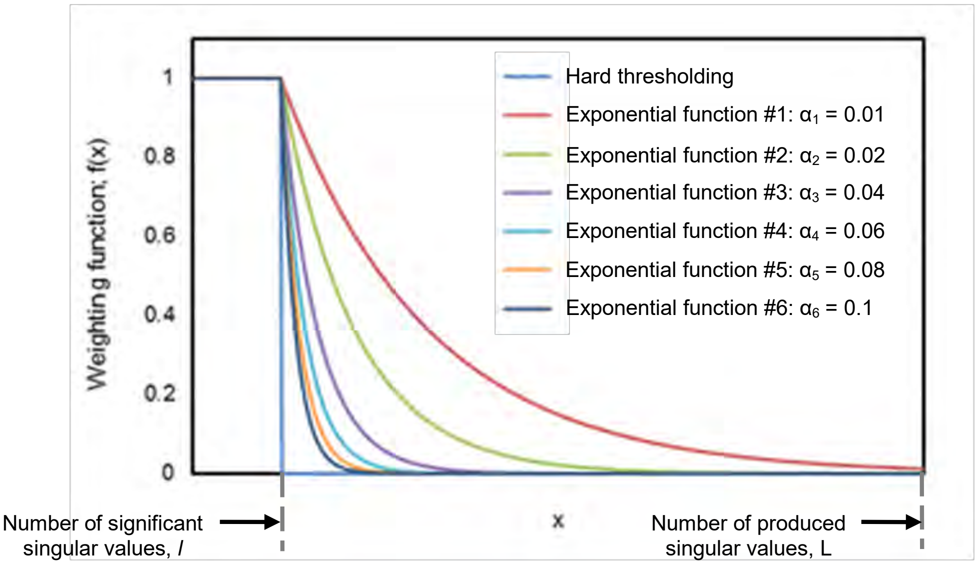

Figure 2: Illustration of weighting functions for singular values.

4. Experimental Setup

4.1 System structure

The rolling bearing fault diagnosis system used in the experiment for implementation of the proposed SVD method is schematically illustrated in Figure 3. In addition, a picture of the test rig is shown in Figure 4. As can be seen, an accelerometer (100 mv/g accelerometer of PCB) is positioned on top of the bearing housing to capture the rolling bearing vibration signals in the vertical direction.

The speed of the shaft and the amount of axial loading are measured through an optical encoder and force sensor, respectively. 150N load is applied to the bearing along axial direction during the test using a hydraulic piston. The rotating speed of the shaft is 1200 RPM (20 Hz). The data acquisition (DAQ) system, namely, NI9234, collects the bearing vibration signal with a sampling frequency of 17068 Hz, through a LabVIEW interface.

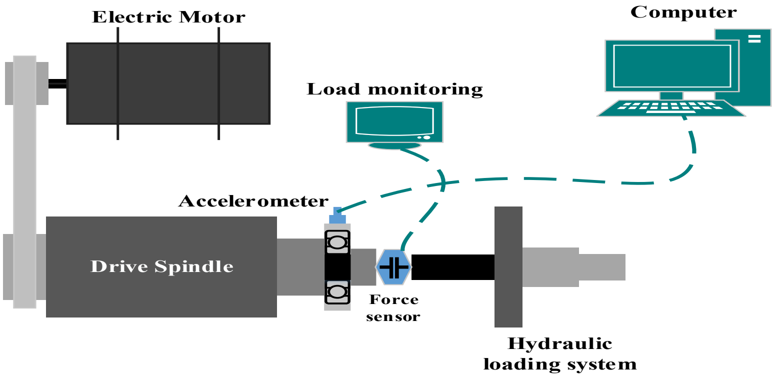

Figure 3: Schema of rolling bearing fault diagnosis test setup.

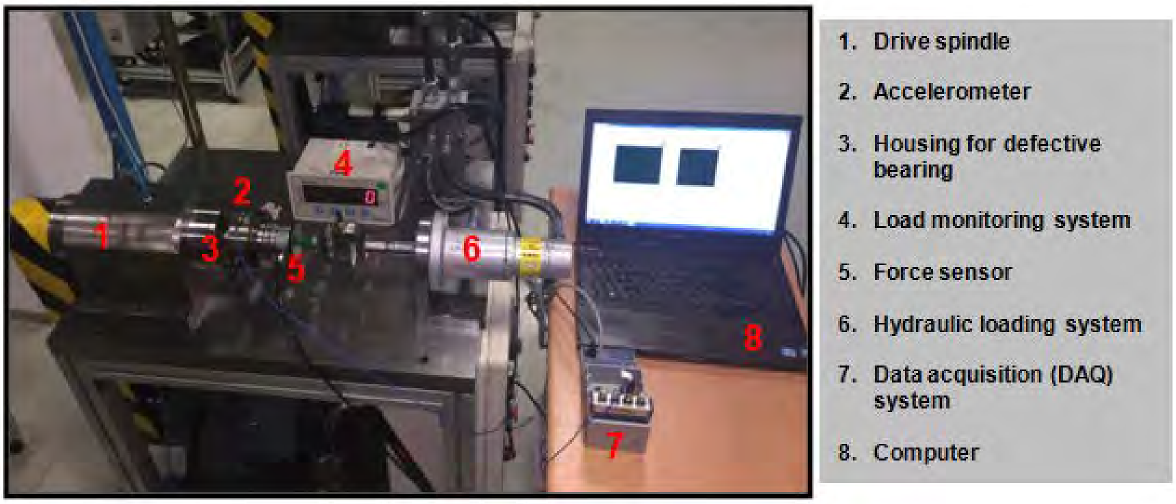

1. Drive spindle
2. Accelerometer
3. Housing for defective bearing
4. Load monitoring system
5. Force sensor
6. Hydraulic loading system
7. Data acquisition (DAQ) system
8. Computer

Figure 4: Experimental test setup.

4.2 Test ball bearing

One single-row deep grove ball bearing type ORS6205 having outer race localized defect is employed in this study. The geometry details of ORS6205 type ball bearing are listed in Table 1. A localized fault is artificially introduced to the tested ball bearing. The position of the defective area on the outer race is positioned on the top of the ball bearing. In addition, Figure 5 shows the outer race defective test ball bearing.

Table 1: Geometry details of ORS6205 ball bearing.

Outer Race Diameter	Inner Race Diameter	Balls Diameter	Number of Balls	Bearing Width	Contact Angle
52 mm	20 mm	7.5 mm	9	15 mm	0 °

It is well known that, the fundamental fault frequency for an outer race defective ball bearing can be estimated from ball bearing geometry. The fundamental fault frequency for outer race where outer race is stationary and inner race rotates with shaft can be formulated as

$$\mathrm{BPFO} = \frac{\mathrm{N_B}}{2}\mathrm{F_s}\left(1 - \frac{\mathrm{D_b}\cos\beta}{\mathrm{D_p}}\right) \tag{10}$$

where $\mathrm{N_B}$, $\mathrm{F_s}$, $\mathrm{D_b}$, $\mathrm{D_p}$, and β are number of balls, shaft rotating frequency, ball diameter, pitch diameter, and ball bearing contact angle, respectively. The BPFO is estimated as 73 Hz accordingly.

Figure 5: Artificially outer race defective ORS6205 ball bearing.

5. Results and Discussion

The performances of the de-noising method described in section 6 are investigated using measured data in this section. Figure 6 shows the raw vibration signal measured from the housing of outer race defective ball bearing for a time period of 1 s and the amplitude spectrum. In what follows, the performance of the proposed approach for rolling bearing fault detection is assessed in detail in both time and frequency domains.

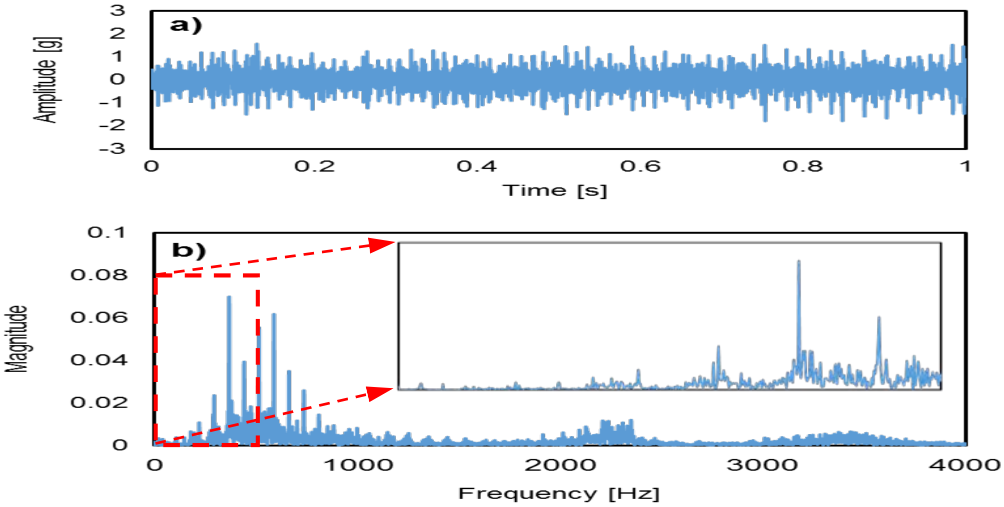

Figure 6: Captured vibration signal from the defective bearing in a) time and b) frequency domain.

5.1 Time domain de-noising

The noise elimination method in time domain is applied to the raw time domain vibration signal presented in Figure 6a. A Hankel matrix with 500 rows is then formed and the total number of produced singular values to be used for noise elimination process is determined systematically. Based on a series of experiments, it is concluded that the first 15 singular values are considered to be sufficient for the elimination of the background noise in time domain.

The de-noised vibration signals based on various weighting functions and Hard thresholding of singular values are plotted in Figure 7. In order to have a better understanding of de-noising effects in time domain, the envelope analysis is performed for the original signal and its de-noised versions (i.e. Hard thresholded and exponential fun. #6) up to 500 Hz and the results are presented in Figure 8. It is seen that, in spite of the fact that the overall amplitudes of envelope spectrum of the de-noised signal are somewhat reduced, the envelope spectrums of the de-noised signal have lower noise level than that of the original signal, hence yielding a slightly better detection of the related fault frequency (BPFO). According to the obtained results in Figure 8, it is obvious that weighting of the non-significant singular values using exponential fun. #6 yields to better noise elimination results compared to the hard thresholding.

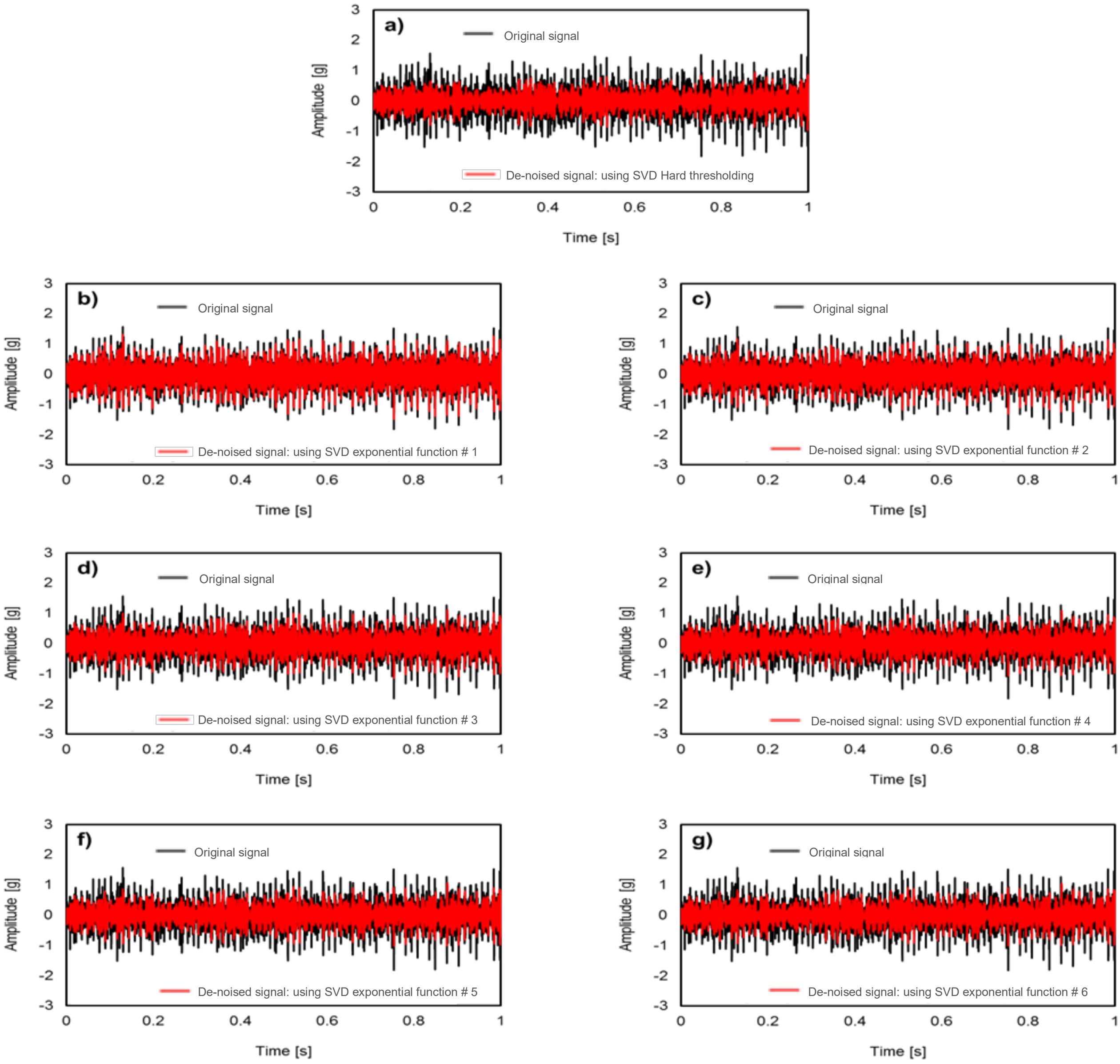

Figure 7: Original and SVD-based de-noised vibration signals.

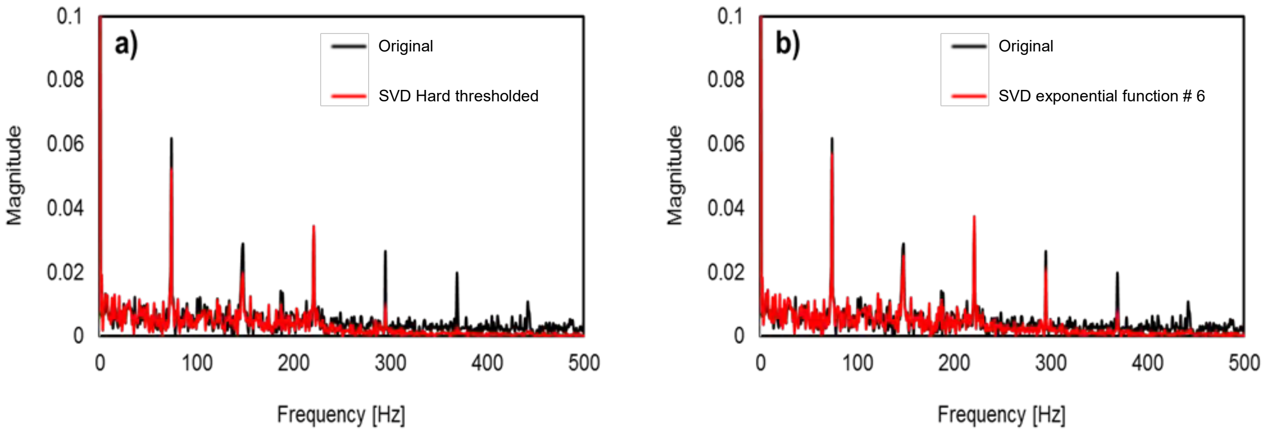

Figure 8: Envelope spectrums of original and SVD-based de-noised vibration signals.

5.2 Frequency domain de-noising

In this section, SVD of the Hankel matrix based de-noising process is applied to the amplitude spectrums of ball bearing vibration signals. For this purpose, again, a Hankel matrix with 500 rows is formed using the spectrum vectors obtained via FFT. Figure 9 and Figure 10 illustrate, respectively, the original and the SVD-based de-noised amplitude spectrums for Hard thresholding and various weighting functions by including different numbers of most significant singular values (i.e. 20, 40, and 60) up to 500 Hz. As can be seen, the original amplitude spectrum in Figure 9 is unable to indicate the expected fault frequency clearly. It is well-known that the amplitude spectrum of the vibration signal is not capable of displaying the fault frequency. In such cases, envelope analysis is the most common method for the fault frequency detection. However, inspection of the de-noised spectrums in Figure 10 reveals that noise removal from vibration spectrum makes the fault frequency and its harmonics very visible. As an alternative to envelope spectrum, the SVD-based de-noised spectrum can be used for rolling bearing fault detection. Although, comparing the results in Figure 10 shows that including the first most significant 20, 40 or 60 singular values do not make much difference, it can be concluded that weighting of the non-significant singular values yields slightly better detection result compared to the Hard thresholding.

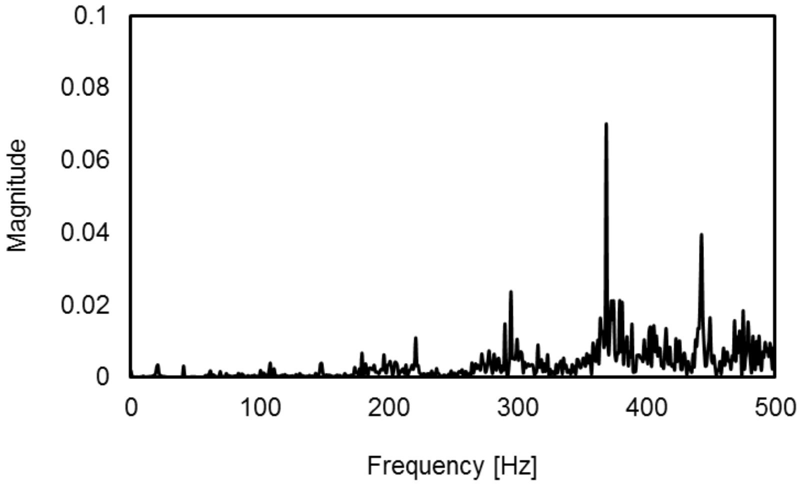

Figure 9: Amplitude spectrum of the captured vibration signal in Figure 6a.

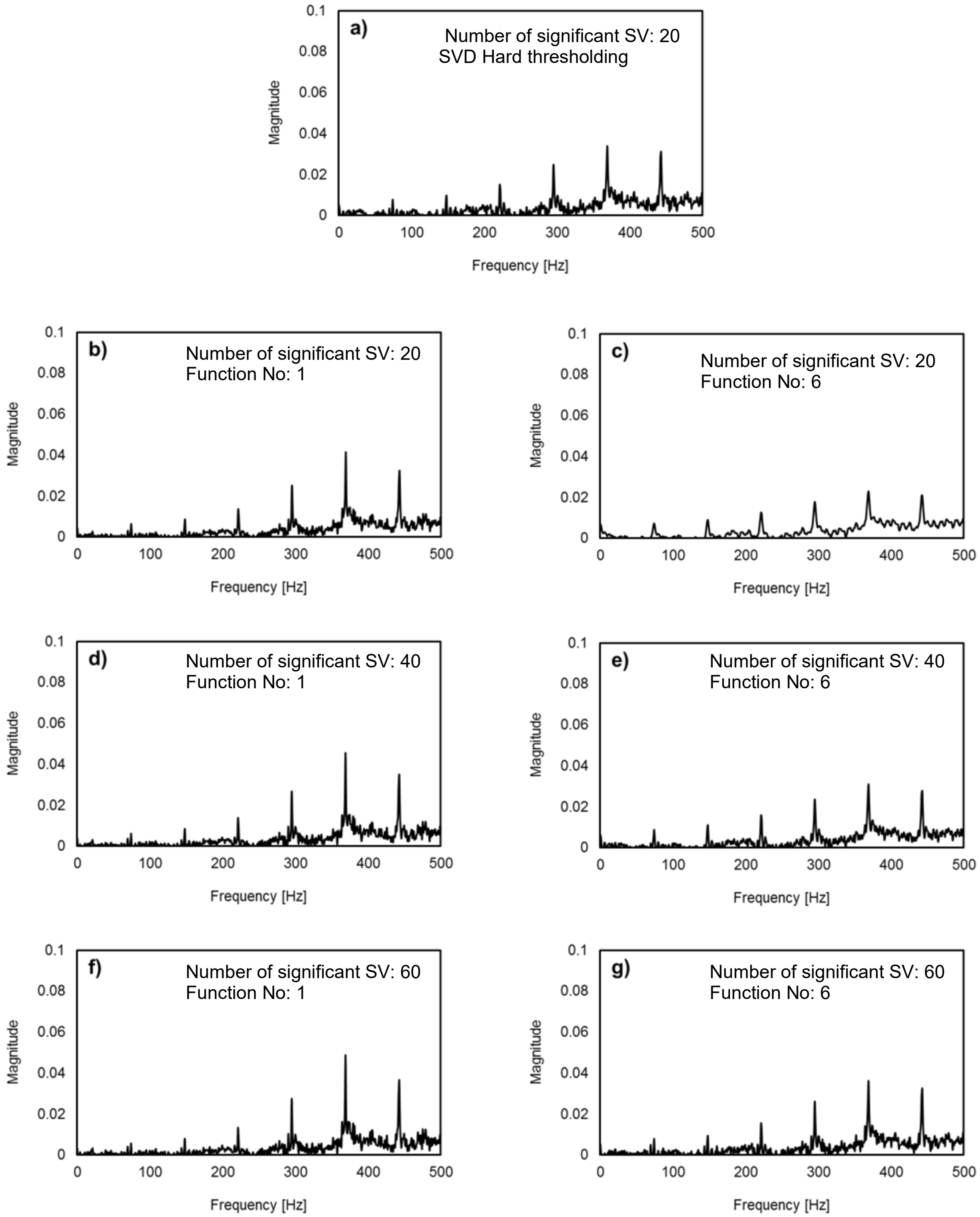

Figure 10: Original and SVD-based de-noised amplitude spectrums.

6. Conclusions

In this study, the SVD-based de-noising approach is reviewed and revised for rolling bearing localized fault detection in both time and frequency domains. The Hankel matrix is used for forming the trajectory matrix in order to perform de-noising operation in the field of Condition Monitoring and ball bearing fault detection is demonstrated. It is found that de-noising in frequency domain appears to yield more successful fault identification than the de-noising in time domain. It is also shown in this study that de-noising the amplitude spectrum using the SVD-based method makes the fault frequency much sharper and very visible. This suggests that the fault identification using the de-noised amplitude spectrum can be a viable alternative to envelope analysis. It should be noted, however, that the effectiveness of the de-noising method depends on appropriate selection of the threshold level. Therefore, the number of most significant singular values which needs to be included for the reconstruction process is an important parameter hence, a systematic identification of this threshold is recommended. It is worth stating that weighting of the non-significant singular values in SVD method may yield slightly better detection results in both time and frequency domain compared to the Hard thresholding. Finally, the effectiveness of the proposed approach needs to be investigated under non-stationary operating conditions.

Acknowledgment

This study has been supported by ORS Bearings Inc., Ankara, Turkey.

References

[1] N. Tandon and A. Choudhury, "A review of vibration and acoutic measurement methods for the detection of defects in rolling element bearings," *Tribology International*, vol. 32, no. 8, pp. 469 - 480, 1999.

[2] Zh. Feng, M. Liang, and F. Chu, "Recent advances in time–frequency analysis methods for machinery fault diagnosis: A review with application examples," *Mechanical Systems and Signal Processing*, vol. 38, no. 1, pp. 165 - 205, 2013.

[3] A. Rai and Sh. Upadhyay, "A Review on Signal Processing Techniques Utilized In The Fault Diagnosis Of Rolling Element Bearings," *Tribology International*, vol. 96, pp. 289 - 306, 2016.

[4] R. B. Randall, *Vibration-based Condition Monitoring: Industrial, Aerospace and Automotive Applications*. Illinois: John Wiley and Sons Ltd, 2011.

[5] R. Zimroz, W. Baltermus, T. Barszcz, and J. Urbanek, "Diagnostics of bearings in presence of strong operating conditions non-stationarity — a procedure of load-dependent features processing with application to wind turbine bearings," *Mechanical Systems and Signal Processing*, vol. 46, no. 1, pp. 16 - 27, 2014.

[6] R. Ricci, P. Borghesani, S. Chatterton, and P. Pennacchi, "The combination of empirical mode decomposition and minimum entropy deconvolution for roller bearing diagnostics in nonstationary operation," in *In: Proceedings of the ASME International Conference on Design Engineering Technical Conferences and Computers and Information in Engineering*, Chicago, IL, USA, August 12–15, 2012.

[7] Y. Zhang, M. Liang, Ch. Li, and Sh. Hou, "A Joint Kurtosis-Based Adaptive Bandstop Filtering and Iterative Autocorrelation Approach to Bearing Fault Detection," *Journal of Vibration and Acoustics*, vol. 135, no. 5, pp. 051026 - 051026 - 17, 2013.

[8] N. Sawalhi, R. B. Randal, and H. Endo, "The enhancement of fault detection and diagnosis in rolling element bearings using minimum entropy deconvolution combined with spectral kurtosis," *Mechanical Systems and Signal Processing*, vol. 21, no. 6, pp. 2616 - 2633, 2007.

[9] M. P. Norton and D. G. Karczub, *Fundamentals of noise and vibration analysis for engineers*, Second ed. ed. Newyork: Cambridge University Press, 2003.

[10] R. Golafshan and K. Y. Sanliturk, "SVD and Hankel Matrix Based De-Noising Approach For Ball Bearing Fault Detection and Its Assessment Using Artificial Faults," *Mechanical Systems and Signal Processing*, vol. 70-71, pp. 36 - 50, 2016.

[11] W. Guo, P. W. Tse, and A. Djordjevich, "Faulty Bearing Signal Recovery From Large Noise Using A Hybrid Method Based On Spectral Kurtosis And Ensemble Empirical Mode Decomposition," *Measurement*, vol. 45, no. 5, pp. 1308 - 1322, 2012.

[12] Y. Jiang, J. Kan, Z. Zhang, G. Cheng, and J. Wen, "Machine Fault Diagnosis Based On Reassigned Wavelet Scalogram and SVD," *International Journal of Advancements in Computing Technology*, vol. 4, no. 20, pp. 10 - 21, 2012.

[13] M. Kang and J.-M. Kim, "Singular value decomposition based feature extraction approaches for classifying faults of induction motors," *Mechanical Systems and Signal Processing*, vol. 41, no. 1-2, pp. 348-356, 2013.

[14] B. Kilundu, X. Chiementin, and P. Dehombreux, "Singular Spectrum Analysis for Bearing Defect Detection," *Journal of Vibration and Acoustics*, vol. 133, no. 5, pp. 051007-051007/7, 2011.

[15] H. Liu, X. Wang, and C. Lu, "Bearing Fault Diagnosis under Variable Conditions Using Hilbert-Huang Transform and Singular," *Mathematical Problems in Engineering*, vol. 2014, pp. 1-10, 2014.

[16] Y. Chen and P. Zhang, "Bearing Fault Detection Based on SVD and EMD," *Applied Mechanics and Materials*, vol. 184-185, pp. 70-74, 2012.

[17] R. Golafshan and K. Y. Sanliturk, "The Effect of SVD Based Noise Elimination Methods Applied For Ball Bearing Fault Detection," in *Proceedings of TrC-IFToMM Symposium on Theory of Machines and Mechanisms*, Izmir, Turkey, 14-17 June, 2015.

[18] X. Zhao and B. Ye, "Similarity of signal processing effect between Hankel matrix-based SVD and wavelet transform and its mechanism analysis," *Mechanical Systems and Signal Processing*, vol. 23`, no. 4, pp. 1062 - 1075, 2005.

[19] S. Jensen, P. Hansen, S. Hansen, and J. Sørensen, "Reduction of broad-band noise in speech by truncated QSVD," *IEEE Transactions on Speech and Audio Processing*, vol. 3, no. 6, pp. 439 - 448, 1995.

[20] B. Muruganatham, M. Sanjith, B. Krishnakumar, and S. S. Murty, "Roller element bearing fault diagnosis using singular spectrum analysis," *Mechanical Systems and Signal Processing*, vol. 35, no. 1-2, pp. 150 - 166, 2013.

[21] B. Muruganatham, S. M.A., K. B.K., S. Murty, and P. Sw, "Inner race bearing fault detection using Singular Spectrum Analysis," in *Proceedings of IEEE International Conference on Communication Control and Computing Technologies (ICCCCT)*, Ramanathapuram, India, 7-9 October 2010.

[22] C.R. Pickrel, "Estimating the rank of measured response data using SVD and principal response functions," in *Proceedings of the Second International Conference on Structural Dynamics Modeling,Test Analysis and Correlation, DTA/NAFEMS*, 1996.

CFD-based analysis of thermal shear localization in EHL films

Achim Feldermann
RWTH Aachen University
Institute for Machine Elements and Machine Design

Dr.-Ing. Hermann van Lier
RWTH Aachen University
Institute for Machine Elements and Machine Design

Prof. Dr.-Ing. Georg Jacobs
RWTH Aachen University
Institute for Machine Elements and Machine Design

Abstract

Experiments on a ball-disc-tribometer show a friction reduction at low oil temperatures, which is contrary to expectations. In order to investigate this effect more detailed, CFD-based TEHL simulations are performed for three test cases with different oil inlet temperatures. For the low temperature case, a thermal shear band develops within the oil film. The corresponding velocity profile across the lubrication gap height is close to a step function, localizing the heat generation in a central layer of the contact. Consequently, the viscosity decreases locally by several orders, which results in an overall friction reduction. Due to the high viscosity gradients inside the lubricant, pressure variations across the lubrication gap height occur. In order to determine the degree of pressure variations across the lubrication film height in advance, a dimensionless parameter is proposed.

Introduction

In the last decades, simulations of elastohydrodynamic lubrication (EHL) problems have been based on the Reynolds equation. To derive this equation from the Navier-Stokes equations, inertia and gravity terms are not considered, the velocity gradients along the contact length are neglected and a constant pressure across the lubrication gap height is assumed[1]. By using a computational fluid dynamics (CFD) approach[2,3,4,5,6], the Navier-Stokes equations can be solved and the previously mentioned limitations can be eliminated. As a result, all gradients inside the lubricant can be fully resolved.

For isothermal conditions, the fluid parameters do usually not vary significantly across the lubrication gap height. However, a non-uniform temperature distribution may occur under thermal elastohydrodynamic conditions, which leads to high viscosity gradients in film thickness direction. One possible result of this may be the experimentally observed friction reduction by VAN LIER with decreasing oil temperatures[7]. Several years ago, similar results have been reported by WILLERMET[8] and WEBSTER[9].

In order to understand the measured friction reduction, CHANG et al. performed Reynolds-based EHL simulations[10]. They revealed that the friction reduction is mainly connected to thermal shear bands inside the contact zone and a localization of the heat generation in a central layer of the contact. Consequently, the viscosity decreases locally by several magnitudes, finally leading to an overall friction reduction. However, due to the high viscosity variations across the lubrication film height, the assumption of constant pressure in film thickness direction made by the Reynolds equation might not be valid anymore.

Therefore, this paper presents CFD-based TEHL simulations of an infinite line contact and reviews the assumption of constant pressure in film thickness direction under such conditions. For this, experimental results from EHL2-tribometer tests will be presented for different rolling speeds and oil temperatures. Thereafter, the simulation model is described and used to analyze the influence of varying oil inlet temperatures on the pressure and flow fields inside the contact zone. In the end, a dimensionless parameter is proposed, which can serve as an indicator of the degree of pressure variations across the lubrication film height under thermal elastohydrodynamic conditions.

Experimental results

Friction curves for different oil temperatures and rolling speeds have been measured on a ball-on-disc tribometer. The lubricant is an ISO VG 320 mixed from FVA3 and FVA4 oils. The normal contact load is 35 N, which results in a maximum Hertzian pressure of approximately 985 MPa. As shown in Figure 1, the friction curve behaves as expected for low rolling speeds. With decreasing temperature, the friction increases due to the higher viscosity level.

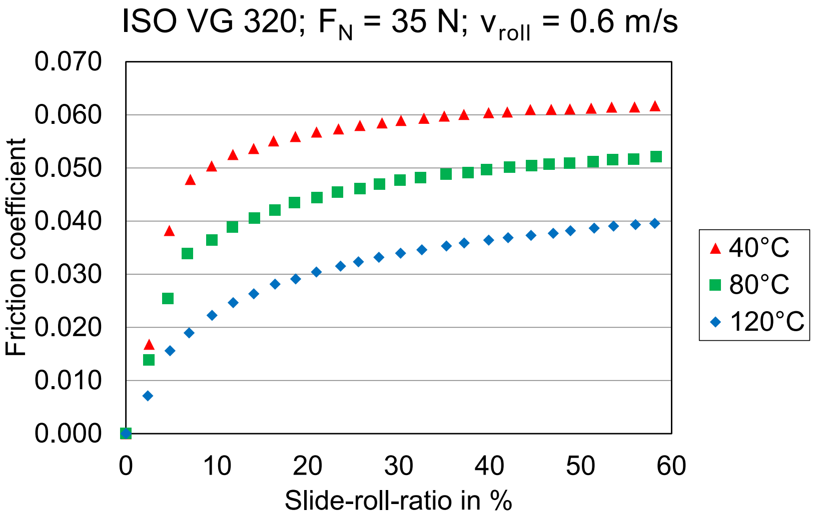

Figure 1 Friction curves at a rolling speed of 0.6 m/s

However, when the rolling speed increases (Figure 2) and the oil temperature is reduced sufficiently, the friction curve deviates from the expected shape and the friction decreases.

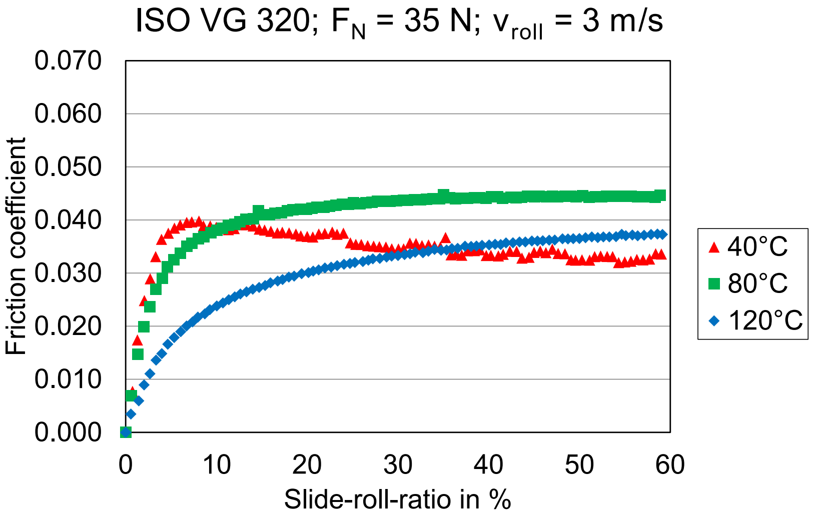

Figure 2 Friction curves at a rolling speed of 3 m/s

As this reduction is only visible for high rolling speeds and low temperature levels, this behavior can most likely be attributed to thermal effects inside the contact zone, such as thermal shear bands. Therefore, these conditions are used as reference for the following detailed CFD-based TEHL simulations.

Simulation method

In order to investigate the influence of varying oil inlet temperatures on the pressure and flow fields, the simulation method illustrated in Figure 3 is used in this work.

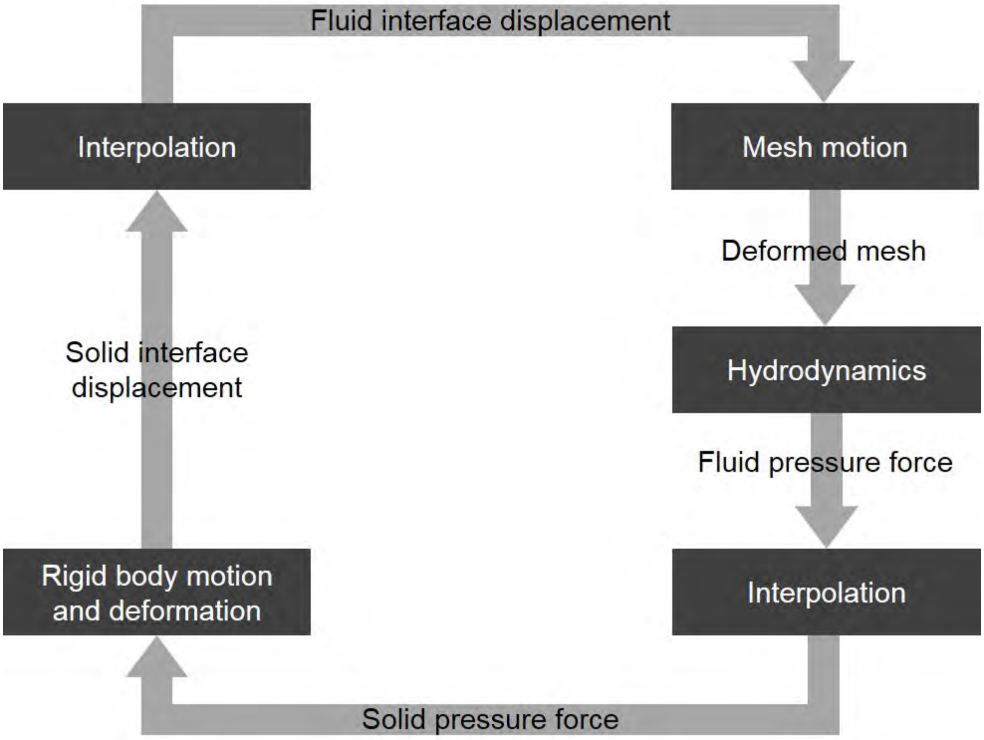

Figure 3 Procedure for CFD-based TEHL simulations[5,6]

Based on the calculated solid pressure forces and either a discretized and condensed finite-element model or an elastic half-space approximation, the rigid body motion and the deformation of the solid are determined. The resulting solid interface displacements are interpolated to the fluid interface mesh and used as boundary conditions for a mesh motion solver, which deforms the internal fluid mesh to maintain a good mesh quality. Thereafter, the hydrodynamics are solved iteratively. The resulting fluid pressure forces are again interpolated to the solid interface mesh and a new iteration is started until a steady state is reached. In the following, only the equations used in the hydrodynamics block will be presented. For the governing equations of all other blocks, it is referred to Ref. 5 and Ref. 6.

Hydrodynamics

The hydrodynamic solver used in this work is based on the solver *CAVITATINGFOAM,* which is available in FOAM-EXTEND. This solver employs a homogenous equilibrium model for cavitation, which means that the two phases liquid and vapour are supposed to be in mechanical and thermodynamic equilibrium[11]. The amount of vapour is described by the vapour fraction γ, given by

$$\gamma = \frac{\rho - \rho_{Liquid}(p_{Sat})}{\rho_{Vapour}(p_{Sat}) - \rho_{Liquid}(p_{Sat})} \tag{1}$$

with the densities ρ_{Liquid} and ρ_{Vapour} of the liquid and the vapour at cavitation pressure p_{Sat}. Based on this vapour fraction, the fluid properties are obtained by linear interpolation between the phases. Hence, the mixture density ρ, the mixture compressibility ψ and the mixture dynamic viscosity η become

$$\rho = \gamma \cdot \rho_{Vapour} + (1-\gamma) \cdot \rho_{Liquid} \tag{2}$$

$$\psi = \gamma \cdot \psi_{Vapour} + (1-\gamma) \cdot \psi_{Liquid} \tag{3}$$

$$\eta = \gamma \cdot \eta_{Vapour} + (1-\gamma) \cdot \eta_{Liquid} \tag{4}$$

Due to the assumption that the two phases are in equilibrium, only one set of continuity, momentum and energy equation has to be solved for the liquid-vapour mixture. These equations are implemented in an Arbitrary Lagrangian-Eulerian (ALE) formulation[12], in order to simulate the moving mesh problem of elastohydrodynamic lubrication, that is

$$\frac{\partial \rho}{\partial t} + (\mathbf{v} - \bar{\mathbf{v}}) \cdot \nabla \rho + \rho \nabla \cdot \mathbf{v} = 0 \tag{5}$$

$$\rho \left\{ \frac{\partial \mathbf{v}}{\partial t} + \left[(\mathbf{v} - \bar{\mathbf{v}}) \cdot \nabla \right] \mathbf{v} \right\} = -\nabla p + \nabla \cdot \tilde{\boldsymbol{\tau}} \tag{6}$$

$$\rho \left\{ \frac{\partial h}{\partial t} + (\mathbf{v} - \bar{\mathbf{v}}) \cdot \nabla h \right\} = \tilde{\boldsymbol{\tau}} : \nabla \mathbf{v} + \frac{dp}{dt} - \nabla \cdot \mathbf{q} \tag{7}$$

Here, $\mathbf{v}$ is the material velocity, $\bar{\mathbf{v}}$ is the mesh velocity, p is the pressure, h is the enthalpy, $\mathbf{q}$ is the heat flux vector and $\tilde{\boldsymbol{\tau}}$ is the viscous stress tensor, given by

$$\tilde{\boldsymbol{\tau}} = \eta \cdot \left[\nabla \mathbf{v} + (\nabla \mathbf{v})^T \right] - \frac{2}{3} \eta \tilde{\mathbf{i}} \nabla \cdot \mathbf{v} \tag{8}$$

with the unit tensor $\tilde{\mathbf{i}}$. This set of conservation equations is solved iteratively by applying the PISO algorithm[13].

Rheology

An ideal gas model with a constant compressibility and a constant dynamic viscosity is chosen to represent the vapour. The density of the oil is described by the non-linear Dowson-Higginson equation of state

$$\rho_{Liquid} = \rho_0 \frac{2K_0 + (K_0' + 1)p}{2K_0 + (K_0' - 1)p} \tag{9}$$

with the commonly used parameters K_0=1.67 GPa and K_0'=6.67 and the density ρ_0 at ambient pressure[14]. The oil viscosity is described by the model proposed by Houpert[3]

$$\eta_{Houpert} = \eta_{Roelands} \exp\left\{ \left[\ln(\eta_0) + 9.67 \right] \left[1 + 5.1e^{-9} p \right]^Z S_0 \frac{T_0 - T}{T_0 - T_{ref}} \right\} \tag{10}$$

with the Roelands viscosity according to

$$\eta_{Roelands} = \eta_0 \exp\left\{ \left[\ln(\eta_0) + 9.67 \right] \left[\left(1 + \frac{p}{p_{ref}} \right)^Z - 1 \right] \left[\frac{T - T_{ref}}{T_0 - T_{ref}} \right]^{-S_0} \right\} \tag{11}$$

In this equation, η_0 is the viscosity at ambient pressure and ambient temperature T_0, p_{ref} is the Roelands reference pressure, T_{ref} is the reference temperature and S_0 and Z are given by

$$S_0 = \frac{\beta(T_0 - T_{ref})}{\ln(\eta_0) + 9.67} \tag{12}$$

$$Z = \frac{\alpha_p}{5.1e^{-9} \left[\ln(\eta_0) + 9.67 \right]} \tag{13}$$

where β is the temperature-viscosity coefficient and α_p is the pressure-viscosity coefficient. Furthermore, non-Newtonian behaviour is taken into account by the Eyring model[14], so that the liquid viscosity is finally described by

$$\eta_{Liquid} = \frac{\tau_0}{\varepsilon} \sinh^{-1}\left(\frac{\eta_{Houpert}\, \varepsilon}{\tau_0} \right) \tag{14}$$

with the Eyring stress τ_0 and the shear rate ϵ.

Thermal boundary conditions

In order to solve the energy equation in the fluid, thermal boundary conditions representing the solids are necessary. In the used simulation model, two different boundary conditions are available. For moving solids, the solution of a moving heat source on a semi-infinite body is applied[15]. For a one-dimensional line contact, this solution reads

$$T(x) = T_S + \frac{1}{\sqrt{\pi \rho_{Solid} C_{Solid} \lambda_{Solid} u_{Solid}}} \int_{-\infty}^{x} \frac{q(\hat{x})}{\sqrt{x-\hat{x}}} d\hat{x} \tag{15}$$

where ρ_{Solid}, C_{Solid}, λ_{Solid} and u_{Solid} are the density, the heat capacity at constant pressure, the thermal conductivity and the velocity of the solids. q describes the heat flux and T_S is the initial wall temperature of the solid, which in this paper is assumed to be identical to the oil inlet temperature. This boundary condition, however, is only valid for non-zero solid velocities. For stationary solids, thermally reduced finite-element models can be imported. Based on the thermal loads (heat fluxes) the temperature can then be calculated. The procedure is similar to the one described in Ref. 5 and Ref. 6 for the calculation of the elastic deformation.

Case study

After having described the simulation procedure, it is applied to a typical steel-steel contact between a plane and an infinite cylinder with a radius of 10 mm, a rolling speed of 3 ms^{-1} and a slide-roll-ratio of 0.2. The fluid is an ISO VG 320 mineral oil and the external force is chosen in a way, that the Hertzian pressure equals the pressure in the experiments. Table 1 gives an overview of all relevant simulation parameters.

Parameter	**Symbol**	**Value**
Density liquid	ρ_0	894.8 kg/m³
Viscosity liquid	η_0	0.281 Pas
Temperature-viscosity coefficient liquid	β	0.05 K^{-1}
Pressure-viscosity coefficient liquid	α_p	2.87e-8 Pa^{-1}
Eyring stress	τ_0	5 MPa
Compressibility vapour	ψ_{Vapour}	9.6e-5 m²/s²
Viscosity vapour	η_{Vapour}	8.97e-6 Pas
Saturation pressure	p_{Sat}	5000 Pa
Roelands pressure	p_{ref}	1.98e8 Pa
Reference temperature	T_{ref}	138 K
Thermal conductivity liquid	λ_{Liquid}	0.15 W/(mK)
Thermal conductivity vapour	λ_{Vapour}	0.025 W/(mK)

Thermal conductivity solid	λ_{Solid}	47 W/(mK)
Heat capacity liquid	C_{Liquid}	2300 J/(kgK)
Heat capacity vapour	C_{Vapour}	1800 J/(kgK)
Heat capacity solid	C_{Solid}	450 J/(kgK)
Magnitude of external force	F	250 N/mm
Reduced elastic modulus	E_{red}	3.557e11 N/m^2
Density solid	ρ_{Solid}	7850 kg/m^3

Table 1 Simulation parameters

For the density, a zero gradient condition is applied at all boundaries. The boundary condition for the pressure is zero gradient at the walls and ambient pressure at the inlet and outlet. The velocities are set according to the kinematics for all walls and determined by the mass flux at the inlet and outlet. All divergence terms are discretized using a Gauss upwind scheme. The Laplacian terms are evaluated by a Gauss linear corrected scheme and the gradient terms are discretized according to a Gauss linear scheme. The density and temperature equations are solved by the diagonal incomplete LU preconditioned bi-conjugate gradient solver for asymmetric matrices while the diagonal incomplete-Cholesky preconditioned conjugate gradient solver for symmetric matrices is used for the pressure equation.

In the following, the influence of different oil inlet temperatures on the pressure, film thickness and velocity profiles will be investigated and the validity of the assumption of constant pressure in film thickness direction under thermal elastohydrodynamic conditions will be discussed.

Influence of oil inlet temperature

Figure 4 shows the pressure profiles for three different oil inlet temperatures. For the highest temperature of 120°C, the pressure profile equals approximately the Hertzian pressure distribution.

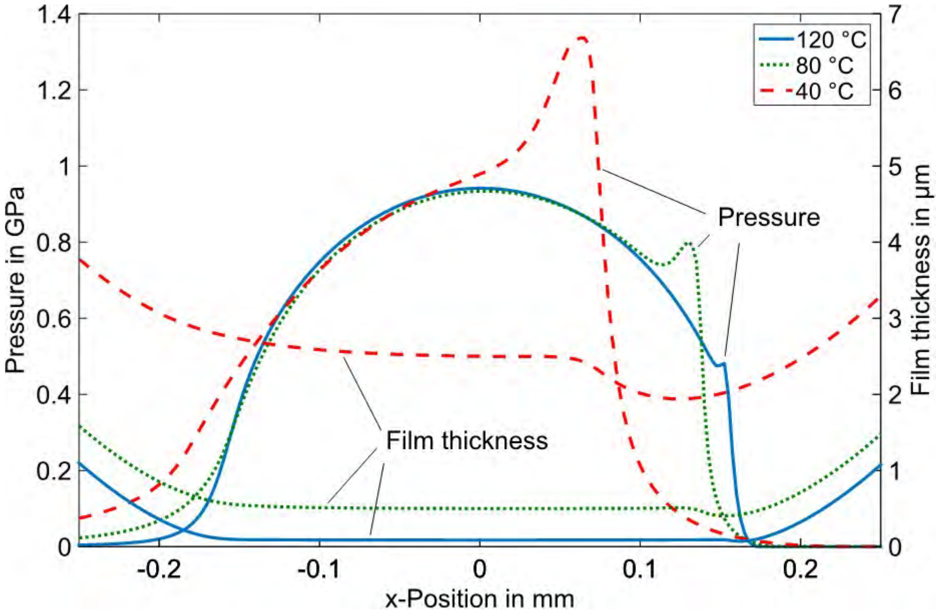

Figure 4 Calculated pressure profiles for different oil inlet temperatures

For lower temperatures, a pressure peak at the constriction becomes pronounced, which moves upstream with decreasing oil inlet temperatures. Furthermore, the high pressure region decreases for lower temperatures. Looking at the friction, the smaller high pressure region should reduce the region of high shear stresses. However, the higher pressure at lower temperatures results in a much higher viscosity and a higher friction. A similar effect can be observed for the film thickness. Comparing the 40°C case and the 120°C case, the film thickness increases approximately by a factor of 30, thereby reducing the shear rates significantly. However, at 40°C, the viscosity of the oil at ambient pressure is 80 times higher than in the 120°C case, so that in total the friction increases. Hence, these results are not able to explain the friction reduction measured for low oil inlet temperatures.

In the following, the velocity profiles will be discussed. The velocity profiles across the film thickness at position x=0 mm are illustrated in Figure 5. At this position, the influence of the pressure on the flow field is negligible and the Couette flow dominates.

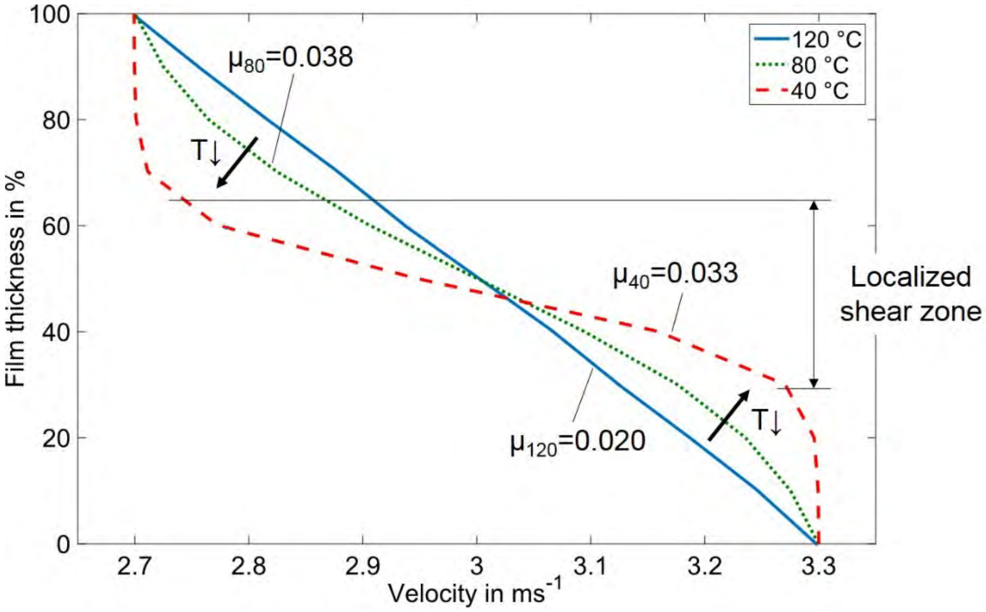

Figure 5 Calculated velocity profiles and friction values for different oil inlet temperatures

For high oil inlet temperatures, a linear velocity profile (Couette flow) can be observed. With decreasing temperature, however, the profile deviates from this shape and becomes more like a step function, localizing the shear in a small central layer of the contact. Hence, the heat generation becomes also localized in this layer, which decreases the viscosity locally and finally leads to a self-energizing thermal friction reduction. For clarification, the calculated coefficients of friction are also given in Figure 5 and show the same tendency as the ones in the experiments. However, the actual friction values differ, probably due to modelling a line contact instead of a point contact. The discussed thermal effect is also reflected by the contact temperatures for the three different cases, shown in Table 2.

	T_{Oil} = 40°C	T_{Oil} = 80°C	T_{Oil} = 120°C
Minimum Temperature	313 K	353 K	393 K
Maximum Temperature	388 K	371 K	398 K
Difference	75 K	18 K	5 K

Table 2 Contact temperatures

As expected, the temperature variation inside the contact zone becomes much larger for decreasing oil inlet temperatures due to a higher viscosity level and a thicker oil film. The temperature distribution for the 40°C case and the corresponding lines with identical viscosity values are shown in Figure 6.

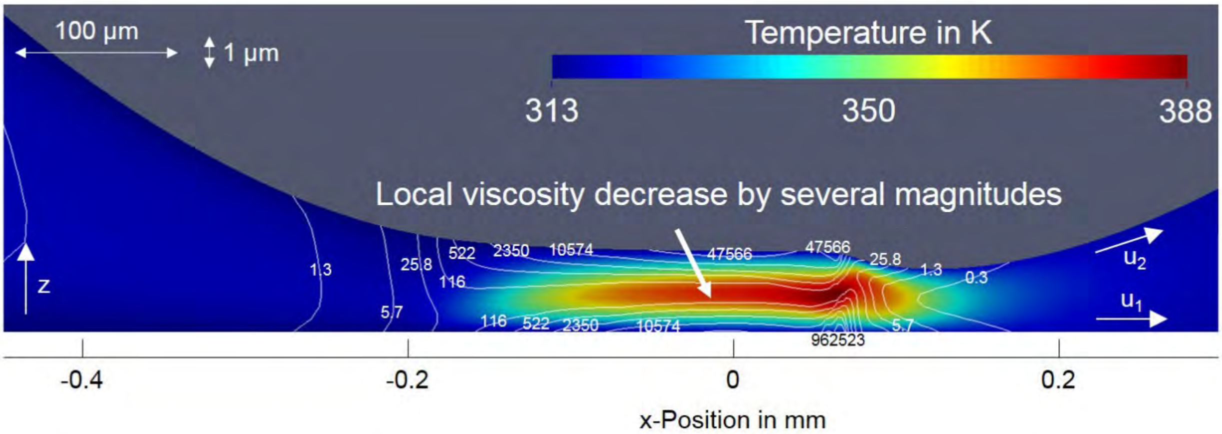

Figure 6 Calculated temperature and viscosity distribution for the 40°C case

While the viscosity is approximately constant at the inlet of the contact, the viscosity in the high pressure zone varies by approximately four magnitudes across the lubrication film height due to temperature variations. For the other cases, similar temperature and viscosity distributions can be observed, but the viscosity variations are significantly smaller (less than two magnitudes for the 80°C case and less than one magnitude for the 120°C case). In Figure 7, the flow field in x-direction is presented for two different color scales in order to visualize the thermal shear band. In the upper part, the real scale is applied and two typical phenomena become apparent. At the inlet, the film thickness decreases and the oil cannot be transferred through the contact and a recirculation occurs. The second phenomenon can be seen at the constriction. Due to the lower film thickness in this area, the velocity has to increase to satisfy continuity. If the same plot is scaled differently (lower part of Figure 7), the thermal shear band becomes clearly visible. There are two blocks across the film thickness, which move with the same speed as the two solids. The difference in speed is compensated in the low viscosity area, where the shear resistance is much lower. As mentioned above, this results in a localized heat generation and a self-energizing effect.

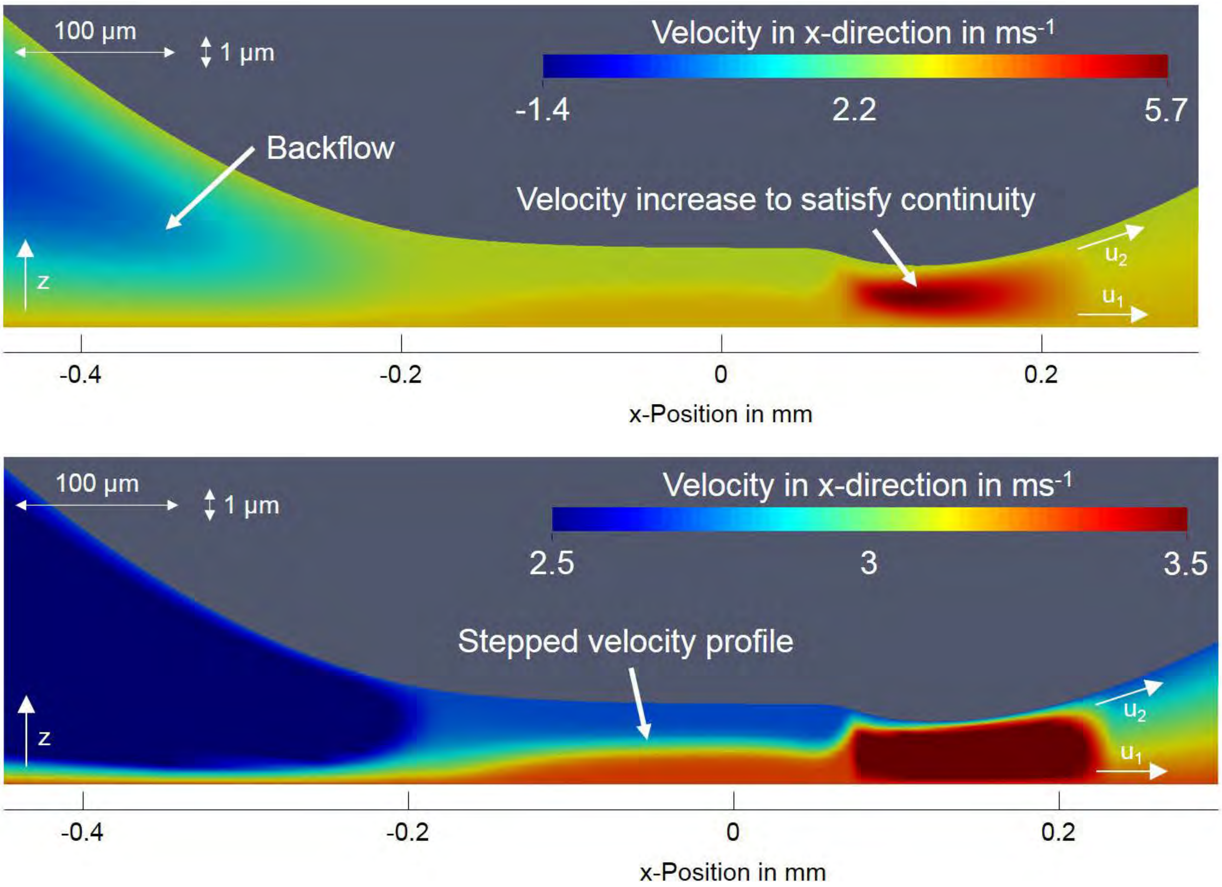

Figure 7 Calculated velocity field for the 40°C case

So far, these findings are in accordance with the results of CHANG et al.[10]. In the next section, the validity of the assumption of constant pressure across the lubrication film height under such conditions is discussed.

Validity of constant pressure across the lubrication film height

Figure 8 shows the pressure distribution and the isobars in the high pressure region for the 40°C case.

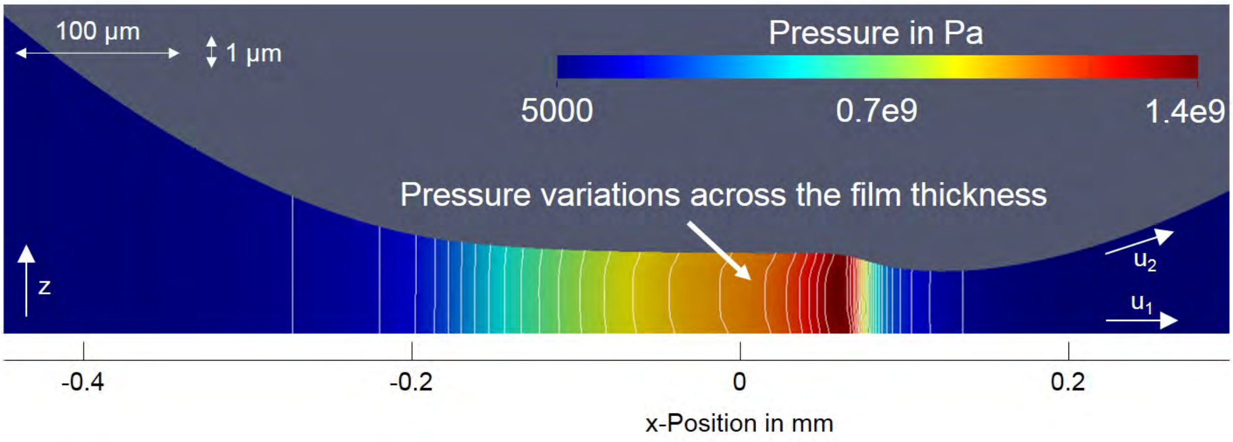

Figure 8 Calculated pressure distribution for the 40°C case

As can be observed, there are small pressure variations across the film thickness in the high pressure region, which cannot be captured by the Reynolds equation. In order to understand the origin of these variations, it is necessary to consider the Navier-Stokes equation in film thickness direction z for an infinite line contact, that is[1]

$$\underbrace{\rho\left(\frac{\partial w}{\partial t}+u\frac{\partial w}{\partial x}+w\frac{\partial w}{\partial x}\right)}_{\text{Inertia term}}=-\underbrace{\frac{\partial p}{\partial z}}_{\text{Pressure term}}+\underbrace{\frac{\partial}{\partial x}\left(\eta\frac{\partial w}{\partial x}\right)+\frac{\partial}{\partial x}\left(\eta\frac{\partial u}{\partial z}\right)+\frac{\partial}{\partial z}\left(2\eta\frac{\partial w}{\partial z}-\frac{2}{3}\eta\left[\frac{\partial u}{\partial x}+\frac{\partial w}{\partial z}\right]\right)}_{\text{Friction term}} \qquad (16)$$

For the derivation of the Reynolds equation, the inertia term and the friction term are usually neglected and a constant pressure in film thickness direction is assumed. However, for large viscosity variations across the film height, the last term on the right hand side becomes relevant. This also explains, why these pressure variations are not seen in the other two cases with higher temperatures and lower viscosity gradients.

Hence, the validity of the assumption of constant pressure across the film thickness seems to be limited by the occurrence of thermal shear bands. According to CHANG, the dimensionless parameter S_L may be used to determine the degree of thermal shear localization across the lubrication film[16]. This parameter is given by

$$S_L=\sqrt{\frac{\beta\eta_{eff}\Delta u^2}{\lambda}} \qquad (17)$$

with the temperature-viscosity coefficient β, the lubricant thermal conductivity λ, the sliding velocity Δu and the isothermal effective viscosity η_{eff}. In this work, the isothermal effective viscosity is calculated as

$$\eta_{eff}=\frac{h\tau_0}{\Delta u}\sinh^{-1}\left(\frac{\Delta u}{h\tau_0}\eta_{Houpert}(T=T_0)\right) \qquad (18)$$

with the central film thickness h. Table 3 gives an overview of the dimensionless parameter S_L for the three investigated cases in this paper.

Oil inlet temperature	Dimensionless parameter
40°C	S_L=6.29
80°C	S_L=3.25
120°C	S_L=1.88

Table 3 Values of the dimensionless parameter S_L

According to CHANG[16], thermal shear localization is usually developed for values of S_L>5 and becomes severe for values of S_L>10. This is in good agreement with the simulation and experimental results, which only show a thermal shear band for the lowest oil inlet temperature.

In order to prove the validity of this dimensionless parameter to predict also pressure variations across the lubrication film height, simulation results of two parameter variations are presented in Figure 9. For comparison, the pressure distribution for the unmodified 40°C case is also shown in Figure 9a. In Figure 9b, the thermal conductivity of the solid has been increased by 100 %. Theoretically, this should increase the heat transfer across the film height and lead to a more uniform temperature distribution and thus to lower viscosity gradients. In Figure 9c, the temperature-viscosity coefficient has been reduced by 50 %, which theoretically should result in a higher temperature and viscosity level. However, the influence of the temperature on the viscosity is reduced, so that the viscosity variations become smaller. Looking at the dimensionless parameter, both parameter variations give the same value of S_L=4.45. Hence, these two variations should yield identical results and decrease the degree of thermal shear localization and the degree of pressure variations across the film thickness.

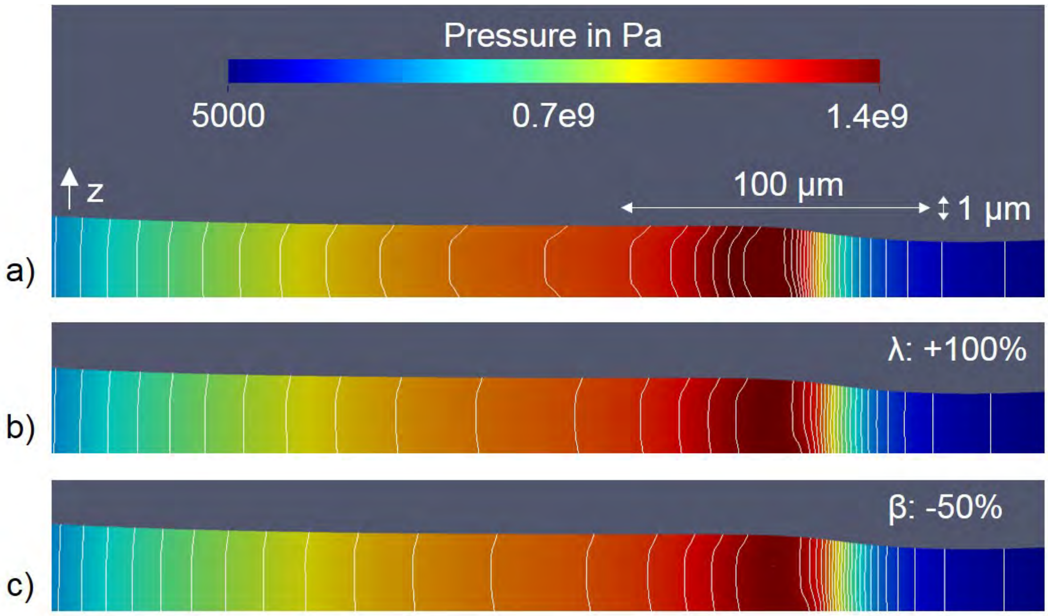

Figure 9 Calculated pressure distribution for different thermal parameters

As can be seen, this behaviour is indeed visible in the simulation results. Although the temperature and viscosity levels of both parameter variations are not identical within the contact, the pressure distributions look very similar and the degree of pressure variations across the film thickness is reduced (see the bending of the isobars). This stresses the fact that only the viscosity gradients are responsible for these pressure variations. As shear localization also requires large viscosity gradients across the film thickness, the dimensionless parameter S_L with the criterion $S_L \gg 5$ developed by CHANG[16] seems to be a good indicator not only for the degree of shear localization but also for the degree of pressure variations across the film thickness under thermal elastohydrodynamic conditions.

Conclusion

In this work, a CFD-based TEHL simulation method has been applied to three test cases with different oil inlet temperatures in order to understand the unexpected friction reduction measured on a ball-disc-tribometer for low oil temperatures. The simulation results reveal that a thermal shear band develops when decreasing the oil inlet temperature. The velocity profile across the lubrication gap height changes from the usual Couette-Poiseuille profile to a step function, localizing the heat generation in a central layer of the contact. This decreases the lubricant viscosity locally by several orders and reduces the overall friction. Furthermore, the high viscosity gradients inside the lubricant lead to pressure variations across the lubrication gap height. To predict the degree of pressure variations across the film thickness in advance, the dimensionless quantity S_L seems to be a good indicator. For values of $S_L \gg 5$, pressure variations are most likely to occur and the assumption of constant pressure across the film thickness made by the Reynolds equation should be reviewed critically.

Acknowledgments

This research has been funded by the Excellence Initiative of the German federal and state governments.

References

1. Bartel, D. 2010, Simulation von Tribosystemen, 1st ed., Vieweg+Teubner Verlag, Wiesbaden
2. Almqvist, T. and Almqvist, A. and Larsson, R., 2004, “A comparison between computational fluid dynamics and Reynolds approaches for simulating transient EHL line contacts”, Tribol. Int., 37, pp.61-69.
3. Hartinger, M. and Dumont, M.-L. and Ioannides, S. and Gosman, D. and Spikes, H., 2008, “CFD Modeling of a Thermal and Shear-Thinning Elastohydrodynamic Line Contact”, J. Tribol., 130, pp.041503-1-041503-16.
4. Hajishafiee, A. and Dini, D. and Kadiric, A. and Ioannides, S., 2013, “A fully coupled finite volume solver for elasto-hydrodynamic lubrication problems with particular application to rolling element bearings”, Proc. World Tribol. Cong., Italian Tribology Association, Torino, Italy, Paper 1151.
5. Feldermann, A. and Neumann, S. and Jacobs, G., 2015, “CFD Modeling of Elastohydrodynamic Lubrication Using Reduced FE-Models”, EcoTrib, Swiss Tribology, Zurich, Switzerland.
6. Feldermann, A. and Neumann, S. and Jacobs, G., 2015, “CFD Simulation of Elastohydrodynamic Lubrication with Reduced Order Models for Fluid-Structure Interaction”, TurkeyTrib, Istanbul, Turkey.
7. Van Lier, H., 2015, “Neuhärtungsgefährdung von Radial-Zylinderrollenlagern durch Lastaufschaltungen in Betriebspunkten mit Käfigschlupf“, Doctoral thesis, RWTH Aachen University.
8. Willermet, P. A. and McWatt, D. G. and Wedeven, L. D., 1999, “Traction Behavior Under Extreme Conditions”, SAE Technical paper 1999-01-3612,
9. Webster, M. N. and Lee, G. H. and Chang, L., 2006, “Effect of EHL Contact Conditions on the Behavior of Traction Fluids,” Tribol. Trans., 49, pp.439-448.
10. Chang, L. and Qu S. and Webster, M.N. and Jackson, A., 2006, “On the Mechanisms of the Reduction in EHL Traction at Low Temperature”, Tribol. Trans., 49(2), pp.182-191.
11. OpenFOAM User Guide, n.d., from http://cfd.direct/openfoam/user-guide/ (accessed 14 May 2016).
12. Stein, E. and De Borst, R., 2004, Encyclopedia of Computational Mechanics, 1st ed., John Wiley & Sons, New York, USA, Chap. 14.

13. Issa, R.I., 1985, “Solution of the Implicitly Discretized Fluid Flow Equations by Operator-Splitting”, J. Comput. Phys., 62, pp.40-65.

14. Bair, S., 2007, “High Pressure Rheology for Quantitative Elastohydrodynamics”, 1st ed., Elsevier, Amsterdam, Netherlands.

15. Jaeger, J. C, 1943, "Moving sources of heat and the temperature at sliding contacts", Proc. Roy. Soc. N. S. W., 76, pp.203-224.

16. Chang, L., 2006, “A parametric analysis of the thermal shear localization in elastohydrodynamic lubrication films”, J. Tribol., 128, pp.79-84.

An experimental approach on slip behaviour of tapered roller bearings

Thorsten Fingerle, M.Sc. / Kevin Greib, B.Sc. / Prof. Dr.-Ing. Bernd Sauer

Summary

Authors present an experimental study on slip behaviour of tapered roller bearings used at the high speed shaft of wind turbine gearboxes. Parameters with main impact on slippage are identified by pre-tests. In the main test these parameters are varied over a larger range and a mathematical relationship is derived from those results. Doing so, it was possible to propose a formula for the calculation of the minimum load for tapered roller bearings. Finally this calculation method was compared to known equation e.g. from bearing manufacturers and the literature.

Keywords: slippage, tapered roller bearings, smearing, minimum load

Introduction

In wind turbine gearboxes cylindrical roller bearings (CRB) as well as tapered roller bearings (TRB) are used to support the system's load. Due to relatively high gear ratios of i ≈ 100, there are different requirements for bearings in wind turbine gearboxes depending on their position. In the majority of cases a planetary stage is used to carry the rotor torque, where planet bearings are under high load with low speed. In contrast, bearings at the output shaft need to support low loads and high revolutions. Furthermore, in order to reduce noise, helical gearing is applied in most cases. Therefore, TRB are used to retain the resulting axial loads. Figure 1 illustrates the use of bearings in wind turbine gearboxes with focus on the high speed shaft.

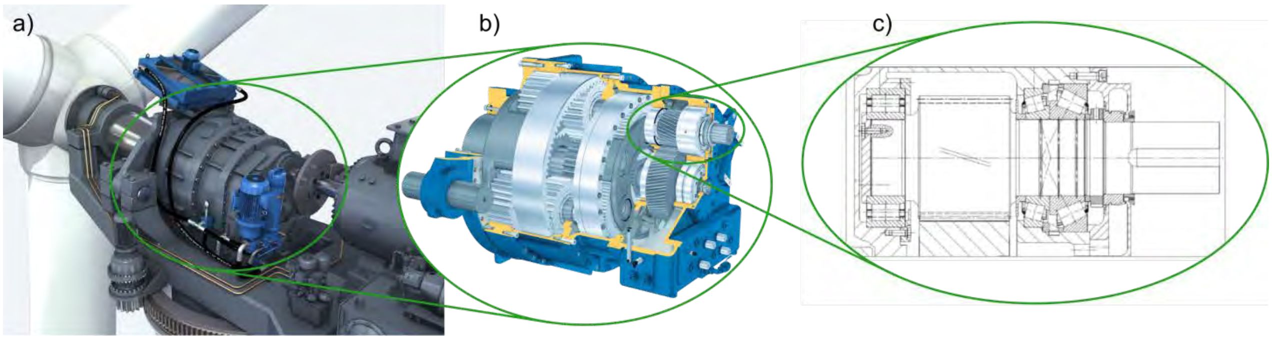

Figure 1: Use of rolling bearings at high speed shafts of wind turbine gearboxes: a) wind drive train, b) gearbox with three planetary stages and a spur gear stage, c) high speed shaft with CRB and paired TRB to retain axial load as a result of helical gearing

In practice, the method of bearing lifetime calculation follows ISO16281 [1] and is based on material fatigue, where the material fatigue limit load is related to the occurring load. Calculations are based on the theoretical model of Lundberg and Palmgren [2]. According to their theory the fatigue damage has its origin on the material's subsurface in the area of maximum shear stress. By deriving the material characteristics from experimentally determined Woehler curves the theory supplies a survival probability for bearing material and in conclusion the bearing itself. Other damage mechanisms are not taken into account. As mentioned above, bearings in wind turbine gearboxes are used in a wide variety of conditions depending on their position. However, their design is based on the same calculation process according to ISO16281 [1]. In the majority of cases, however, material fatigue is not the damage mechanism at output shafts. Here, conditions of high speeds and low loads result in bearing failures prior to their predicted lifetime, which cannot be solely reduced to material fatigue. There have been damages observed due to slippage. Especially smearing failures occur at cylindrical roller bearings as well as tapered roller bearings in field. While the slip behaviour of CRB as well as smearing are investigated [3][4][5][6], slippage of TRB has not been a focus of recent studies. One reason for this could be that preloaded tapered roller bearings are not normally at risk for slippage. But in some cases TRB are used without enough preload due to increasing operating temperatures (e.g. wind turbine gearboxes). Therefore, this article aims to investigate parameters influencing slip behaviour under those conditions. Thereby, this study provides a basic understanding of slippage conditions in TRB in order to avoid smearing failures.

State of research

Bearing speeds, slippage and minimum load

Cage revolution is defined by the geometrical relation between the raceways and the roller. As shown in Figure 2, the cage circumferential velocity depends on the proportion of roller radius and bearing pitch radius.

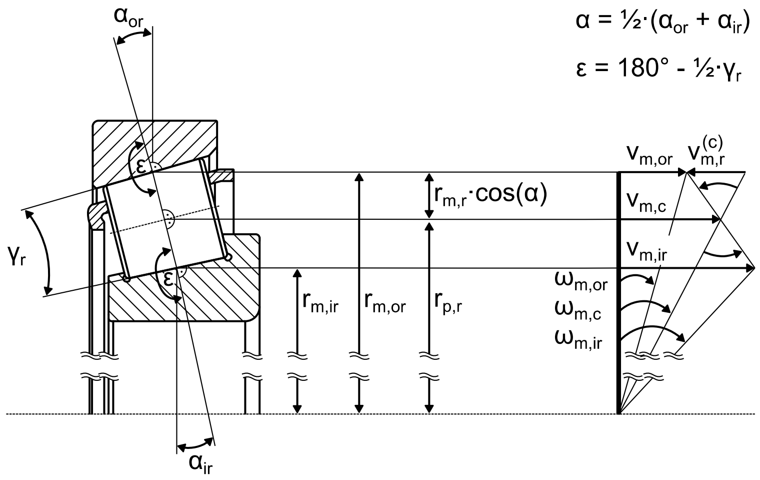

α	:resulting contact angel [°]
α_{rw}	:contact angel raceways [°]
γ_r	:tapered roller included angle [°]
$r_{m,rw}$	:mean radius raceways [mm]
$r_{p,r}$	:bearing pitch radius [mm]
$\omega_{m,rw}$	:mean angular velocity raceways [rad/s]
$\omega_{m,c}$	:mean angular velocity cage [rad/s]
$v_{m,rw}$	:circumferential velocity raceways [mm/s]
$v_{m,c}$	:circumferential velocity cage [mm/s]
$v^{(c)}_{m,r}$	:circumferential velocity roller related to cage [mm/s]

Figure 2: Circumferential velocities and geometry of a tapered roller bearing, modified acc. to [7]

In the majority of applications, the outer ring is fixed in the housing while the inner ring is mounted on the shaft turning with its speed. For this case and under assumption of slip-free conditions, $n_{c,kin}$ and $n_{r,kin}$ are calculated as follows [7]:

$$n_{c,kin} = \frac{n_{ir}}{2} \cdot \left(1 - \frac{\cos(\alpha_{or})}{\frac{d_m}{d_r}} \right) \tag{1}$$

$$n_{r,kin} = -\frac{n_{ir}}{2} \cdot \left(\frac{d_m}{d_r} - \frac{\cos^2(\alpha_{or})}{\frac{d_m}{d_r}} \right) \tag{2}$$

where

n_{ir}:	revolution of inner ring [1/s]
α_{or}:	outer raceway contact angle [°]
d_m:	bearing pitch diameter [mm]
d_r:	roller diameter [mm]

Figure 3a illustrates the load situation for a tapered roller bearing with a rotating inner ring but fixed outer ring. The external radial load is applied to the inner ring and results in a ring displacement. Due to the shift of the inner ring, the radial deflection at any rolling element depending on its angular position around the scope is a function of contact force. For static equilibrium, the applied load must equal the sum of the rolling elements loads [8]. The area of loaded rollers is called load zone. Figure

3b describes the normal force for one roller during one revolution of the cage. In addition, the speed curve is shown. If the external load is high enough, the roller reaches its kinematic speed within the load zone as shown in eq. (2). Inside the unloaded zone the roller has less contact to the raceways and slows down. Friction between the inner ring flange and the cage decelerate the roller until re-entering the load zone under high acceleration within the next circulation.

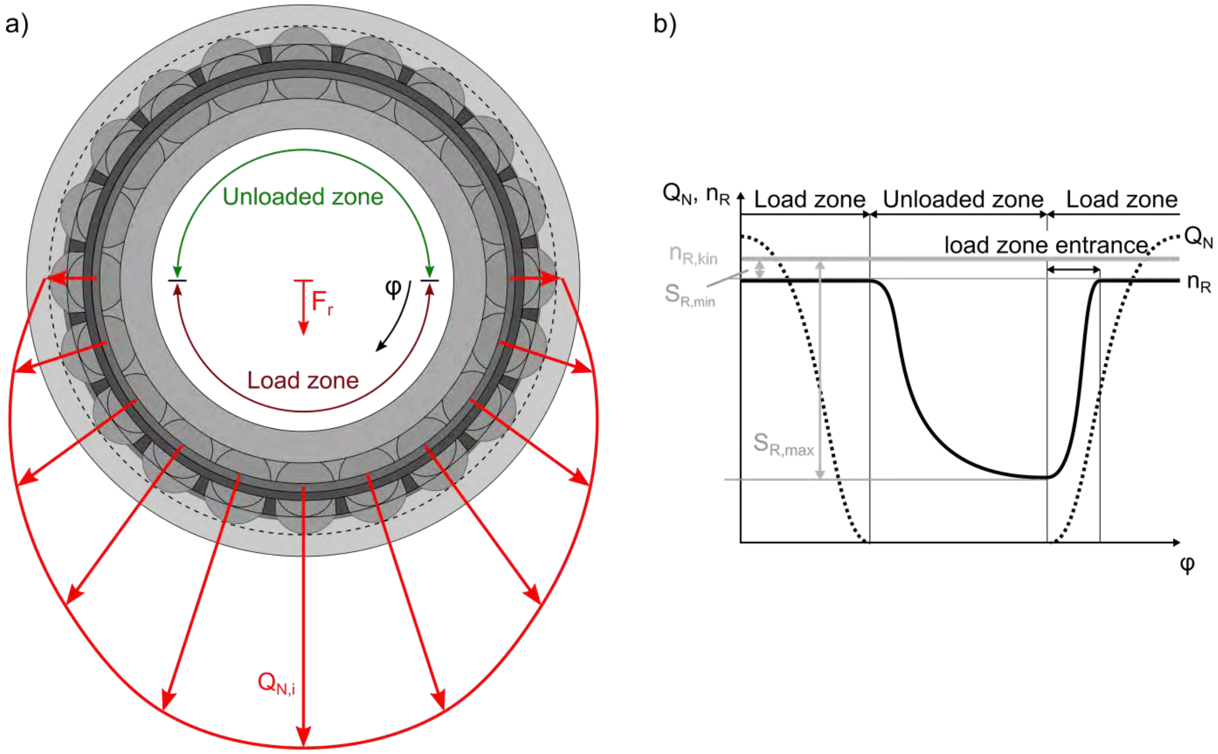

Figure 3: a) example of a load zone for a TRB, b) resulting kinematic zones for one scope [9]

Scherb [10] distinguished slippage values between the loaded and unloaded zone, where the maximum roller slippage is defined in the unloaded zone. As explained above, the roller is slowed down in this area due to friction forces resulting from contact between end flange and cage pocket, and therefore, the gap to the kinematic revolution is maximal. The maximum roller slip is defined as follows:

$$S_{r,\max} = \left(1 - \frac{n_{r,\min}}{n_{r,kin}}\right) \cdot 100\% \tag{3}$$

where

$n_{r,min}$: measured minimum roller revolution [1/s]

$n_{r,kin}$: kinematic roller revolution acc. to eq. (2) [1/s]

If the external load is too low, roller slippage occurs within the load zone. This indicates minimum roller slippage, which can be calculated as described in eq. (4).

$$S_{r,\min} = \left(1 - \frac{n_{r,\max}}{n_{r,kin}}\right) \cdot 100\% \tag{4}$$

where

$n_{r,max}$: measured maximum roller revolution [1/s]

$n_{r,kin}$: kinematic roller revolution acc. to eq. (2) [1/s]

Bearing manufacturers provide formulas to estimate a safe operation relating to slip. In addition to that, research projects dealt with the same topic. In general, the minimum load separates safe and unsafe load conditions. If the external load drops below the minimum load bearing failures may occur. The limit value for minimum load according to FAG and SKF for tapered roller bearings is based on the dynamic load rating C_{dyn} [11][12].

$$F_{\min,FAG,SKF} = 0.02 \cdot C_{dyn} \tag{5}$$

where

C_{dyn}: dynamic load rating [kN]

Spechtel derived a formula from experiments focussing on accelerated bearings [5] and defined slip-free condition by a radial minimum load as follows:

$$F_{r,\min,Spechtel} = f_g \cdot f_b \cdot f_s \cdot f_v \cdot C_0 \tag{6}$$

where

f_g: basic factor [-]

f_b: acceleration factor [-]

f_s: fluid factor [-]

f_v: viscosity [-]

C_0: static load rating [kN]

Using the static load rating C_0 offers the benefit that the minimum load only depends on geometry, while the dynamic load rating C_{dyn} includes changing parameters like number of rollers and material quality. These factors are part of an ongoing process of optimization and therefore not useful for a universal formula [5].

Damage mechanisms due to slippage

Bearing operation on slip conditions may result in two different types of damage mechanisms. Firstly, smearing is understood as a type of adhesive wear. Due to high relative movement between roller and raceways in combination with high contact pressure the oil film may collapse. This results in solid-to-solid contact, where surfaces of contact partners weld and rip. Due to this pre-damage a consequential abrasive bearing failure occurs after a period of time. In each case bearings fail prior to their calculated lifetime.

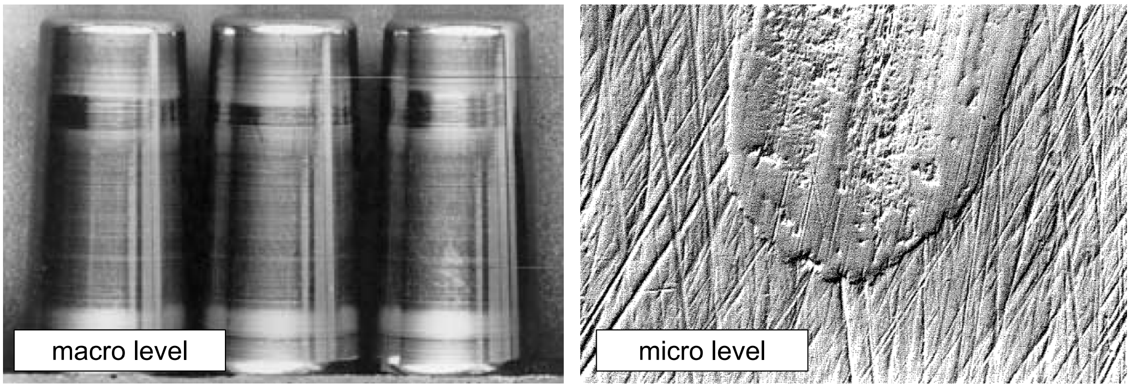

Figure 4: Smearing damage on macro [9] and micro level [13]

A smearing damage (Figure 4) can be recognised by visual inspection of roughened surface areas in circumferential direction (macro level). Using a microscope, it is possible to detect a smear (micro level).

Secondly, re-hardening is another damage mechanism caused by slippage. It requires high contact temperatures due to high contact pressures and increasing friction values. Under such conditions a structural change right under the surface may occur due to energy input on the surface. Within the boundary zone austenitizing temperature is reached for a short period of time followed by self-quenching. This process is remarkable faster than usual heat treatment with temperature ramps up to 10000 K/s [14][15]. An etched sample is shown in Figure 5, where the re-hardening zone can be recognised as a white etching layer (WEL).

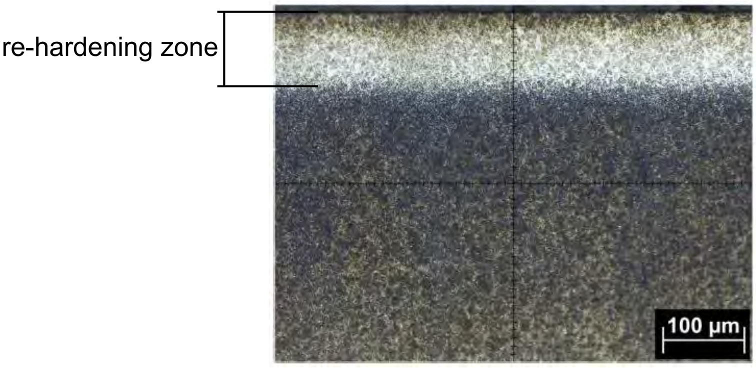

Figure 5: Sample with re-hardening zone (white etching layer) [14]

Besides smearing and re-hardening, research projects assumed that slippage has an influence on white etching cracks (WEC) [16].

All damage mechanisms show that it is necessary to build up a deeper understanding of slippage in terms of critical operating conditions and influencing parameters.

Test rig

The experiments were operated with a bearing test rig, built to investigate cylindrical roller bearings of high speed shafts in wind turbine gearboxes [3]. To analyse TRB, the test rig was redesigned. Figure 6 illustrates the setup used for the experiments shown in this paper.

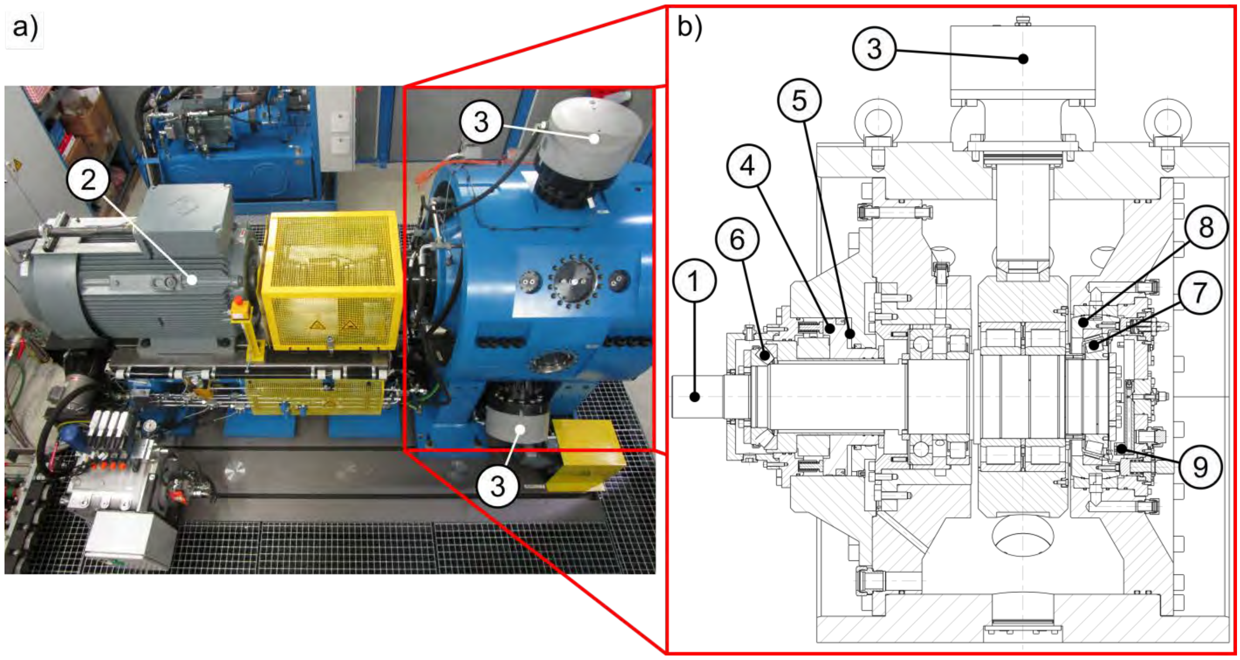

Figure 6: Test rig to analyse roller bearings at high speed shafts of gearboxes for wind turbines, a) overview, b) drawing; tested TRB: 30234; C_{dyn}*=590 kN, wind oil ISO VG 320*

The driveshaft (1) is turned by a 200 kW asynchronous motor (2). The test rig allows axial as well as radial loading. The radial load is applied by three hydraulic cylinders (3), placed at 90°, 210° and 330° around the scope. By superposition of the three single forces, the resulting load can be applied at any angle between 0° and 359°. The axial load is put on by a flange (4), which moves when the hydraulic oil pressure increases in the hollow space (5). Force is transmitted by a self-aligning spherical roller thrust bearing (6) into the shaft. Due to this design, axial force can only be applied in one direction. Therefore, the installation condition of the test bearing (7) was given before the redesign started. The TRB is mounted in a ball-and-socket joint (8) to enable tilting and skewing between its outer and inner ring (0' - 10'). In addition to that the direction of the oil injection can be varied for the test bearing by a rotating arm (9). Furthermore, the charge volume of the oil injection can be changed between 0 l/min and 7 l/min. The oil temperature (25°C - 90°C) and the oil level (0 mm - 400 mm) are also varying parameters. To investigate its influence on the dynamic behaviour of TRB, preloading can be changed by shim rings in a range from -1000 µm up to +1000 µm. Table 1 summarises the adjustable parameters.

Category	Parameter	Unit	Values range
Loading	Preloading	µm	-1000 to 1000
	Axial load	kN	0 to 2000
	Radial load	kN	0 to 2000
	Load angle	°	0 to 359
Misalignment	Tilting	'	0 to 10
	Skewing	'	0 to 10
Lubrication	Charge volume	l/min	0 to 7
	Direction of oil injection	°	30 to 330
	Oil temperature	°C	25 to 90
	Oil volume	%	0 to 100
Revolution	Revolution	min^{-1}	0 to 2000

Table 1: Adjustable parameters of roller bearing test rig

Measurement of roller and cage revolution

The target values of the experimental approach are cage and roller slip. Therefore, the revolutions of the cage and one roller have to be measured. The measuring principle for the roller speed is shown in Figure 7. A diametrical magnet is fixed to the end wall of one roller while an inductor is integrated on the cover plate in front of the test bearing. Upon roller turning, the magnet induces a current to the inductor. The corresponding voltage is detected. A similar procedure as shown by Stadler [17], but without magnetising the whole roller. Nevertheless, by evaluating the zero-crossing points, minima and maxima, the roller revolution can be calculated around the full scope. Alternatively, it is possible to evaluate the roller revolution by frequency demodulation [18].

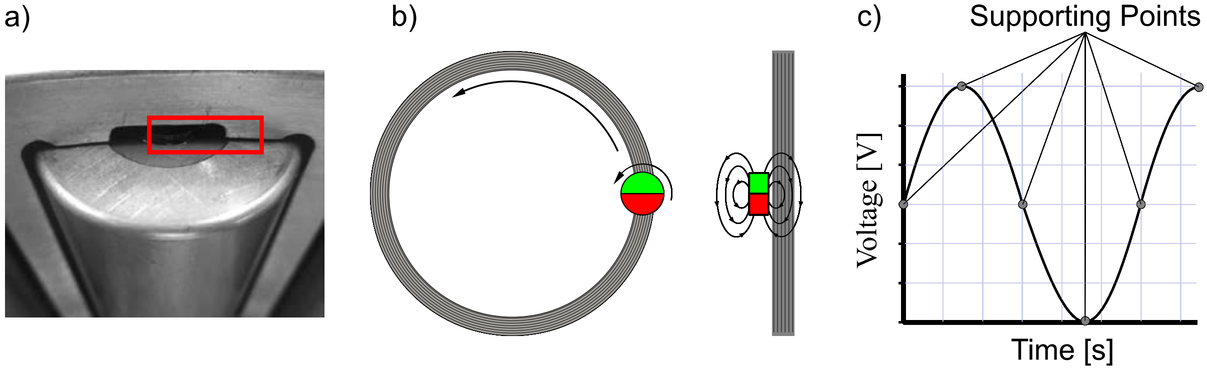

Figure 7: Measuring principle of roller revolution around the full scope by using a diametrical magnet a) and an inductor b) resulting in a voltage signal c)

The cage revolution is measured by a hall sensor and a magnet, which is mounted on the cage. The sensor detects the magnet at any pass. Hence, the cage revolution is calculated by counting the peaks per second. Furthermore, the magnet is displaced by 180° to the measured roller. Matching the time signal of cage and roller, the location of the roller with the measuring system is clearly defined around the full scope.

Identification of main influencing parameters for slippage in TRB

Aiming to identify the main influencing parameters, pre-tests have been carried out. All adjustable parameters of the roller bearing test rig are investigated in regards to their influence. For such tasks it is useful to apply the variable search technique according to Shainin [19]. The method can be described as a screening process used to identify the key factors and their settings on a specific system [19]. A major advantage of this method is its efficiency. Thereby, it is possible to identify the main influencing parameters with a low number of experiments.

A preliminary step in this technique is the determination of two extreme values for each parameter. The values in the column “best/high slip” lead to the best possible outcome for this test (Table 2), while values given in the column “worst/low slip” result in the least favourable outcome. Determination of the setting values is based on previous tests or experience, the latter being a difficulty of this method. Table 2 shows the determination of all adjustable parameters.

Category	Parameter	Unit	"best" / high slip	"worst" / low slip
Loading	Preloading	µm	-200	200
	Axial load	kN	1	15
	Radial load	kN	4	27
	Load angle	°	270[a]	90[b]
Misalignment	Tilting	'	0	5
	Skewing	'	0	5
Lubrication	Charge volume	l/min	5	0.5
	Direction of oil injection	°	-90[c]	90[d]
	Oil temperature	°C	45	70
	Oil volume	%	15[e]	0
Revolution	Revolution	min^{-1}	1500	700

Table 2: Determination of all adjustable parameters for pre-testing; [a]against gravity direction; [b]in gravity direction; [c]in front of load zone; [d]behind load zone; [e]lower roller coverage; tested TRB: 30234; C_{dyn}*=590 kN; wind oil ISO VG 320*

Preloading was chosen based on experience, while values for axial and radial load were determined in previous tests. In respect to load angle, it was assumed that the position of load zone against gravity direction increases slippage because of lower contact forces between the rollers and raceways. Higher values of tilting and skewing angles are reducing slip due to occurring constraining forces on the roller. Theoretically, the lubricating film has an influence on slip behaviour because the lower the lubricant film height, the more solid-to-solid contact occurs. Thus, the friction forces increase and the slippage drops. For this reason, charge volume with higher values is supposed to increase slippage. The direction of oil injection may have an influence. Changing the parameter in relation to load zone seemed therefore appropriate. Additionally, the lower the oil temperature, the thicker the oil film. As explained before, the risk for solid-to-solid contact is reduced and higher values of slippage are expected under low temperatures. The oil volume increases frictional torque and thus resistance as well as power loss. As a result, slippage values drop. For that reason, the lower roller is covered with oil for level “best” (value=15 %; no coverage with oil equals 0 %).

When the values for the testing conditions “best” and “worst” are determined, reference tests need to be performed. Therefore, all parameters are set to level “best” simultaneously (acc. to Table 2). After taking measurements, all parameters are changed to setting “worst”. The two runs are then replicated six times to test for statistically significance [20]. Data is checked by evaluating median and range (eq. (7), (8)). To finally investigate which parameter has an influence on the target, all parameters are set to level “best” while changing each parameter one by one to “worst”. If the target value is affected by the varied parameter, it results in a deviation from the reference line in the plot. Figure 8 shows a typical Shainin plot. In this example factor “E” has a major influence on the target value while “H” has a minor impact on it. All other parameters have no significant influence on target.

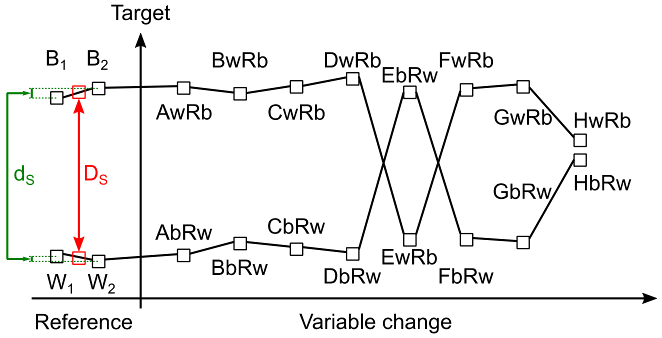

Figure 8: Scheme of a Shainin plot

$$D_S = \left| \frac{B_1 + B_2}{2} - \frac{W_1 + W_2}{2} \right| \tag{7}$$

$$d_S = \frac{|B_1 - B_2| + |W_1 - W_2|}{2} \tag{8}$$

where

$B_{1,2}$: Reference best [*]

$W_{1,2}$: Reference worst [*]

*target unit

Main factors influencing slippage in TRB

All adjustable parameters are investigated with respect to their influence on three slip factors according to Scherb [10]: cage slippage as well as minimum and maximum roller slippage was considered. As described, the reference tests have to be significantly different between the chosen values for settings “best” and “worst”. Table 3 shows the results of the calculated median and range according to eq. (7) and (8).

	Cage slippage [%]	Minimum roller slippage [%]	Maximum roller slippage [%]
D_S	51.08	71.13	62.87
d_S	2.70	2.97	2.53
D_S:d_S ≥ 5:1	18.93	23.95	24.88

Table 3: Evaluated median and range of reference levels “best” and “worst” (acc. to eq (7) and (8))

It can be seen that the difference between the chosen values for levels “best” and “worst” are well within the required range according to [20]. Therefore it is possible to use these reference tests as a basis for the following variable change experiments.

Figure 9 shows the Shainin plot for the target minimum roller slippage, illustrating all investigated parameters as well as the reference tests. With respect to the reference line for level “best” (light grey dashed line), axial and radial load have the biggest impact on minimum roller slip behaviour followed by inner ring revolution. Initially, these factors were expected to be the main influencing parameters, which is now experimentally confirmed. Axial load is able to abolish slippage completely while radial load has a slightly lower impact on slippage. This results from a more efficient extension of the load zone due to axial load. Besides those three determined parameters, load angle has a minor influence on minimum roller slippage. There is obviously a difference between the load application in or against gravity direction. By amending the load angle in gravity direction, slip drops by 40 %. This influence might correlate with the bearing size. Higher roller and cage weight result in more mass inertia. Especially when the load zone is located at the bottom, additional dynamic forces due to centrifugal forces result in higher contact and friction forces and thus less slip. The last investigated factor influencing TRB slip is oil temperature. The oil film thickness depends on its temperature and is inversely correlated. Therefore, at high oil temperatures low film thickness might result in solid-to-solid contact, increased friction and lower slippage. For all other investigated parameters, no significant influence on minimum slip behaviour could be detected.

In the reference experiment for level “worst”, negative slip values less than 10 % were obtained. Partially, this results from the approximate calculation of the kinematic revolution (eq. 2). Instead of the geometrically more precise mean contact angle between inner and outer ring, the outer ring contact angle α_{or} is used. In an exemplary calculation this reduced the negative slip by 2 % as compared to the calculation suggested in (eq. 2). In addition, the roller revolution could have been underestimated due to micro-geometry (e.g. profile), resulting in negative slip for level “worst”.

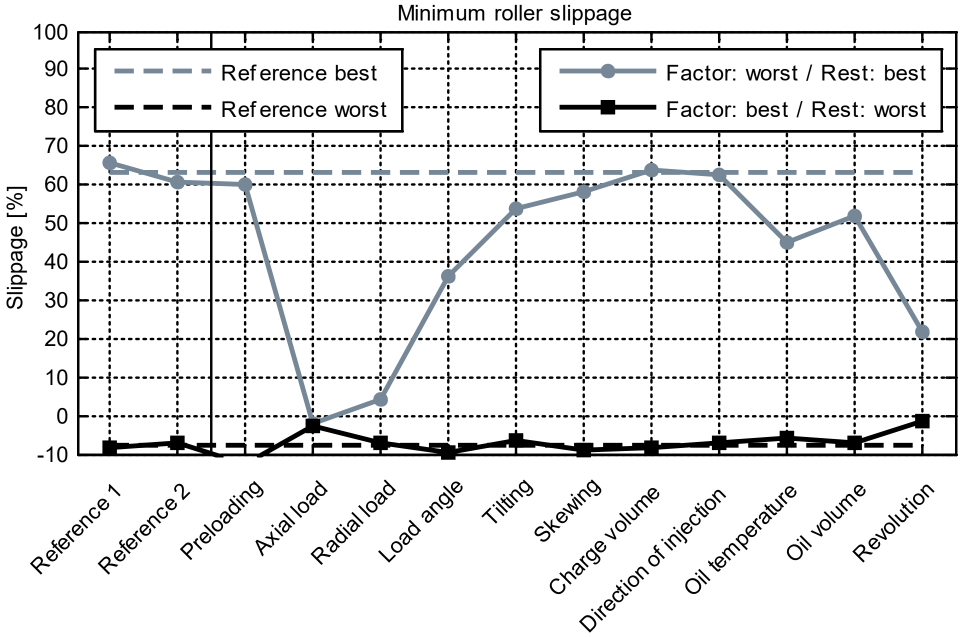

Figure 9: Shainin plot for target value minimum roller slippage; major influence: axial and radial load, revolution; minor influence: load angle, oil temperature, oil volume (tested TRB: 30234; C_{dyn}=590 kN, wind oil ISO VG 320)

Maximum roller slip, the second target investigated, was influenced by the same main parameters as minimum roller slip (Figure 10).

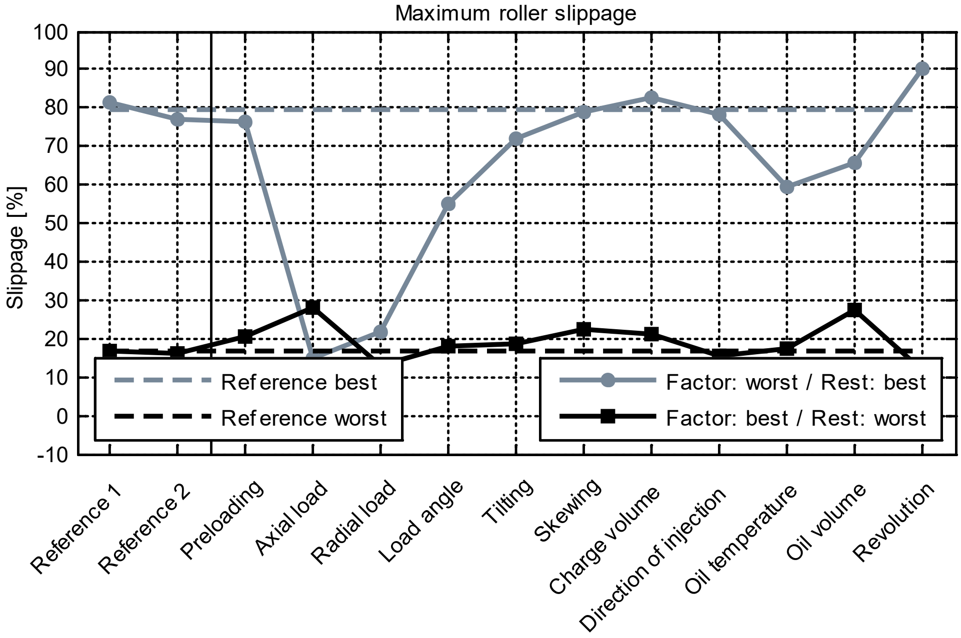

Figure 10: Shainin plot for target value maximum roller slippage; major influence: axial and radial load, revolution; minor influence: load angle, oil temperature (tested TRB: 30234; oil: ISO VG 320)

In Figure 10, the opposite behaviour of revolution compared with the result shown in Figure 9 is remarkable. Slippage increases with decreasing inner ring speed. This is consistent with the finding of van Lier [14] that especially in terms of maximum roller slippage, increasing revolution results in less slip. Van Lier showed that roller differential speed between load zone and unloaded zone is independent from the inner ring revolution. Slippage drop with increasing revolution is explained by definition of slip acc. to eq. (4) as a related factor.

The main influencing parameters on cage slippage are presented in Figure 11. In accordance with minimum and maximum roller slippage, axial and radial load as well as revolution are the main factors influencing cage slip. Preloading has apparently no impact on tapered roller bearing slippage. As shown in Table 2, preloading for testing condition “worst” was set to 200 µm. This equals an axial load of 1 kN which is obviously too low to influence slip behaviour. For theoretical purposes, higher values of preloading must have an impact on slip behaviour because it corresponds to axial load, which was detected as the biggest influencing factor. Therefore, determination of the preloading value in this experiment was made too low. Additional testing with different preloading values is further required to estimate its actual influence.

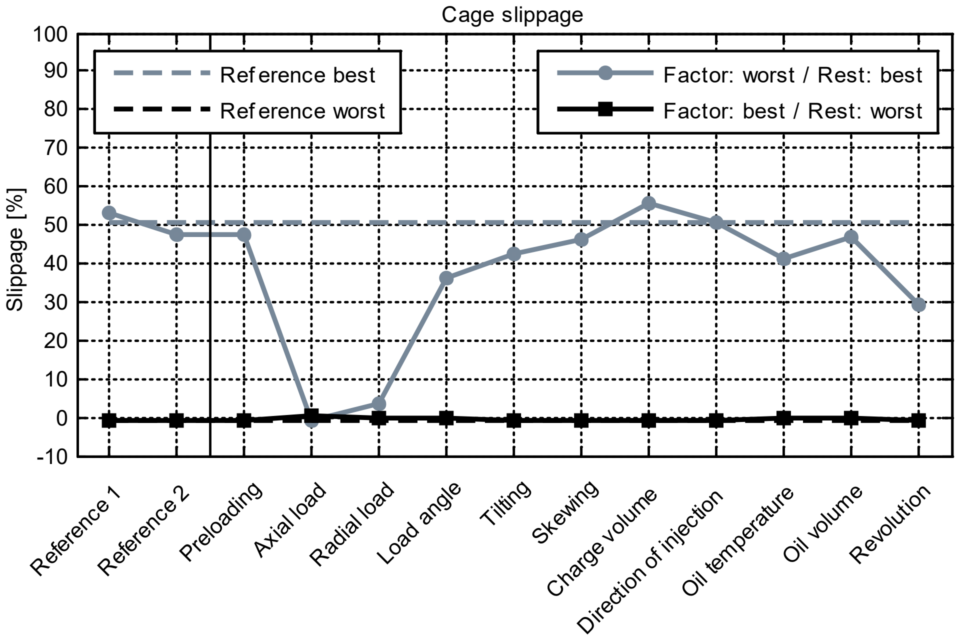

Figure 11: Shainin plot for target value cage slippage; major influence: axial and radial load; minor influence: load angle, oil temperature, revolution (tested TRB: 30234; oil ISO: VG 320)

To summarise the results of pre-testing, Table 4 shows the relative deviation of each parameter to the reference line. The factors are classified by the calculated deviation. A parameter which is able to change the target value by 50 % is considered to have a major influence, while causing more than 17 % change (1/3 of 50 %) is defined as a minor impact. All factors below 17 % are declared as non-influencing parameters.

		Deviation from reference line [%]		
		Min. roller slip	**Max. roller slip**	**Cage slip**
Category	**Parameter**	**Rest "best"**	**Rest "best"**	**Rest "best"**
Loading	Preloading	6	4	6
	Axial load	103	81	101
	Radial load	94	72	92
	Load angle	42	30	29
Misalignment	Tilting	15	9	16
	Skewing	8	0	9
Lubrication	Charge volume	-1	-5	-11
	Direction of oil injection	2	1	0
	Oil temperature	29	25	18
	Oil volume	18	16	7
Revolution	Revolution	66	-14	42

Table 4: Quantitative identification of main factors influencing slippage from pre-tests; major influence (grey); minor influence (light grey); no significant influence (white) (tested TRB: 30234; C_{dyn}=590 kN, wind oil ISO VG 320)

Main experiments

The influence of all detected parameters obtained through pre-testing was investigated in detail by main experiments, aiming to provide a relation between each considered factor and slippage. Due to the high number of parameters “Design of Experiments” (DoE) has been applied to create the experimental design. All in all 230 experiments including 5 retries each stage were done by a d-optimal design. Finally, the tests were evaluated by regression analysis aiming to find a fitting curve for each parameter. Table 5 shows the different stages for the main tests in terms of the influencing parameters. All other factors are kept constant during the experiments. The choice of values for all parameters was based on real application conditions for bearings at high speed shafts of wind turbine gearboxes, hence a typical wind oil was used (ISO VG 320).

Category	Parameter	Unit	Level 1	Level 2	Level 3	Level 4	Level 5	Level 6
Loading	Axial load	kN	0	2.4	4.8	7.2	9.6	12
	Radial load	kN	0	4	8	12	16	20
	Load angle	°	0	90	180	270	-	-
Lubrication	Oil temperature	°C	40	47.5	55	62.5	70	-
	Oil volume	%	0	16.6	33.3	50	-	-
Revolution	Revolution	min^{-1}	700	920	1140	1360	1580	1800

Table 5: Main testing experimental stages for identified influencing parameters; constant parameters: preloading=-200 µm; Tilting & Skewing=0’; charge volume=3.5 l/min; direction of oil injection=0°, tested TRB: 30234; C_{dyn}=590 kN, wind oil ISO VG 320

The parameters axial and radial load can be summarised in the equivalent bearing load P_{eq}. This is a useful way of presenting influence of loading. Due to the contact angle, radial load should not be isolated and treated separately because of its reinforcement. Figure 12 represents the correlation between P_{eq} and slippage with respect to cage slippage, minimum roller slippage and maximum roller slippage.

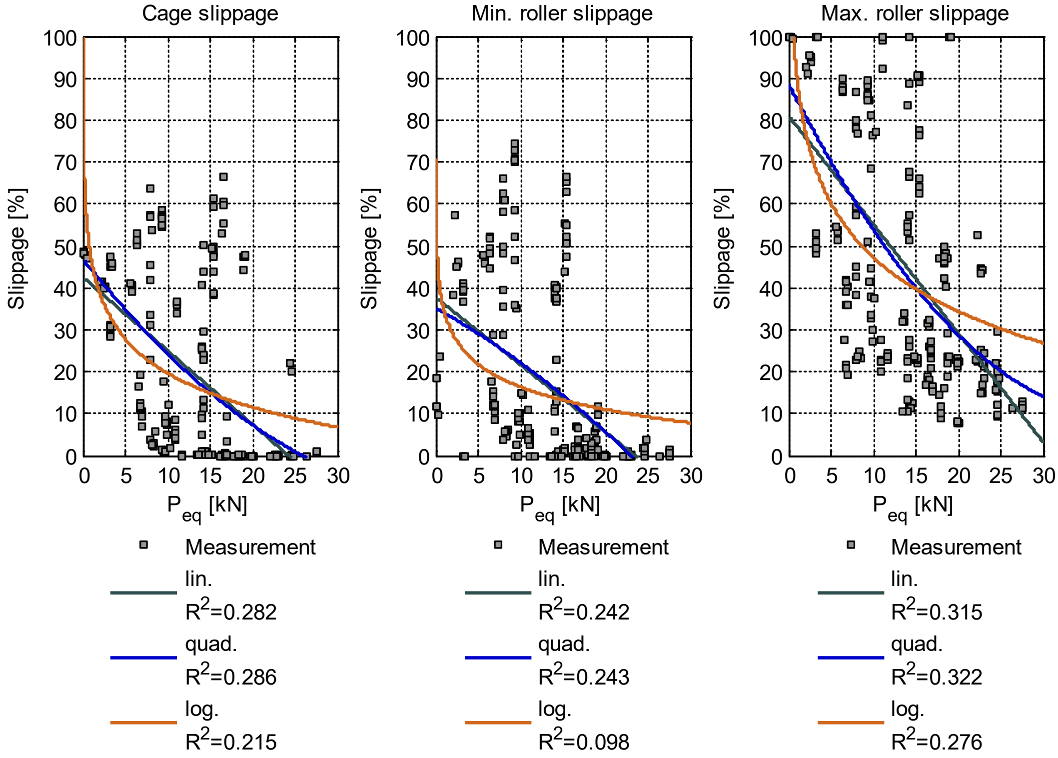

Figure 12: Regression analysis of equivalent bearing load P_{eq} based on main experiments for the three target values: cage slip, minimum and maximum roller slippage; tested TRB: 30234; C_{dyn}=590 kN, wind oil ISO VG 320; measuring points based on a d-optimal design with 230 experiments (5 retries).

The diagram indicates the relation between P_{eq} and slippage for the three considered target values. Aiming to approximate the relation in the best way possible, three mathematical functions were used for every parameter: a linear, quadratic and logarithmic approach were applied to fit the measured data set. To estimate the applicability of the chosen mathematical models, coefficient of determination R^2 was evaluated. Discussing the results for P_{eq}, the fundamental correlation between load and slippage is as expected. The higher the load the lower the slip, due to increasing contact and friction forces. The coefficient of determination indicates the quadratic approach as the most fitting model. The low values obtained for R^2 result from the experimental setup chosen. The parameter fitted is reinforced by other parameters.

Figure 13 illustrates the results regarding axial load F_{ax} derived from the main experiments. In accordance with P_{eq}, the relation between slippage and axial load is best described by a quadratic approach. The diagram shows a similar correlation as that obtained for Peq and slippage. Axial load changes, however, correlate stronger with slippage than P_{eq}.

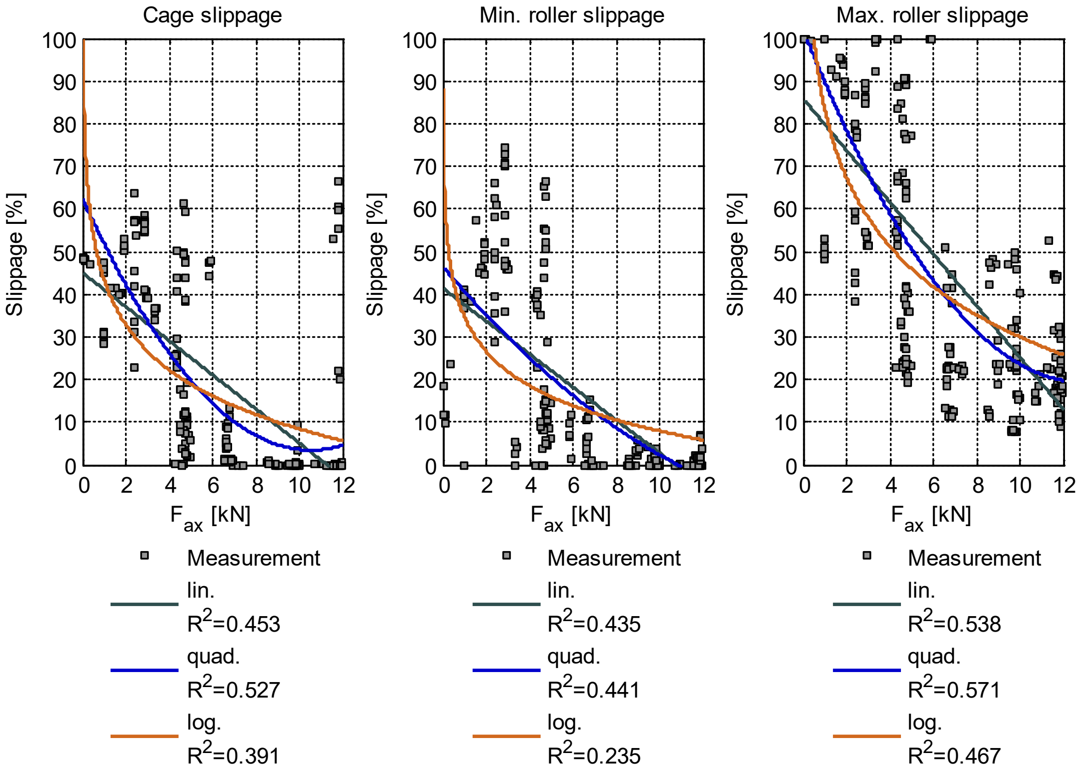
Cage slippage

Min. roller slippage

Max. roller slippage

Figure 13: Regression analysis of axial bearing load F_{ax} based on main experiments for the three target values: cage slip, minimum and maximum roller slippage; tested TRB: 30234; C_{dyn}=590 kN, oil ISO VG 320; measuring points based on a d-optimal design with 230 experiments (5 retries)

The correlation between slippage and inner ring revolution investigated in the main experiments is represented in Figure 14. As proven by low R^2 values, none of the regression models is suitable to describe the correlation between inner ring revolution and the targets. Theoretically, a linear approach should best model the relation between slip and revolution. This applies to the cage slippage and the minimum roller slippage only. As mentioned above, van Lier [14] found the slip behaviour in terms of revolution to be different for maximum roller slippage. This article supports this view and the results of van Lier.

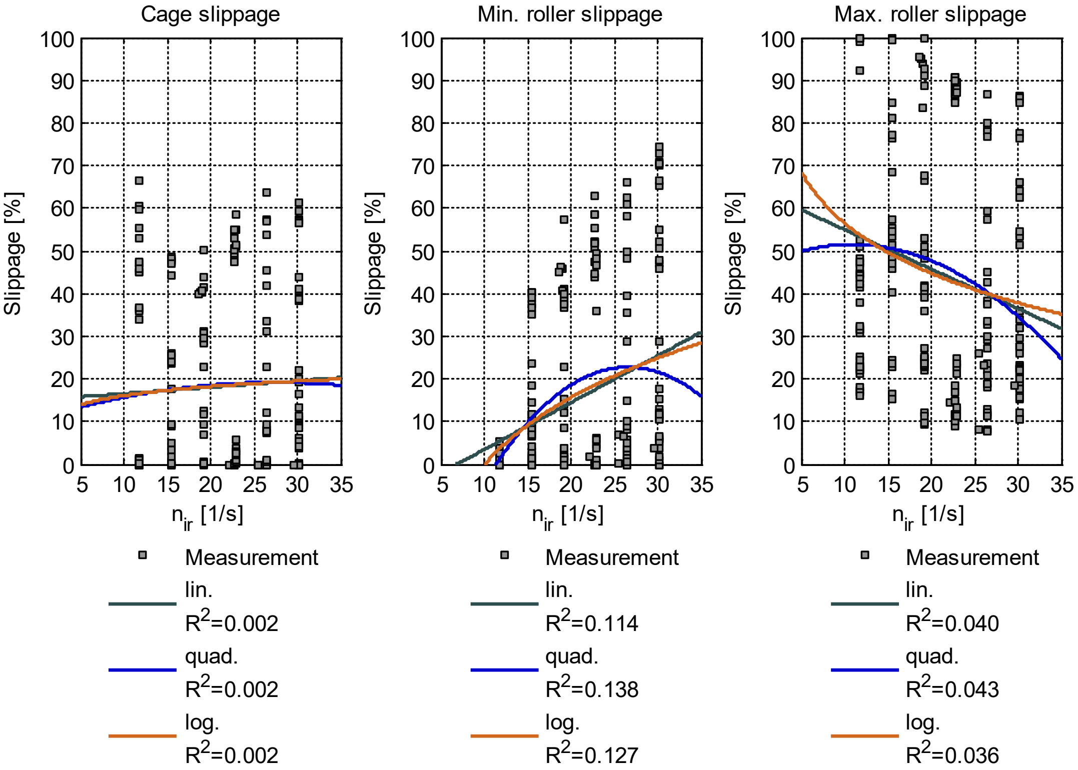

Figure 14: Regression analysis of inner ring revolution n_{ir} based on main experiments for the three target values: cage slip, minimum and maximum roller slippage; tested TRB: 30234; C_{dyn}=590 kN, oil ISO VG 320; measuring points based on a d-optimal design with 230 experiments (5 retries)

Evaluation of minimum load for TRB

So far all conventional methods to calculate minimum load neglect axial load (eq. (5), (6)). Especially for tapered roller bearings this procedure is not applicable. Here, it is recommended to use equivalent bearing load to calculate minimum load. Furthermore, axial load has to be considered for the evaluation. Based on the regression analysis for each influencing parameter, a formula was derived to evaluate the minimum load for the investigated tapered roller bearing. The equation considers even those parameters which had minor impact on slip in pre-tests. Thus, this formula enables the user to calculate the minimum load depending on each influencing parameter. For this purpose, all factors are summed up while considering their specific correlation to slippage. To evaluate the minimum load, the equation was converted to load parameter as shown in eq. (9) and (10) for equivalent bearing load and axial load. Due to the quadratic relations there are two mathematical solutions. The most likely solution in terms of physics is represented by the addition of the root in eq. (9) and (10). The coefficients are the result of the regression analysis for all influencing parameters and valid for the tested tapered roller bearing.

$$P_{eq,\min} = \frac{-\beta_3 \pm \sqrt{\beta_3^2 - 4 \cdot \beta_2 \cdot \left(\beta_3 \cdot h_{Oil}^2 - \beta_7 \cdot h_{Oil} - S - \beta_1 - \beta_4 \cdot \psi - \beta_5 \cdot T_{Oil,in} - \beta_8 \cdot n_{ir}\right)}}{2 \cdot \beta_2} \tag{9}$$

$$F_{ax,\min} = \frac{-\alpha_3 \pm \sqrt{\alpha_3^2 - 4 \cdot \alpha_2 \cdot \left(\alpha_7 \cdot h_{Oil}^2 - \alpha_8 \cdot h_{Oil} - S - \alpha_1 - \alpha_4 \cdot F_r - \alpha_5 \cdot \psi - \alpha_6 \cdot T_{Oil,in} - \alpha_9 \cdot n_{ir}\right)}}{2 \cdot \alpha_2} \tag{10}$$

where

β_i: coefficients for minimum equivalent bearing load [-]

α_i: coefficients for minimum axial load [-]

S: slippage [%]

h_{Oil}: oil volume [%]

ψ: load angle [°]

$T_{Oil,in}$: oil temperature [°C]

n_{ir}: revolution of inner ring [1/s]

F_r: radial load on inner ring [kN]

The diagram in Figure 15 shows the behaviour of minimum equivalent bearing load in relation to inner ring speed and was derived using eq. (9) for different levels of slip compared with conventional minimum load calculations. Obviously, minimum loading is not independent from speed as bearing manufacturers as well as Spechtel assumed. This calculations of minimum load using eq. (5) and (6) with higher speed as they occur in wind turbine gearboxes in field will lead to faulty results.

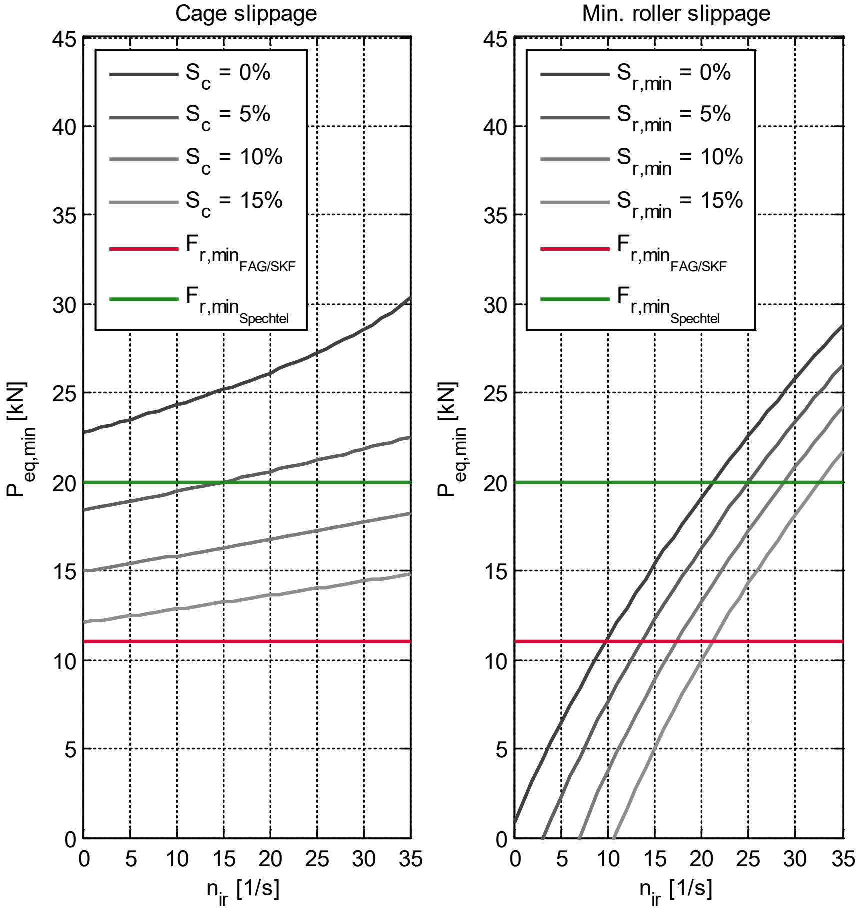

Figure 15: Comparison of minimum equivalent bearing load to typical minimum load calculations; setting for calculation: h_{Oil}=1 % / ψ=90° / $T_{Oil,in}$=70°C ;settings for Spechtel [8]: f_g=0.017 / f_b=0.8 / f_s=1 / f_v=2; valid for tested TRB: 30234; C_{dyn}=590 kN and wind oil ISO VG 320

Besides P_{eq} a prediction of minimum axial loading to avoid slippage can also be interesting. Eq. (10) enables the user to calculate the minimum axial load, as illustrated in Figure 16. Compared with the radial minimum load suggested by bearing manufacturers and Spechtel, minimum axial load calculated by eq. (10) is significantly lower. Even though axial and radial minimum loads are not comparable, this underlines the demand for additional evaluation approaches for TRB minimum load.

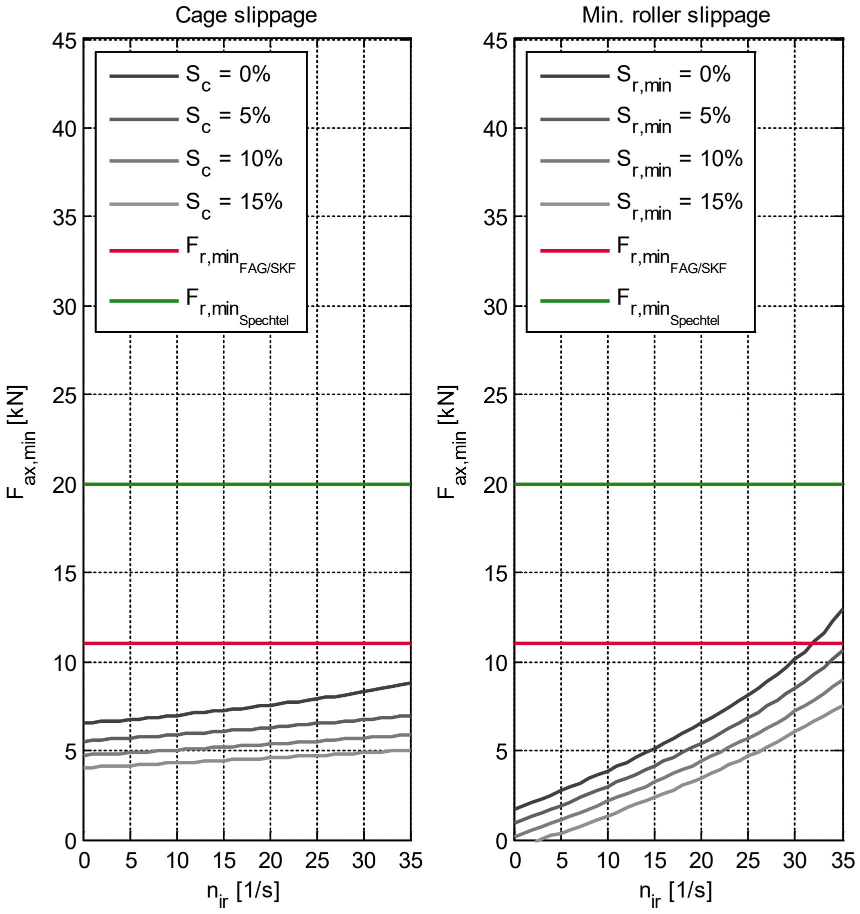

Figure 16: Comparison of minimum axial load to typical minimum load calculations; setting for calculation: h_{Oil}=1 % / ψ=90° / $T_{Oil,in}$=70°C ;settings for Spechtel [8]: f_g=0.017 / f_b=0.8 / f_s=1 / f_v=2; valid for tested TRB: 30234; C_{dyn}=590 kN and wind oil ISO VG 320

Conclusions

The purpose of this study was to determine the main parameters influencing slippage of tapered roller bearings. Using the variable search technique according to Shainin factors with impact on slip have been identified as follows:

- major influence: axial load, radial load, revolution
- minor influence: load angle, oil temperature, oil volume

A remarkable result of the pre-tests was the independence of slip from preloading. The chosen value for preloading might have been too low, even though it is depending on the system's stiffness. Therefore, additional experiments using higher preload are recommended. However, note that increased preload values result in critical bearing operation temperatures.

Moreover, identified parameters were analysed in detail. Due to the large number of necessary tests, DoE was used to set up the experimental design. The measurement data sets have been analysed by regression, leading to a mathematical relation for each influencing parameter concerning slip behaviour:

- axial load: quadratic
- radial load: linear
- revolution: linear
- equivalent bearing load: quadratic
- load angle: linear
- oil temperature: linear
- oil volume: quadratic

Finally, novel formulas for calculation of minimum load for P_{eq} and F_{ax} have been derived. Although validity has only been proven for one specific test setup (bearing TRB 30234 WTO ISO VG 320 oil) the underlying correlations between parameter and slippage should be applicable for other TRB as well. Comparative analysis showed that given formulas of bearing manufacturers as well as Spechtel are not applicable for tapered roller bearings because they do not take speed dependency into account. The authors have revealed that minimum load is depending on inner ring revolution. Furthermore, it is recommended to expand the existing approaches for TRB by axial minimum load and replace radial minimum load with equivalent bearing load.

Bibliography

1. Technical specification, 2008, “Rolling bearings – methods for calculating the modified reference rating life for universally loaded bearings”, ISO/TS 16281
2. Lundberg, G. and Palmgren, A., 1952, “Dynamic Capacity of Rolling Bearings”, Acta Polytechnica Mechanical Engineering Series, Vol. 2, No. 4, Stockholm, Sweden
3. Bajer, P., 2016, “Einflussgrößen auf das Schlupfverhalten von Wälzlagern in Generatorgetrieben”, Ph.D. thesis, MEGT, TU Kaiserslautern, Germany
4. Aul, V. and Kiekbusch, T. and Sauer, B., 2015, “Untersuchungen zum Schlupfverhalten von Zylinderrollenlagern”, 11. VDI Fachtagung “Gleit- und Wälzlagerungen”, VDI-Bericht 2257, pp. 39-52, Schweinfurt, Germany
5. Spechtel, B, 2000, “Winkelbeschleunigung-Lagerverhalten”, FVA-Abschlussbericht, Heft 637, Frankfurt a.M., Germany
6. Tassone, B., 1975, „Roller Bearing Slip and Skidding Damage“, Journal of Aircraft, Vol. 12, No. 4, p. 281
7. Brändlein, J. and Eschmann, P. and Hasbargen, P. and Weigand, K., 2015, Die Wälzlagerpraxis, Vol. 4., Vereinte Fachverlage GmbH, Mainz, Germany
8. Harris, T, and Kotzalas, M., 2007, Rolling Bearing Analysis – Essential Concepts of Bearing Technology, Vol. 5., Taylor&Francis Group, Boca Raton, USA
9. Eglinger, M., 1995, “Anschmiererscheinungen II – Einfluss des Schmierstoffes und der Rollenbeschaffenheit auf die Entstehung von Anschmierungen”, FVA-Abschlussbericht, Heft 465, Frankfurt a.M., Germany
10. Scherb, B., 1997, “Zusammenhang zwischen Käfig- und Wälzkörperdrehzahl bei Zylinderrollenlagern”, Antriebstechnik 362, pp. 65-69
11. Schaeffler (publisher), 2009, Großlager – Hauptkatalog, MATNR 036815632-0000 / GL1 / D-D / 2009063, Germany
12. SKF (publisher), 2014, Wälzlager – Hauptkatalog, PUB BU/P1 10000/2 DE, Germany
13. Schaeffler (publisher), 2000, Wälzlagerschäden – Schadenserkennung und Begutachtung gelaufener Wälzlager, wl 82 102/2 DA / 2013062, Germany
14. van Lier, H., 2015, “Schädlicher Wälzlagerschlupf – Wann ist Wälzlagerschlupf schädlich und führt zum Ausfall des Wälzlagers?”, FVA-Abschlussbericht, Heft 1124, Frankfurt a.M., Germany
15. Dekena, B. and Müller, C. and Walden, L., 2003, “Charakterisierung weißer Schichten nach mechanischer und thermischer Einwirkung durch Fertigungsverfahren”, HTM 58 (2003) 4
16. Guzman, G. and Özel, O., Pinard, P., 2016, “Are WECs reproducible on test benches with realistic operational conditions?”, Bearing World – International Bearing Conference, Hanover, pp. 24-27
17. Stadler, K and Volkmuth, M. and Heemskerk, R., 2009, “Slippage measurements in roller bearings”, Antriebstechnisches Kolloquium (ATK), ISBN 978-3-86130-622-1, Aachen, Germany
18. Bajer, P. and Schwarzer, J., 2014, “Methode zur Auswertung der, durch einen diametralen Magneten induzierten, Spannung in einer Spule zur Bestimmung der Drehzahl eines rotierenden Rollenkörper“, Patent, DE102014214178.8. Juli 2014, Germany
19. Dasgupta, T., 2011, “Another Look At Dorian Shainin’s Variable Search Technique”, Harvard University, Cambridge, USA
20. Kleppmann, W., 2006, Taschenbuch Versuchsplanung, Vol 4., Carl Hanser Verlag, München, Germany

Increase of the damage tolerance of bearing steels by alloy optimization

Brigitte Clausen, Torben Karsch, Hans-Werner Zoch

Summary

In 2010 a joint research project of Institute of Ferrous Metallurgy (IEHK), RWTH Aachen, Institute of Materials Science and Engineering (WKK), Kaiserslautern, Gear Research Centre (FZG), Munich and Foundation Institute of Materials Science (IWT), Bremen, named HiPerComp (High Performance Components), started. The aim was the development of new damage tolerant steels for rolling bearing and gear applications. In this paper the results concerning rolling contact fatigue are presented. According to the development target of damage tolerance enhancement alloy systems with increased amounts of stabilized retained austenite were investigated. Though the development is still in a very early state, inner rings in a pre-damaged state with a 16 times higher fatigue life at moderate loads (p_0 = 2800 MPa) could be produced.

Introduction

The project in total continued over 5 years, with various partners being involved (Figure 1). It started with the development of stress models and the definition of required strength profiles. The next step was to cast promising melts at the Institute of Ferrous Metallurgy, Aachen [1-4]. These were investigated towards their heat treatability at IWT, Bremen [5-6]. The first tests to distinguish between 26 laboratory melts in several heat treatment variants were carried out on dilatometer samples with defined heat treatment at WKK Kaiserslautern [7-8]. Material concepts suitable for further investigation were used to produce gears and inner rings of bearings. The gears were tested at Gear Research Center in Munich [9].

The bearings were analyzed and tested in a rolling contact fatigue test at IWT in Bremen. AISI 52100 standard industrial bearings 6206 were used as reference for the tests.

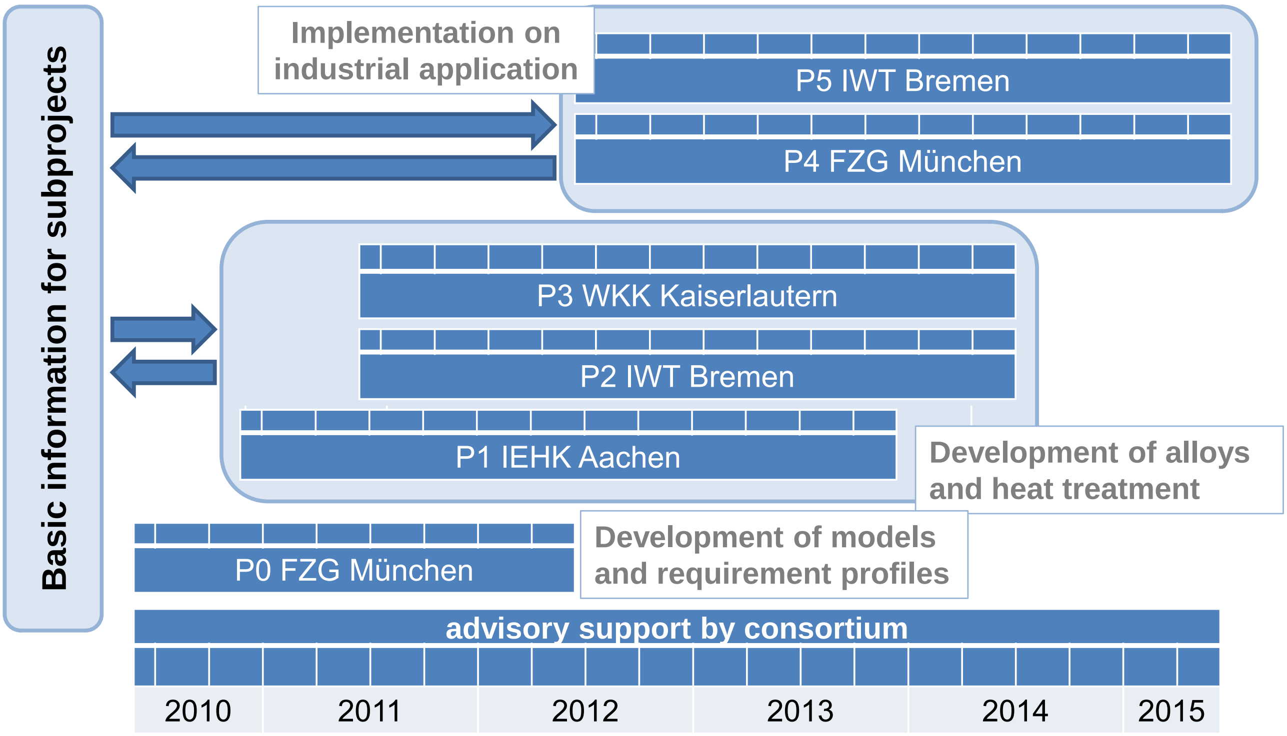

Figure 1: Schedule of the joint research project HiPerComp

Approach

The demands in steels applied in drive components are increasing due to weight reduction requirements. On the other hand the tolerance against failures is decreasing. Since the sensitivity of steel for internal failures is increasing with increasing strength, these demands are contradictory. The approaches to match the aims either are to increase the strength far above the actual demands to increase the safety against failure, so that even the ppm-failures still match the demands. Or, as it was agreed, that the maximum strength even may be decreased, if the damage tolerance is enhanced.

To enhance the strength three strengthening mechanisms were in focus of the joint research project. To increase the effect of solid solution strengthening the gear steel 18 CrNiMo7-6 (1.6587) was alloyed with nickel or silicon. To use the effect of particle strengthening nanometer sized coherent copper clusters were precipitated in a copper alloyed variant of this steel. Further the Hall-Petch effect was used by alloying with niobium and producing an extremely fine grained gear steel.

Bearing steels tend to increase mainly the standard deviation of endurance results with all attempts to increase the maximum strength. It was therefore agreed that increasing the damage tolerance of a bearing steel is more expedient. The idea was to increase and stabilize a defined retained austenite content in the bearings. The stabilized retained austenite was expected to transform to martensite only at extreme stresses at inclusions and micro cracks. The TRIP effect (transformation induced plasticity) causes local compressive residual stresses, due to volume increase, and a local strengthening.

Experimental

Melt production

The chemical compositions of the melts chosen for the rolling contact fatigue tests are summarized in table 1. The reference melt is a typical 52100 standard industrial bearing steel. The two laboratory melts were cast under argon atmosphere as 80 kg melts in a 140 x 140 mm mould. The steels were forged to 60 mm x 60 mm bars by a hydraulic press, followed by a normalizing heat treatment.

	C	Si	Mn	P	S	Cr	Mo	Ni	Al	Cu	O
	Element contents (mass-fraction in %)										ppm
max.	1.05	0.35	0.45	0.025	0.015	1.60	0.10		0.05		
min.	0.93	0.15	0.25			1.35					
reference	0.91	0.25	0.33	0.016	0.007	1.30	0.01	0.03	-	0.02	0.06
Al-alloyed*	0.92	0.25	0.37	0.004	0.002	1.52	0.04	0.13	1.90	0.19	0.12
Si-alloyed*	0.93	1.00	0.34	0.006	0.001	1.50	0.03	0.12	0.03	0.18	0.13

*laboratory melts by IoFM, Aachen

Table 1: Chemical composition of the investigated melts

Heat treatment

The industrial produced reference melt rings were quenched and tempered in an industrial standardized best practice at Schaeffler, Schweinfurt.

The heat treatment parameters for the laboratory melts were determined in a dilatometer, type DIL 805 A/D (BÄHR Thermoanalyse). The heat treatments of the inner rings were carried out in salt bathes. The austenitization was carried out at 900 °C for five minutes. For the bainitizing procedure the rings were quenched to a temperature above the determined martensite start temperature. The isothermal holding time was adjusted to the desired retained austenite content. The QPT-treatment (Quenching and Partitioning) started with quenching beneath martensite start and holding at 150 °C. After 60 seconds the rings were heated to 175 °C and held for another 4 hours. These rings were cooled down to room temperature and tempered at 180 °C for two hours afterwards. The parameters are summarized in table 2.

	52100 reference	Bainitized Al-enr.	QPT Al-enriched	Bainitized Si-enr.
Austenizing	Austenizing	900 °C 5 min	900 °C 5 min	900 °C 5 min
Quenching	---------------------	Above M_S, holding at 220 °C	Beneath M_S, holding at 150 °C 60 s	Above M_S, holding at 220 °C
Isothermal transformation	---------------------	5 hours	----------------------	3 hours
Partitioning	---------------------	----------------------	175 °C 4h	----------------------
Cooling	To RT	To RT		To RT
Tempering	Standard	---------------------	180 °C 2h	--------------------
Microstructure	Tempered martensite, retained austenite (3%), carbides	Bainite, retained austenite (40%)	Tempered martensite, bainite, retained austenite (22%), carbides	Bainite, retained austenite (35%)
Hardness HV1	721 ± 7	627 ± 10	717 ± 10	690 ± 2

Table 2: Heat treatment procedures and investigation results of inner rings

In figure 2 the microstructures of the heat treated inner rings are compared. Figure 2a) shows the fine structured tempered martensite of the reference melt. Fine carbides are evenly spread in the matrix. The microstructure of the laboratory melts is coarser due to the minor deformation degree from melt to ring. Figure 2b) shows bainite needles of differing length (up to 40 µm) in a retained austenite matrix. The etchability of the bainite needles increases with duration of existence at holding temperature. The darkest needles appeared first.

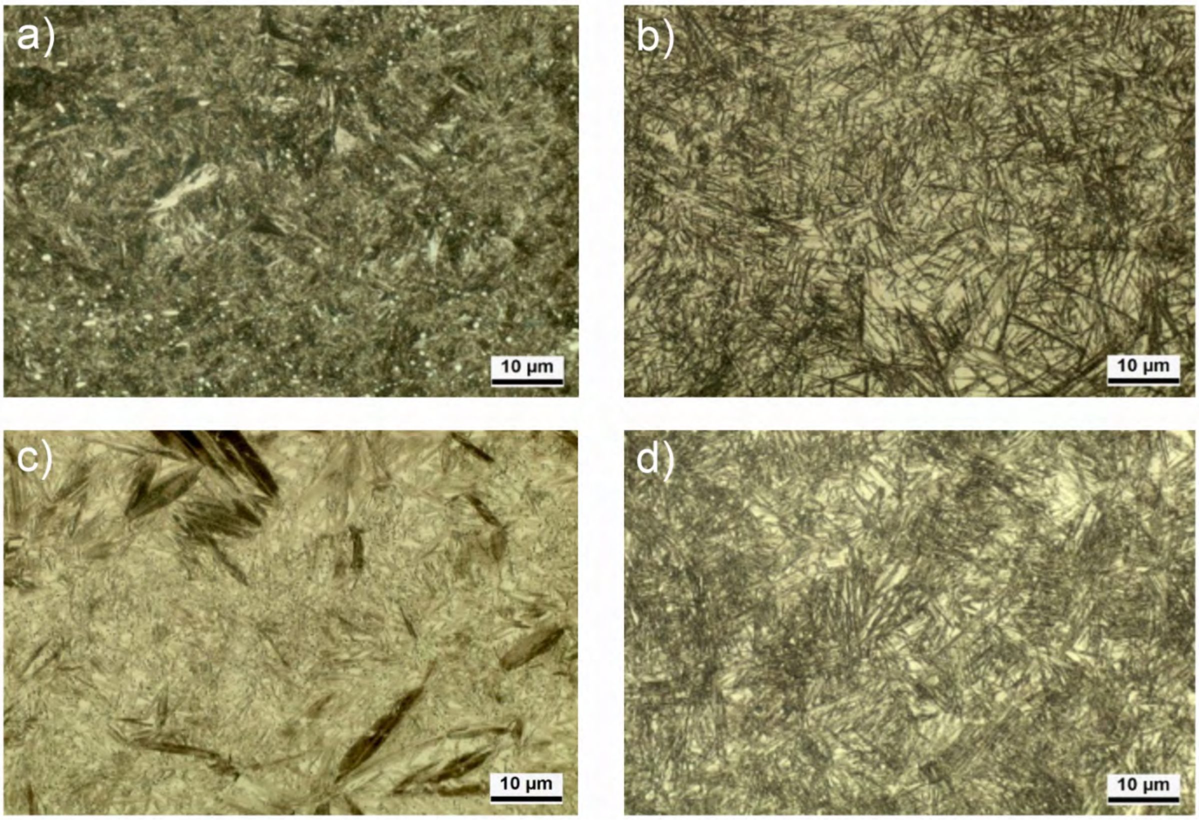

Figure 2: Microstructure of the inner rings after heat treatment. a) Reference melt 52100, quenched and tempered, b) Al-enriched 52100, bainitized, c) Al-enriched 52100, quenched and partitioned, d)Si-enriched 52100, bainitized

In figure 2c) the quenched and partitioned microstructure is shown. The relative dark needles consist of martensite build in the first quench sequence, tempered in the following sequences. The matrix consists of bainite and finely dispersed retained austenite. The silicon enriched melt consists after bainitizing treatment of bainite with finely dispersed retained austenite and small carbides (figure 2d). With lesser magnification bright speckles are visible in the microstructure (Figure 5d). These areas are free of carbides. A higher dissoluted chromium content causes the decreased etchability in these patches.

Rolling Contact Fatigue Test

The bearings were tested in a rolling contact fatigue test facility, type FAG L11 (figure 8). The test facility is equipped with noise measurement to stop the test automatically with the occurrence of failures.

Figure 3: RCF-test at the Foundation Institute of Materials Science in Bremen

The radial load of 4.8 respectively 8.7 kN was applied at room temperature by preloading a tie rod, and controlled by strain gauges on the tie rod. The resulting maximum contact pressure at the inner ring was calculated to 2800 respectively 3400 MPa. The inner rings tested with 2800 MPa maximum contact pressure were artificially damaged before. Eight spherical indentations applied by a HRC testing tip in the middle of the raceway of the inner ring were used to simulate stress peaks due to particle contamination of the lubricant or inclusions at the surface.

The heat treated rings were ground and completed with balls, cage and outer ring to standard DGBB type 6206 at Schaeffler, Schweinfurt (figure 4).

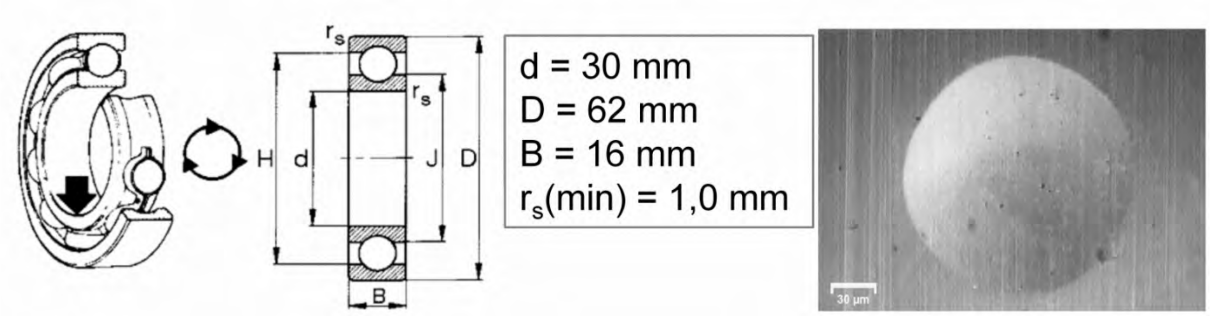

Figure 4: Deep Groove Ball Bearing type 6206; right: indentation in raceway of predamaged bearing (SEM-micrograph)

Results

In figure 5 micrographs of tested rings are compared. With low magnification the differences in the segregation distribution between the industrial melt and the laboratory melts are visible. After rolling contact loading the inner rings show structural changes in the surface region.

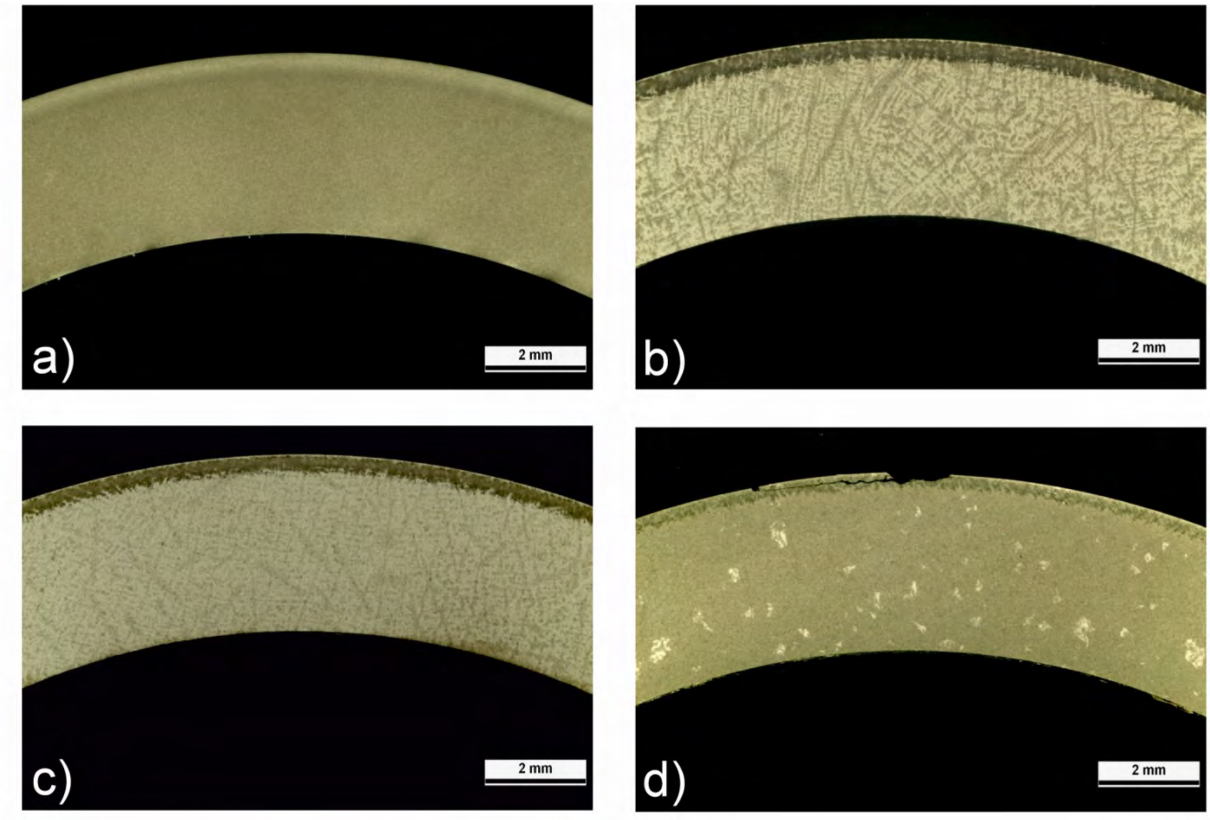

Figure 5: Microstructure of the inner rings tested in contact fatigue tests (p_0 = 3400 MPa): a) reference melt 52100, quenched and tempered (N_B = 8x10^8), b) Al-enriched 52100, bainitized (N_B = 5x10^8), c) Al-enriched 52100, quenched and partitioned (N_B = 1x10^9), d) Si-enriched 52100, bainitized (N_B = 2.8x10^8)

The surface region is shown in figure 6 in higher magnification. The micrographs show typical damages in the highly stressed area. In the reference rings white bands with an angle of about 25° in a fine structure dark etching area appear beneath the surface after rolling contact (figure 6a). Due to the inhomogeneous microstructure before the RCF test the dark etching areas also appear more inhomogeneous in the highly stressed areas of the laboratory melt rings.

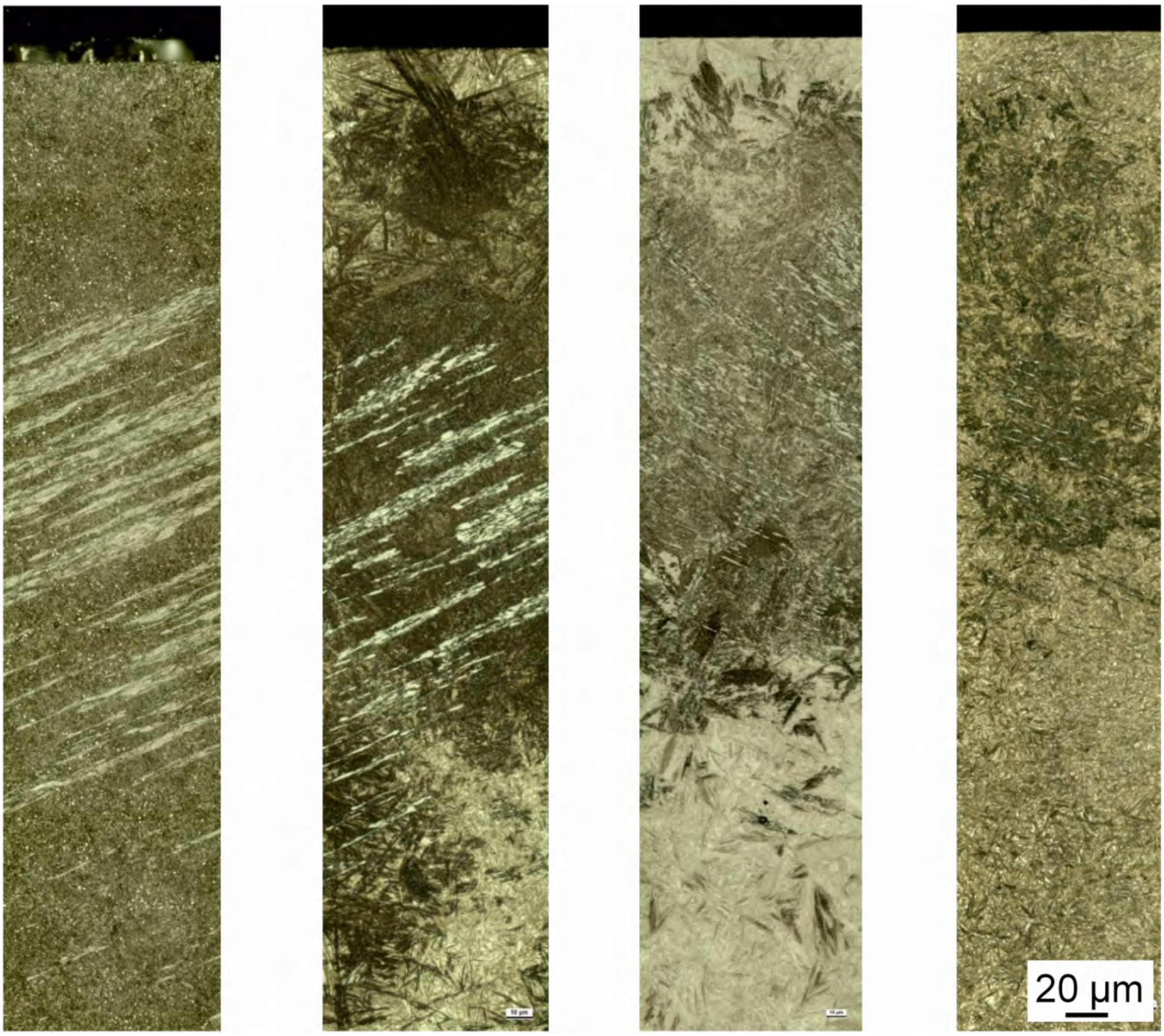

Figure 6: Microstructure of the inner rings tested in contact fatigue tests (p_0 =3400 MPa). a) reference melt 52100, quenched and tempered (N_B = 8x10^8), b) Al-enriched 52100, bainitized (N_B = 5x10^8), c) Al-enriched 52100, quenched and partitioned (N_B = 1x10^9), d) Si-enriched 52100, bainitized (N_B = 2.8x10^8)

The results of the RCF-test at a contact pressure of 3.400 MPa are summarized in Figure 7, showing the calculated failure probability under estimation of a Weibull distribution. The maximum likelihood method was used to exploit the results of experiments where failure occurred not at the inner ring but e. g. at the cage of the bearing. These data are marked as right censored data in the diagram. The highest number of revolutions to failure is achieved with the industrial reference. The value L_{10}, often used to compare different states of inner rings, is shown in table 3. The number of revolutions to failure for a given probability decreases further from the Al-enriched bainitized to the Si-enriched bainitized melt. The least numbers of revolutions are gained with the quenched and partitioned variant.

Failures in the raceway occurred almost independent of the alloying concept due to pitting at the inner ring at aluminum oxides (Figure 8). Only the aluminum enriched bainitized rings showed mainly a different failure. The majority of these tested rings showed no pitting on the surface but signs of wear. A coordinate measurement of these rings resulted in an increase of the bore diameter of the bearings of approximately 15 µm during testing. The measurement of the retained austenite content revealed a reduction from 40 % to below 10 % up to a depth of 10 micrometer. The transformation of retained austenite into martensite caused the inadmissible diameter change.

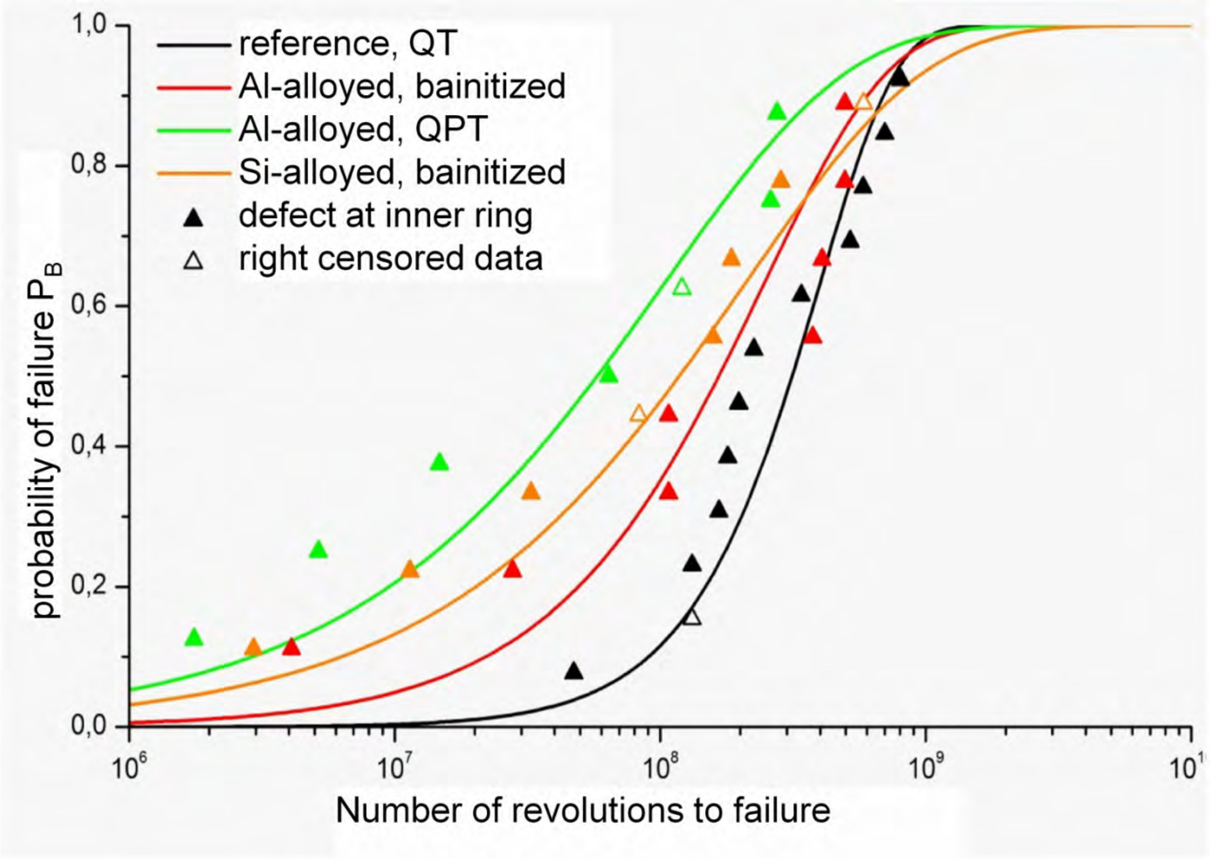

Figure 7: Determination of the failure probability under estimation of a Weibull distribution and using the maximum likelihood method (RCF test, p_0 = 3400 MPa)

p_0 = 3400 MPa	52100 reference	Bainitized Al-enr.	QPT Al-enriched	Bainitized Si-enr.
L_{10}	$1x10^8$	$2x10^7$	$3x10^6$	$7x10^6$

Table 3: Comparison of revolutions to failure at 10 % failure probability in RCF test

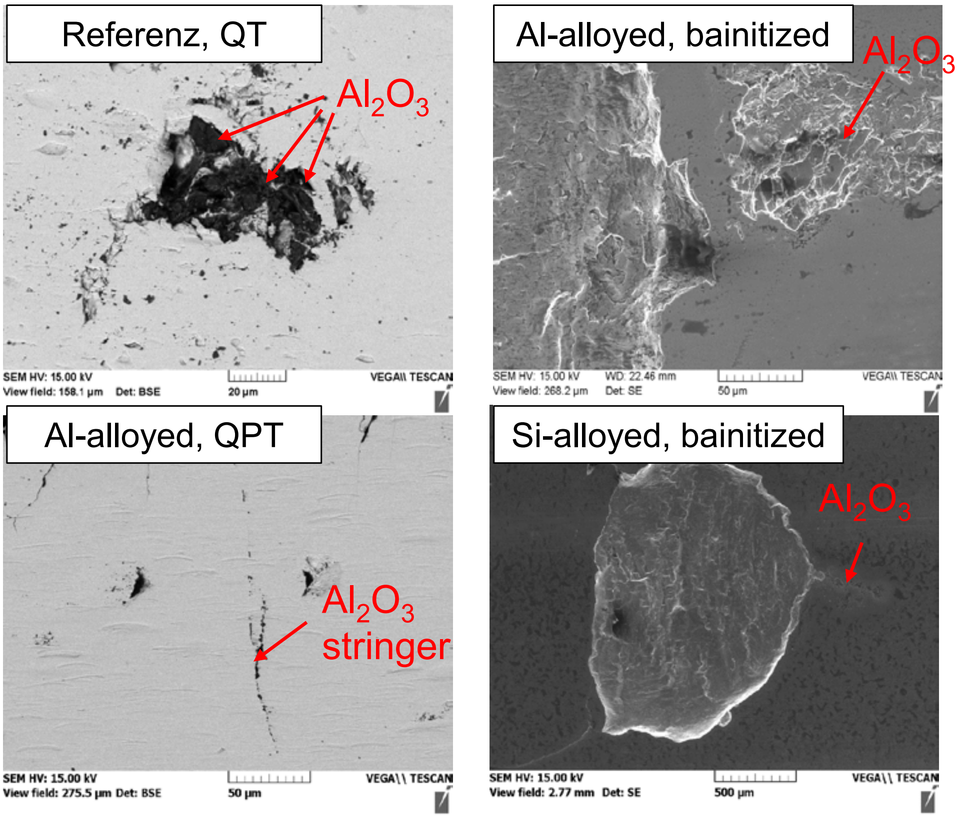

Figure 8: Secondary electron micrographs of failures on the inner rings tested in contact fatigue tests (p_0 =3400 MPa). a) reference melt 52100, quenched and tempered, b) Al-enriched 52100, bainitized, c) Al-enriched 52100, quenched and partitioned, d) Si-enriched 52100, bainitized

To gain a measure concerning the damage tolerance of bearing steels inner rings were tested artificially damaged at moderate loads (p_0 = 2800 MPa). Hardness indentations in the raceway were meant to simulate the stresses due to overrolling of particles in lubricants or surface near inclusions. The results of the RCF test are summarized in figure 9.

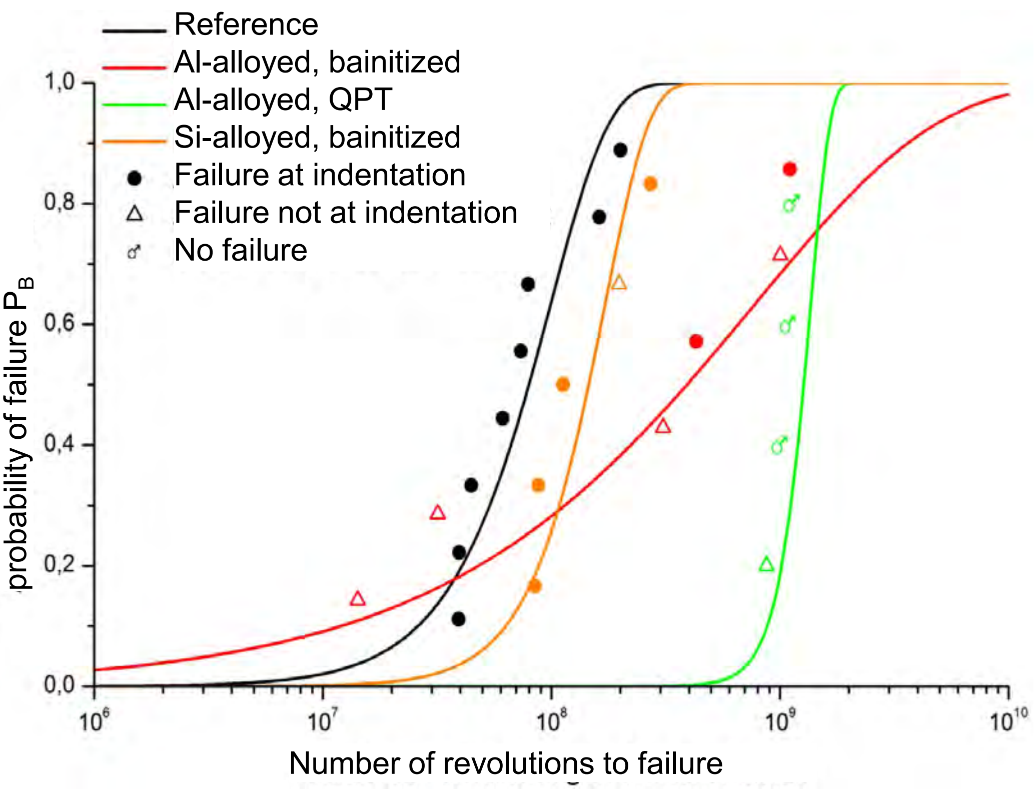

Figure 9: Determination of the failure probability under estimation of a Weibull distribution and using the maximum likelihood method (RCF test, p_0 = 2800 MPa, artificially damaged inner rings)

In this test configuration the failure behavior changed significantly. The industrial produced inner rings failed, starting from the hardness indentations as assumed (figure 10 a and c). The laboratory melts failed mostly at higher revolution numbers and the reasons for failure were not always hardness indentations. The lifetime of the silicon alloyed inner rings did not differ so much from the industrial melt and only one ring showed a pitting not connected to an indentation. The lifetime of the aluminum alloyed bainitized inner rings showed extreme scattering. Only two of the tested rings failed at indentations. However, the aluminum alloyed QPT variant did not fail at indentations (figure 10 b and d) and showed in most cases a lifetime above 10^9 revolutions. Table 4 compares the lifetime at 10 % and 50 % failure probability for the different variants.

P_0 = 2800 MPa	52100 reference	Bainitized Al-enr.	QPT Al-enriched	Bainitized Si-enr.
L_{10}	$2.5x10^7$	$1x10^7$	$9x10^8$	$7x10^7$
L_{50}	$8x10^7$	$4x10^8$	$> 10^9$	$1.4x10^8$

Table 4: Comparison of number of revolutions at 10 % and 50 % failure probability in RCF test with artificially damaged raceways

The value L_{10} of the aluminum enriched QPT variant is 36 times higher than the reference value. The L_{50} value still is more than 16 times higher.

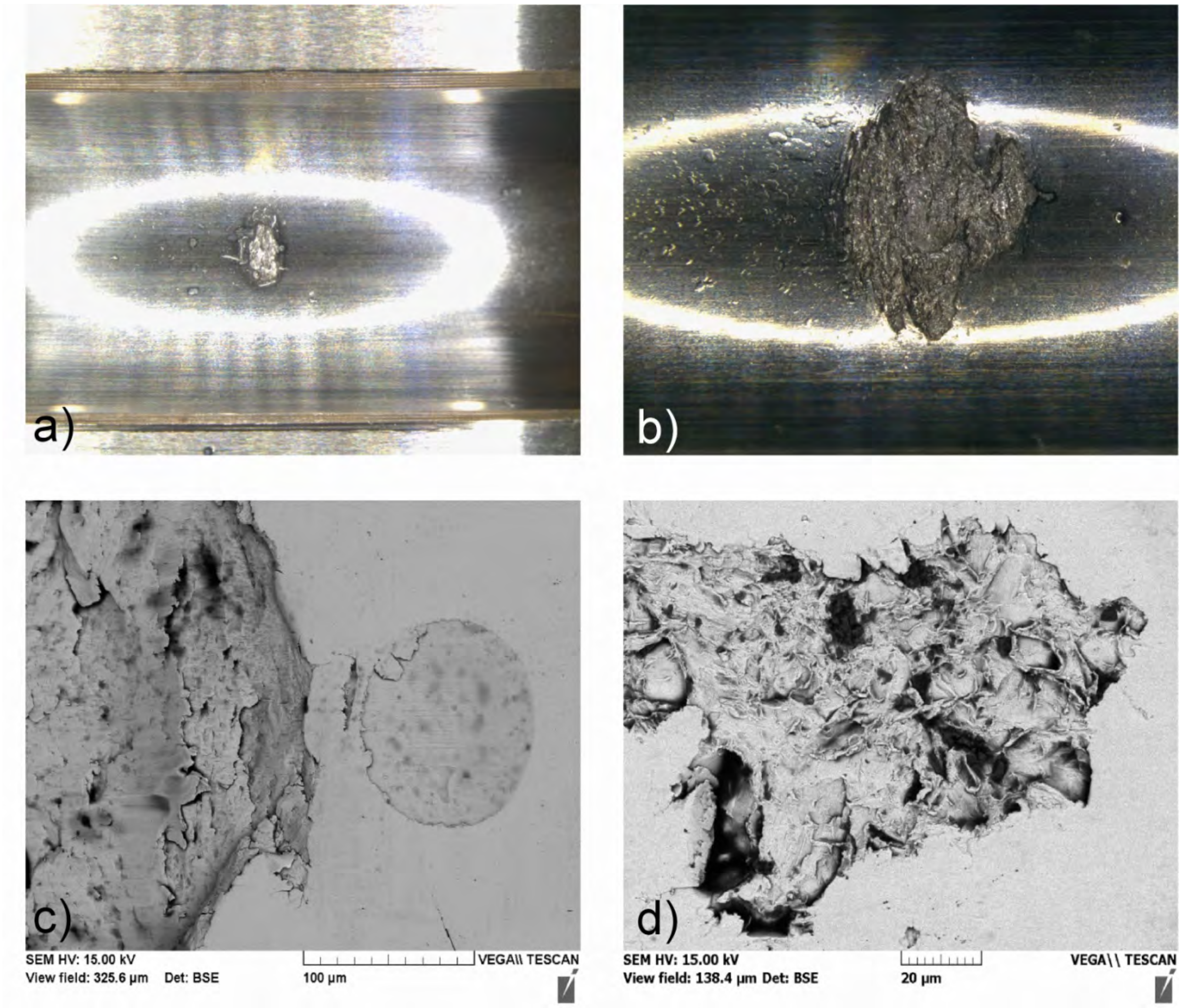

Figure 10: Closer investigations of failures on inner rings tested in contact fatigue tests (p_0 =2800 MPa, artificially damaged). a) and c) reference melt 52100, quenched and tempered, damage correlated to a hardness indentation b) and d) Al-enriched 52100, quenched and partitioned, failure not correlated to the hardness indentation.

Conclusions

At high contact pressures (p_0 = 3400 MPa) the reference is superior to TRIP-steel-variants. The failures are assigned to pittings starting from inclusions. A high amount of retained austenite bears the danger of inadmissible dimensional changes. At moderate contact pressures (p_0 = 2800 MPa) pre-damaged TRIP-steel rings are superior to the reference melt and the failures mostly even do not occur at artificial predamages by hardness indentations.

The newly developed aluminum-rich AISI 52100 melt has got the potential to withstand contaminations in lubricants and surface near inclusions due to the ability to transform small amounts of retained austenite under extreme conditions into martensite. The superiority under artificially damaged conditions is assumed to be even increasable under industrially productions conditions. This success was only possible due to the co-work of steel production, high-troughput testing and heat treatment in this joint cooperation.

Acknowledgements:
This joint cooperation project was funded by the Deutsche Forschungsgemeinschaft (DFG HO 1339/41-1, DFG BL 402/32-1, DFG EI 186/34-1) and the Federal Ministry of Economic Affairs and Energy (BMWi) via the Arbeitsgemeinschaft industrieller Forschungsvereinigungen „Otto von Guericke“ e.V. (AiF) (IGF 16686, IGF 16687, IGF 16688) for which we explicitly thank.

Further the authors want to express their gratitude towards our industrial partners in this joint cooperation for their support, especially Dr. Trojahn, Schaeffler Technologies AG & Co. KG, Schweinfurt.

[1] Bambach, M. D.; Stieben, A.; Bleck, W.: 18CrNiMo7-6 with TRIP-Effect for Increasing the Damage Tolerance of Gear Components-Part I: Alloy Design. Materials Science Forum 783 (2014), S. 633-638.

[2] Bambach, M. D.; Stieben, A.; Bleck, W.: 18CrNiMo7-6 with TRIP-Effect for Increasing the Damage Tolerance of Gear Components-Part II: Microstructure and Mechanical Properties. Materials Science Forum 783 (2014), S. 639-643.

[3] Bambach, M.D.; Bleck, W.; Kramer, H.; Klein, M.; Eifler, D.; Beck, T.; Surm, H.; Hoffmann, F.; Zoch, H.-W.; Radulescu, A.: Tailoring the Hardening Behavior of 18CrNiMo7-6 via Cu Alloying. steel research international 86 (2015). http://dx.doi.org/10.1002/srin.201500129.

[4] Bambach, M.D.; Stieben, A., Bleck, W.: On the Microstructure and Properties of a High Al-Alloyed 100Cr6 Steel, steel research international 86 (2015). http://dx.doi.org/10.1002/srin.201500068

[5] Surm, H.; Hoffmann, F.: Einstellung eines hohen Restaustenitgehaltes zur Nutzung des TRIP-Effektes in aluminiumlegierten durchhärtenden Wälzlagerstählen. HTM - J. Heat Treatm. Mat. 68 (2013) 6, S. 246-257.

[6] Surm, H.; Epp, J.; Hoffmann, F.; Zoch, H.-W.: Adjustment of heat treatment process to aluminum alloyed bearing steel. Metallurgical and Materials Transactions A (angenommen).

[7] Kramer, H., Starke, P., Klein, M., Eifler, D.: Cyclic Hardness Test PHYBAL$_{CHT}$ - short-time procedure to evaluate fatigue properties of metallic materials. International Journal of Fatigue 63 (2014) 78-84.

[8] Kramer, H.; Klein, M.; Eifler, D.: PHYBAL$_{CHT}$: Kurzzeitverfahren zur Abschätzung der Ermüdungseigenschaften metallischer Werkstoffe. HTM Journal of Heat Treatment and Materials 69 (2014) 5, S. 256-264.

[9] Wickborn, C.; Tobie, T.; Stahl, K.: HiPerComp: High performance materials for gears. International Conference on Gears, 2015 (reviewed).

On boundary layers and pressure spikes, a tribute to J.-M. Georges

N. Biboulet [a], A.A. Lubrecht [a]

[a] Université de Lyon, INSA-Lyon, LaMCoS, CNRS UMR 5259, Villeurbanne F69621, France

The current paper studies the boundary layers in the inlet and outlet of a circular EHL contact. It shows that an analysis of pressure and film thickness compared to the Hertzian case is very enlightening. The pressure differences in the inlet have identical shapes, however, two scaling parameters are required to adjust the width and the height of the inlet pressure difference. For the outlet three scaling parameters are required: position, width and height.

Using this approach it is possible to create a rolling friction prediction based on physical parameters.

Keywords

EHL, boundary layer, Hertz, rolling friction.

Notation

Upper case letters generally represent dimensionless parameters.

a Hertzian contact radius $a = \sqrt[3]{\frac{3wR_x}{2E'}}$

E' reduced elastic modulus $\frac{2}{E'} = \frac{1-\nu_1^2}{E_1}\frac{1-\nu_2^2}{E_2}$

h film thickness

p pressure

p_h Hertzian pressure $p_h = \frac{3w}{2\pi a^2}$

R_x reduced radius in direction of motion

u_m mean surface velocity

w load

x coordinate in direction of motion

y coordinate perpendicular to motion

G	dimensionless material parameter $G = \alpha E'$
H	dimensionless film thickness $H = \dfrac{hR_x}{a^2}$
dH	dimensionless film thickness difference
L	dimensionless Moes parameter $L = G\sqrt[4]{U}$
M	dimensionless Moes parameter $M = W\sqrt[4]{U^3}$
U	dimensionless speed parameter $U = \dfrac{2\eta_0 u_m}{E' R_x}$
W	dimensionless load parameter $W = \dfrac{w}{E' R_x^2}$
P	dimensionless pressure $P = \dfrac{p}{p_h}$
dP	dimensionless pressure difference
X	dimensionless coordinate in direction of motion $X = x / a$
X_s	dimensionless location of the pressure spike
Y	dimensionless coordinate perpendicular to motion $Y = y / a$
α	pressure viscosity coefficient
η_0	ambient viscosity

Introduction

One of the most enigmatic features in EHL has been the outlet pressure spike as first shown by Petrusevitch [1]. In the outlet zone the pressure distribution exhibits a logarithmic singularity. This pressure singularity is accompanied by a local film thickness reduction. Numerical calculations by Dowson and Higginson [2] and Hamrock and Dowson [3] show the spike shape evolution as a function of the operating conditions. Safa and Gohar [4] were the first to successfully measure the spike using a sensor deposited on the discs.

Theoretical analyses of the EHL contact and the presure spike were performed by Greenwood [5], Archard and Baglin [6] and Hooke [7]. More recently Kudish [8,9] and Snoeijer et al. [10] have studied the EHL contact, using a boundary layer approach and focussing on the inlet and outlet zones.

Even though existence of the pressure spike has been recorded for many decades, the precise behaviour has remained elusive because of numerical and experimental difficulties. The work by Biboulet et al. [11] showed that it was possible to infer the detailed pressure spike shape from very precise film thickness measurements. The work by Venner et al. [12] studied the boundary layers in EHL contacts. The current paper studies the spike shape and location as a function of the operating conditions, using fine grid calculations and a boundary layer analysis. As both its changing position and its singular character make a head-on study complicated, the inlet boundary layer was studied as a first step. A quick comparison shows that the pressure difference behaviour in inlet and outlet zone are very similar. Using this difference with the dry contact Hertzian pressure distribution, the inlet boundary layer is examined. It is shown that the pressure difference is first positive, then it reaches a sharp peak, before a smooth negative zone occurs. For increasing loads (M) the width of the inlet pressure difference sweep reduces as well as its peak height. True to a boundary layer, its width tends to zero. Scaling the height and the width on the dimensionless load parameter (M) makes all the pressure difference curves collapse onto one another.

Circular EHL contact

Today many solvers exist that can solve the Reynolds and elastic deformation equations

to provide the pressure distributions P(X,Y) as a function of the operating conditions.

The authors have used multilevel methods [13,14,15] to obtain solutions on very fine grids.

For historical reasons the Moes parameters [16,17] will be used: M and L.

Figure 1 shows the center line pressure distribution P(X,0). For increasing load one observes that the inlet pressure sweep decreases and that the pressure spike height decreases as well as its location moves towards the X=1 position.

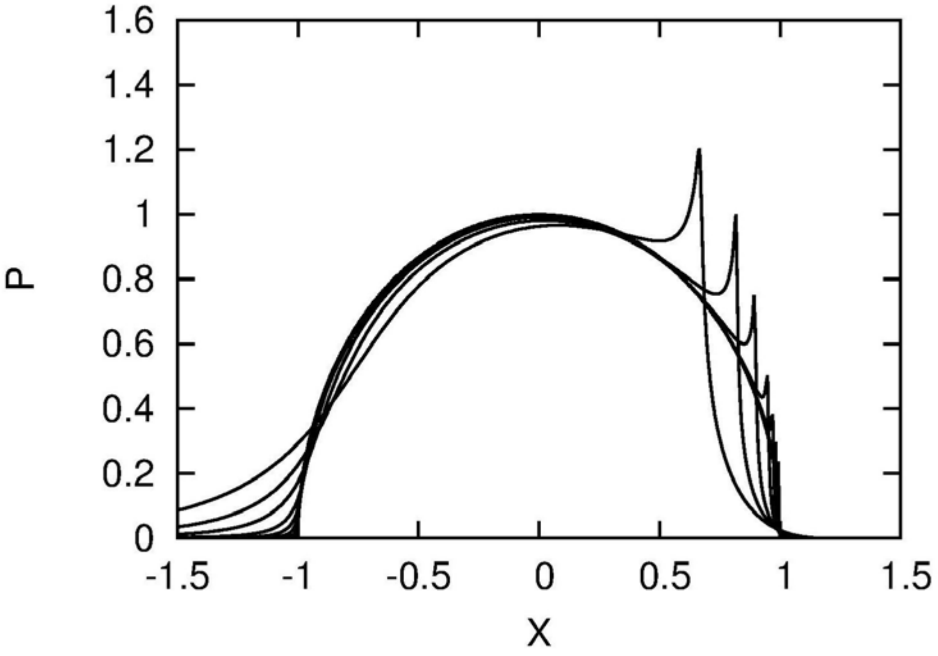

Figure 1: Central line pressure distribution P(X,0) for L=10, M=5,10,…,1000, the pressure peak moves to the right for increasing M.

As the spike height rapidly becomes small compared to the Hertzian pressure distribution, a pressure difference is defined

$$dP(X) = P(X) - \sqrt{1 - X^2}$$

or:

$$dP(X,Y) = P(X,Y) - \sqrt{1 - X^2 - Y^2}$$

for 2 dimensions

Figure 2 shows this pressure difference distribution. It can be observed that for higher loads (M-values) the pressure difference in the inlet and outlet zones tends towards a boundary layer phenomenon, the pressure differences become smaller and more localised. In the inlet the boundary layer is localised at X=-1.

In the outlet, the boundary layer position is not fixed, but moves towards X=1 for increasing M-values.

However, both in the inlet and outlet the *shape* of the pressure difference is the same: a gradual increase, a sharp drop, a gradual increase. As such one can hope that it is possible to find horizontal and vertical scaling factors that create a single master curve.

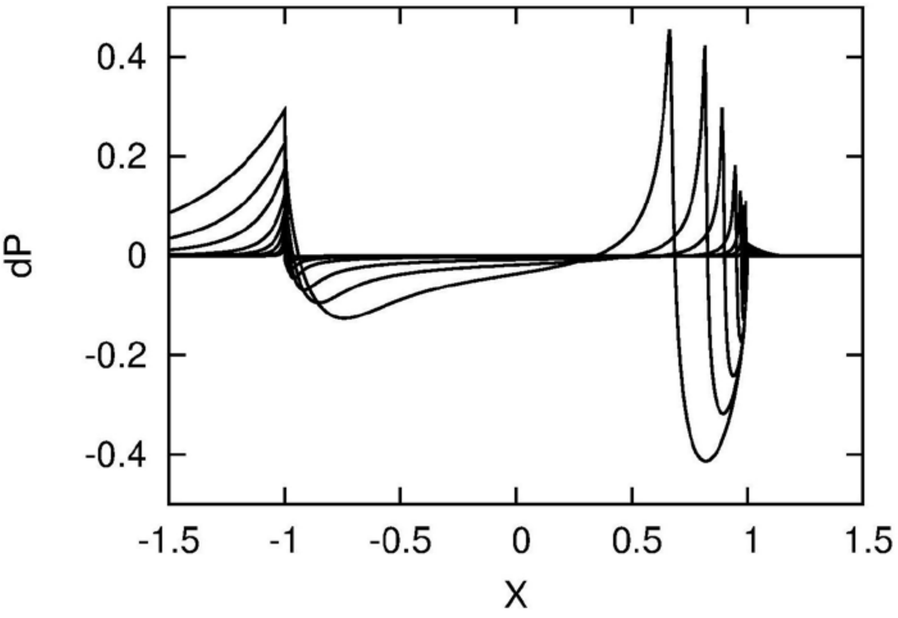

Figure 2: Central line pressure difference distribution dP(X,0) for L=10, M=5,10,…,1000, peak height reduces and peak moves to the right for increasing M.

As was already observed in [11], the central line pressure difference actually describes rather precisely the pressure difference in a much larger (angular) area as can be observed from the next figure. In figure 3 the pressure difference is indicated by colour: yellow means zero difference, red means positive difference, blue means negative difference.

On the central line Y=0 the pressure difference evolution can be followed from inlet to outlet.

The lower half of the figure shows how the inlet and outlet boundary layers become narrower for a tenfold load increase.

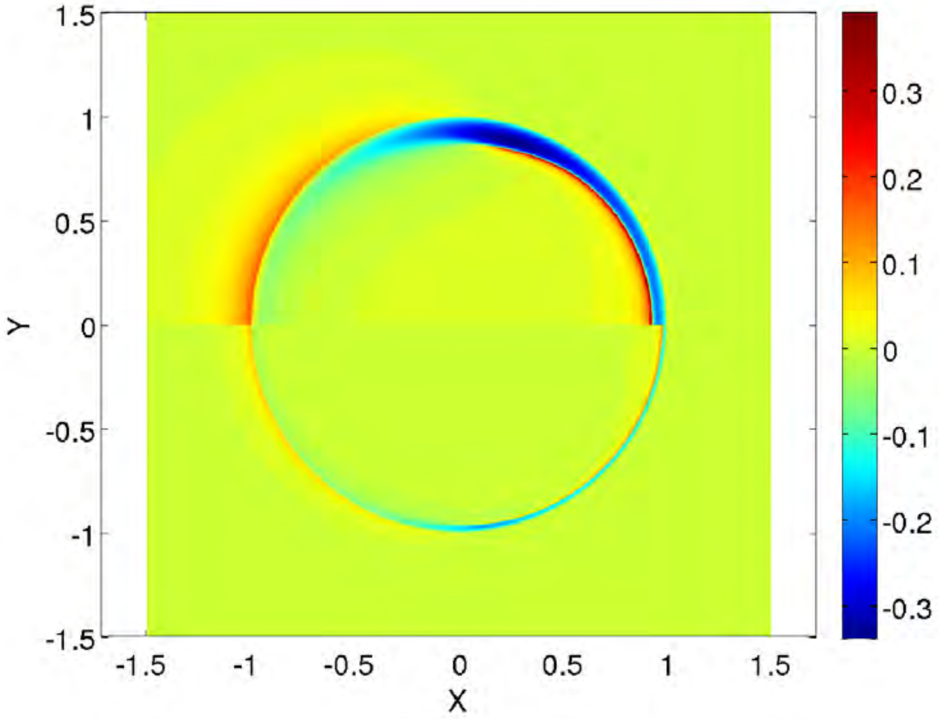

Figure 3: Pressure difference dP(X,Y, M=100 (top) and M=1000 (bottom), L=10, illustrating the boundary layer behaviour.

Inlet analysis

The inlet scaling requires only two parameters, as the position of the inlet singularity is

fixed at X=-1. This can be easily understood as the pressure difference substracts a Hertzian, discontinuous, pressure from a continuous one. As such the difference will show a discontinuity in X=-1 and a less interesting one in X=1. Let us start our analysis in the inlet and zoom in on the behaviour around X=-1. Figure 4 shows a zoom of the inlet pressure differences around X=-1.

The behaviour can be described as a gentle pressure increase until X=-1, followed by a rapid decrease where the pressure difference becomes negative. From here on the negative pressure difference reaches an extreme value and then gradually tends to zero.

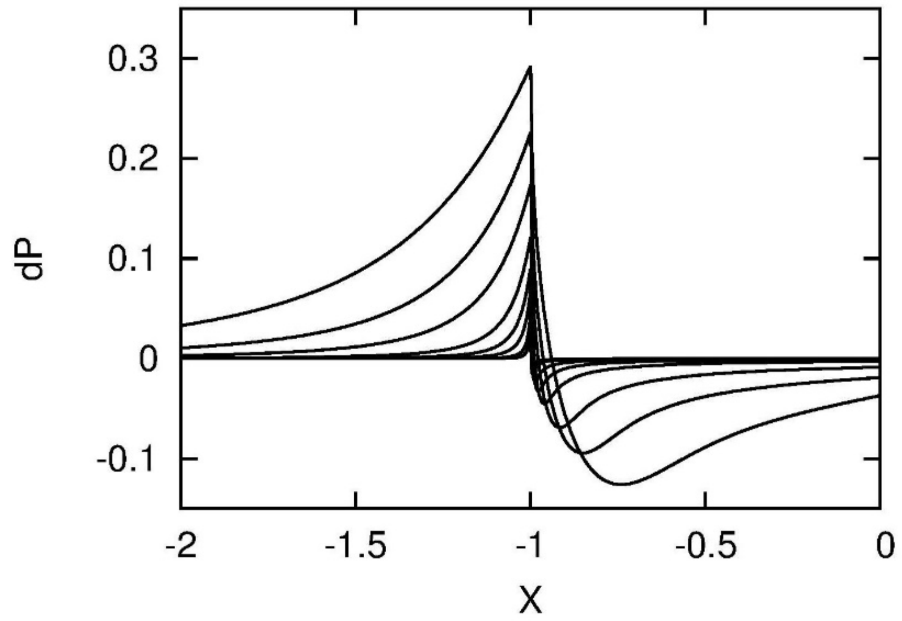

Figure 4: Central line inlet pressure difference distribution dP(X,0) for L=10, M=5,10,…,1000, the peak height reduces for increasing M.

It is clear that both the vertical axis and the horizontal axis need to be stretched for increasing M-values. Curve fitting the width of the boundary layer shows that its width decreases as $M^{-3/4}$, hence a modified $\bar{X}$ parameter is suggested.

We want to maintain the centering of the inlet boundary layer on $\bar{X} = -1.0$, as such its full definition is:

$$\bar{X} = -1 + (X + 1) \bullet M^{3/4}$$

In order to obtain the vertical scaling factor, both the spike height as well as the trough depth were measured and the best fitting exponent was found to be $M^{-0.4}$. Thus a modified pressure $\bar{P}$ is defined as:

$$\bar{P} = P \bullet M^{2/5}$$

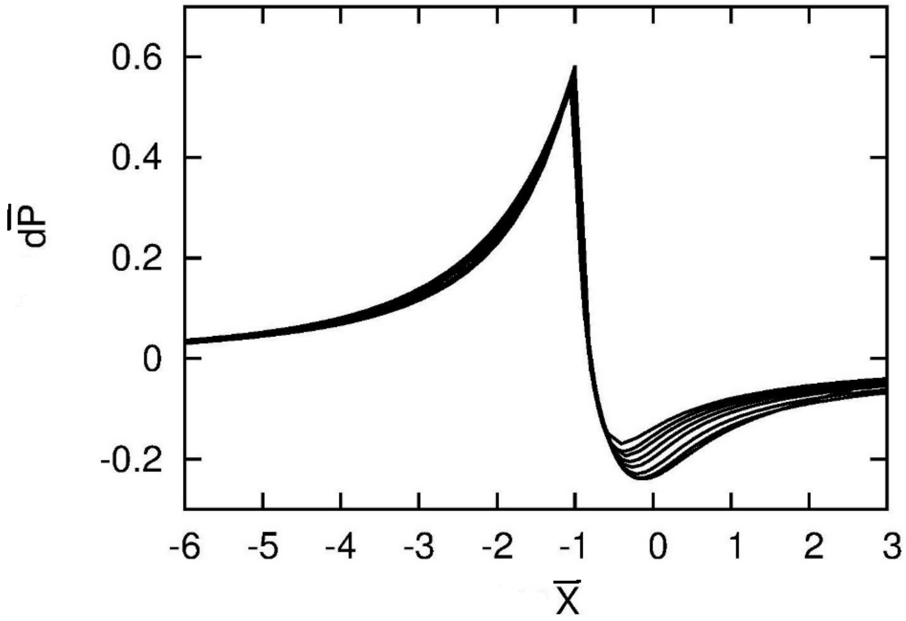

Figure 5: Superposition of the central line inlet pressure difference distributions $d\,\overline{P}(\overline{X})$ *for L=10, M=5,10,…,1000.*

Figure 5 shows a rather nice superposition of the seven curves, especially in the inlet $\overline{X} < -1.0$. The fit is slightly worse for $\overline{X} > -0.5$. This aspect will be addressed later. As such one can consider that the inlet boundary layer width of a circular contact scales with $M^{-3/4}$ and that its pressure difference fluctuations scale with $M^{-2/5}$. Therefore the outlet boundary layer can now be studied. The film thickness fit is given in [14].

Outlet analysis

Figure 6 shows a zoom of the outlet boundary layer. It can be observed, that the spike position moves towards X=1 for increasing M-values and that the spike height and width both decrease with increasing M, as was the case in the inlet. Compared to the inlet, the pressure rise is similar, a gentle increase reaching a maximum, followed by a rapid decrease. However, the negative pressure difference is much more profound than in the inlet. Finally, the pressure difference becomes positive again and shows a small singularity in X=1.

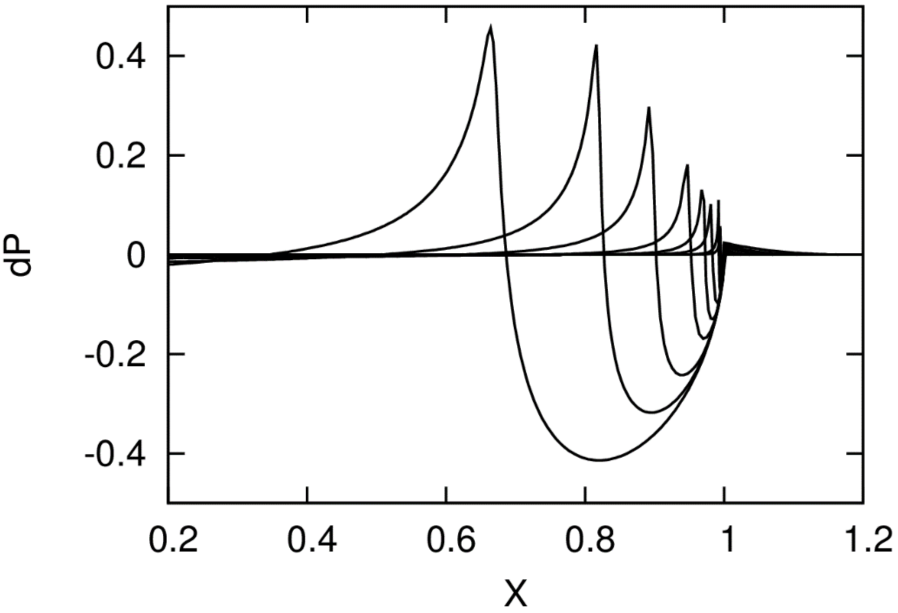

Figure 6: Central line outlet pressure difference distribution $dP(X,0)$ *for L=10, M=5,10,…,1000, the peak moves to the right for increasing M.*

First of all the pressure spike position X_s has to be determined. It was observed that the distance from X=1 decreased in a regular way for increasing M-values. As such the distance to X=1 is curve-fitted.

$$X_s = 1 - M^{-3/4}$$

And the following shift is proposed:

$$1 + X - X_s = X + M^{-3/4}$$

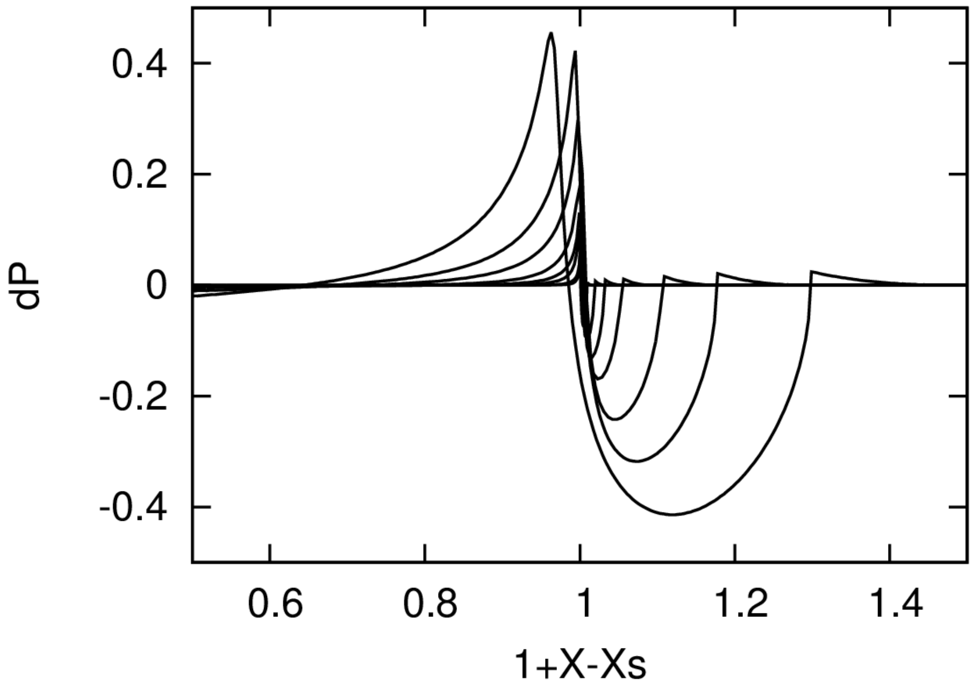

Figure 7: Central line outlet pressure difference distribution dP(1+X-X$_s$,0) for L=10, M=5,10,…,1000, the peak height decreases for increasing M.

From Figure 7 it can be seen that the peak is more or less correctly centered on X=1 and that, as in the inlet, the pressure differences have a similar shape. As such one can try to find scaling factors in X and P to scale all output pressure differences onto a single curve.

As a first approach the scaling factors found in the inlet are used:

$$\bar{X} = (1 + X - X_s) \bullet M^{3/4} = (X + M^{-3/4}) \bullet M^{3/4} = 1 + X \bullet M^{3/4}$$

and

$$\bar{P} = P \bullet M^{2/5}$$

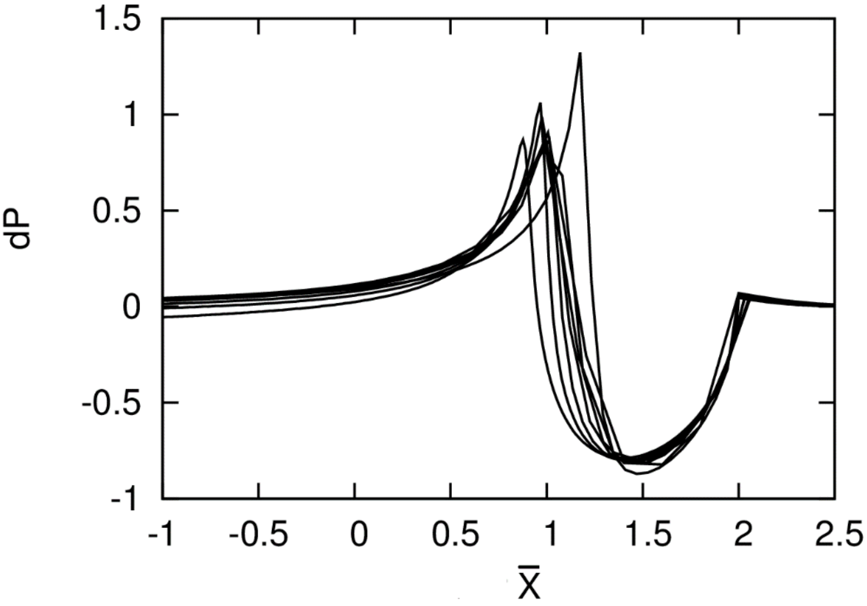

Figure 8: Central line outlet pressure difference distribution $d\bar{P}(\bar{X}, Y=0)$ *for L=10, M=5,10,…,1000.*

Figure 8 shows that the fit for the outlet boundary layer is not as good as for the inlet (Figure 5). Both the position and the height of the spike are not very well captured.

The biggest discrepancy is obtained for the lowest load case M=5, which has the largest and widest pressure spike. As such the explanation of the bad fit can not come from a large discretisation error! For low loads, the pressure difference in the outlet is superimposed on a large Hertzian pressure. This large (overall) pressure influences both the local viscosity and the local density. A similar explanation holds for the negative part of the pressure difference in the inlet. These viscosity and density effects generate nonlinear effects, which cause the scaled curves to separate.

For the limit case of high loads, (high M values) it can thus be safely concluded that the boundary layer approach and its three scaling parameters are accurate approximations.

Rolling Friction

Close to pure rolling, the friction in an EHL contact is dominated by the Poiseuille term: the integral of the film times the pressure gradient. This integral can be rewritten using integration by parts as:

$$\int\int H(X,Y)\frac{\partial P}{\partial X}\,dX\;dY = \int P(X,Y)\,H(X,Y)\,|_{-\infty}^{+\infty}\;dY - \int\int P(X,Y)\frac{\partial H}{\partial X}\,dX\;dY$$

The first term on the right hand side is zero, as the pressure is zero at the integration boundaries.

In order to understand where the rolling friction is generated we study the central line contribution first. The Poiseuille friction contribution on the central line Y=0 is cumulated from -∞ to X. Figure 9 shows its evolution: the rolling friction increases slowly in the inlet until the Hertzian zone is reached at X=-1. Then the value is constant until X=0.8, as dH/dX=0 (or at least very small). Finally, a very local increase is observed corresponding to the pressure spike. Thus it can be concluded that the rolling friction emanates from the two previously studied boundary layers.

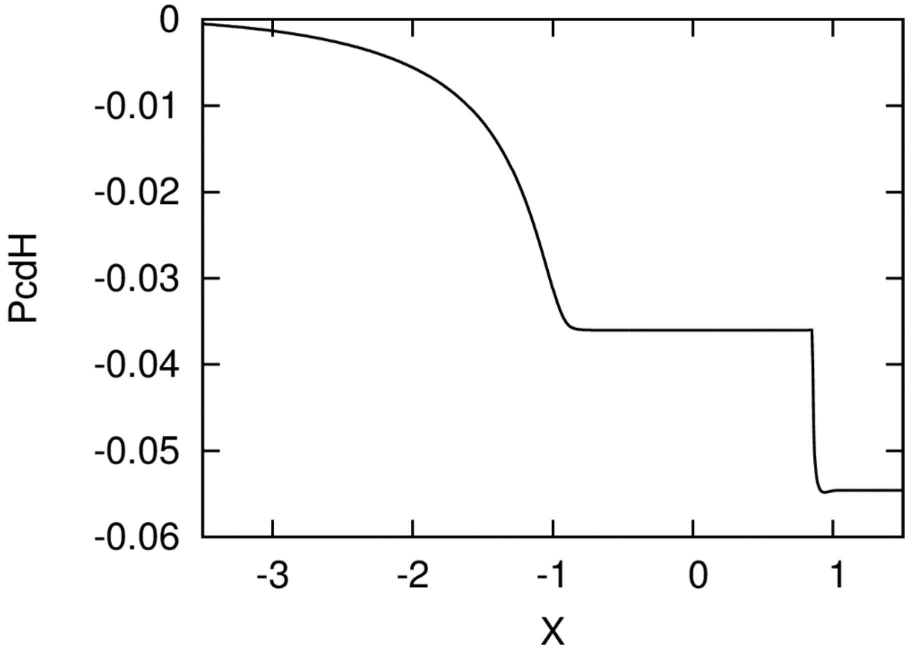

Figure 9: Cumulated Pressure times Film gradient (X,Y=0), M=100, L=10.

Now we study the rolling friction integrated over X as a function of Y.

Figure 10 shows that the major contribution comes from the central film area |Y|<0.8 and that the contribution drops off quickly for |Y|>1.0.

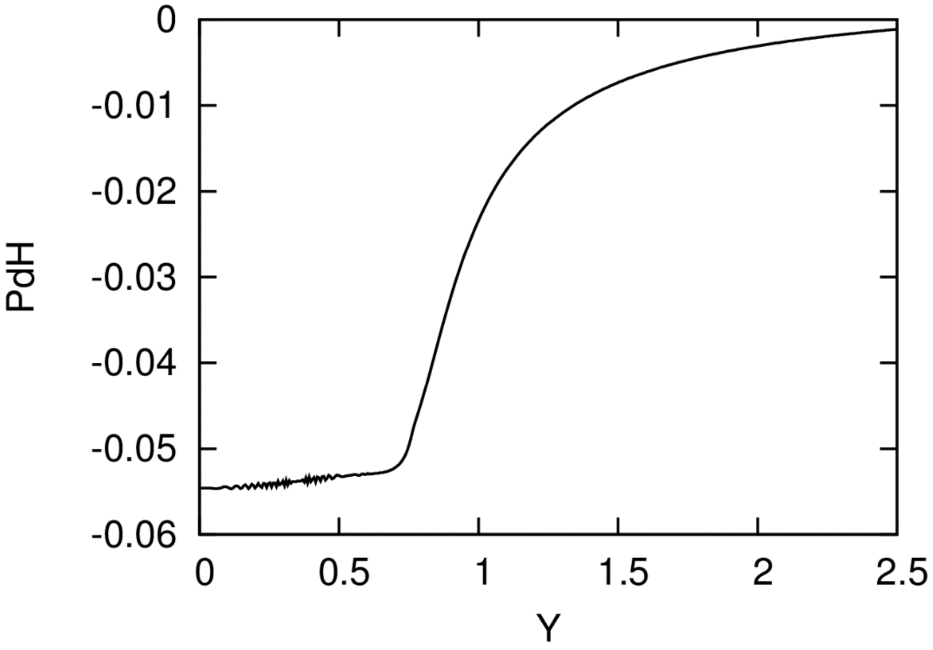

Figure 10: Pressure times Film gradient integrated over X as a function of Y, M=100, L=10.

The work on the boundary layers can now be employed to study the rolling friction.

The pressure P and film thickness H can be split in two parts: The Hertzian part and the difference. The integral becomes:

$$\int\int (P_H + dP)\frac{\partial(H_H + dH)}{\partial X}\ dX\ dY$$

The product of the Hertzian components is zero, the product of the difference terms dP dH is small and neglected. Hence the integral is:

$$= \int\int P_H \frac{\partial dH}{\partial X}\ dX\ dY + \int\int dP \frac{\partial H_H}{\partial X}\ dX\ dY$$

The first integral is zero in the inlet zone, the second is zero in the high pressure zone.

Using the pressure scaling $\bar{P}$ and film thickness scaling $\bar{H}$, a scaled rolling friction can be predicted over a very wide range of operating conditions.

The result can be made dimensional again, yielding a precise rolling friction prediction based on physical parameters!

Conclusion

The EHL contact can be considered as a Hertzian contact with an inlet and an outlet boundary layer.

In the inlet boundary layer the flow evolves from iso-viscous to heavily piezo-viscous.

In the outlet boundary layer the flow evolves from heavily piezo-viscous to iso-viscous.

The pressure difference in inlet and outlet layers have a similar shape.

The pressure difference in inlet and outlet can be scaled using the same parameters,

Two parameters are required to scale the inlet: width ($\bar{X}$) and height ($\bar{P}$).

Three parameters are required to scale the outlet: position X_s, width ($\bar{X}$) and height ($\bar{P}$).

The inlet boundary layer has an overall positive contribution to the load.

The outlet boundary layer has an overall negative contribution to the load.

The rolling friction evolution can be predicted using the scaling parameters.

BIBLIOGRAPHY

[1] Petrusevich, A.I.. 1951, ``Fundamental Conclusions from the Contact Hydrodynamic Theory of Lubrication," *Izv. Akad. Nauk SSR (OTN)* **2**, pp. 209-223

[2] Dowson, D. and Higginson, G.R., 1966, "Elasto Hydrodynamic Lubrication", *Oxford Pergamon.*

[3] Hamrock B.J. and Dowson D., 1977, ``Isothermal elastohydrodynamic lubrication of point contacts, part II- Fully Flooded Results," *ASME Journal of Lubrication Technology*, **99**, pp. 264-275.

[4] Safa, R.J. and Gohar, 1985,``A theoretical analysis of the isothermal elastohydrodynamic lubrication of concentrated contacts I. Direction of lubricant entrainment coincident with the major axis of the Hertzian contact Ellipse, " *Proc. R. Soc. Lond.*, **A 397**, pp. 245-269.

[5] Greenwood, J.A., 1972, ``An extension of the Grubin theory of elastohydrodynamic lubrication," *J. Phys D: Appl. Phys*, **5**, pp. 2195-2211.

[6] Archard J.F. and Baglin K.P., 1975, ``Nondimensional Presentation of Frictional Tractions in Elastohydrodynamic Lubrication, Part 1: Fully Flooded Conditions," *ASME Trans.*, pp. 398-411.

[7] Hooke, C.J., 1977, ``The Elastohydrodynamic Lubrication of Heavily Loaded Contacts," *J. of Mech. Eng. Science*, **19, 4** , pp. 149-156.

[8] Kudish I.I. and Covitch M.J., 2010, ``Modeling and analytical methods in tribology", *Chapman and Hall/CRC.*

[9] Kudish I.I., 2013, ``Asymptotic analysis of lubricated heavily loaded point contacts", *Lubrication Science*, **25**, pp. 478-505.

[10] Snoeijer, J.H., Eggers, J. and Venner, C.H., 2013, ``Similarity theory of lubricated Hertzian contacts," *Physics of Fluids*, **25**, 101705.

[11] Biboulet N., Sperka, P., Venner, C.H., Lubrecht, A.A. and Krupka, I", 2013, ``Obtaining the pressure spike and maximum shear stress from optical interferometry data", *Tribology International, Elsevier*, **62**, pp. 1-7.

[12] Venner C.H., Biboulet N. and Lubrecht A.A., 2014, ``Boundary Layer Behaviour in Circular EHL Contacts in the Elastic-Piezo-Viscous Regime," *Tribology Letters,* **56(2),** pp. 375-386.

[13] Brandt, A.}, 1977, ``Multi-Level Adaptive Solutions to Boundary Value Problems", *Math. Comp*. **31, 2**, pp. 333-390.

[14] Brandt, A. and Lubrecht, A.A., 1990, ``MultiLevel Matrix Multiplication and Fast Solutions of Integral Equations", *J. Comp. Phys.* **90, 2**, pp. 348-390.

[15] Venner C.H. and Lubrecht A.A., 2000, ``MultiLevel Methods in Lubrication," Elsevier Tribology Series, **19**.

[16] Herrebrugh, K., 1968, ``Solving the incompressible and isothermal problem in Elastohydrodynamic lubrication through an integral equation, *ASME J. of Tribology*, **90**, pp. 262--170.

[17] Moes H., 2000, ``Lubrication and beyond", *University of Twente web-site*.

Dynamics simulation of rolling element bearings considering elastohydrodynamic cage contacts

Dipl.-Ing. Katrin Seiler
Dr.-Ing. Stephan Tremmel
Prof. Dr.-Ing. Sandro Wartzack
Friedrich-Alexander-Universität Erlangen-Nürnberg (FAU), Engineering Design

Dipl.-Ing. (FH) Bodo Hahn
Dr.-Ing. Michael Plogmann
Dipl.-Ing. (FH) Oliver Graf-Goller
Schaeffler Technologies AG & Co. KG

Abstract

Rolling bearings that run under high centripetal acceleration show increased friction in their cage contacts. Hence, the hydrodynamics as well as the deformation of the cage have to be taken into consideration in rolling element bearing dynamics simulations. This paper shows how to consider a full-elastically modelled cage in an elastic dynamics simulation for rolling element bearings to improve the accuracy of simulation results (esp. relating to friction torque). The deformed contact geometry is reconstructed from the cage's nodes through cubic splines. After that the distance between the deformed cage geometry and the outer ring is calculated, which is considered as the lubrication film thickness. Finally, the contact pressure is calculated depending on the lubrication film thickness by using the short journal bearing theory. The contact calculation is compared to the elastic multi-body dynamics simulation program AVL Excite^{TM}. Furthermore, the simulation results considering the elastically modelled cage are evaluated to simulation results of a rigidly modelled cage using the rolling element bearings multi-body dynamics simulation program CABA3D. It can be seen that there is a significant influence on the pressure distribution and the friction torque if a rigidly modelled or a full-elastically modelled cage is utilized. The hydrodynamics and the cage's elasticity should not be neglected in rolling bearing dynamics simulations for bearings that run under high centripetal accelerations.

Introduction

Dynamics simulations of rolling element bearings are amongst others more and more used to develop new energy-efficient bearing applications. Therefore, it is very important calculating friction as good as possible in such simulations. Rolling and sliding friction occurs in the contacts between rollers and raceways. These friction losses normally represent the most important fraction of the friction torque under usual conditions without external centripetal acceleration or major deformations of bearing or housing components. Therefore, the contact and lubrication conditions are already considered precisely in the contacts between rollers and raceways. The sliding friction in the cage's contacts, for example between cage pockets and rollers or cage and outer ring, often is just simplified taken into consideration by using a constant friction coefficient representing the lubricated material pairing of the contact. But high friction losses can occur in the cage contacts of the bearing under high centripetal accelerations, for example in piston rod bearings or in planet gear bearings [1,2]. Therefore, the sliding friction in the lubricated cage contacts should be taken into consideration more precisely.

Under centripetal accelerations the outer ring guided cage is shifted relatively to the outer ring, which leads to an eccentricity between cage and outer ring. In addition the cage deforms with increasing centripetal acceleration and comes into contact with the outer ring (see figure 1). The deformations and friction increase with higher centripetal accelerations and this may also lead to higher wear. A higher friction torque in the contact between cage and outer ring has an influence on the cage's kinematics and thus can change the whole bearing's kinematics [3].

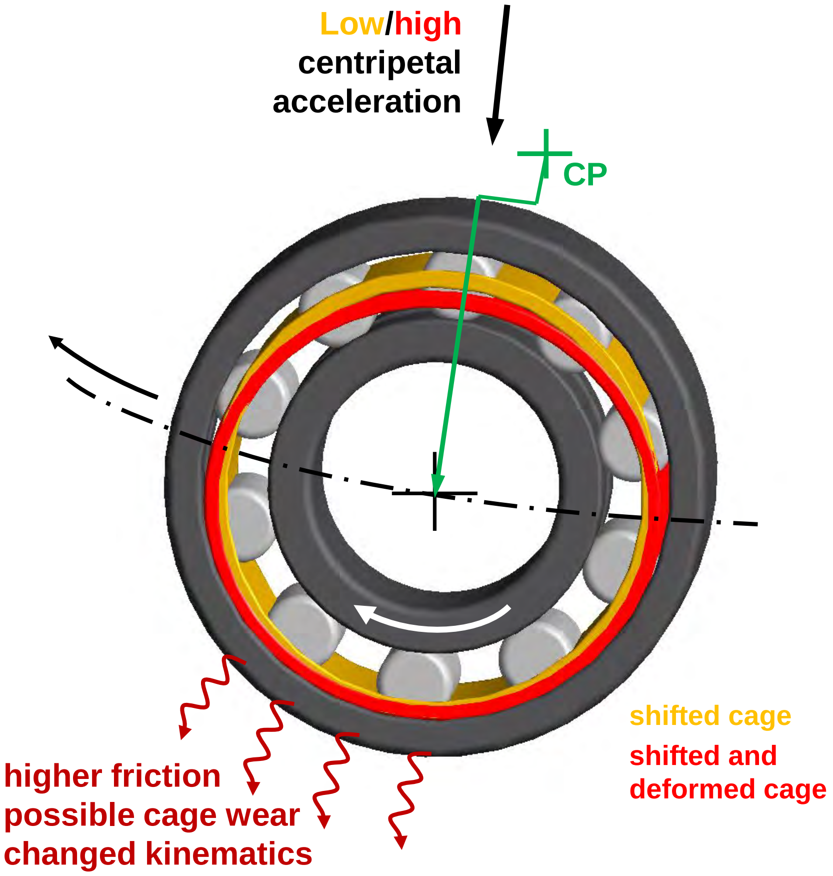

Figure 1: Shifted and deformed cage under centripetal acceleration

First approaches to consider the elastic deformation of the cage in a 2-dimensional dynamics simulation program for rolling element bearings were published by Pothoff and Siepmann [4,5]. The cage deformation is determined with the help of so-called deformation numbers which are calculated in a previously performed finite element simulation. Liang continued their work and used a simplified, alternative cage ring, whose width is adjusted to the same mass as the original cage. The cage ring is discretized in circular beams corresponding to the number of rolling elements. The stiffness of one circular beam is calculated. After that the stiffness of the cage is represented by the reassembling of all circular beams. This simplification leads to a time efficient calculation [6]. Hahn developed an elastic cage model consisting of cage segments which are connected with spring-damper-elements. The stiffness matrix of one segment is calculated in a previous finite element simulation and is represented in the cage model by the stiffness of the spring-damper-elements [7]. Wohlgemuth et al. used the commercial multi-body dynamics simulation program Adams™ which provides an interface for the integration of elastic bodies. The elastic cage model has to be reduced in a finite element program, before it can be used in the dynamics simulation [8]. Weinzapfel et al. developed a new elastic cage model consisting of cage pockets with a rigid contact surface which are connected with rigid beams to the finite elements of the cage [9]. A full-elastically modeled cage is also presented in a quite new work by Ashtekar et al. [10]. The contact between rigid bodies and the finite elements of the elastic body is solved by a new contact algorithm which distributes the contact force to the neighbored finite element nodes dependent on their distance to the resultant force.

The hydrodynamic lubrication in the contact between cage and outer ring is often calculated by use of the short journal bearing theory [11,12,13]. This approach offers an analytical calculation method for the hydrodynamics in the cage/outer ring contact. Hahn [7] considers the friction torque and the damping of the lubrication between cage and outer ring and in the cage pockets/roller contacts. The friction torque between cage and outer ring is calculated by a discretization of the film thickness over the circumference. The friction force of every segment is calculated by the approach of plane sliders of infinite width and is integrated over the circumference of the contact. The contact forces resulting from the hydrodynamic pressure are not considered in [7]. Furthermore, the hydrodynamics between the cage bars' surfaces and the outer ring is neglected.

Especially under high centripetal accelerations the hydrodynamics of the lubrication in the cage/ring contacts and in the cage/rolling element contacts as well as the elastic deformation of the cage have to be taken into consideration more precisely. Therefore, the cage's guiding surfaces as well as the cage's bars are considered in the contact calculation between cage and outer ring. The hydrodynamic pressure at the cage's bars and the guiding surfaces are calculated separately based on the short journal bearing theory. That simplification leads to an analytical, time efficient equation for the pressure calculation. Furthermore, the calculation is numerically stable and so it can be used in the dynamics simulation for rolling element bearings. The normal force and the friction force of the contact are obtained from the pressure and the lubrication film thickness. Furthermore, the cage's movement causes a squeeze force which is considered in the hydrodynamic contact model, too. This consideration of the hydrodynamics in the contact between cage and outer ring was presented by the authors first in [3,14,15] and was transferred in CABA3D [16], which was developed at Schaeffler Technologies.

In this paper the elastohydrodynamics in the contact between cage and outer ring is still calculated separately for the guiding surfaces of the cage and the cage bars (see figure 2). Hence, hydrodynamics can be well approximated using the short journal bearing theory [15].

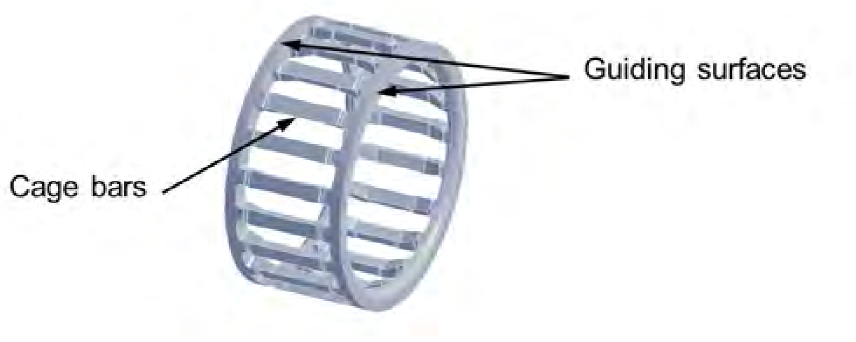

Figure 2: Model of the cage consisting of two guiding surfaces and a certain amount of cage bars

Considering a full-elastically modelled cage

Considering a full-elastically modelled cage in dynamics simulations, the mass matrix and the stiffness matrix describing the cage behavior must be obtained from a finite element program first. Furthermore, the master nodes, whose degrees of freedom are still available after applying a suitable reduction method, and the number of modes have to be determined for the reduction of the model. Additional interface nodes, which are necessary to return the forces to the elastic body, have to be defined precisely. The selected interface nodes should be able to adequately represent the deformed cage geometry. For this reason an equal distribution of the interface nodes over the guiding surfaces of the cage and at least one interface node in the middle of each cage bar is used.

Afterwards, the matrices have to be reduced to some less hundreds of degrees of freedom. In this work the CRAIG-BAMPTON method [17] is used. That leads to a calculation-time-efficient consideration of parts with a linear-elastic deformation behavior in the dynamics simulation for rolling element bearings. Now the positions and velocities of the interface nodes $I_{1\ldots N}$ are known in every time step of the elastic-body dynamics simulation and can be used for further contact calculations.

To combine elastic cage deformation and hydrodynamics in the cage contacts, the deformed geometry of the cage has to be reconstructed from the interface node positions at first. As it can be seen in figure 3, the interface nodes are developed from the circumference of the guiding surface into the x-z-plane first. For example cubic splines can be used for the interpolation of the deformed cage geometry between the defined interface nodes as supporting points. Additional spline points $S_{1\ldots N}$ are calculated on the spline, which can be used as additional grid nodes for the calculation of the hydrodynamics. After that the distance between the deformed guiding surface of the cage and the contact partner can be determined at each spline point and interface point over the whole guiding surface. This distance represents the gap between the contact partners and so the lubrication film thickness $h_{1...N}$ if expecting a fully lubricated contact. Otherwise starvation effects should be considered in the contact calculation.

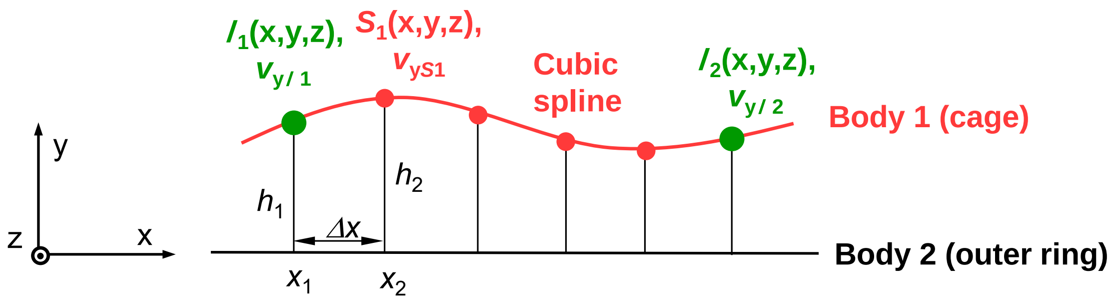

Figure 3: Interpolated guiding surface and calculation of the lubrication film thickness

The lubrication film thickness and the relative radial velocity in y direction v_y at the spline points as well as the relative velocity between the contact partners in x direction u_{rel} and the lubrication's viscosity $\eta(p,\vartheta)$ are needed to calculate the hydrodynamic pressure p(x,z) by equation 1. The lubrication's viscosity is depending on pressure and temperature and is calculated by ROELANDS' equation [18] which can be used within pressures of a medium level [19]. The width of the guiding surface is represented through b.

$$p(x,z)=\frac{3\eta(p,\vartheta)}{h(\mathrm{x})^3}\left(\frac{b}{2}\right)^2\left[u_{\mathrm{rel}}\frac{\Delta h}{\Delta x}+2v_{\mathrm{y}}\right]\cdot\left(1-z^2\right) \tag{Eq. 1}$$

with: $\frac{\Delta h}{\Delta x}=\frac{h_2-h_1}{x_2-x_1}$

$p(\mathrm{x,z})$	Pressure
$\eta(p,\vartheta)$	Dynamic viscosity
$h(\mathrm{x})$	Lubrication film thickness
b	Width
u_{rel}	Hydrodynamic velocity between contact partners
v_{y}	Normal velocity in y direction
ϑ	Lubrication's temperature

This analytical equation of the pressure is derived from the REYNOLDS equation based on the short journal bearing theory. The REYNOLDS equation is integrated two times using the boundary conditions $p(z=\pm1)=0$ and $\mathrm{d}p/\mathrm{d}z(z=0)=0$. The half SOMMERFELD solution, which means that negative pressures are set to 0, is used to zero negative pressures. Eq. 1 leads to a parabolic pressure distribution in z direction [20]. The pressure is integrated over z and x, see equation 2, to obtain the load on every spline node.

$$F_{\mathrm{i}}=\frac{b}{2}\int_{-1}^{1}p(\mathrm{x,z})\cdot\mathrm{dz}\cdot\Delta x \tag{Eq. 2}$$

F_{i}	Load at a S_{i}

The calculation of the total friction force considers the liquid friction force fraction $F_{\text{fric liquid}}$ and the solid friction force fraction $F_{\text{fric solid}}$, which are calculated by equations 3 and 4.

The liquid friction force fraction is calculated by the integration of the shear stresses τ. The shear stresses in the lubrication film thickness $h(x)$ can be estimated for a short journal bearing by $\eta u_{rel}/h(x)$ [20]. The shear stresses are calculated by EYRING's equation [21] because a NEWTONian rheology model may lead to unrealistic high stresses [19].

$$F_{\text{fric liquid i}} = \frac{b}{2}\int_{-1}^{1}\left(1-\lambda\left(h(x),R_{\text{q}}\right)\right)\cdot \underbrace{\tau_0 \sinh^{-1}\left[\left(\frac{\eta(p,\vartheta)}{\tau_0}\right)\frac{u_{\text{rel}}}{h(x)}\right]}_{\text{EYRING: } \tau_0 \cdot \sinh^{-1}\left(\frac{\tau}{\tau_0}\right)}\cdot \mathrm{d}z\cdot \Delta x \qquad \text{Eq. 3}$$

$F_{\text{fric liquid i}}$	Liquid friction force at a S_{i}
$\lambda\left(h(x),R_{\text{q}}\right)$	ZHOU's factor
τ_0	EYRING's stress at transition from linear to nonlinear behavior
τ	Shear stress in the lubrication film thickness, $\tau = \eta(p,\vartheta)\mathrm{u}_{\text{rel}}/h(x)$

The solid friction force fraction depends on the normal contact force, which can be obtained by the integration of the pressure over z and x. The normal contact force is multiplied with a solid friction coefficient $\mu_{\text{fric solid}}$ for sliding which represents the material pairing outer ring/cage with oil-wetted surfaces. The exact friction coefficient, depending on the material pairing and the lubricant, should be experimentally measured to receive results with high accuracy.

$$F_{\text{fric solid i}} = \mu_{\text{fric solid}}\cdot\frac{b}{2}\int_{-1}^{1}\lambda\left(h(x),R_{\text{q}}\right)\cdot p(x,z)\cdot \mathrm{d}z\cdot \Delta x \qquad \text{Eq. 4}$$

$F_{\text{fric solid i}}$	Solid friction force
$\mu_{\text{fric solid}}$	Solid friction coefficient

Both friction fractions are weighted by ZHOU's factor $\lambda(h(x),R_{\text{q}})$. The ZHOU's factor depends on the root-mean-squared roughness R_{q} of the contact partners and the height of the lubrication film thickness $h(x)$ [22]. Both friction fractions are summed.

The resultant force R(x,z) between two interface nodes (see figure 4) consisting of cage load and friction force and its positon relative to the interface nodes are calculated so that the force can be proportionately distributed to the neighbored interface nodes. The forces are returned to the interface nodes, which leads to a new deformation state of the cage and to an acceleration of the nodes' velocity. Then the calculation starts again until the equilibrium state is reached and all time steps are calculated.

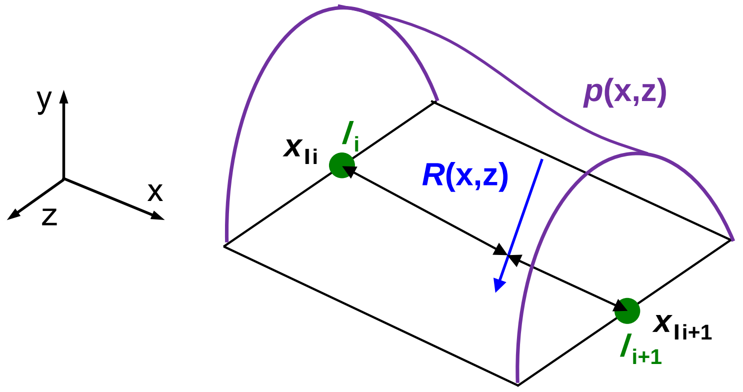

Figure 4: Calculated pressure and distribution of the resultant forces to the interface nodes

However, some assumptions and simplifications are made within the presented elastohydrodynamic model to realize a time efficient calculation. A fully lubricated contact is assumed. Starvation effects are not considered yet. The misalignment of the cage has an influence on the calculated friction torque. The misalignment is already considered by individual lubricating film thicknesses at both guiding surfaces. It is therefore possible to incorporate the influence of misalignments on the friction torque in the future. High friction leads to an increase of the contact temperature and has for example an influence on the lubricant's or the cage's material properties. Therefore, an average operating temperature is estimated for the contact calculation.

The presented calculation of the elastohydrodynamic contact between cage and outer ring was implemented in CABA3D.

Model verification

The simulation results using the before described elastohydrodynamic model between cage and outer ring were compared to those of a multi-body dynamics simulation program with hydrodynamic contacts named AVL Excite™ [23]. AVL Excite™ is able to consider the elastic deformation in journal bearings. So the same geometric model of a thin cage guiding ring was built in AVL Excite™ and the elastic-body dynamics simulation program elastic CABA3D. The width of the guiding ring is 5.3 mm, the diameter is 62.775 mm and the thickness is 2 mm. The guiding surface rotates with 3890 min^{-1} in an outer ring with a diameter of 63 mm. The contact is lubricated with oil of the type ISO VG 32 at 60 °C. Figure 5 shows the pressure and the lubrication film thickness, which occur at a load of 100 N. One guiding surface of the cage is loaded with about 100 N at a centripetal acceleration of 3000·g in the rigid calculation as presented in [15]. The cage and the outer ring are made of steel. Therefore, a typical friction coefficient for boundary friction condition between two oil wetted surfaces is 0.07 and is used in the contact calculation.

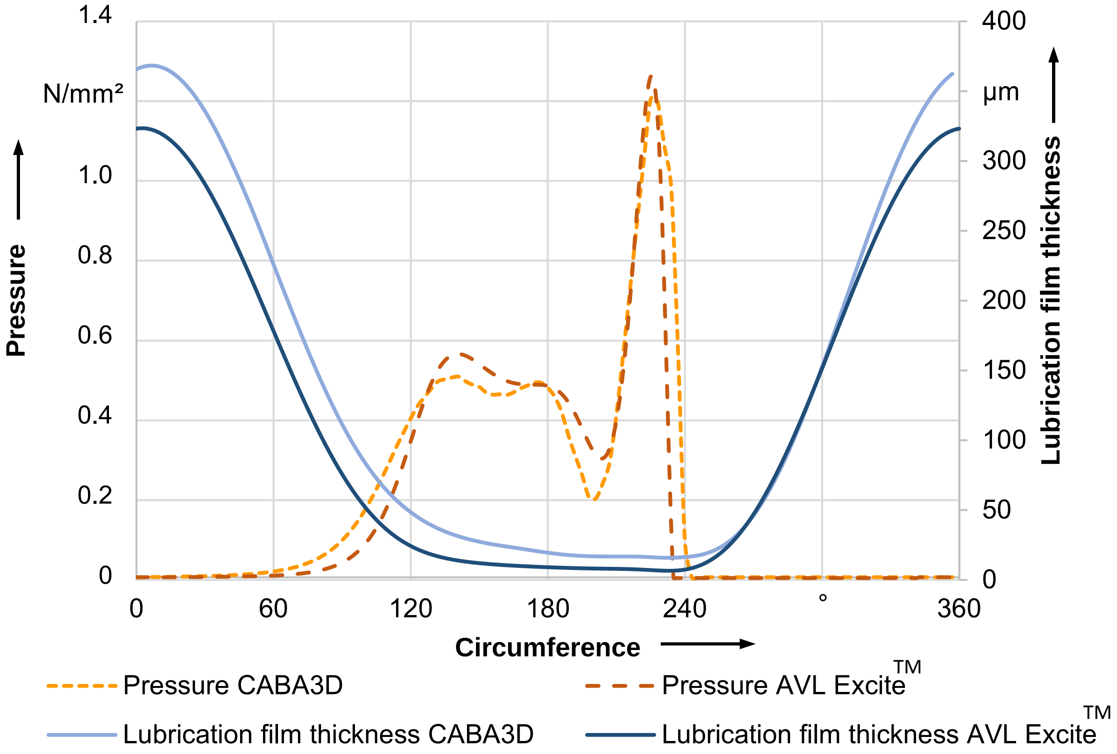

Figure 5: Comparison of pressure and lubrication film thickness calculated in CABA3D and AVL Excite™ at a load of 100 N

The pressure and lubrication film thickness calculated in elastic CABA3D and AVL Excite™ are plausible and correlate qualitatively well. The film thickness decreases continuously from the inlet until the lowest film thickness is reached around 240° and shows a contraction at the outlet. The film thickness is slightly higher in CABA3D because the analytical calculated pressure leads to a higher load on the cage. The pressure distribution depends on the film thickness. That leads to a wide pressure distribution between a circumference angle of 60° and 200° and a high pressure peak at the outlet. The pressure in the middle of the contact zone shows two small pressure peaks due to the deformation of the guiding surface of the cage.

At lower loads, as it can be seen in figure 6, the two small pressure peaks are fusing to one pressure peak because of the smaller cage deformation. The pressure peak at the contact outlet calculated with AVL Excite™ shifts to the middle of the contact zone at lower loads while the pressure peaks calculated in elastic CABA3D are still located at the same position. However, the pressure distributions which are received from elastic CABA3D and AVL Excite^{TM} correlate qualitatively well even at lower loads like 40 N and 60 N.

The elastohydrodynamic pressure calculated with an elastically modelled cage was compared to the hydrodynamic pressure distribution performed with a rigidly modelled cage as presented in [3,14]. As it can be seen in figure 7, the rigidly modelled cage shows one high pressure peak before the lowest film thickness is reached at 180°. The pressure is extended over a relatively small zone. The elastically modelled guiding surface deforms and that leads to a much wider but lower pressure distribution at the same load of 100 N.

The comparison of the pressure distributions of the rigidly and elastically modelled guiding surfaces shows the importance of the consideration of elasticity and hydrodynamics in the contact between cage and outer ring under high loads.

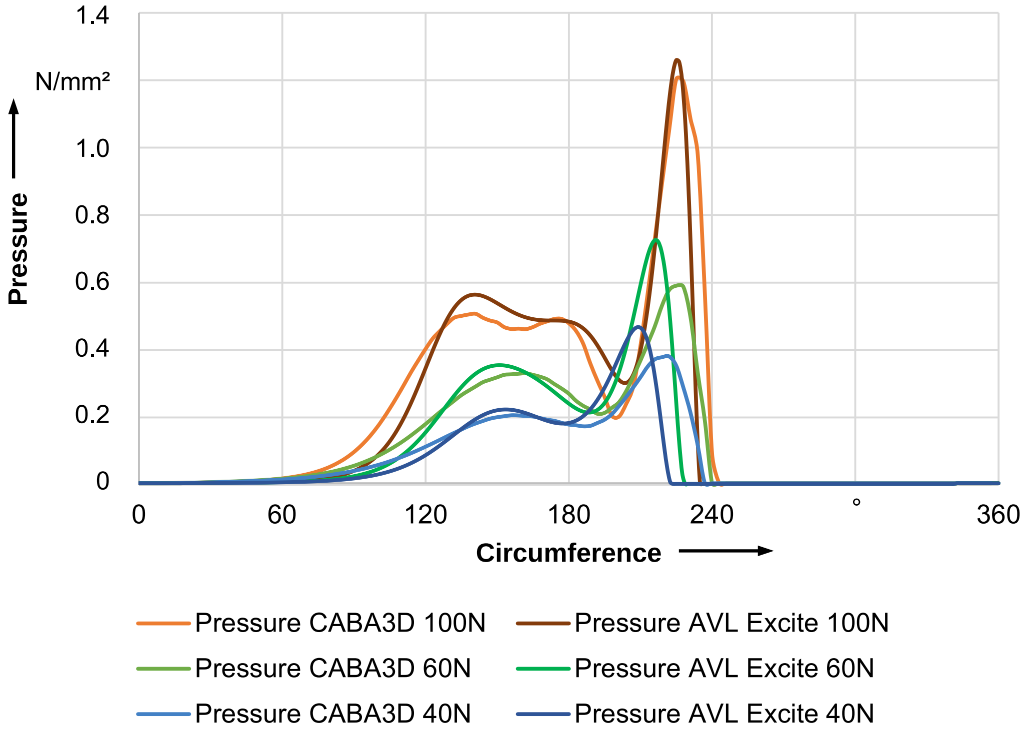

Figure 6: Pressure distribution at different loads calculated in CABA3D and AVL Excite^{TM}

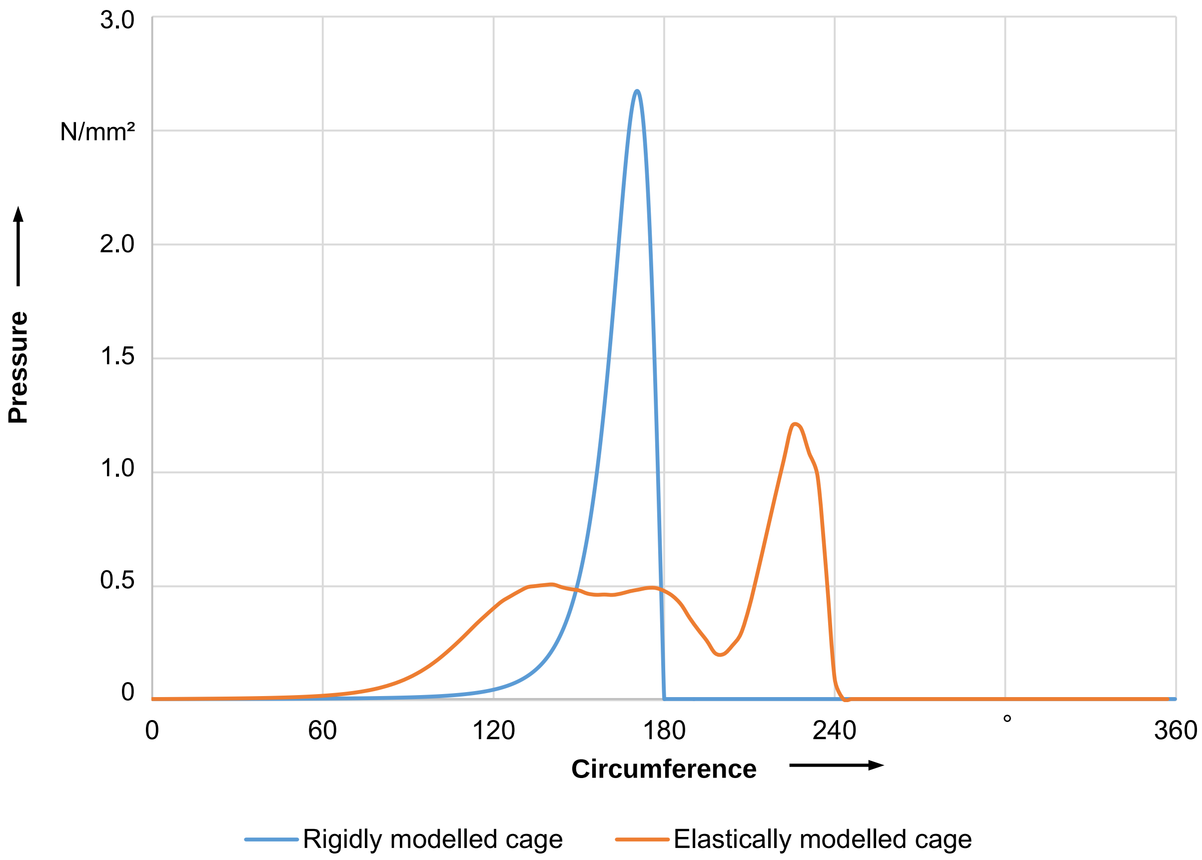

Figure 7: Comparison of the pressure distribution calculated with a rigidly and elastically modelled cage at a load of 100 N

Consequences for the friction torque

The elastic deformation of the cage leads to a higher friction torque in the cage/outer ring contact, especially at high loads as they occur under high centripetal accelerations. A piston rod bearing for example undergoes accelerations up to 3000·*g*. The influence of the cage deformation modelling on the friction torque can be seen in figure 8. A cage of a needle bearing, consisting of the guiding surfaces which are connected with the cage bars (figure 1), was built both with a rigidly modelled cage and an elastically modelled cage. Both variants use the same hydrodynamic contact calculation in the cage/outer ring contact. This contact calculation and the validation with a rigid journal bearing program was presented in [3,14] and [15].

If the cage is loaded with very small forces, for example 20 N, there is no significant difference between the friction torque in the cage/outer ring contact calculated with the rigidly or the elastically modelled cage. Since the small forces lead to no significant deformation the rigidly modelled cage in CABA3D can still be used for the most bearing applications under stationary conditions. With increasing load the rigidly modelled cage shows a slightly increasing friction torque. At a load of 500 N, which is according to a centripetal acceleration of 3000·*g*, the friction torque is just nearly the double of the friction torque at 20 N. While using the elastically modelled cage in the dynamics simulation with its elastohydrodynamic contact calculation the friction torque shows a significant higher gradient. At high loads, for example 500 N, the friction torque is 450 % of the friction torque at 20 N.

The cage deforms and comes into contact with the outer ring under high loads. That leads to a wider pressure and the low film thickness causes higher shear stresses over a wider contact area in the lubrication film. That leads to a higher friction torque between the cage and the outer ring if the cage is calculated elastically.

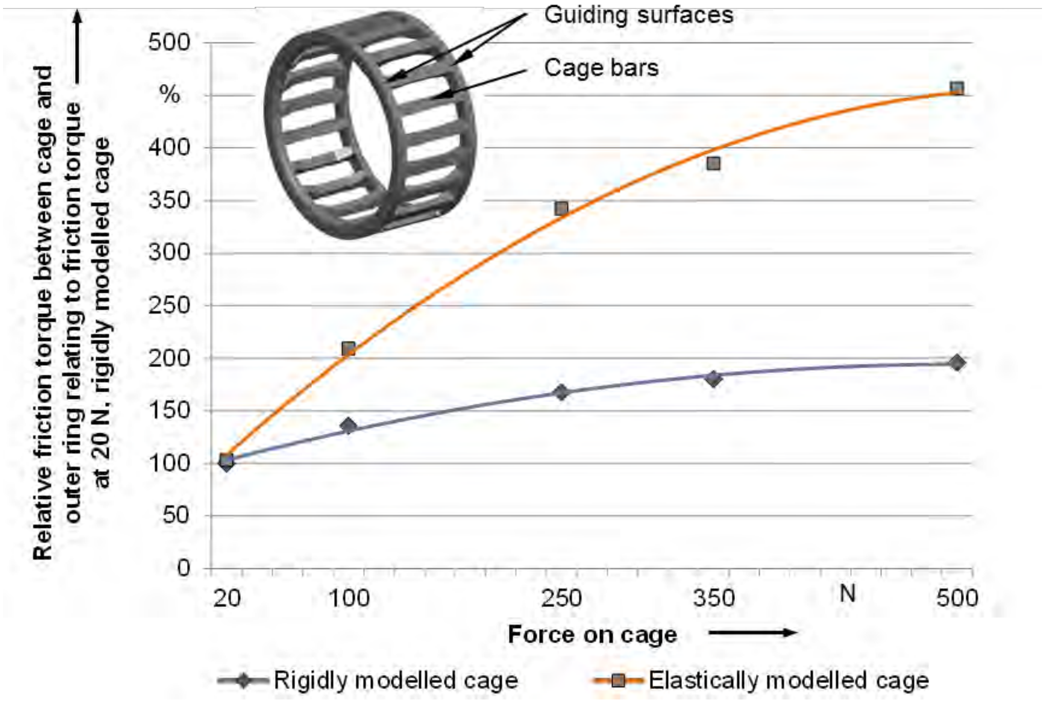

Figure 8: Comparison of the friction torque in the cage/outer ring contact calculated rigidly and elastically

This simulation study shows that the friction torque between cage and outer ring is strongly influenced, whether the contact calculation is based on a rigidly or an elastically modelled cage. The higher friction torque in this contact leads to a higher total friction torque of the bearing which has an influence on the bearing's kinematics again. Therefore, a full elastically modelled cage should be used when high deformations are expected, caused for example by high loads on the cage or by centripetal accelerations. Under low loads the contact calculation based on a rigidly modelled cage shows sufficient results and can still be used for most bearing applications under stationary conditions.

Summary and conclusion

An approach for describing elastohydrodynamics in the cage/outer ring contact of rolling element bearings was presented. The friction torque in the elastic contact between cage and outer ring is now calculated more precisely and the dynamic simulation is nevertheless time efficient. The elastic-body calculation of the guiding surface of a cage was compared with AVL Excite^{TM}, which is an established, specialized multi-body dynamics simulation program including a hydrodynamic contact calculation. A good accordance between the pressure distribution and the lubrication film thickness can be stated. Using the elastohydrodynamic model has a high influence on the pressure distribution and the friction torque in the cage/outer ring contact of rolling element bearings. The full elastically modelled cage leads to a much wider pressure distribution and a higher friction torque in that contact than the rigidly modelled cage under high loads. As the friction torque may affect the bearing's kinematics for high loads, which can occur in applications like piston rod or planet gear bearings, the hydrodynamics of the lubrication as well as the elastic deformation of the cage should not be neglected in bearings that run under high centripetal accelerations.

In the future the elastohydrodynamic model could be extended, so that starvation effects, the influence of the cage's misalignment on the film thickness of one guiding surface or the contact heating due to friction can be taken into consideration. Furthermore, the lubrication in the contact between cage pockets and rollers combined with the cage's elasticity will be considered more precisely. But it is still not known whether there is a sufficient lubrication in the cage's contacts for the formation of the hydrodynamics or whether starvation effects will occur. Therefore, the validation with experimental research will be carried out in the future [24].

Acknowledgment

The authors would like to thank Schaeffler Technologies AG & Co. KG for permission to publish these results.

References

[1] Von Hollen, J.: Reibung von Kurbelwellen-Wälzlagern. Ph.D. thesis, Hannover, 2013.

[2] Schroeder, M.; et al.: Reibungsverluste im Kurbeltrieb von Verbrennungsmotoren – ein Vergleich von Gleit- und Wälzlagern. GfT-Tribologie-Fachtagung, 22.-24.9.2014, Göttingen. pp. 73/1–73/15.

[3] Seiler, K.; Stadler, M.; Tremmel, S.; Hahn, B.; Wartzack, S.; Graf-Goller, O.: Modellierung der Käfigführung für Wälzlagerdynamiksimulationsprogramme – Ein Beitrag zur betriebssicheren Lagerauslegung. Tribol. Schmierungstech. vol. no. 60 (2013) issue no. 6, pp. 29–36.

[4] Potthoff, H.: Anwendungsgrenzen vollrolliger Planetenrad-Wälzlager. Ph.D. thesis. Ruhr-Universität Bochum, 1986.

[5] Siepmann, T.: Reibmomente in Zylinderrollenlagern für Planetenräder. Ph.D. thesis. Ruhr-Universität Bochum, 1987.

[6] Liang, B.: Berechnungsgleichungen für Reibmomente in Planetenradwälzlagern. Ph.D. thesis. Ruhr-Universität Bochum, 1992.

[7] Hahn, K.: Dynamik-Simulation von Wälzlagerkäfigen. Ph.D. thesis. TU Kaiserslautern, 2005.

[8] Wohlgemuth, M.; Sauer, B.: Strategien zur Simulation von Wälzlagerkäfigen in feststoffgeschmierten Rillenkugellagern. Trib. Schmierungstech. vol. no. 54 (2007) issue no. 4, pp. 18-22.

[9] Weinzapfel, N.; Sadeghi, F.: A Discrete Element Approach for Modeling Cage Flexibility in Ball Bearing Dynamic Simulations. J. Tribol. vol. no. 131 (2009) issue no. 2, pp. 021102-1-11.

[10] Ashtekar, A.; Sadeghi, F.: A New Approach for Including Cage Flexibility in Dynamic Bearing Models by Using Combined Explicit Finite and Discrete Element Methods. J. Tribol. vol. no. 134 (2012) issue no. 4, pp. 041502-1-12.

[11] Gupta, P.K.: Advanced Dynamics Of Rolling Elements. Springer Verlag, 1984.

[12] Nelias, D.; Sainsot, P.; Flamand, L.: Power Loss of Gearbox Ball Bearing Under Axial and Radial Loads. Tribol. Trans. vol. no. 37 (1994), issue. no. 1, pp. 83-90.

[13] Gou, J.: Dynamische Simulation schnellaufender Zylinderrollenlager. Ph.D. thesis. Technische Universität Carolo-Wilhelmina Braunschweig, 1997.

[14] Seiler, K.; Stadler, M.; Tremmel, S.; Hahn, B.; Wartzack, S.; Graf-Goller, O.: Modeling of cage guidance in a rolling bearing multi-body dynamic simulation program for a power efficient bearing design. In: Society of Tribologists and Lubrication Engineers (Eds.), vol. no. 2. STLE 69th Annual Meeting & Exhibition, 18.-22.5.2014, Orlando, pp. 532-534.

[15] Seiler, K.; Tremmel, S.; Wartzack, S.; Hahn, B.; Graf-Goller, O.: Einfluss der Schmierstoffhydrodynamik in der Käfigführung auf die Wälzlagerreibung und -kinematik. In: VDI-Berichte 2257. Gleit- und Wälzlagerungen. 6.-7. Mai 2015, Schweinfurt. Düsseldorf: VDI Verlag, 2015, pp. 351–363.

[16] Koch, O.; Plank, R.; Weber, J.: Wälzlageroptimierung durch dreidimensionale dynamische Simulation. In: VDI-Berichte Nr. 2069. Gleit- und Wälzlagerungen. 9.-10. Juni 2009, Wiesloch. VDI Verlag GmbH, Düsseldorf, 2009, S. 43-52.

[17] QU, Z.-Q.: Model Order Reduction Techniques – With Applications in Finite Element Analysis. 1. Auflage. London: Springer, 2004.

[18] Roelands, C. J. A.: Correlational aspects of viscosity-temperature-pressure relationship of lubricating oils. Ph.D. thesis. Universität Groningen, 1966.

[19] Bartel, D.: Simulation von Tribosystemen. Universität Magdeburg, Habilitation, 2009.

[20] Lang, O. R.; Steinhilper, W.: Gleitlager. Konstruktionsbücher Bd. 31. Berlin: Springer, 1987.

[21] Ree, T.; Eyring, H.: Theory of non-Newtonian Flow 1: Solid plastic system. Journal of Applied Physics, vol. no. 26 (1955), issue no. 7, pp. 793-800.

[22] Zhou, R.-S.; Hoeprich, M.-R.: Torque of Tapered Roller Bearings. ASME Journal of Tribology, vol. no. 113 (1991), issue no. 3, pp. 590-597.

[23] AVL: Excite Power Unit User Guide, 2013.

[24] Hochrein, D.; Tremmel, S.; Wartzack, S.; Graf-Goller, O.: A New Test Rig for the Investigation of Rolling Bearings in the Centrifugal Field. In: Society of Tribologists and Lubrication Engineers (Eds.), STLE 71th Annual Meeting & Exhibition, 15.-19.5.2016, Las Vegas.

Enhanced boundary zone rolling contact fatigue strength through hybrid machining by hard turn-rolling

Denkena, B., Poll, G., Maiß, O., Pape, F., Neubauer, T.

1. Summary

The lifetime of roller bearings is significantly influenced by the material properties of the subsurface area. During classical manufacturing processes as for example grinding and honing, the surface integrity is not influenced that much. Especially the induced residual stresses depth is not high enough to enhance the resulting endurance. It is known, that alternative manufacturing processes as hard turning and deep rolling are able to realize comparable part quality while at the same time inducing very high compressive residual stresses to a sufficient depth. To implement these two similar processes in high productive process chains, an innovative tool concept for a hybrid hard turn-rolling process is presented within this paper. This process will decrease the surface roughness peaks significantly with an increased productivity. Investigating the interaction of both processes shows that the deep rolling is dominant for inducing compressive residual stresses. Roller bearing tests were conducted on roller bearing inner rings type NU206 to investigate the change in residual stress profiles for hard turned and deep rolled as well as standard honed roller bearings. Using deep rolling a stable residual stress profile is induced, which leads to an increased lifetime of 200%. This increase in the expected endurance could be predicted using the lifetime model of Neubauer.

Keywords: hybrid machining, hard turning, deep rolling, roller bearing

2. Introduction

Roller bearings are highly loaded and often used parts in mechanical engineering. Due to the high cyclic loads, the requirements on the bearings material properties are very high. 100Cr6 steel (German standard corresponding to AISI52100) is well established for this application [HEN02]. In hardened state the steel offers high hardness. Classical bearing failures are induced by fatigue. For well lubricated bearings fatigue starts in the subsurface zone at the depth of the highest stress in the material [EHW53, HAR84, AK87]. There micro-cracks first occur. With ongoing cyclic load these cracks increase in size and reach the surface region. This damage is generated as disruption (pittings).

The machining process of the bearings is characterized by high productivity and accuracy. Due to the increasing amount of customized bearings the manufacturers need to specialize their products. One possibility to influence the performance of a bearing is by changing the surface integrity. Surface and subsurface hardness, topography or residual stresses influence the bearing endurance with respect to the applied loading. Especially the residual stress state increases the desired lifetime of a bearing, as shown by Hacke [HACK11] or Papst et al. [PAPS12]. This effect could also be shown by Voskamp [VOSK96] and Gleß [GLES09]. It is assumed to be caused by compressive residual stresses in the surface zone induced by a short time exposure to higher loads.

Conventional manufacturing processes as grinding and honing are not able to positively influence the surface integrity in a wide range and induce subsurface residual stresses only into small depths from the surface [KLOC05]. An alternative process chain is hard turning and a subsequent surface treatment by deep rolling [ROET03]. Process parameters as cutting speed v_c and feed f or tool geometry as corner radius r_ε and cutting edge geometry influence the surface quality and surface integrity [DENK15]. In high precision hard turning processes, surface roughness values of less than Rz = 0.6 µm are achievable [KOCH96]. The use of large corner radii r_ε in combination with small feed values generates a small theoretical surface roughness. However the used cutting edge geometry affects the chip formation and thus the surface quality. Due to the ploughing effect [ALBR60], material is pressed into the surface and deformed elasto-plastically instead of being removed with the chip, a Spanzipfel remains on the surface and increases the surface roughness [SOKO55]. Brammertz correlated the height of the Spanzipfel with the minimum uncut chip thickness h_{min} [BRAM61]. Using large cutting edge radii r_β the minimum uncut chip thickness h_{min} increases [REHE16], which leads to a higher surface roughness [DENK15]. Independent of process parameters, hard turning always creates periodic surface profiles with high peak to valley ratio.

Deep rolling is a surface treatment using a cemented carbide or ceramic ball which is pressed onto the surface with high pressure p_w and moved with a rolling velocity v_w across the surface [ROET03]. The load is applied by a hydraulic fluid up to p_w = 600 bar or an aerosol up to p_w = 200 bar. Deep rolling smoothes the surface roughness by plastic deformation of the surface peaks. Due to its high contact stresses between the rolling ball with a diameter of d_k = 2 – 13 mm the process induces very high compressive residual stresses of up to σ_{max} = -1200 MPa for AISI 52100 bearing steel [ROET03]. In deep rolling a characteristic residual stress profile occurs. It always induces compressive stresses which are smaller at the surface than with an increasing distance from the surface. The maximum compressive stress σ_{max} occurs within the depth of the maximum von Mises stresses of the Hertzian Contact. Increasing the rolling pressure the maximum compressive residual stress gets higher and moves into greater depth. At some point the highest possible amount of compressive stresses is induced for the used material, then σ_{max} remains constant and only z_{max} increases [BERS82]. Another important effect of deep rolling is its effect on workpiece hardness. Due to the high plastic deformations within the subsurface area the dislocation density increases. This leads to higher hardness. Similar to the residual stresses, the hardness has got a maximum within the subsurface area. This maximum increases with the rolling pressure until a material maximum is reached. After that it also increases its distance from the surface, which also correlates with the Hertzian Contact stresses [BERS82].

Both processes have advantages regarding the surface integrity against the standard manufacturing processes grinding and honing. However, in most cases process chains for machining bearings are highly productive and fully automated. Applying simple hard turning and deep rolling in the given process chain will increase the cost. Therefore new concepts have to be invented. The aim of this paper is to analyze the effects of process parameters of a new hybrid machining process on the surface quality, presented by Maiß et al. [MAIS16]. The hybrid process hard turn-rolling combines the processes hard turning and deep rolling in one tool. Both processes are conducted simultaneously, which increases the productivity and enables the use of hard turning and deep rolling in highly productive process chains. With bearing tests the influence of the processes on the endurance of roller bearings is analyzed.

3. Experimental procedure

The experiments are divided into three parts. First, the effect of the new hybrid turn-rolling process on the surface quality is analyzed. To explain the effects in detail, the effects of the single processes are analyzed as a second step. At the end, different machined roller bearings are tested in a four bearing test rig.

For the machining a high precision lathe Hembrug Microturn 100 is used. The inner rings of roller bearings type NU206 (AISI 52100, 62 HRC) are clamped with a hydraulic expansion mandrel to ensure high accuracy comparable to standard roller bearings. An innovative tool concept combining hard turning and deep rolling in one tool is developed for the experiments. The tool combines a tool holder DDJNL2525 for a cemented carbide cutting insert type DNMA150616 with a hydrostatic deep rolling tool Ecoroll HG3. The cutting insert and tool holder combination provides a rake angle of γ = -6°, a clearance angle of α = 6° and a cutting edge angle of κ = 93°. The corner radius of the insert r_ε = 1.6 mm fits to the deep rolling ball diameter d_k = 3.175 mm. The cutting tool is made out of cemented carbide, coated with a Ti(C,N) + Al_2O_3 multilayer coating, the deep rolling ball material is silicon nitride.

The tool concept enables positioning of the deep rolling ball directly behind the cutting edge, as it can be seen in Figure 17. The deep rolling tool can be shifted in feed direction to position the ball in a valley or on a peak of the turning groove. According to the position of the rolling ball in a valley or on a peak the surface quality and residual stress distribution should be influenced. The hypothesis is that by positioning the tool in a valley, the deep rolling will be applied on a warm surface. Due to the machining the surface temperature increases. It is known, that thermo-mechanical deep rolling or warm deep rolling will lead to higher and more stable residual stresses. In this case the surface roughness will not be influenced by the process. In contrast to that, deep rolling on the roughness peaks will cause high and aimed plastic deformations of the surface peaks to reduce the roughness and decrease the peak to valley ratio. Due to the high heat conductivity the area will be almost cold and the residual stresses are only influenced by the deep rolling itself.

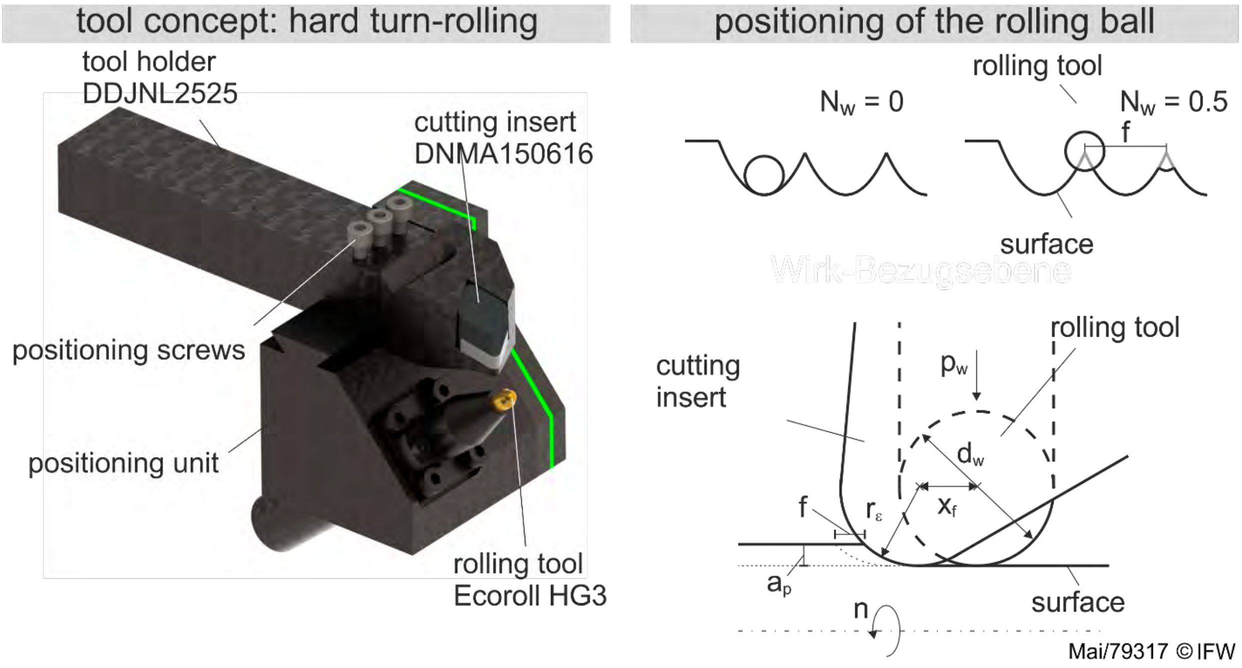

Figure 17: Tool concept for the hybrid hard turn-rolling process

For the experiments the process parameters feed f and rolling shift factor N_w are varied, as shown in

Table 6. The rolling shift factor N_w describes the position of the rolling tool on the turned surface and is described by $N_w = x_f/f$, where x_f is the axial distance between cutting edge and rolling tool.

Parameter	**unit**	**value**
cutting speed v_c	m/min	150
depth of cut a_p	mm	0.1
feed f	mm	0.1; 0.15; 0.2
rolling pressure p_w	bar	300
rolling shift factor N_w	-	0; 0.5

Table 6: Experimental parameters for the hard turn-rolling process

In a second step the single processes are investigated to explain the effects in hard turn-rolling. Therefore hard turning experiments with different cutting edge radii and feed values are conducted. The feed is varied between f = 0.05 - 0.2 mm. The cutting edge geometry is changed by means of symmetric cutting edge radii from $r_\beta = 40 – 100$ µm. For the deep rolling process a variation overlap factor u and rolling pressure p_w is applied. The overlap factor u describes the amount of the contact area of the rolling ball which overlaps during the next revolution. It is calculated by

$$u = 1 - \frac{b}{f_w} \tag{1}$$

where b is the diameter in feed direction of the Hertzian contact ellipse and f_w the rolling feed per revolution. To identify the interactions of both processes the machined roller bearings are tested in screening tests and fatigue life tests on a four bearing endurance test rig (Figure18:). A loading of C/P = 4 is applied. In the screening test the bearings are running for t = 50 h and t = 120 h with n = 4050 min^{-1}. The fatigue life tests are conducted in sudden-death mode and analyzed by the Weibulldeviation. Full lubrication conditions are used within the test. The oil temperature is T = 60°C.

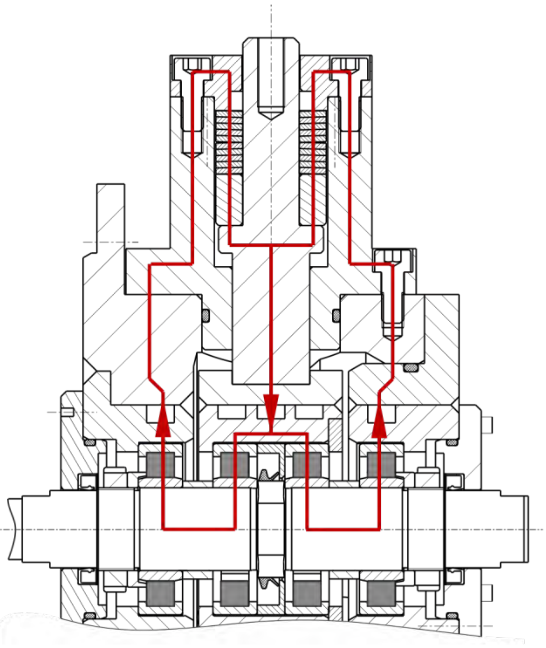

Figure18: Schematic of the Bearing Test Rig

The influence of the machining and loading is described by analyzing surface quality and subsurface residual stresses. The surface roughness is measured tactilely by a Mahr Pertometer Concept with a Gaussian filter and a cut-off of λ = 0.8 mm. Residual stress measurements are made by X-ray diffractometer GE XRD 3000 P with Cr-Kα-radiation.

4. Machining roller bearings by hard turn-rolling

The innovative hybrid process combines the advantages of a highly flexible machining process, as hard turning, with an improved surface integrity design through surface treatment by deep rolling. Due to the presented tool concept the surface roughness can be influenced with a higher accuracy compared to a serial use of the processes. The positioning system of the tool holder allows an accurate positioning of the rolling tool on the machined surface peaks of about ±2 µm. For the position of the deep rolling tool exactly behind the cutting edge in the same surface groove the rolling shift factor is N_w = 0. According to theory the surface should be heated up by the turning process, which increases the penetration depth for inducing residual stresses. Is the rolling ball shifted by x_f equals the half of the used feed value (N_w = 0.5) it is positioned on the topography peaks of the hard turned surface. In this case, the surface quality is improved. Figure 19 shows the results for a feed value of f = 0.2 mm. The mean surface roughness Rz is not significantly decreased for a turn-rolling process with N_w = 0. For both the hard turning and the turn-rolling process with N_w = 0, the resulting surface roughness is above Rz = 3.5 µm. Positioning the rolling ball on the roughness peak decreases the surface roughness by about 50 % to Rz = 1.7 µm. The functional surface roughness values Rk and Rpk show the effect of the deep rolling process. The core roughness is not significantly influenced by the rolling shift factor. The deep rolling only decreases the height of surface peaks. The peak roughness Rpk is decreased from Rpk = 1.5 µm after the turning operation to Rpk = 0.25 µm after the hybrid process with $N_w = 0.5$. Additionally the skewness of the resulting surface roughness for a rolling shift factor Nw = 0.5 is always negative, which will have a positive effect on the lubrication of the roller bearing.

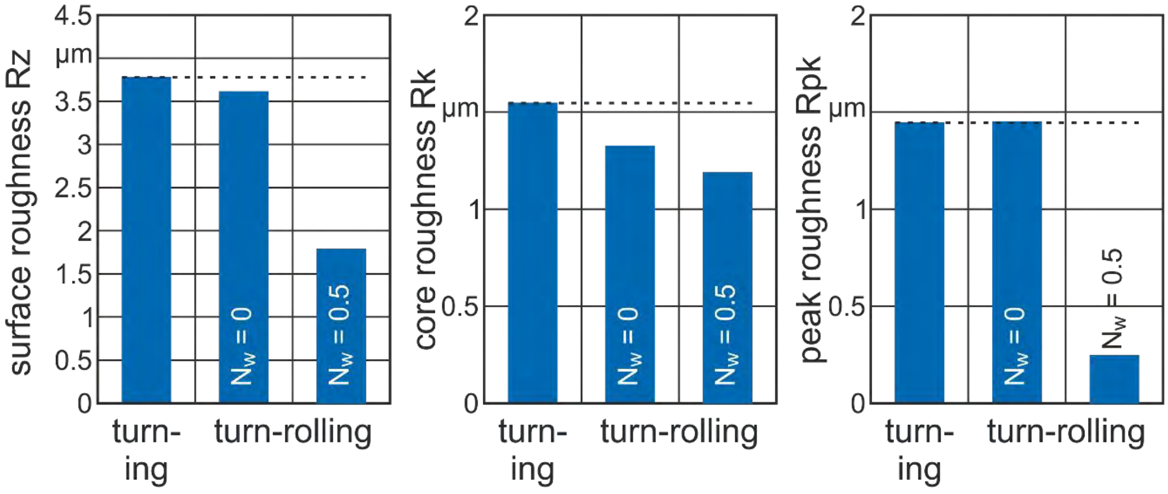

process: turn-rolling
cutting speed: v_c = 150 m/min
feed: f = 0.2 mm
depth of cut: a_p = 0.1 mm
rolling pressure: p_w = 30 bar
rolling shift factor: N_w = variable

cutting insert: DNMA150616
edge radius: r_ε = 1.6 mm
rolling tool: HG3
ball diameter: d_k = 3.175 mm
material: AISI 52100
hardness: 62 HRC

Mai/79314 ©IFW

Figure 19: Effect of rolling shift factor on surface quality

Using a feed value of f = 0.2 mm would be a rough turning operation for hard turning. The presented results already show that hard turn-rolling can increase the productivity in finishing processes. A surface roughness of Rz < 1 µm can be easily achieved at higher feed values. Increasing the feed from f = 0.1 mm to 0.2 mm leads to a known increase of surface roughness in the single turning operation. The measured surface quality before the deep rolling is applied increases from Rz = 2.5 µm to Rz = 4 µm. This increase is generated by the known geometric contact between corner radius and surface. For a rolling shift factor of $N_w = 0$ the surface roughness decreases slightly by about 1 µm for all different feed values. The deep rolling ball is pressed into the turning groove. The corner radius and the ball radius have almost the same values. If the ball penetrates into the surface the surface peaks get in contact with the ball. This leads to a small plastic deformation of the surface peaks. If the tool is positioned directly on the surface peaks, this effect becomes much more intense. The highest contact stresses occur. They lead to very high plastic deformations and a decreased surface roughness. As shown in Figure 20 the Rz-values decrease at least 50% for all analyzed feed values. The delta of the roughness values before and after deep rolling increases almost linearly with higher feed value. Pressing the rolling ball with a defined rolling force F_w (2) onto a roughness peak will deform this peak and the contact area between the peak and the rolling ball increases as long as the contact stresses are higher than the critical shear stresses. In case of feed f = 0.2 mm the inclination of the roughness peaks is higher than for f = 0.1 mm. Therefore a contact area increase occurs at higher plastic deformations.

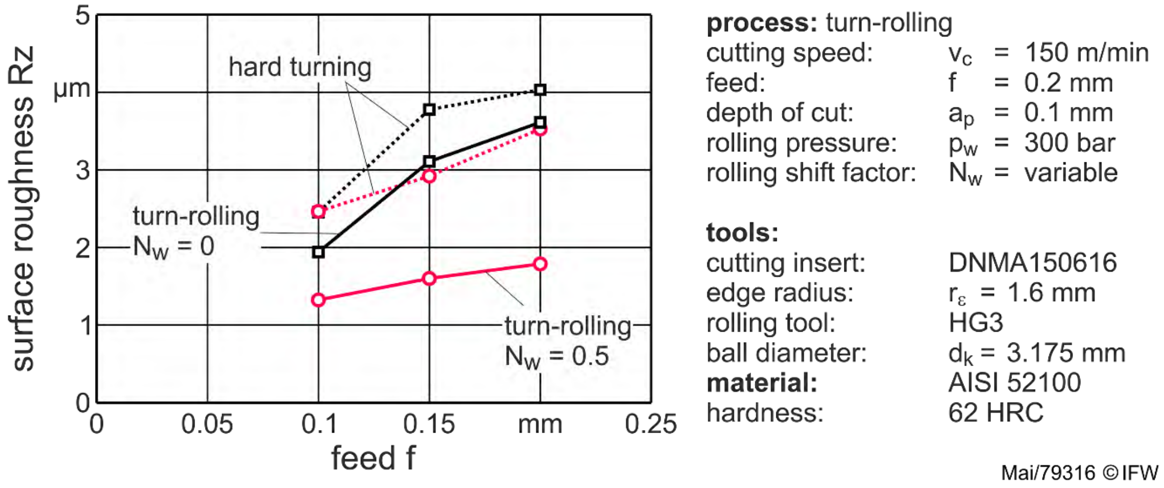

process: turn-rolling
cutting speed: v_c = 150 m/min
feed: f = 0.2 mm
depth of cut: a_p = 0.1 mm
rolling pressure: p_w = 300 bar
rolling shift factor: N_w = variable

tools:
cutting insert: DNMA150616
edge radius: r_ε = 1.6 mm
rolling tool: HG3
ball diameter: d_k = 3.175 mm
material: AISI 52100
hardness: 62 HRC

Mai/79316 ©IFW

Figure 20: Influence of feed on surface roughness in hard turn-rolling

From the previous experiments it is known, that the most important factor on surface quality after hard turning is the feed value and its interaction with the used cutting edge rounding [DENK15]. Both parameters are also very important to create subsurface residual stresses. However, a conflict of aims occurs. To induce the wanted high compressive stresses within the subsurface area, large cutting edge radii have to be used. In this case the ploughing effect increases which leads to large values for the minimum uncut chip thickness h_{min} and thus to higher surface roughness values even for very small feed values, as it can be seen in Figure 21.

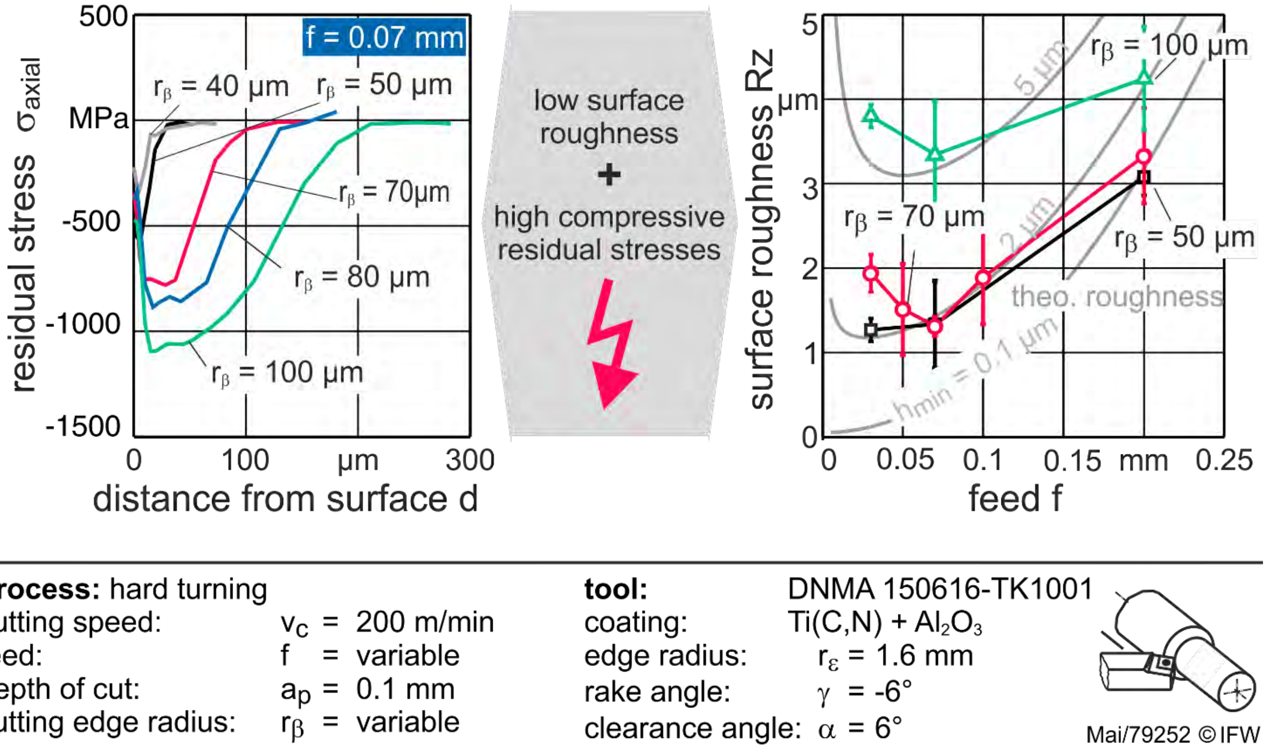

process: hard turning
cutting speed: v_c = 200 m/min
feed: f = variable
depth of cut: a_p = 0.1 mm
cutting edge radius: r_β = variable

tool: DNMA 150616-TK1001
coating: Ti(C,N) + Al_2O_3
edge radius: r_ε = 1.6 mm
rake angle: γ = -6°
clearance angle: α = 6°

Mai/79252 ©IFW

Figure 21: Conflict of interests by inducing high compressive stresses and low surface roughness values by hard turning

For an increased endurance of the machined roller bearings this demonstrates the importance of the deep rolling process. For the deep rolling process a simple hypothesis for the effects of process parameters on surface quality can be obtained. If only plastic deformation occurs, the penetration depth of the rolling ball can be described by the Hertzian contact area. For ideal surfaces this leads to the idea, that the surface roughness can be calculated by shifting this contact area by the feed value, as it is demonstrated in Figure 22. In a simplified approach the Hertzian contact area is calculated by the rolling pressure p_w and the ball diameter d_k. Therefore the only important value to describe the surface roughness should be the overlap factor. Figure 22 also shows the results for the deep rolling process with a variation of rolling pressure (Figure 22, left) and overlap factor u (Figure 22, right) for different ball diameters. Increasing the rolling pressure from p_w = 200 to 400 bar the surface roughness remains constant at about Rz = 1 µm. These results are independent from the used ball diameter. In contrast to this an increased overlap factor leads to an almost linear decrease of the surface roughness from Rz = 2 µm for u = 44 % to Rz = 0.5 µm for a very high overlap factor of u = 98 %. Again this results are independent from the used ball diameter. Concluding these findings, for the given conditions the surface roughness in deep rolling is only influenced by the overlap factor resulting from the used feed values.

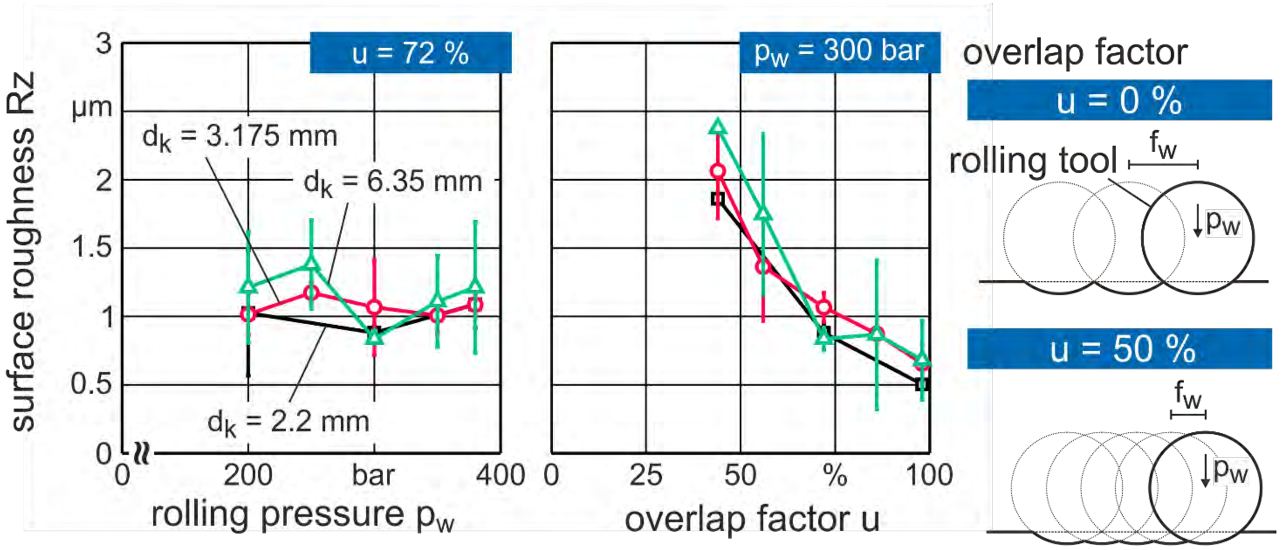

process: deep rolling			**rolling tool:**	Ecoroll HG3
rolling pressure:	p_w	=	variable	tool material:	ceramic
balldiameter:	d_k	=	variable	workpiece material:	AISI 52100 (62 HRC)
rolling velocitiy:	v_w	=	150 m/min	maschine tool:	Hembrug
overlap factor	u	=	variable		Slantbed 100

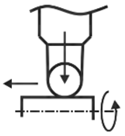

Mai/79233 ©IFW

Figure 22: Influence of deep rolling on surface roughness

The single processes are both mainly influenced by the feed values and so is the hybrid process. However, with the used deep rolling parameters it will never be possible to fully deform the roughness peaks. Therefore an interaction between both processes has to influence the resulting surface quality. To show this two different hard turning operations were performed. The parts are deep rolled afterwards and the surface improvement is measured. In both processes the feed values are changed. For the hard turning a sharp cutting edge with r_β = 22 µm and a chamfer angle of γ_f = 15° is used. For the first hard turning process (hard turning 1) a feed of f = 0.2 mm is used, hard turning 2 uses f = 0.05 mm. For machined roller bearing inner rings, surface roughness values Rz = 2.3 µm for hard turning 1 and R = 1.3 µm for hard turning 2 can be generated. Applying the same deep rolling process with different overlap factors for both hard turning operations, leads qualitatively to the same roughness improvement as shown in Figure 23. Both graphs are parallel and just shifted by an almost constant value. Is hard turning 1 with the higher surface roughness considered, the resulting surface roughness is also higher. It can be seen, that both processes have to be adjusted to each other. For small overlap factors the deep rolled surface roughness increases. Which means no improvement can be found. The deformed areas of the rolling groove can be clearly identified on the surface. For smoother surfaces after hard turning this effect increases.

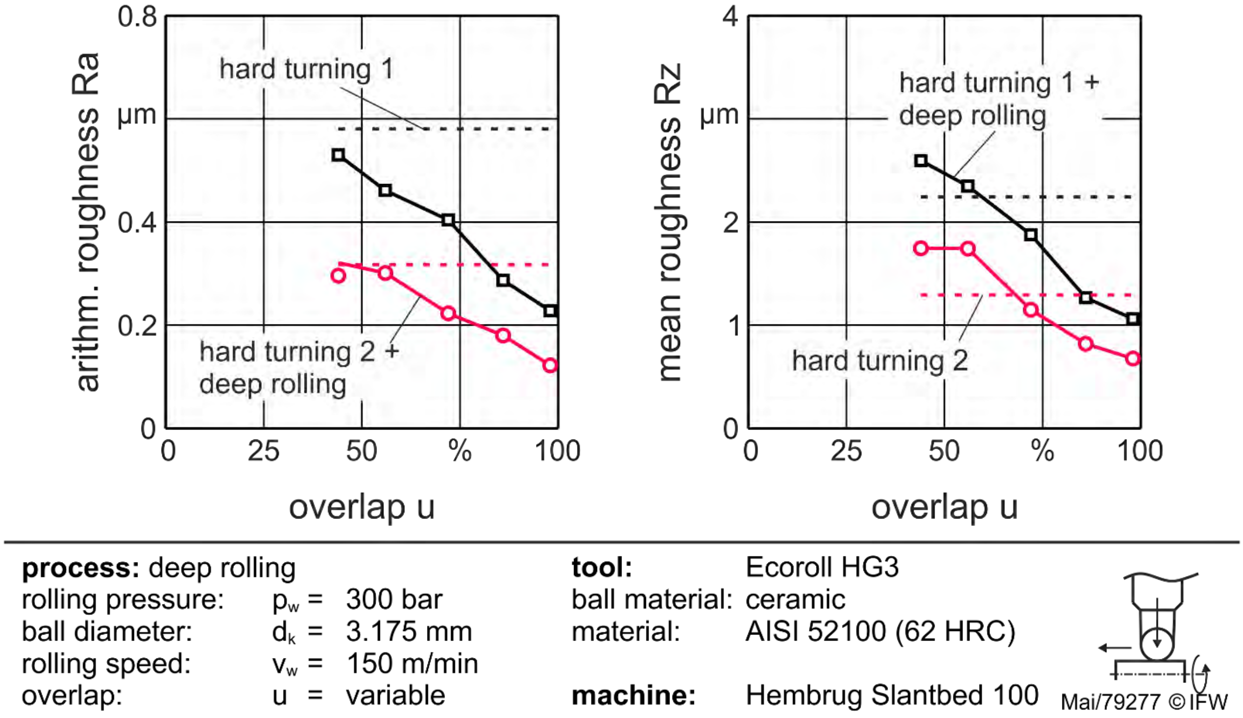

Figure 23: Influence of the hard turned surface on the resulting surface roughness in deep rolling

For the hybrid process hard turn-rolling the feed value is the most important factor. It influences the surface topography for the hard turning process. In interaction with the overlap factor respectively the feed and the position of the deep rolling ball on the roughness peaks, the resulting surface roughness is influenced. If the rolling ball is positioned within the turning grooves the surface roughness is only decreased by a small margin. If positioned directly onto a surface peak from the hard turning process, the resulting surface roughness can be decreased by up to 50%.

As presented in Figure 24 hard turning leads to very high compressive residual stresses, if large cutting edge radii are used. However it is known, that hard turning with large cutting edge radii also leads to microstructural changes [DENK15] which has to be avoided in bearing manufacturing. It is assumed that the influenced surface layer for hard turning is relatively small compared to the deep rolling process. Residual stress measurements are conducted for hard turned roller bearings with a sharp cutting edge r_β = 22 µm and a large cutting edge rounding r_β = 100 µm. As shown in Figure 24 the residual stresses are significantly different by means of the maximum compressive residual stress and the penetration depth. Applying the same deep rolling process on both specimens leads to the same residual stress state. The high plastic deformations due to Hertzian contact stresses up to p_{max} = 8 GPa and the shakedown effect, described by Merwin and Johnson [MERW63] lead to this effect. For the hybrid hard turn-rolling process this leads to the conclusion that only the deep rolling process influences the resulting residual stress state.

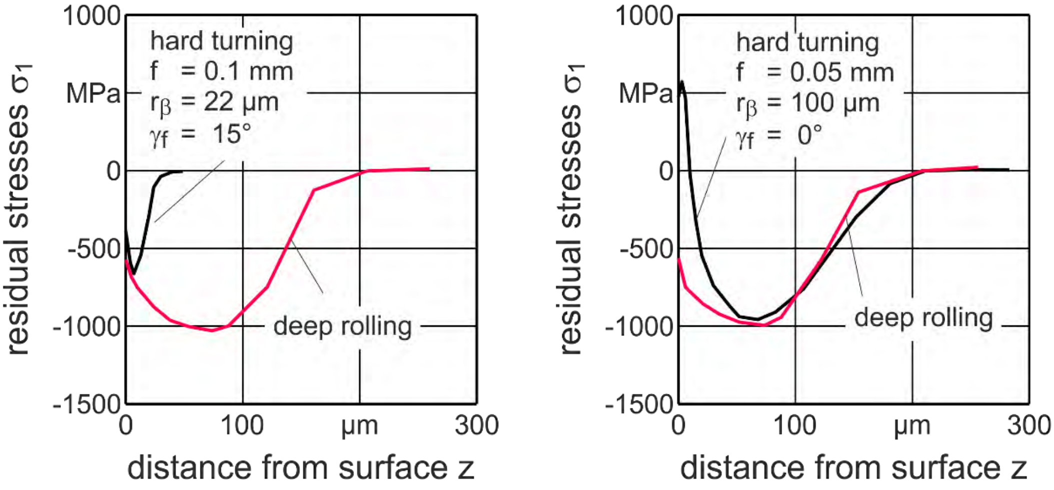

process: hard turning + deep rolling
cutting speed: v_c = 200 m/min
feed: f = variable
depth of cut: a_p = 0.1 mm
rolling pressure: p_W = 400 bar
rolling speed: v_W = 150 m/min
rolling feed: f_W = 0.155 mm
cutting insert: DNMA150616
edge radius: r_ε = 1.6 mm
rolling tool: HG3
ball diameter: d_K = 3.175 mm

Mai/79315 ©IFW

Figure 24: Residual stresses after deep rolling and influence of previous hard turning operations

To analyze the effects of process parameters in deep rolling on the induced residual stresses, deep rolling experiments are conducted. Within the experiments the same hard turning process is used and the rolling pressure, ball diameter and overlap factor are varied. An increase of the rolling pressure from p_w = 200 to 400 bar leads to an increased maximum compressive residual stress σ_{max} in axial and circumferential direction (Figure 9). Both measurement directions correlate with the main stress directions σ_1 and σ_2. In circumferential direction slightly lower compressive residual stresses are identified, therefore the circumferential direction represents the first main residual stress σ_1. This is the same for all conducted deep rolling experiments. An increased ball diameter from d_k = 2.2 – 6.3 mm leads to an increased penetration depth and therefore a higher distance from the surface z_{max} of the maximum compressive stress. The maximum compressive stress does not change with an increased ball diameter. Both findings can be correlated by the effects of the Hertzian contact stress. The rolling pressure has got a linear effect on the rolling force F_w [ROET03].

$$F_w = p_w \cdot \pi \cdot \left(\frac{d_k^2}{4}\right) \qquad (2)$$

Where the inclination of the linear function depends on the ball diameter d_k. Therefore an increased rolling pressure for the same ball diameter increases the maximum Hertzian contact stress p_{max} and thus the stresses within the subsurface area. Applying the same rolling pressure for different ball diameters, the rolling force changes respectively. For small ball diameter the rolling force decreases as well as the contact area. Therefore the Hertzian contact stress p_{max} increases. In contrast to that, the penetration depth of the subsurface stresses depends only on the contact area. A smaller contact area leads to smaller penetration depths.

The overlap factor does not change the Hertzian contact stresses, however the residual stress state is significantly influenced by the overlap factor. The reason for this is the mentioned shakedown process. For an overlap factor of u = 50% one point of the surface is deep rolled twice. If the overlap factor increases to almost u = 100% each point is deep rolled 100 times. In each revolution the residual stress state from the previous revolution interacts with the load stresses and increases the new residual stresses.

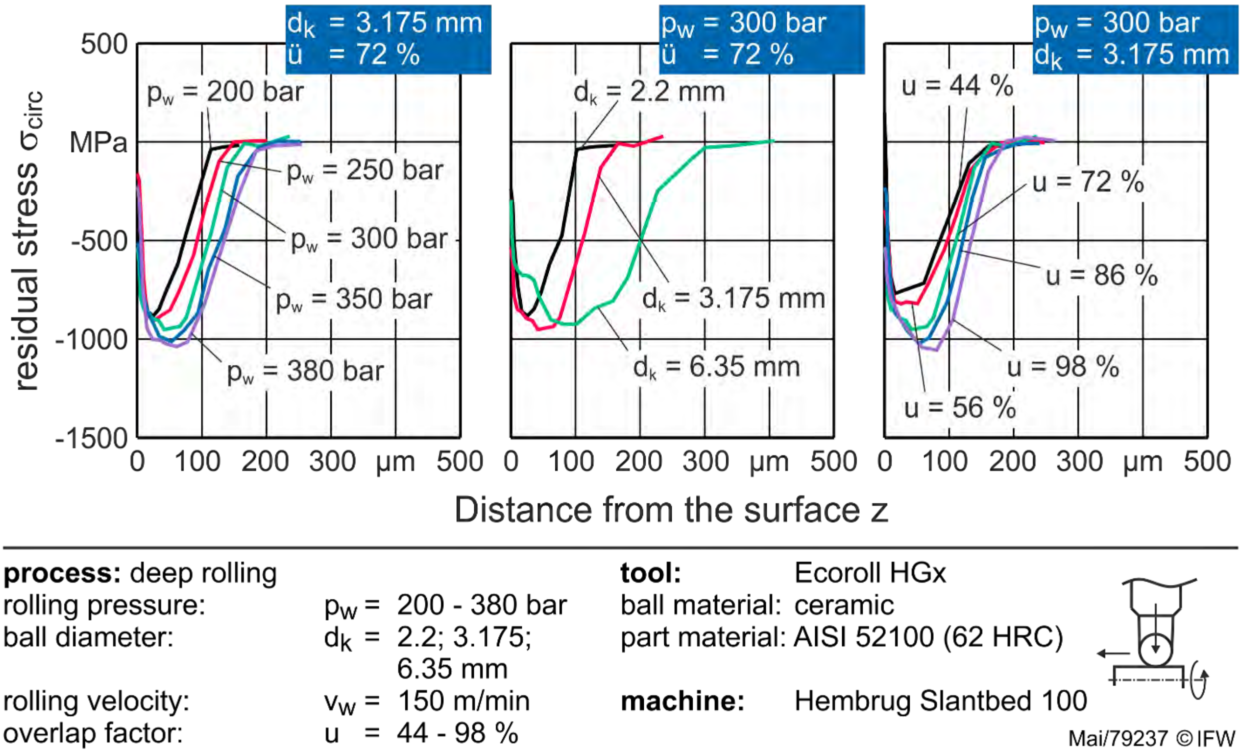

process: deep rolling
rolling pressure: p_W = 200 - 380 bar
ball diameter: d_K = 2.2; 3.175; 6.35 mm
rolling velocity: v_W = 150 m/min
overlap factor: u = 44 - 98 %

tool: Ecoroll HGx
ball material: ceramic
part material: AISI 52100 (62 HRC)
machine: Hembrug Slantbed 100

Mai/79237 © IFW

Figure 25: Effects of deep rolling on residual stress depth profiles

5. Surface integrity changes in machined roller bearings by loading

To compare the influence of the residual stresses of the manufacturing process, bearing endurance tests were performed at various runtimes under a relative bearing load of C/P = 4. For the standard honed inner rings a maximum contact pressure of p_{max} = 2.5 GPa is calculated due to the crowned profile. In case of the hard turned and deep rolled bearing rings the profile is in a linear slope, thus a maximum contact pressure of p_{max} = 2.3 GPa is calculated. The experiments are performed under full lubrication conditions.

Figure 26, a) shows the formation of residual stresses in the honed bearing rings due to the rolling contact. A bearing before test shows residual stresses only for the first few microns of depth. At higher depths no significant residual stresses can be proved. After 3.9 million revolutions residual stresses with a maximum value of σ_{max} = -420 MPa can be measured in a depth between 100 and 150 µm. With longer test duration after 100 million revolutions, the residual stresses are built up in higher depth with the same values of about σ_{max} = -650 MPa. Voskamp showed this behavior by the investigations of deep groove ball bearings [Vos96]. Figure 26, b) presents the corresponding crowned bearing inner ring profile with the calculated contact pressure. The roller features a zylindrical profile on the contact area,

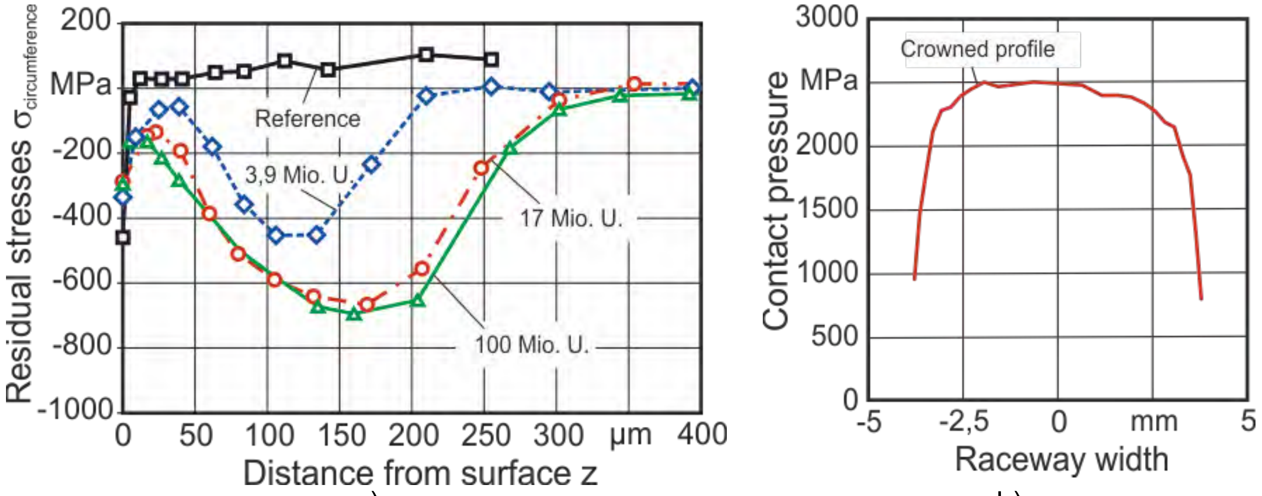

a) b)

Figure 26: Changes of residual stresses due to loading of standard honed bearing inner rings

Subsequently bearing endurance tests were performed with hard turned bearing rings. The residual stress state of these rings is comparable to the honed variant (Figure 27, a)). At a depth of more than 20 µm no residual stresses can be detected for the unused bearing. The residual stresses develop analogously to the honed bearings. The residual stresses build up takes place a little bit slower and reaches lower values of about σ_{max} = -500 MPa due to the lower maximum contact pressure in the rolling contact. The contact pressure for the bearing inner ring is depicted in Figure 27, b). As the residual stress pattern is similar to the honed bearings, a positive effect of the residual stresses concerning the fatigue life is not expected.

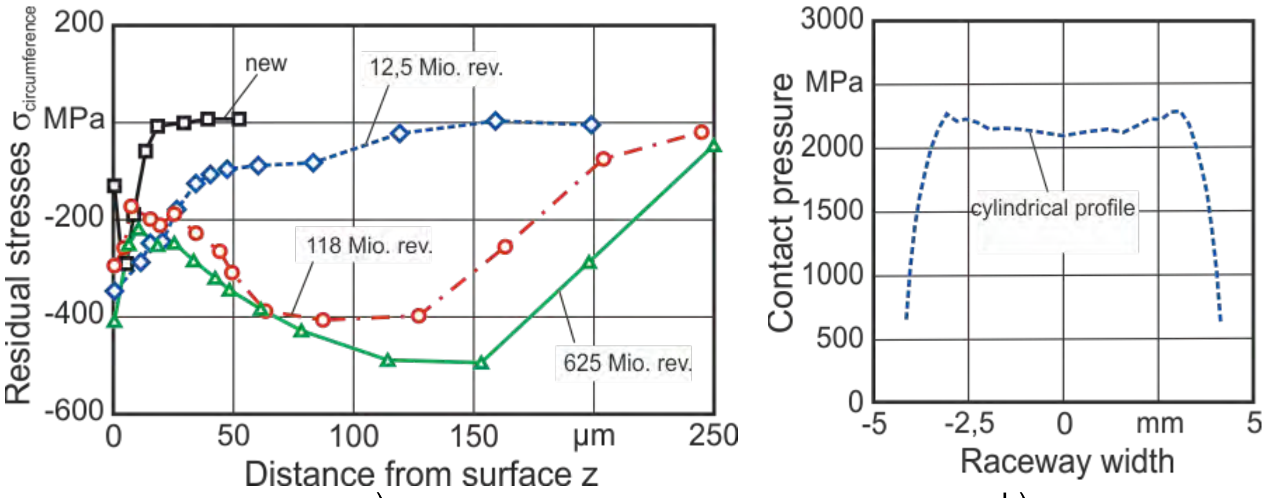

a) b)

Figure 27: Changes of residual stresses due to loading of hard turned bearing inner rings

In case of the deep rolled bearing inner rings, residual stresses are induced to the subsurface region previously to the testing. The development of the residual stresses is shown in Figure 28, a). In the unused state after machining, these stresses are highest in a depth of 100 µm with a value of σ_{max} = -900 MPa. After a run time of 29 million revolutions the residual stresses do not change up to a depth of 100 µm. At greater depths an expansion takes place. After a running time of 378 million revolutions, the residual stresses are reduced to a depth of 130 µm while in greater depths the high residual stresses are still remaining. The profile and the contact pressure for a deep rolled inner ring are depicted in Figure 28, b).

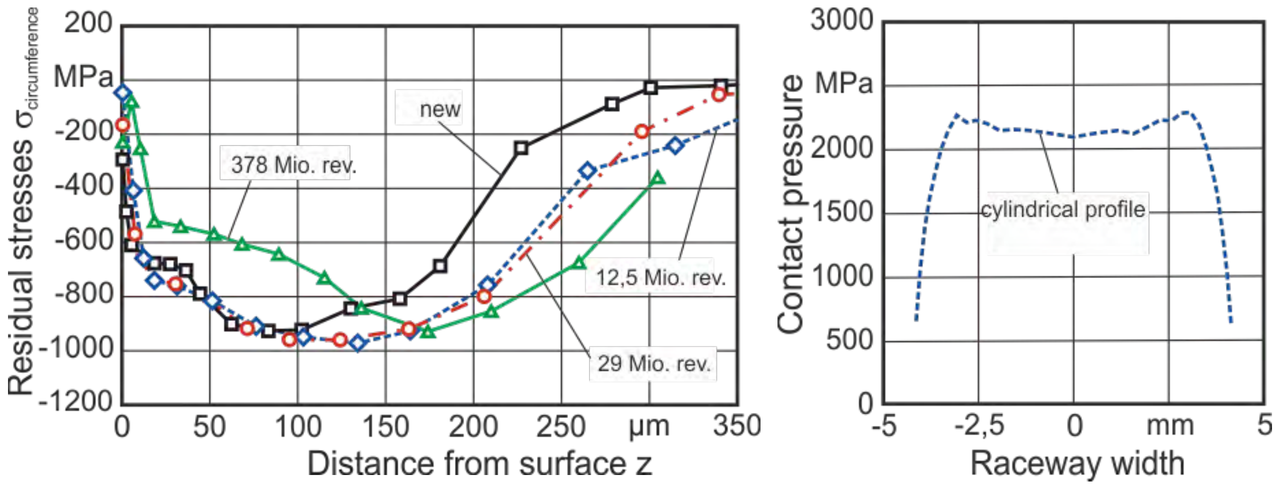

a) b)

Figure 28: Changes of residual stresses due to loading of deep rolled bearing inner rings

Neubauer presented a simulation model to consider the initial residual stresses within a roller bearing to calculate the resulting endurance [NEUB16]. The resulting stress field from the superposition of load stresses and residual stresses is computed in order to compare these findings with theoretical predictions based on the approach of Ioannides et al. [IOAN99]. To do so, an FE model of a bearing inner ring was set up to compute the resulting three dimensional stress field from the superposition of load stresses and residual stresses. The stresses are only regarded as input for the new stress state.

As input variables the external load as Hertzian pressure distribution at the surface and the residual stress depth profiles (defined as initial stresses in the model) are used. The orthogonal shear stress beneath the surface is calculated. The resulting stress field is applied to the fatigue life model of Ioannides et al. [IOAN99]. The equation is:

$$\ln\frac{1}{S} \approx N^e \cdot \int_V \frac{(\tau_i-\tau_u)^c}{z'^h} dV \qquad (3)$$

By including a stress fatigue limit τ_u the model of Lundberg and Palmgren (1947) is extended. For the term τ_i the criterion of Dang-Van as fatigue stress criterion is applied:

$$\tau_i = \tau_{0max} - k_{hyd} \cdot p'_{hyd} \qquad (4)$$

The model includes the maximum orthogonal shear stress and the local hydrostatic pressure p_{hyd}, corrected for residual and hoop stress. The hydrostatic pressure can also be calculated with the FE model. The measured probability of surviving for the bearings was compared to the calculated probability of surviving with and without the influence of residual stresses by deep rolling (Figure 29). The calculation model fits the experimental results quite well. Next the probability of surviving was calculated for the honed, hard turned and deep rolled bearings (Figure 30). The improvement in bearing fatigue life can be accounted to the induced residual stresses. The probability of failure for the hard turned and deep rolled bearings illustrates the improvement additionally (Figure 15).

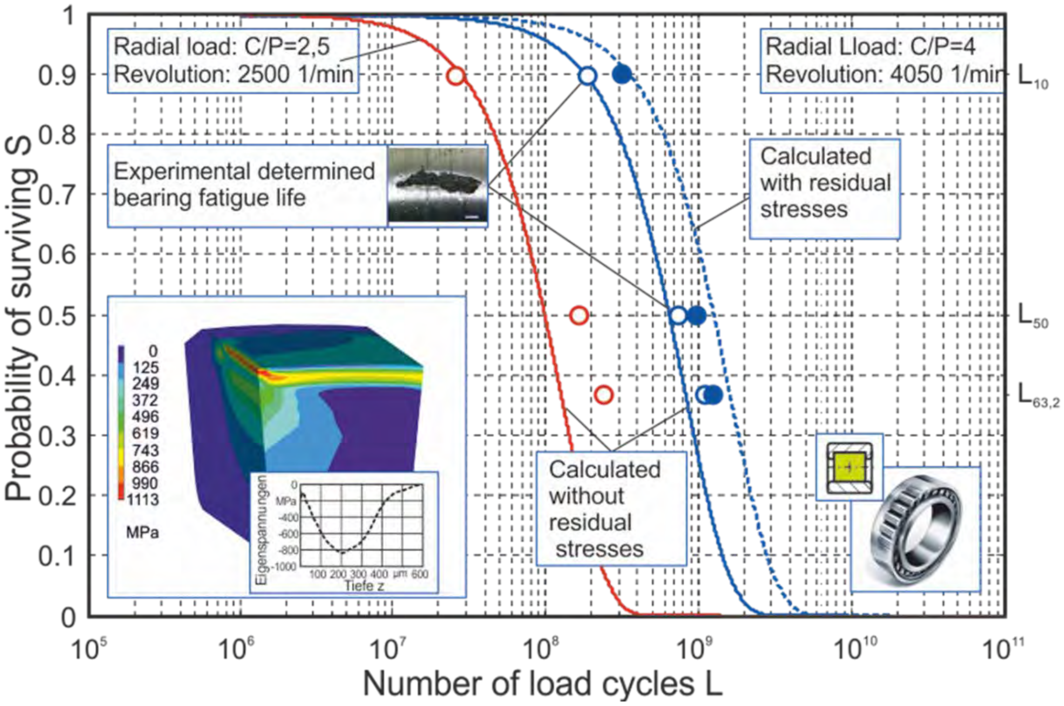

Figure 29: Comparison of calculated and experimental achieved probability of surviving

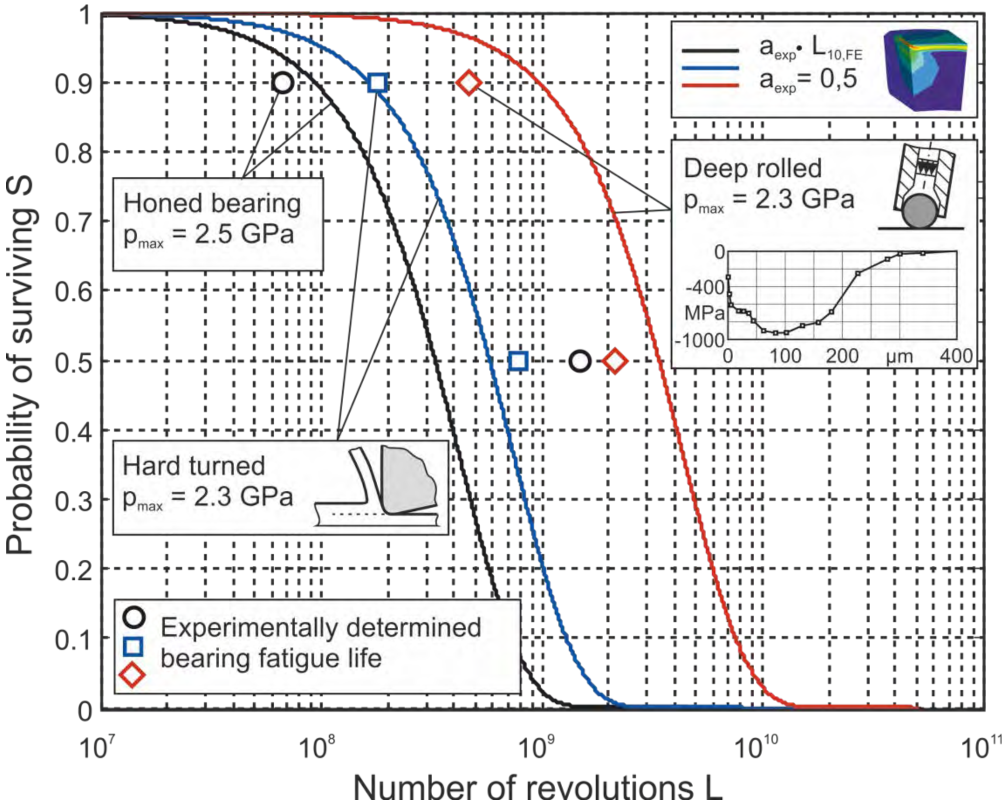

Figure 30: Comparison of calculated and experimentally achieved probability of surviving for honed, hard turned and deep rolled bearing inner rings

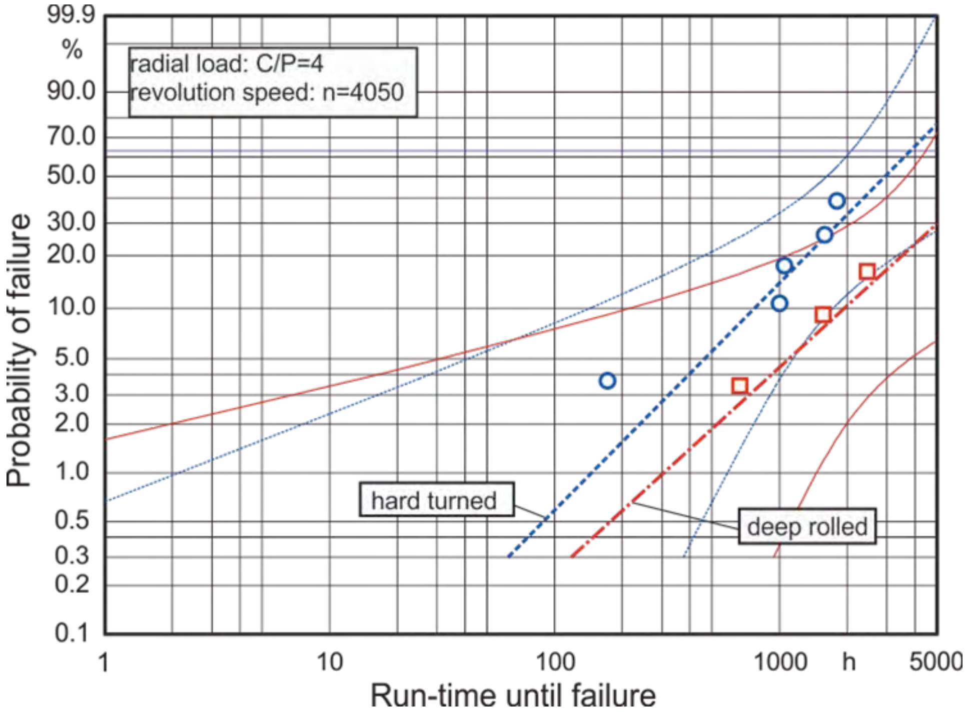

Figure 31: Comparison of calculated and experimentally achieved probability of surviving for hard turned and deep rolled bearing inner rings

6. Conclusion and outlook

To increase the productivity and improve the lifetime of roller bearings a new concept for a hybrid machining process by hard turning and deep rolling is presented. It is known, that the reduction of surface roughness peaks and high compressive residual stresses increase the endurance of bearings. The process can be used to create a specific surface integrity design during the machining of roller bearing inner rings. This effect can be achieved by positioning the deep rolling tool exactly on the roughness peaks to create a plateau surface. Machining experiments show, that by using this concept, the surface roughness can be reduced significantly. Especially the roughness peaks Rpk decrease by positioning the rolling tool exactly on the surface peaks of the hard turned surface ($N_w = 0.5$). Applying the hard turn-rolling, productivity can be increased. By using a roughing feed of $f = 0.2$ mm a surface finish of $Rz < 1.5$ µm is created. It is shown, that the deep rolling process is the only significant process to induce residual stresses in the finished bearing. The residual stress state can be estimated by the Hertzian contact during deep rolling.

During loading tests the surface integrity of roller bearings changes. This change is analyzed for different machined roller bearing inner rings. In standard honed roller bearings the near surface residual stresses increase due to the rolling load. In a distance of $z = 150$ µm a stable maximum compressive residual stress occurs for the given conditions. The tested hard turned bearings show the same behavior because the residual stress are only induced up to $z = 20$ µm. The same depth profile is induced as for the honed bearings. Deep rolling induces high compressive residual stresses and the depth profile exceeds that of honed bearings significantly. This leads to the fact, that within 29 million revolutions no significant changes occur, the residual stresses degenerate with much longer running times in depths of up to 130 µm. Endurance tests show that this pre-loading increases the L10 lifetime of the roller bearings by about 200%. Surface roughness decreases for all three manufacturing processes during the bearing test. Both can be preempt during the manufacturing process by the hybrid hard turn-rolling process.

The next steps within this research will be to measure the residual stresses after hard turn-rolling to proof the significant effect of deep rolling and to analyze turn-rolled bearings in screening and endurance tests. For an industrial use of the process the influence of tool wear has to be investigated.

7. Acknowledgement

The authors thank the DFG (German Research Foundation) for supporting this project in the context of the research program Ressource Efficient Machine Elements (SPP1551).

8. References

[ALBR60] Albrecht, P.: New developments in the theory of metal-cutting process – Part I. ASME Transactions Journal of Engineering for Industry, Vol. 84/4, 1960, p. 348 – 358

[AK87] Albert, M., Köttritsch, H. Steyr (Hrsg.): Wälzlager, Springer-Verlag, 1987

[BERS82] Berstein, G., Fuchsbauer, B.: Festwalzen und Schwingfestigkeit. Materialwissenschaft und Werkstofftechnik, Vol. 13/3, 1982, p. 103 - 109

[BRAM61] Brammertz, P.-H.: Die Entstehung der Oberflächenrauheit beim Feindrehen. Industrie-Anzeiger, Vol. 2, 1961, p. 25 – 32

[DENK15] Denkena, B., Grove, T., Maiß, O.: Influence of the cutting edge radius on surface integrity in hard turning of roller bearing inner rings. Production Engineering – Research and Development, Vol. 9, 2015, p. 299 – 305

[DENK16] Denkena, B., Grove, T., Maiß, O.: Influence of hard turned roller bearings surface on surface integrity after deep rolling. Proceedia CIRP, 2016, accepted paper

[EHW53] Eschmann, Hasbargen, Weigand: Die Wälzlagerpraxis – Handbuch für die Berechnung und Gestaltung von Lagerungen, Verlag von R. Oldenbourg, München, 1953

[GLES09] Gleß, M.: Wälzkontaktermüdung bei Mischreibung, Otto-von-Guericke-Universität Magdeburg, Thesis 2009

[HACK11] Hacke, B., Radnai, B., Hinkelmann, K.: Berücksichtigung von Betriebszuständen, Sonderereignissen und Überlasten bei der Berechnung der Wälzlager-Lebensdauer in Windenergieanlagen und Großgetrieben, Abschlussbericht FVA-Forschungsheft Nr. 967, AiF-Nr. 15227 N, 2011

[HAR84] Harris, T. A.: Rolling Bearing Analysis, Second Edition, Wiley Interscience, 1984

[HEN02] Hengerer, F.: Wälzlagerstahl 100Cr6 – ein Jahrhundert Werkstoffentwicklung, HTM 57, 2002

[IOAN99] Ioannides, E., Bergling, G., Grabelli, A.: An analytical formulation for the life of rolling bearings. Acta Polytechnica Scandinavica, Mechanical engineering series No. 137, 1999

[KLOC05] Klocke, F., Brinksmeier, E., Weinert, K.: Capability of Hard Cutting and Grinding Processes. CIRP Annals – Manufacturing Technology, Vol. 54/2, 2005

[KOCH96] Koch, K.-F.: Technologie des Hochpräzisions-Hartdrehens. Dr.-Ing. Dissertation, RWTH Aachen, 1996

[MAIS16] Maiß, O., Denkena, B., Grove, T.: Hybrid machining of roller bearing inner rings by hard turning and deep rolling. Journal of Materials Processing Technology, Vol. 230, 2016, p. 211 – 216

[MERW63] Merwin, J.E., Johnson, K.L.: An analysis of plastic deformation in rolling contact. Proceedings of the Institution of Mechanical Engineers, Vol. 177/25, 1963, p. 676 - 690

[NEUB16] Neubauer. T.: Betriebs- und Lebensdauerverhalten hartgedrehter und festgewalzter Zylinderrollenlager. Dr.-Ing. Dissertation, Leibniz Universität Hannover 2016

[PABS12] Pabst, A., Hubert, T., Tremmel, S., Wartzack, S.: Berücksichtigung von Druckeigenspannungen in wälzbeanspruchten Werkstoffbereichen von Wälzlagern, GfT-Fachtagung 2012, Göttingen

[REHE15] Rehe, M.: Herleitung prozessbezogener Kenngrößen der Schneidkantenverrundung im Fräsprozess. Dr.-Ing. Dissertation, Leibniz Universität Hannover, 2015

[ROET03] Röttger, K.: Walzen hartgedrehter Oberflächen. Dr.-Ing. Dissertation, RWTH Aachen, 2003

[SOKO55] Sokolowski, A. P.: Präzision in der Metallbearbeitung. VEB Verlag Technik, 1955

[VOSK96] Voskamp, A.: Microstructural changes during rolling contact fatigue - metal fatigue in the subsurface region of deep groove ball bearing inner rings, Technische Universität Delft, Thesis, 1996

Bearing life and efficiency – evaluation of the influence of preload with tools from the FVA Workbench

Leonhardt, C.; Bader, N.; Otto, M.; Poll, G; Stahl, K.

1. Abstract

The rating life and efficiency behaviour of rolling element bearings are predominantly affected by the operating conditions. Especially in adjusted bearing arrangements the load consists not exclusively of the external force, which is for instance caused by gear meshing forces but also from the preload of the arrangement. To get a reliable design that includes high rating life with low friction losses, appropriate design methods have to be applied to get an optimal preload. Concerning the rating life, sophisticated models have been standardized, whereas the methods for the friction torque calculation show in general deviations from experimental results. In this paper a model to calculate the friction torque is presented. The approach has a local view on the rolling contact and provides the determination of different torque parts which can be summed to the overall bearing torque. The here presented model has been validated by experimental testing and showed good agreement with the measurement results. To show an exemplary application of the before mentioned calculation methods a calculative example of an adjusted bearing arrangement in a gear stage has been carried out. The focus of the investigations was set on the preload and the operating temperature as varied parameters and their impact on the rating life and the efficiency behaviour of the bearing.

2. Introduction

The manufacturers of rolling bearings aim to increase the durability and reliability of their products constantly. Besides the rating life of the rolling bearing, efficiency issues have become increasingly important. This objective results in the effort to reach low bearing losses at a high rating life. This goal is not only influenced by the bearing itself, but primarily by the operation conditions (e.g. load, lubrication, operation temp. etc.). Especially in adjusted bearing arrangements the load of the bearings can be influenced highly by the initial preload of the bearing/shaft system.

This paper presents the results of a calculative investigation on the effects of the preload in an adjusted bearing arrangement. The focus is on the rating life of the bearing arrangement on the one hand and efficiency issues on the other hand. Besides the initial preload the influence of the operating temperature will be taken into account. It has significant effects on the lubrication conditions in the rolling contact and can affect the preload of the bearing arrangement due to thermal expansion of the surrounding parts. In the literature investigations on the preload of adjusted bearing arrangements are often presented in the context of machine tools (spindle bearing systems). Xiaohu [Xiao16] et al. for example shows results on investigations of a non-uniform preloaded spindle bearing system with focus on the accuracy of the spindle arrangement. Than and Huang [Than15] focused upon the thermal behaviour of a spindle bearing application in theoretical investigations depending on the preload of the bearing arrangement. Tudose et al [Tudo16] presented a methodology to find the optimal preload in order to optimise the life of the bearing arrangement.

The studies in this paper consider rating life and friction torque in order to get a comprehensive result in the design process. To demonstrate the capability of the presented calculation methods, a straightforward gearbox model has been implemented. Therefore the “FVA-Workbench 4.0” has been used as an appropriate software tool. As a user interface it provides the functionality of research software that has been developed at different research institutes. This research software was created with the support of the FVA (“Forschungsvereinigung Antriebstechnik”). In the post-processing of the calculative investigations conducted in this paper the rating life and the torque loss in the bearing arrangement have been evaluated.

Bearing Lifetime Calculation

The standard design criterion of bearings in most applications is the rating life, which is typically limited by material fatigue. In the last century many efforts have been made to estimate the rating life of a bearing by means of mathematical formulations.

In most cases subsurface fatigue, also known as pitting is the underlying damage type in the context of bearing rating life. The mechanism of pitting is crack initiation and propagation in the material due to cyclic load in the bearing. It has been observed that the cracks start to grow at impurities or inclusions in the material. Crack initiation is induced by local stress peaks at the material imperfections in case the material load exceeds a certain stress level (fatigue limit load). Numerous experimental investigations have shown that the cracks origin is normally located in a certain depth of the material which is related to the maximum value of orthogonal shear stress in the Hertzian theory assuming optimal lubrication conditions in the contact between rolling element and the raceway. With further load cycles the crack propagates towards the surface. Once the crack has reached the surface, pieces of material can break out of the surface resulting in the typically known appearance of a pitting damage. The loose material parts may be overrun by the rolling elements, which leads to dents in the raceway and rolling element contact surfaces and therefore further stress peaks in the material. Hence the pitting damage has a progressive behaviour.

In order to describe the fatigue damage properly and reliable, many model approaches have been developed to estimate the rating life of a bearing assuming given operating conditions. Sadeghi et al. [Sad09] classifies two different types of models to describe the rolling contact fatigue: probabilistic engineering models and deterministic research models. The former is based on experimental testing data, whereas the research models contain theoretical assumptions on failure mechanisms and mechanical material behaviour. One of the early efforts in terms of bearing lifetime predictions has been made by Lundberg and Palmgren [Lun47, Lun52]. Their model deals with the orthogonal shear stress τ_0 as criterion for crack initiation. Cracks occur on stochastically distributed discontinuities in the material. Based on the Weibull statistical strength theory [Wei39] the probability of survival of a stressed volume V is (equation 1):

$$\ln \frac{1}{S} = A \frac{N^e \tau_0^c V}{z_0^h} \tag{1}$$

The depth of the maximum shear stress is denoted as z_0 and N describes the number of load cycles that the stressed volume V was exposed to. The other parameters have to be defined by experimental testing. Ioannides und Harris [Ioan85] refined the model of Lundberg and Palmgren by discretising the stressed material. Additionally a threshold value for the maximum orthogonal shear stress τ_0 was introduced. This value considers the fact that no failure is detected when bearings run under good lubrication conditions and comparably low loads. Based on these achievements different modifications of these models have been developed. Over the years the roller bearing rating life calculation found its way into a standardisation process. ISO 281 [ISO281] contains a lifetime calculation that considers simple load cases with minor computational expense. These models were refined gradually and consider lubrication conditions in the contact, impurities and more complex load cases with augmented computational effort (cf. [DINISO281], [DIN26281, ISO16281]). In 2015 a new model (SKF Generalized Bearing Life Model – GBLM), that incorporates subsurface fatigue and surface fatigue, was presented by Morales-Espejel [Mor15]. At the moment this model is not suitable for standardisation.

The theoretical research models are based on mechanical considerations that describe the stress and strain condition in the material. Considering the load of the material the rating life is predicted with the aid of two types of models: crack initiation and crack propagation or mixed forms of these models. [Sad09]

3. Materials and Methods

Due to increasingly stringent regulations concerning CO_2-emissons and the aim to reduce power consumption, a comprehensive consideration of the gearbox system is required. Besides the calculation of the bearing itself the behaviour of the shaft bearing system has to be involved, because the deformations and displacements of the shaft have a significant impact on the load distribution in the bearing. Furthermore effects like lubrication and thermal budget have to be taken into account to get reliable results. Extensive calculation methods and the use of iterative algorithms make the application of software tools mandatory. For the calculations in this paper the “FVA-Workbench 4.0” is used.

The FVA Workbench

The FVA Workbench is a graphical user interface that provides the functionality of a comprehensive gearbox design tool. The software makes use of calculation submodules, which have been developed by various research institutes in the context of FVA funded projects. The modules used for the calculations in this paper are RIKOR [RIKOR] and LAGER2 [LAGER2] which have been mainly developed by the Gear Research Centre (FZG,) at Technical University of Munich. Furthermore a method to calculate the bearing friction torque is presented in this paper. Its implementation is realised in the submodule LFP, which is attached to LAGER2 and has been developed by the IMKT in Hanover.

As a comprehensive software tool the “FVA Workbench 4.0” provides the functionality of an overall system design tool. After the analysis of the power flow in the gearbox the gear meshing forces are determined. Based on these discrete forces the mechanical equilibrium is found by means of iterative algorithms taking into account the nonlinear stiffness behaviour of rolling element bearings. During these calculations the load distribution on the flank of the gears is taken into account and can be optimised by a calculated flank modification. This functionality is provided by the FVA module RIKOR. On the part of the rolling element bearings the submodule LAGER2 performs calculation methods on rating life and friction torque. The bearing load is passed from RIKOR to LAGER2.

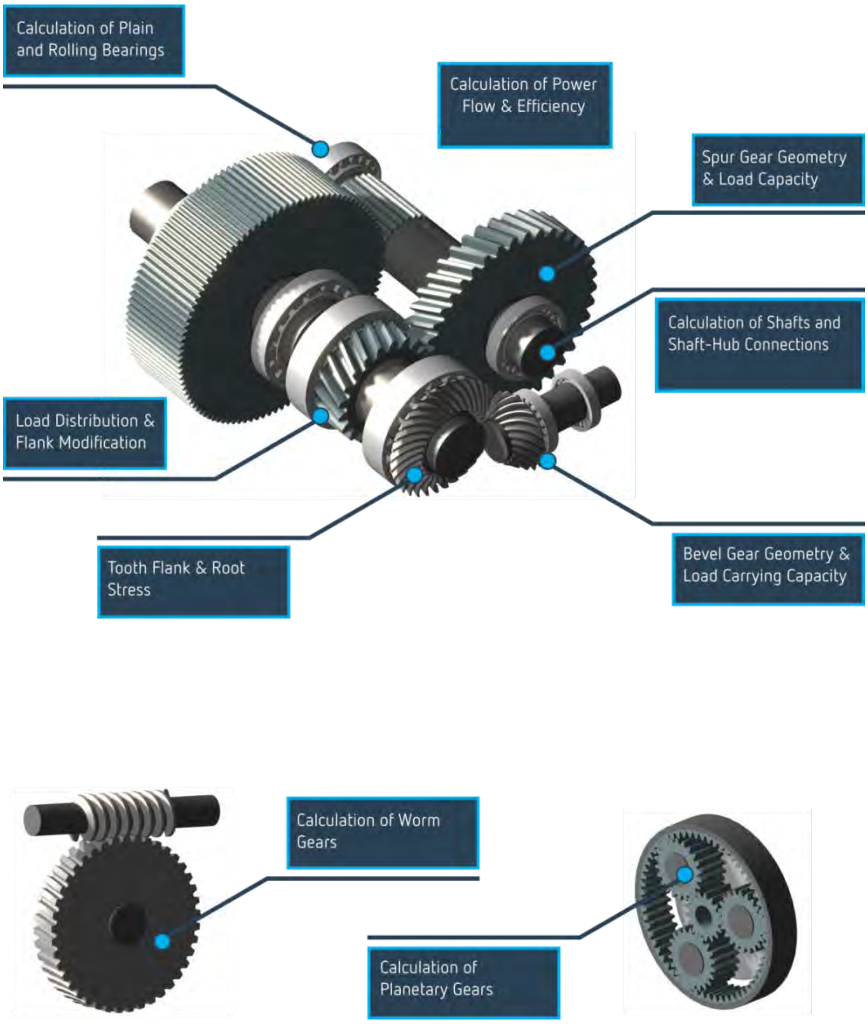

Figure 32: Calculation methods provided by the FVA Workbench

LAGER2

The focus of the software tool LAGER2 is on the calculation of rolling element bearings and is a useful tool during the design process or the selection of an appropriate bearing for universal applications. LAGER2 includes a five degrees of freedom model of the bearing and can handle most types of rolling element bearings. Based on the external loads (external forces, moment, displacements, tilting) LAGER2 determines by means of the internal geometry the load distribution in the bearing including maximum Hertzian stresses in ball bearings and the stress distribution over the axis of the rolling element in roller bearings. These results can be used to compute the rating life according to the present state of standardisation DIN 26281/ISO/TS 16281 [DIN26281, ISO16281]. Additionally enhanced calculations which include the current state of science and technology as for instance the estimation of the slip tendency of the bearing rings in the bearing seat are implemented. Furthermore LAGER2 contains a submodule that calculates the friction torque of the bearing. This module was developed in the context of the research project “Low Friction Powertrain” (LFP) [LFP12] and is an addition besides the friction models published by the bearing manufacturers included in LAGER2. The applied approach is premised on a local view on the rolling element contacts. The load of the individual contacts is transferred from LAGER2 to the LFP submodule.

4. Enhanced model of bearing torque calculation

In the following section a short overview of the implemented calculation algorithms for the bearing torque is shown. The focus will however be on the calculation of losses in angular contact ball bearings. The main losses occurring in rolling element bearings are depicted in Figure 33.

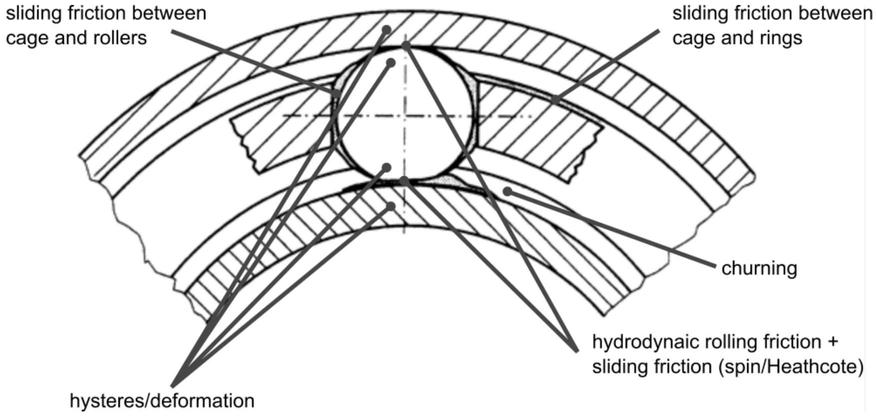

Figure 33: Mechanisms leading to losses in rolling element bearings

One of the first well known calculations for the bearing losses was proposed by Palmgren in 1957 [Pal57]. He divided the bearing torque T_{bear} into load dependent T_1 and load independent T_0 parts

$$T_{bear} = T_1 + T_0 \tag{2}$$

The estimation of the load independent portion is achieved using empirical constants which consider bearing type, operating conditions, and lubrication. Due to the use of empirical values such models often show deviations from experimental measurements when applied outside of the operating conditions used to determine the input parameters.

The principle of dividing the losses into the physical causes has held to the current day and most calculations divide the torque into load independent and load dependent parts. Subsequently the load dependent losses are estimated by taking their respective mechanisms into account. This is also visible in the current catalogue calculation methods e. g. in [SKF14] shown in equation (3). This method considers rolling torque T_{Roll}, sliding torque T_{slide}, and torque due to lubricant flow T_{drag}. The seal torque is not further discussed as bearings without seals are the focus of the current paper.

$$T_{total} = \Phi_{ish} \cdot \Phi_{rs} \cdot T_{roll} + T_{drag} + T_{slide} + T_{seal} \tag{3}$$

The factor Φ_{ish} represents the film thickness, and Φ_{rs} the track replenishment. These factors thus consider lubricating conditions e. g. starvation effects.

Whilst several models have been proposed to calculate losses in EHL contacts e. g. [HEB08, HEV08] these methods often rely on time consuming numerical calculations. Thus the aim was to develop a calculation method yielding acceptable accuracy with tolerable calculating times. This model is described in detail in the following section.

The calculation methods in LAGER2 are based on results from FVA388I and II [FVA388 I+II] as well as results from the research project Low Friction Powertrain [LFP12]. As stated above the torque is calculated by summing up the torque due to several mechanisms.

The load dependent torque parts are calculated considering the torque T_{deform} resulting from irreversible deformation energy proposed by Johnson [John85]:

$$T_{deform} = \frac{2}{3\pi} \cdot \kappa \cdot b \cdot Q \tag{4}$$

The factor κ represents the material specific damping constant. The deformation losses for one contact given in equation 4 are the summed according to Steinert [Stei95] leading to the total deformation losses:

$$T_{deform,tot} = \sum_{i=1}^{Z} \left| \frac{\omega_{roll}}{\omega_{ir}} \right| \cdot \left(T^{i}_{deform,ir} + T^{i}_{deform,or} \right) \tag{5}$$

The hydrodynamic rolling torque T_{Roll} between rollers and raceway is calculated according to the model proposed by Gohar [Goha88]. The above described losses have been thoroughly investigated. The focus on the new loss calculation was thus on the losses influenced by the lubricant rheology i. e. sliding losses. These consist of two parts:

$$T_{sliding} = T_{Heathcote} + T_{spin} \tag{6}$$

In the case of ball bearings these sliding losses are mainly the losses by roller spin and the losses by differential slip i. e. Heathcote slip. During calculation of the roller kinetics these two mechanisms cannot be separated. The spin torque is influenced by the speed of the bearings. With rising speed the spin in the outer race contact decreases until pure rolling is achieved. The torque T_{spin} resulting from spin torque is calculated as proposed by Steinert [Stei95]

$$T_{spin} = \int_{A} r \cdot \tau \, \mathrm{d}A \tag{7}$$

The shear stress τ is calculated according to a lubricant model.

When considering ball bearings the torque $T_{Heathcote}$ created by the Heathcote effect (i. e. differential slip due to different radii of the ball as well as elastic deformations, and thus non-ideal rolling conditions in most of the contact area) must be considered. This is done by using the calculations proposed by Harris [Harr07]. The calculated slip (combination of Heathcote and spin) induces a shear rate in the lubricant, which in turn causes the forces counteracting the roller movement i. e. friction.

The shear rate imposed on the lubricant results in a shear stress. The shear stress is modelled by considering a simplified non-Newtonian lubricant behaviour. This is necessary due to the high pressures and shear rates present in the EHL contacts. This model is based on the assumption of a Maxwell fluid behaving as shown in Figure 34.

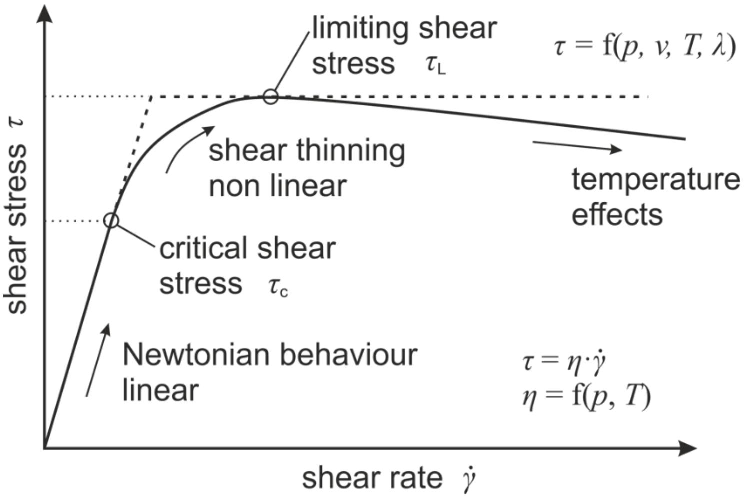

Figure 34: Lubricant behaviour under shear according to Bair [Bai07]

In regions of low shear rate the lubricant reacts in a Newtonian manner i. e. a linear relationship between shear rate and shear stress.

$$\tau = \eta \cdot \dot{\gamma} \tag{8}$$

At a critical shear stress τ_c the lubricant is assumed to exhibit shear thinning behaviour until reaching a limiting shear stress τ_{lim}. This limiting shear stress imposes a limit on the force transferable through the lubricant film. To calculate the maximum force i. e. maximum friction force the lubricant needs to be investigated further. Several methods have been proposed ranging from rheological measurements [Bai07], molecular simulations, to traction tests. In this paper the results obtained from traction tests are used to characterise the maximum shear stress. It must be noted however, that the traction curves do not depict lubricant behaviour and always incorporate system specific portions. Furthermore the heating occurring in the EHL contact during the traction tests is often neglected. Figure 35 shows results from traction experiments conducted on a twin disc test rig. The maximum shear stress τ_{max} has been marked. By varying temperature, pressure, and slide to roll ratio (SRR) friction maps can be obtained e. g. [Bjoe11].

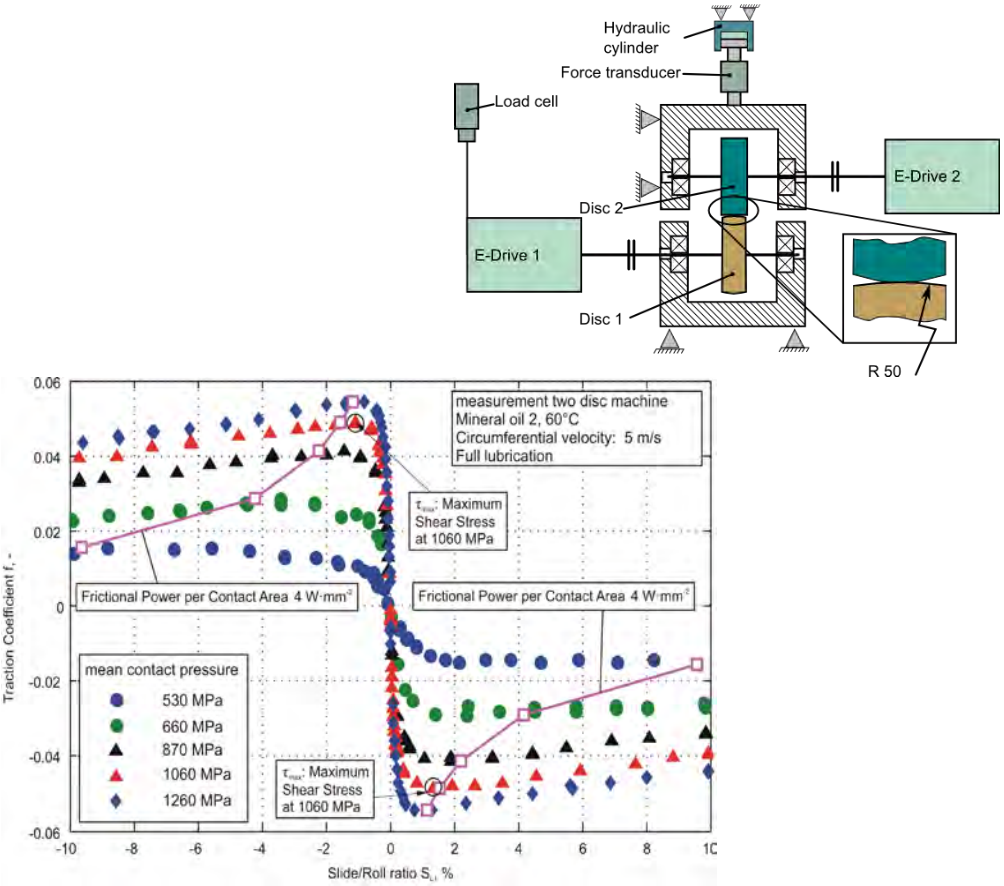

Figure 35: Traction curves from twin disc experiments

When obtaining the data from the traction experiments thermal effects are neglected and only the maximum value is used to describe the lubricant. Wang obtained a near linear relationship between the maximum shear stress reached in the experiment and the pressure (Figure 36 left), whilst the temperature of the lubricant showed only little influence [Wang15]. This relationship is used to set up a simple rheological model, shown in Figure 36 right.

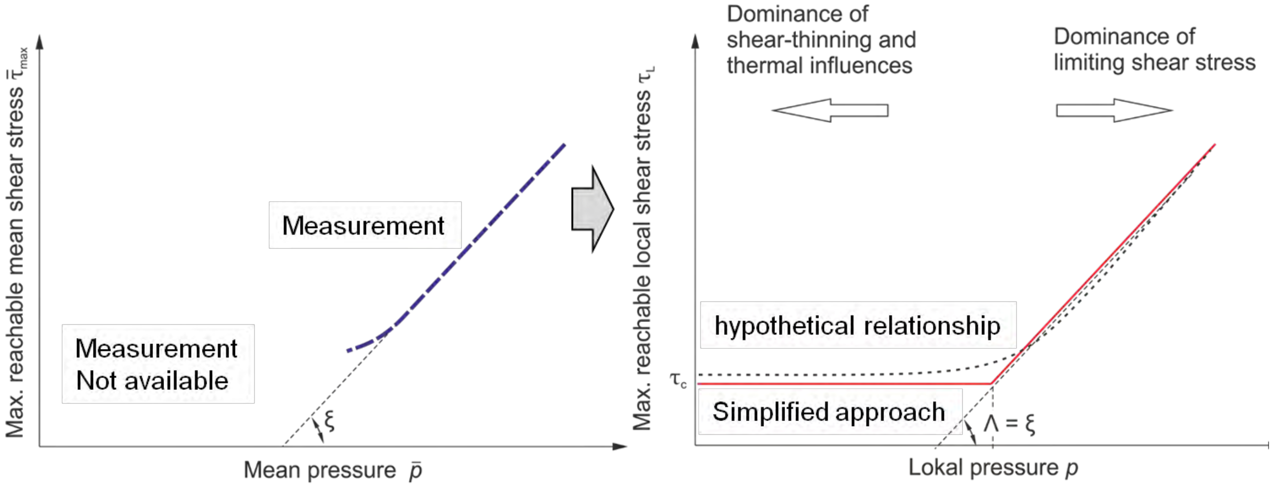

Figure 36: Relation between pressure and maximum shear stress. Left: Measurement, right: Model acc. [Wang15]

The model assumes the lubricant behaviour to be Newtonian, until a pressure dependent maximum shear stress is reached. At moderate to high pressures the maximum shear stress is assumed to be the data obtained from the traction experiment, whilst at low pressures (typically below ~500 MPa) the maximum shear stress transmittable is assumed to be the critical shear stress i. e. onset of shear thinning. Thus τ_{max} can be written as:

$$\tau_{max} = \begin{cases} \tau_c & ,p < p_s \\ \xi \cdot (p - p_0) & ,p \geq p_s \end{cases} \tag{9}$$

ξ and p_0 from linear fits of twin disc experiments. With $p_s = \frac{\tau_c}{\xi} + p_0$. Values of ξ are in the range of 0,06 to 0,08 and values for p_0 are between 450 and 580 MPa. This model is partly empirical needing input data in the form of traction curves, but has the advantage that it can be applied in fast analytical calculations.

To obtain the bearing losses utilising this fluid model the contact is discretised and the sliding velocities of each contact element are calculated. Together with the film thickness calculated e. g. by the Dowson Higginson formulae a local shear rate is obtained. From the pressure distribution the local contact pressure is calculated and using the rheological model from equation (9) the maximum shear stress of the contact element is obtained. Using shear rate and the local viscosity a Newtonian shear stress is calculated. If this shear stress is higher than the maximum allowable (by equation (9)) shear stress the shear stress is truncated at the maximum allowable value. Subsequent integration of all elements yields the total frictional force.

Subsequently the presented parts from the bearing losses are summed up to yield the resulting total torque of the bearing:

$$T_{bear} = T_{deform} + T_{roll} + \underbrace{T_{slide}}_{T_{spin} + T_{Heathcote}} \tag{10}$$

Losses occurring from cage roller and cage ring contacts are assumed to be negligible. All calculations assume an oil jet lubrication. When specifying an oil bath lubrication the churning losses are estimated via the method proposed in the SKF catalogue and need to be added to the above torque.

Model validation

To validate the model the calculated bearing losses are compared with experimental results from bearing friction measurements. The test setup incorporated two axially loaded deep groove ball bearings of the type 6008. The bearing torque was measured using a torque transducer. The bearings were lubricated using oil jet lubrication. The test setup is shown in Figure 37.

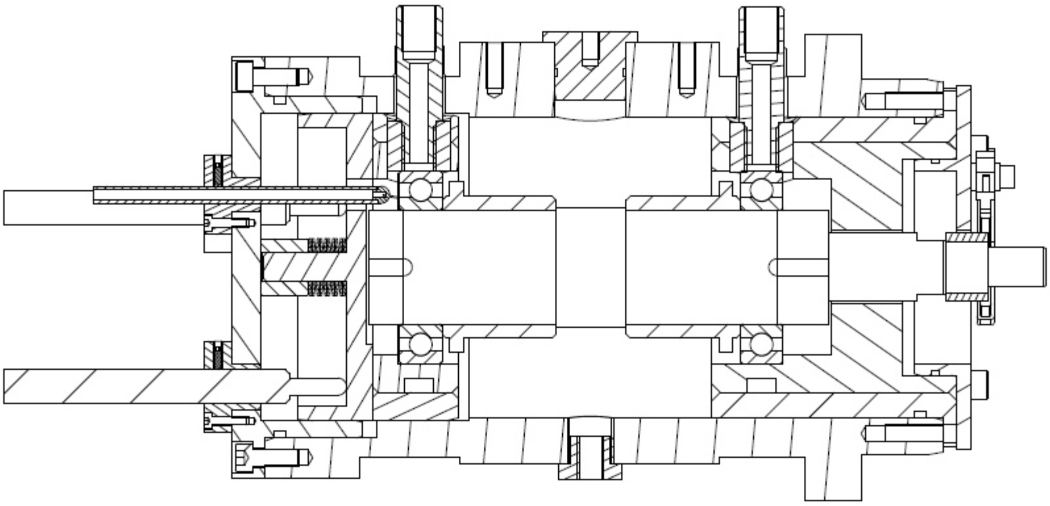

Figure 37: Test setup for bearing torque measurement [Wit13]

Figure 38 shows the results comparing the measured torque with the calculated losses. It is evident, that the total torque calculated coincides with the measured data. Furthermore the contributions of the friction mechanisms are shown. It can be noted that the contribution of hydrodynamic rolling friction and friction due to deformation is small compared to the friction resulting from sliding losses i. e. sum of Heathcote and spin.

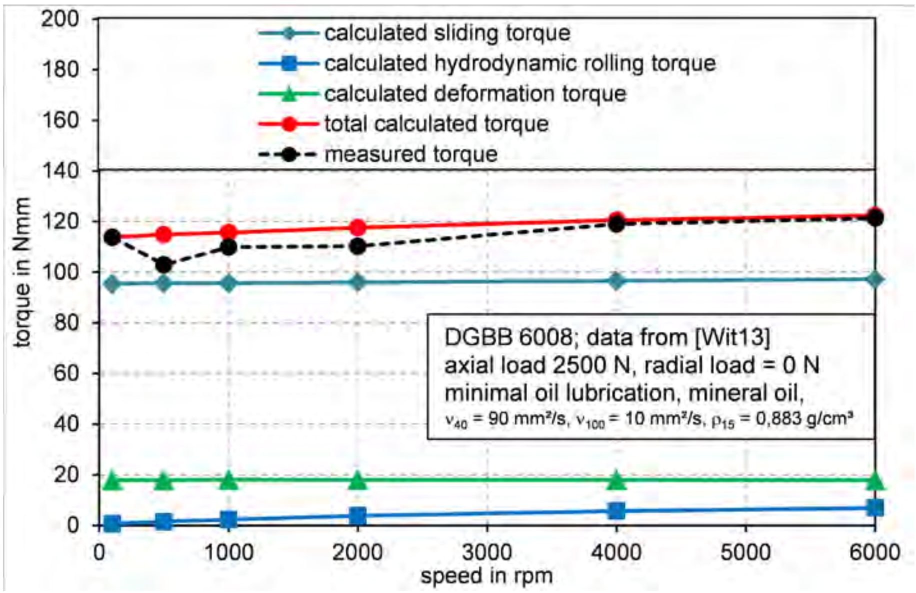

Figure 38: Comparison of calculated losses with experiment

Other bearing types can also be calculated by these methods. These include tapered roller bearings and cylindrical roller bearings. In these bearing types the additional contacts exhibiting slip e. g. flange roller contact are treated in the same fashion as the sliding friction in the roller bearings.

5. Calculation example

In order to assess the efficiency and rating life of a bearing in diverse applications, a comprehensive software tool is demanded. In the context of this paper a calculation example is presented to show the utilisation of the before mentioned calculation methods by means of the FVA Workbench. In most cases bearing arrangements are applied in gearbox systems, which should be picked up in this example.

The calculation of the bearing arrangement is performed in the context of a standardised FZG back-to-back test rig (cf. Figure 39). The test rig consists of two gearboxes with the same gear ratio that are arranged in a back-to-back configuration and loaded by a load clutch. As a consequence a static torque is introduced in the system. Once the test rig is driven by the electric motor the power is transmitted by the gears whereas only the power loss is introduced into the power circuit. This test rig is capable of providing investigations on different failures modes in gears such as pitting, micro pitting, scuffing or efficiency testing. With additional measurement equipment it is possible to perform investigations on the impact of tooth flank corrections on the dynamic behaviour. The gears can be lubricated by oil injection lubrication and oil bath lubrication. In the former lubrication mode the oil flow can be controlled by an oil supply unit. In both lubrication types the temperature can be adjusted in order to get specified and repeatable operating conditions.

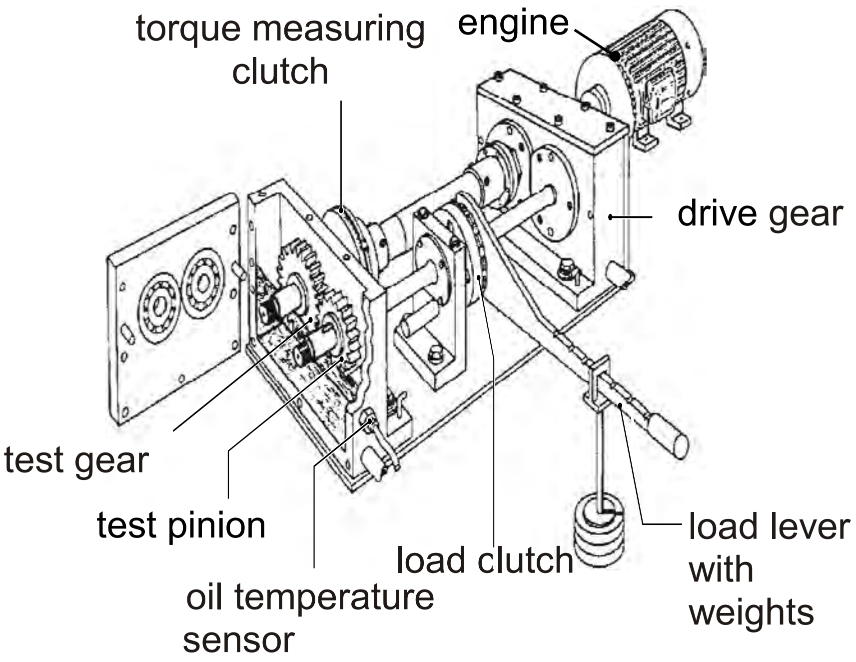

Figure 39: FZG back-to-back test rig

The focus of the calculations will be set on the gear stage, which is mounted in the test gear box (left gearbox depicted in Figure 39). Gear geometry is selected according to a test gearing set used in the research project FVA 364 III [FVA364 III]. The investigations performed in the context of that research project included measurements on the temperature behaviour of various bearing types using the here selected gear stage (cf. Figure 40).

Gear geometry:

Centre distance	91.5	[mm]
Module	3,75	[mm]
Number of teeth	23/24	[-]
Width	45	[mm]
Normal pressure angle	20	[°]
Helix angle	15.2	[°]
Transverse contact ratio	1.46	[-]

Figure 40: Model of the gear stage

Besides the gears the gear stage consists of two angular contact ball bearings (7206-B-TVP) that are applied in an X-arrangement in order to support the shaft loaded by the meshing forces. The external dimensions of the bearings are: outer diameter of 62mm, inner diameter of 30mm and a width of the bearing of 16mm. The pressure angle of the bearing including 13 rolling elements is 40° in the unloaded state. In the following the bearing highlighted in green (cf. Figure 40) is chosen as subject of investigation.

As a lubricant, FVA reference oil FVA3 is used, a mineral oil that contains no extreme pressure additives (EP-additives). The gear stage is lubricated with oil bath lubrication.

The operating conditions have been chosen according to FVA 364 III [FVA364 III] in order to get realistic assumptions on the thermal budget (oil temperature, temperature gradient in the bearing etc.) which are based on experimental measurements. The load of the gear stage is set to 300 Nm with a rotational speed of 3000 rpm which equals 94.2 kW transmitted power in the gear stage. The varied parameters during the investigation were mainly the operating temperature (assumed equal to the oil temperature) and the initial preload of the bearing arrangement. The range of the oil temperature is 20°C to 140°C, the values of the initial preload cover the range from 0µm to 150µm.

The calculation methods used in the modules of the FVA Workbench consider the deformation of the shafts an the gears in the process of determining the bearing load. The effects that result from these considerations shouldn't be neglected, hence they can influence the load distribution and therefore the efficiency behavior and rating life of the bearing significantly. Besides the mechanical part LAGER2 takes into account the temperature gradient between inner ring and outer ring. Due to the thermal expansion of the bearing elements the clearance in the bearing at operating temperature will be affected. The operating temperature itself will have an impact on the viscosity of the lubricant and therefore affect the thickness of the lubricant film which can reduce the rating life of the bearing arrangement. The temperature gradient inbetween the bearing rings is modeled as dependent on the operating temperature of the gearbox following equation 11:

$$\Delta T_{IR/AR} = \Delta T_{IR/AR,min} + \frac{\Delta T_{IR/AR,max} - \Delta T_{IR/AR,min}}{T_{op,max} - T_{op,min}} \cdot (T_{op} - T_{op,min}) \tag{11}$$

The temperature gradient $\Delta T_{IR/AR}$ has a linear correlation to the operating temperature ΔT_{op}. The total change of the temperature gradient from minimum to maximum operating temperature is 20° C inspired by the measurements in FVA 364 III [FVA364 III].

Besides the methods implemented in LAGER2 and RIKOR the thermal expansion of the shaft due to the operating temperature is considered. The thermal expansion of the axially rigid shaft is modelled by a linear law of thermal expansion:

$$\Delta l = l_0 \cdot \alpha \cdot \Delta T \tag{12}$$

The coefficient of thermal expansion is $12.5 \cdot 10^{-6}$1/K, which complies with the material characteristics of 16MnCr5 in a temperature range from 20°C to 200°C. The stiffness of the housing is taken into account by a simple spring model (cf. Figure 41). The stiffness of the housing is represented by $c_{housing}$ whereas the stiffness of the bearing is modelled with the stiffness $c_{bearing}$. Both of the stiffnesses are assumed to be constant, in consequence the stiffness of the housing and the bearing are supposed to show a linear behavior. The points to which the springs are linked to are representatives for the inner ring (IR) and the outer ring (OR) of the bearing. Their deviation from their initial position in the unloaded state is discribed by the variables Δx_{IR} and Δx_{OR}.

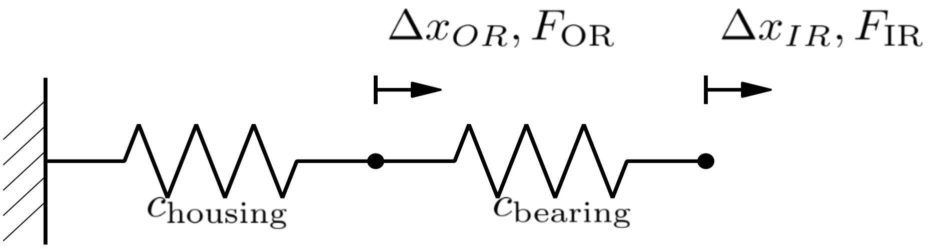

Figure 41: Model of the housing stiffness

The compression of the bearing $\Delta x_{bearing}$ due to the thermal expansion of the shaft can be described by the difference of the deviation of the inner ring and the outer ring. These considerations result in following equation:

$$\Delta x_{bearing} = \Delta x_{OR} - \Delta x_{IR} = \left(\frac{c_{bearing}}{c_{bearing} + c_{housing}} - 1 \right) \cdot \Delta x_{IR} \tag{13}$$

Following this model, only part of the thermal expansion of the shaft is absorbed by the bearing. The other part leads to a deformation of the housing (cf. equation 13). The ratio of the two shares is defined by the ratio of the stiffness of the bearing and the stiffness of the housing which is assumed to be constant in this calculation example.

Results

The focus on the post processing of the calculations is on the rating life and the efficiency behaviour of the bearing which are both important characteristics in the design process of a bearing application. If these matters don't correspond to the requirements a further design loop has to be carried out.

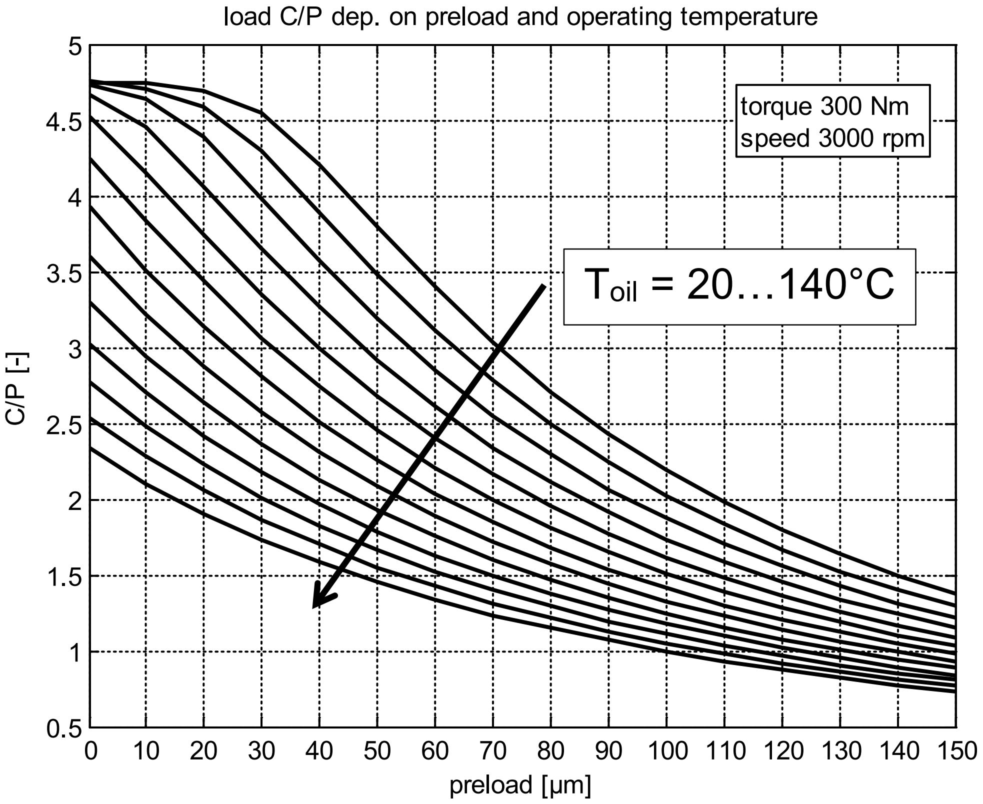

Figure 42: load of the bearing against initial preload and operating temperature

The rating life in this example is fundamentally affected by the load and the load distribution in the bearing as well as by the lubrication conditions that are mainly influenced by the operating temperature. The load of the bearing can be seen in Figure 42 depending on the operating temperature and the initial preload of the bearing arrangement. It can be recognised that the value of specific load of the bearing C/P decreases with increasing initial preload which means an increasing bearing load. The same effect can be seen concerning the increasing operating temperature that results in a thermal expansion of the shaft, which can be interpreted as additional preload on the bearing arrangement. Furthermore it can be seen, that the increase of the load caused by the operating temperature is higher looking at lower initial preloads. This observation can be explained by the fact that the share of the preload which is due to the thermal expansion, decreases with increasing initial preload. The effect can be attributed directly to the increasing operating temperature because the radial load is held constant for the whole calculation.

The effect of the varying operating temperature can be seen on the mechanical view of the system which is represented by the load of the bearing and the lubrication parameters such as for instance the lubrication film thickness. This effect is considered in the calculation of the rating life in terms of the life adjustment factor a_{DIN}.

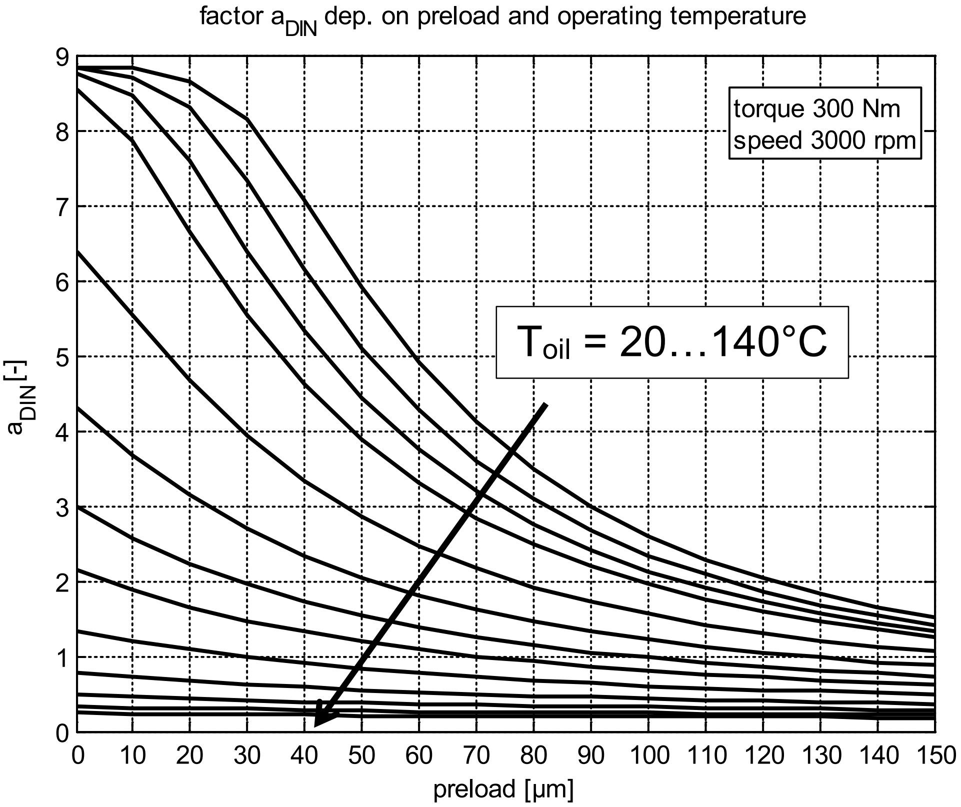

Figure 43: factor a_{DIN} against preload and operating temperature

The state of the art standardised calculation method concerning the rating life of universally loaded bearings is the modified reference rating life defined in DIN 26281/ISO/TS 16281 [DIN26281, ISO16281]. For ball bearings the equation is defined as:

$$L_{nmr} = a_1 \cdot a_{DIN} \cdot \left(\frac{C}{P_{ref}}\right)^3 \tag{14}$$

The here presented calculation example deals with the commonly used failure probability of ten percent, which leads to a life adjustment factor a_1 = 1. The life adjustment factor a_{DIN} is a function of the viscosity ratio κ (represents the lubrication film thickness) and the load of the bearing P.

$$a_{DIN} = f\left(\frac{C_u}{P}, \kappa\right) \tag{15}$$

An increasing oil temperature leads to a decreasing viscosity, which in turn reduces the viscosity ratio κ and therefore the life adjustment factor a_{DIN} as depicted in Figure 43. The influence of the preload of the bearing arrangement is taken into account with the bearing load P. The effect of the bearing load P on the life adjustment factor a_{DIN} decreases with growing operating temperatures, hence the effect of the operating temperature on the lubrication conditions dominates the factora_{DIN} . Regarding the factor for instance at a value of 140°C there is nearly no effect of the load recognisable, whereas the operating temperature has always a noticeable effect in the investigated range of the initial preload.

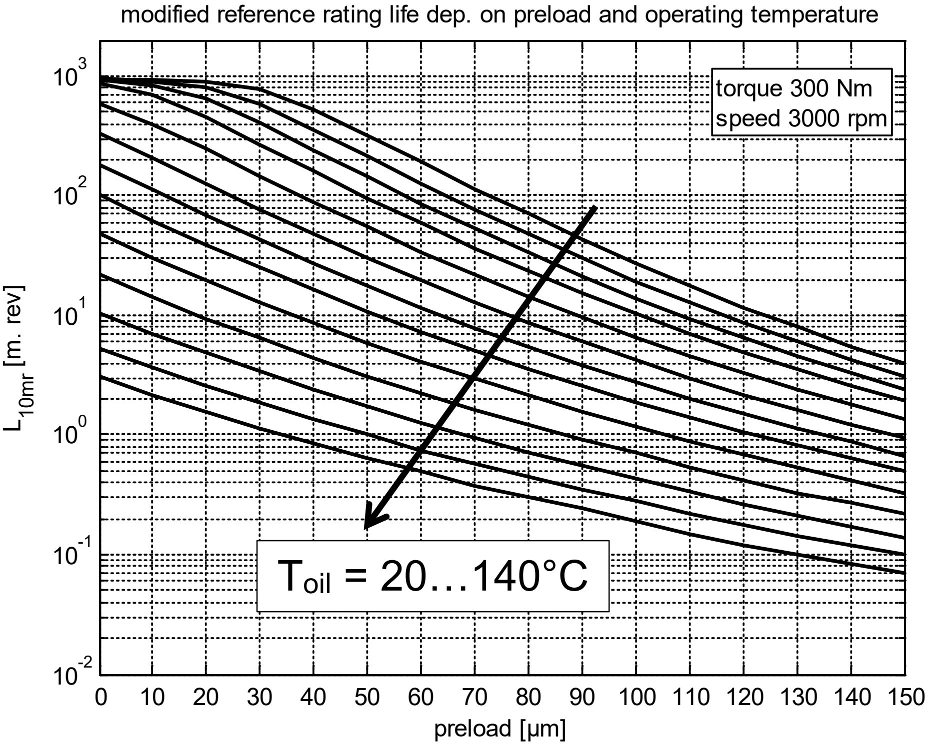

Figure 44: rating life against preload and operating temperature

These above mentioned effects of the load and the lubrication conditions have an effect on the rating life of the bearing arrangement. The increasing oil temperature acts on the one hand on the bearing load due to the thermal expansion of the shaft and on the other hand on the lubricant viscosity. The declining viscosity has a negative effect on the life adjustment factor a_{DIN}. The rising load acts on the load ratio C/P and additionally on the factor a_{DIN}. These two effects superpose in the calculation of the modified reference rating life due to the multiplication of these two impact factors. This results in a steep decline (semi-logarithmic scale) in the rating life (cf. Figure 44) with ascending initial preload and operation temperature. Generally it can be recognised, that the rating life is more sensitive towards the operating temperature in the region of low initial preloads than in the higher section of the investigated range. This observation can be traced back to the fact, that the additional load induced by thermal expansion is much bigger compared to the initial load induces by the initial preload.

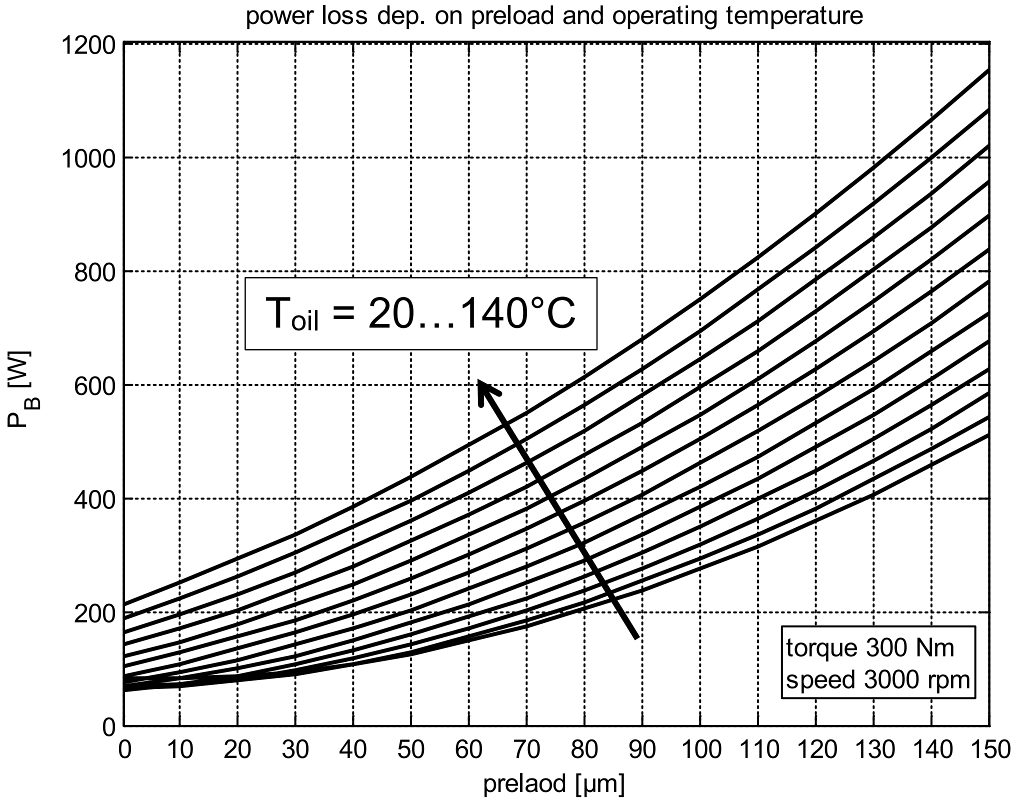

Figure 45: power loss against preload and operating temperature

The power loss of the bearing P_B depending on the operating temperature and the preload, which characterises the efficiency behaviour of the bearing, is depicted in Figure 45. Due to the constant rotational speed the power loss has the same behaviour as the torque loss of the bearing. The actual values differ by a factor considering the rotational speed. The power loss shows an inverse tendency compared to the rating life. As depicted in Figure 45 the P_B increases with higher preloads and higher operating temperatures. This effect is due to the higher load in the bearing. Higher contact pressures between the rolling elements and the raceways increase the contact surface between these two elements which results in rising friction losses and rising heat generation.

6. Discussion

In this paper a method to calculate the bearing friction torque was presented. The model is based on a local view of the contact and provides a separate calculation of different torque shares that are subsequently integrated to the global torque of the bearing. The proposed model for the calculation of bearing losses incorporates losses due to deformation, hydrodynamic rolling, and sliding. The rheological model allows for a fast analytical calculation of sliding losses. A validation with experiments showed good agreement between experiments and calculations. However, some bearing losses are still not incorporated and need further investigation. These are mainly contacts between cage and rollers, as well as churning losses.

The second focus of this paper was the investigation of the impact of the initial preload and operating temperature on the rating life and the efficiency behaviour of an adjusted bearing arrangement. The general effects have been illustrated by a straight forward example of a single gear stage. As a suitable software the FVA Workbench with its integrated submodules has been used to implement the model and execute the calculations. Besides the methods included in the submodules LAGER2 and RIKOR the thermal expansion of the shaft and the elasticity of the housing have been taken into account by an external model to calculate the rating life of the bearing according to DIN 26281/ISO/TS 16281 [DIN26281, ISO16281] and the bearing friction torque. The results of the calculation efforts have shown that a higher preload has a negative effect on the rating life of the investigated bearing. The same effect can be recognised with increasing operating temperature because the rising temperature equals besides the deterioration of the lubrication conditions in the rolling contact an increase of the bearing load due to the shaft expansion. Regarding the power loss of the bearing the same effect can be seen. Based on these results it would be a logic conclusion to select the initial preload of the bearing arrangement as small as possible. However in the design process other requirements have to be fulfilled. To get a proper load distribution on the tooth flank of the gears a minimum stiffness of the bearing arrangement has to be ensured. Additionally requirements like zero backlash and noise issues have to be considered in the selection process of the bearing initial preload. In the shown calculation example very strict conditions have been chosen in order to emphasise the shown effects. Generally the preload rises with increasing temperature in the X-arrangement implemented in this example. This effect can be diminished by a suitable choice of the housing material. Well selected material characteristics of the housing material like the coefficient of thermal expansion and the modulus of elasticity can reduce the compression of the bearing due to the thermal shaft expansion to a minimum. This is a desirable goal to ensure the reliability of the bearing arrangement. Generally the temperature increase of the bearing can be a self-enforcing effect: the rising preload increases the power loss and therefore the heat development which in turn increase the preload. This process progresses until the thermal equilibrium is reached. The result can be bad lubrication conditions in the rolling contact and a high load state in the bearing, which might reduce the rating life and the efficiency of the bearing application crucially.

In conclusion the calculation example has shown the initial preload and the operating temperature of the bearing as not negligible effects. It has also become clear, that the choice of an appropriate preload has always to be a compromise between the load carrying capacity of the bearing and other design criterions. Consequently a comprehensive approach has to be pursued in order to get reliable and significant results in the design process. Therefore the application of sophisticated software tools is demanded to support a comprehensive and effective design process.

7. Literature Cited

[Bai07] Bair, S.: High Pressure Rheology for Quantitative Elastohydrodynamics. Tribology and Interface Engineering Series, No.54, Elsevier, 2007

[Bjoe11] Björling, M.: Friction in Elasto Hydrodynamically Lubricated contacts - The influence of speed and slide to roll ratio Luleå University of Technology, phd thesis, 2011

[DINISO281] DIN ISO 281 Beibaltt 1:2003-04: Rolling bearings – Dynamic load ratings and rating life – Life modification factor a_{DIN} and calculation of the modified rating life"

[DIN26281] DIN 26281:2010-11: " Rolling bearings – Methods for calculating the modified reference rating life for universally loaded bearings (ISO/TS 16281:2008 + Cor. 1:2009)"

[FVA364 III] Schleich, Th.: „Erweiterung der FVA-Programme RIKOR und LAGER2 zur Bestimmung der Lebensdauer von Wälzlagern in Industriegetrieben", Forschungsvereinigigung Antriebstechnik e.V., Frankfurt/Main, 2011

[FVA388I] Baly, H.; Poll, G.: Reibung fettgeschmierter Wälzlager / Forschungsvorhaben der Forschungsvereinigung Antriebstechnik e.V., Frankfurt/Main, 2005, Forschungsheft Nr. 388

[FVA388II] Meyer, C.: Reibung fettgeschmierter Wälzlager II, / Forschungsvorhaben der Forschungsvereinigung Antriebstechnik e.V., Frankfurt/Main, 2009, Forschungsheft Nr. 388 II

[Goha88] Gohar, R.: Elastohydrodynamics. Ellis Horwood LTD, John Wiley & Sons Inc., New York, 1988

[Harr07] Harris, T. Kotzalas, M.: Advanced Concepts of Bearing Technology, 5 th ed., Taylor&Francis Group, Boca Raton London New York, 2007.

[HEB08] Habchi, W., Eyheramendy, D., Bair, S. Morales-Espejel, G.: Thermal Elastohydrodynamic Lubrication of Point Contacts Using a Newtonian/Generalized Newtonian Lubricant, In: *Tribol Lett* (2008) 30:41–52, DOI 10.1007/s11249-008-9310-9

[HEV08] Habchi, W., Eyheramendy, D., Vergne, P. Morales-Espejel, G.: A Full-System Approach of the Elastohydrodynamic Line/Point Contact Problem, In: *Journal of Tribology* (2008) 130:021501, DOI: 10.1115/1.2842246

[Ioan85] Ioannides, E. and Harris, T.: “A New Fatigue Life Model for Rolling Bearings”, ASME Journal of Tribology, 107, pp. 367-378, 1985

[ISO16281] ISO/TS 16281:2008-06: “Rolling bearings – Methods for calculating the modified reference rating life for universally loaded bearings”

[ISO281] ISO 281:1990-12: “Rolling bearings, dynamic load ratings and rating life”

[John85] Johnson, K. L.: Contact Mechanics. Cambridge University Press, 1985

[LAGER2] Schleich, Th.; „LAGER2 3.1 Programm zur Berechnung von Lagern –Benutzeranleitung- FVA 364III, 2010

[LFP12] Wang, D., Poll, G.: Low Friction Powertrain: Wirkungsgrad optimiertes Getriebe /Forschungsvorhaben der Forschungsvereinigung Verbrennungskraftmaschinen e.V., Frankfurt/Main, 2012, Abschlussbericht

[Lun47] Lundberg, G. and Palmgren, A.: „Dynamic Capacity of Rolling Bearings“, Acta Polytech. Scand., Mechanical Engineering. Series 1(3), pp.1-52, 1947

[Lun52] Lundberg, G. and Palmgren, A.: „Dynamic Capacity of Rolling Bearings“, Acta Polytech. Scand., Mechanical Engineering. Series 2(4), pp 96-127, 1952

[Mor15] Morales-Espejel, G. E., Gabelli, A., de Vries, A. J. C.: „A Model for Rolling Bearing Life with Surface and Subsurface Survival and Tribological Effects“ Tribology Transactions (5 Vol.58), pp. 894-906, 2015´

[Pal57] Palmgren, A.: Neue Untersuchungen über Energieverluste in Wälzlagern. In: VDI-Berichte Band 20 (1957)

[RIKOR] Stiller, S.: “RIKOR J 1.0.0 – Erweiterung Ritzelkorrekturprogramm (RIKOR) zur Bestimmung von Stirnradgetrieben”, FVA-Heft 1077, 2013

[Sad09] F. Sadeghi, B. Jalalhmadi, T. S. Slack, N. Raja and N. K. Arakere: “A Review of Rolling Contact Fatigue”, Journal for Tribology (Vol. 131), 2009

[SKF14] SKF:Hauptkatalog. SKF GmbH, 2014

[Stei95] Steinert, T.: Das Reibmoment von Kugellagern mit bordgeführtem Käfig, RWTH Aachen, Diss., 1995

[Than15] Than, Van-The and Huang, Jin H.: Nonlinear Thermal Effects on High-Speed Spindle Bearings Subjected to Preload”, Tribology International, 2015

[Tudo16] Tudose, L., Rusu, F., Tudose, C.: “Optimal design under uncertainty of bearing arrangements”, Mechanism and Machine Theory 98, pp. 164-179, 2016

[Xiao16] Xiaohu, L., Huanfeng, L., Yanfei, Z., Jun, H.: “Investigations of non-uniform preload on the static and roational performance for spindle bearing system”, 2016

[Wang15] Wang, D.: Berechnung der Wälzlagerreibung aufgrund weiterentwickelter rheologischer Fluidmodelle. (*Calculation of bearing friction based on further developed rheological fluid models*), Dissertation, IMKT, Hannover, 2015

[Wei39] Weibull, W.:”A Statistical Theory of the Strength of Materials”, Generalstabens Litografiska Anstalts Förlag Stockholm, 1939

[Wit13] Wittek, E.: Tribologisches Verhalten neuartiger Fuel Economy Öle in Wälzlagern/Forschungsvorhaben der Forschungsvereingigung Antriebstechnik e.V., Frankfurt/2013, Forschungsheft Nr. 619

Development and certification of rotor main bearings for multi MW wind turbine generators

Dr. Ing. Bernd Lüneburg, thyssenkrupp Rothe Erde GmbH, Lippstadt

Dr. Ing. Daniel Becker, thyssenkrupp Rothe Erde GmbH, Lippstadt

Dipl.-Ing. Rainer Grzybowski, DNV - GL, Renewables Certification, Hamburg

Summary

Wind turbine generators (WT) and their related main bearings have to ensure highest availability and reliability. These bearings have to withstand changing dynamic and high static loads under demanding environmental conditions. National and international standardization and classification societies like DNV GL have developed and published standards and guidelines. WT satisfying these requirements can be regarded as a fail-safe. Standards, which have been developed internationally are often modified for national application or are even expanded. This also applies to the bearing guidelines.

At international level the determination of the dynamic load capacity and the basic rating life of rolling bearings are described in ISO/TS 16281. This has been transferred to DIN 26281 and DIN ISO 281 for the determination of the nominal lifetime. In 2010 the "Guideline for the Certification of Wind Turbines" was published by the Germanischer Lloyd (GL). In 2012, a new edition of Offshore Guideline for wind turbines has been published on this basis. For bearing design of WT the GL guideline references to the DIN ISO standards. These standards and guidelines describe the general requirements for main bearings.

Within this publication a comparative study on different fatigue life time determination procedures is presented [17]. The analyses are carried out for a three-row roller bearing and a tapered roller bearing of same cross section. The load distributions of both bearing types are comparable whereas the three-row roller bearing reveals a significant lower max. contact pressure in the raceway system than the taper roller bearing design. The estimated lifetime values in accordance with DIN 26281 are compared to the results of multi-axial local strain and stress based approaches based on “Fatemi - Socie” [10], [11] and “Dang-Van” [8], [9].

Strictly applying DIN 26281 respectively ISO/TS 16281 standard, which gives different calculation procedures dependent on the individual contact angle of the raceway system, the estimated lifetimes of the raceway systems are significant different for both bearing types. For the three-row roller design, the estimated lifetime is about 17% less than the corresponding value for the taper roller bearing. The review of the lifetimes based on multi-axial local and stress based approaches show a reversed picture.

Both the fatigue analysis based on Dang-Van and the concept based on Fatemi-Socie reveal a significant lower cyclic loading of the raceway system and hence an increase in service life for the three-row roller bearing. Furthermore, material and production-related influencing factors are insufficiently considered performing a lifetime rating based on DIN 26281 respectively DIN ISO 281. Especially the compressive residual stresses induced by the surface hardening process may significantly increase the strength durability of the material in and below the contact surface of the rolling contact. From this point, a decrease in sensitivity to imperfections such as predamage, material inclusions and wear debris induced fatigue is expected. This leads to a lower probability of failure and an increase in service lifetime.

A conclusion of the analyses performed is, that especially for large-sized diameter rotor main bearings used as “momentum bearings” a rating based on local stress respectively strain based concepts may lead to more realistic results than the standard DIN ISO 281 respectively DIN 26281 approach.

Up to now, these results achieved have not been taken in account in the above-mentioned guidelines for the certification of rotor main bearings.

The intention of this paper is to form the base for a discussion about an extension of these guidelines focusing on advanced, physically based concepts rating the lifetime of raceway systems taking into account bearing-specific material properties, manufacturing processes and load situation.

1. Introduction and task description

1.1 Introduction

Slewing bearings designed as a three-row roller or taper roller bearings (see Figure 1), are commonly used for rotor main bearing application. The stationary and rotating rings of these bearings should be bolted to the companion structures in order to ensure safe force and momentum transmission and wear-free operation over the total lifetime of the wind turbine generator. Forces and moments generated by the blades and the hub of wind turbine generators are transmitted from the rotating main shaft to the stationary components by a single bearing, a so-called “momentum bearings” (Figure 1).

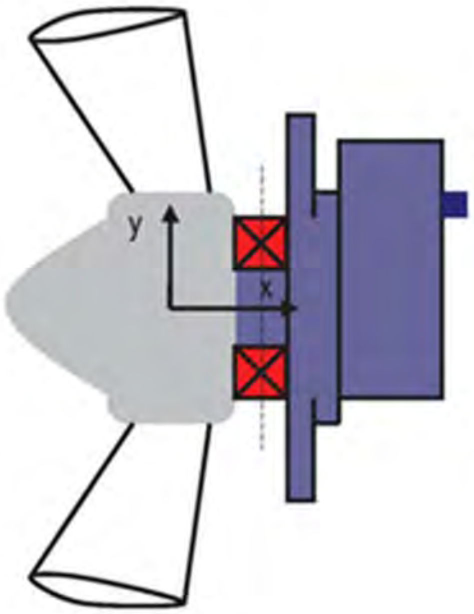

Figure 1: Rotor main bearing designed as momentum bearing [18]

Rotor main bearings are highly dynamic stressed components, which are exposed to a wide range of severe operating conditions in the field. Therefore, and due to their size, the rotor bearings designed as “momentum bearings” are specially designed for use in wind energy application. Figure 2 shows a taper and a three row roller bearing of multi- MW wind turbines.

Figure 2: Taper roller (left) and three row roller bearing (right) of multi- MW wind turbine, thyssenkrupp Rothe Erde GmbH

In Figure 3, the limits and criteria of load capacities for roller bearings are shown in general. In addition to the well known standard fatigue limit according to ISO 281 respectively ISO/TS 16281, other factors which have currently not been taken into account in standardized calculation methods and rules can limit the range of application and reduce the service lifetime.

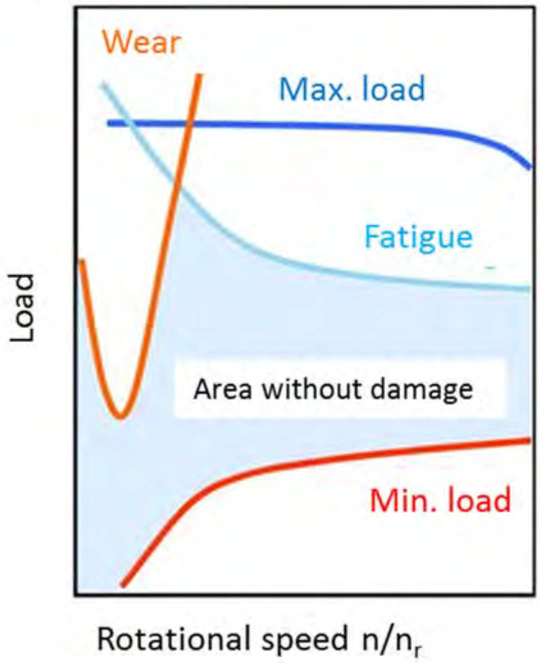

In addition to that,

- micropittings
- wear marks induced by full or partial slip
- early failure induced by White Etching Cracks (WEC)

may also limit the service lifetime of roller bearings.

Figure 3: Range of application for roller bearings [15]

The guidelines DIN ISO 281 and DIN 26281 are an - in industry and research - widely used set of rules used for the dimensioning of bearings regarding fatigue life. Depending on the geometry of the bearing and the geometric nominal contact angle of the rolling element, a numerical procedure rating the radial respectively axial bearing capacity is given.

As part of the certification of the rotor main bearing, the rating of the raceway lifetime in accordance with DIN 26281 is required. The rated lifetime of the raceway system must exceed the design lifetime of the wind turbine generators (WT). Furthermore, the contact pressure between raceway and rolling element should be as low as possible and must not exceed certain values.

For the development and design of main bearings, loads are required. Global rotor loads are transferred by use of classification methods in load spectra. Here, the temporal relation of the individual load components is lost. By superimposing the individual load components, it is generally possible to generate load data for rotor main bearing application. However, based on more accurate design loads, a more realistic and reliable design of the component can be achieved.

For the design and hence for the certification, it is important that the global loads are fully taken into account in order to capture the external loads acting on the main bearing as accurately as possible. A typical load frequency distribution of wind turbines with load bins in the full and partial load ranges for an average wind speed of 7.5 m / s is shown in Figure 4.

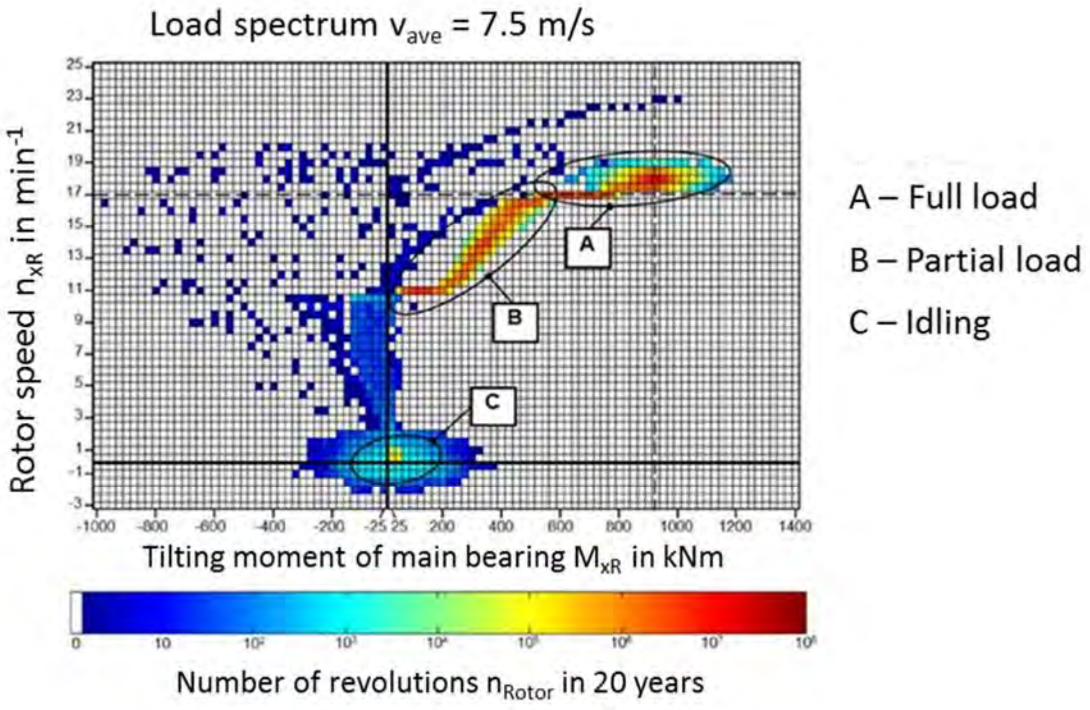

Figure 4: Load / frequency distribution for wind turbine generators [15]

1.2 Task description

According to DIN 26281, the raceway lifetime of a three-row roller bearing under momentum load conditions is rated differently from that of a taper roller bearing. The rating is dependent on the nominal contact angle of the raceway system. This leads to a difference between the axial and radial rating which is hardly applicable to a three-row roller bearing under momentum load conditions.

Figure 5 exemplarily shows the contact pressure over the entire circumference of the maximum loaded raceway for a taper-roller and a three row roller main bearing. Both bearings are identically loaded by momentum load. Due to the differences in the bearing-internal load distribution, the FE-results for the three row-roller bearing conclude a significant lower contact load. In contrast to this the rating strictly following DIN 26281 reveals an increased lifetime for the taper-roller bearing even though the individual contact load is higher.

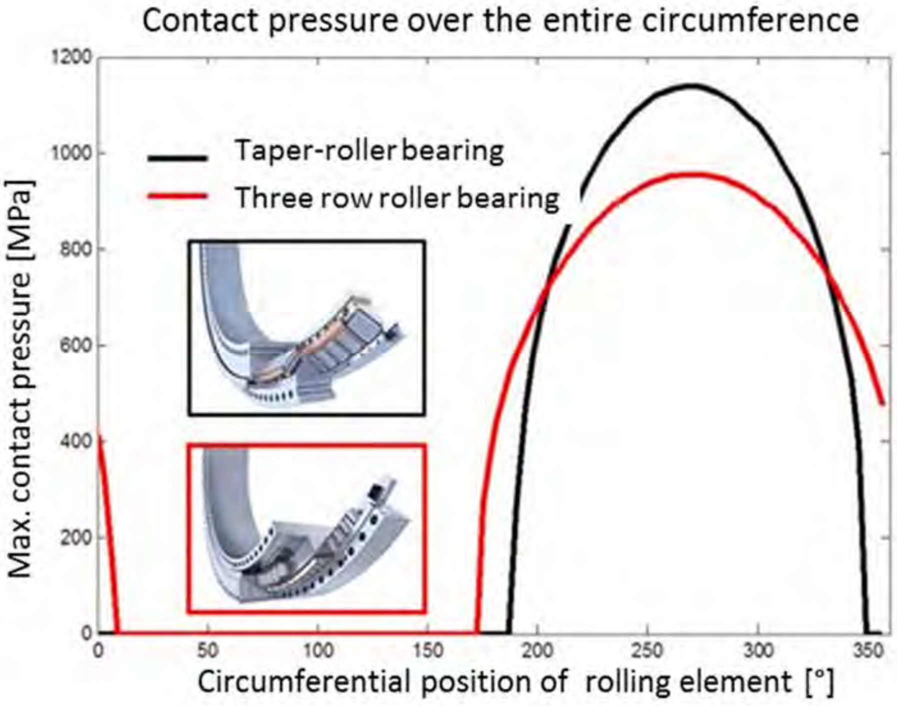

Figure 5: Contact pressure and load distribution for a rotor main bearing of taper roller and three-row roller type under identical momentum load conditions,

In the guidelines for the certification of wind turbines [16] the minimum requirements (life and static safety) are given. However, in many cases rotor main bearings are designed only according to the criterion of the "nominal torque". The different load situation of a main bearing given in Figure 4, namely full load, partial load and idling are rarely considered.

In addition to that, the realistic assessment of loads acting on the rotor main bearing are important for its design. One fundamental requirement for a reliable determination of these load components is an adequate data base for the model generation and the validation of the simulation model itself. The partial safety factors defined in standards and guidelines capture some of these uncertainties. In the future, an even higher accuracy can be expected in determining and predicting the rotor main bearing loads, so that -already now- revising the rules and guidelines, strategies to reduce the partial safety factors are in discussion. This will finally lead to a more economic design process in the future.

2. Concept

In a first step, studies on methods for the lifetime rating of highly loaded main bearing of multi-megawatt wind turbines are performed on the basis of DIN ISO 281 and DIN 26281. For this, a main bearing of a multi-megawatt wind turbine is designed both as three-row roller bearing as well as tapered roller bearing (Figure 5). Considering the standard DIN ISO profiling of the rolling element as well as the misalignment between rolling element and raceway system, the lifetime of the raceway system according to DIN 26281 is rated based on the so called lamina approach. Both main bearing types are of identical dimensions and loaded by the same load condition.

For the studies, a high-resolution, numerical 2D contact model [1, 4] is used. The bearing internal load distribution is assessed based on [2, 3]. In order to eliminate the impact of the companion structures on the performance of the raceway system, the numerical FE-analyses are carried out under the assumption of a hub- respectively bladeside rigid support in this particular case. The current state of numerical simulation tools allows more and more the detailed assessment of the bearing internal load distribution. This ensures that the rotor main bearing is not considered as a mechanically isolated component, but as a part of the entire drive train of the wind turbine generator. This is also considered as one requirement for the certification of wind turbines.

In a second step, for both main bearing designs a comparative assessment of the loading of the individual rolling contact based on the stress-based Dang Van [8], [9] as well as on strain-based Fatemi-Socie concept [1], [10], [11] is performed. Figure 6 shows the different concepts in comparison to DIN ISO 281 respectively DIN 26281.

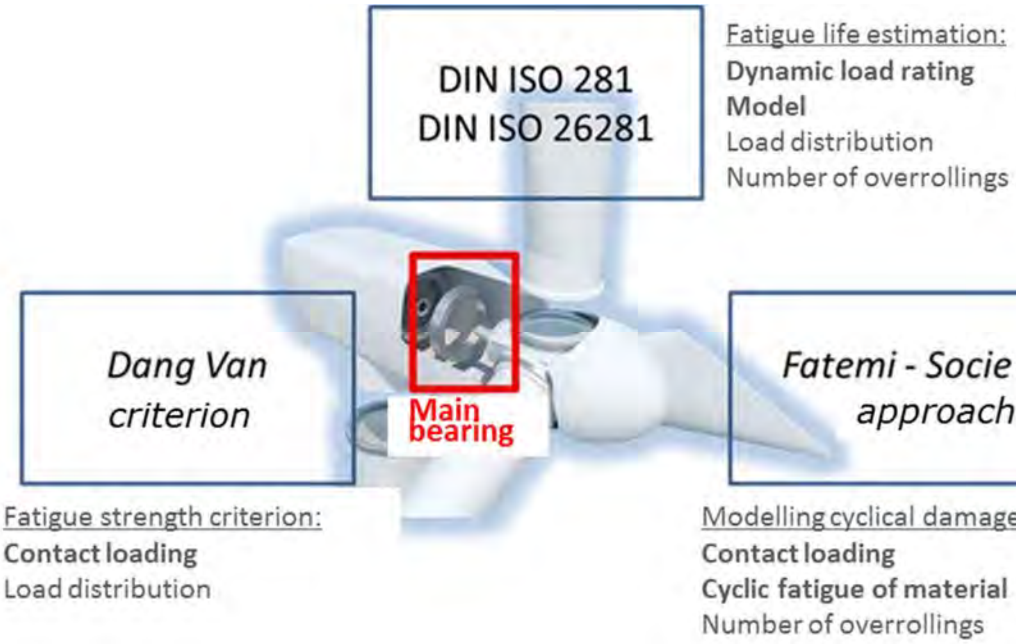

Figure 6: Different concepts used rating the lifetime of the raceway system of main bearings in wind energy application

DIN ISO 281 respectively DIN 26281 allows the assessment of the lifetime of the raceway system based on bearing-design dependent load ratings and implicit assumptions regarding the bearing internal load distribution. In contrast to that the concepts based on Dang Van and Fatemi-Socie take into account the pressure distribution of the individual rolling element as well as cyclic material properties and depth-dependent residual stresses.

2.1 Numerical simulation of contact loading taking crowning of rolling element and misalignment between rolling element and raceway into account

In case of line contact between rolling element and raceway system, the crowning of the rolling element (shape, depth) strongly impacts the load carrying characteristics of the individual rolling element under full as well as under partial load conditions [1], [2], [3]. For a realistic and runtime efficient simulation of the non-linear contact problem, the implementation of a numerical 2d- contact algorithm is mandatory [1]. Within the computational program system REBA (Rothe Erde Bearing Analysis [1], [2]), this task is solved.

Rothe Erde Bearing Analysis (REBA) is an integrated FEM based program system for the economic design of large diameter ball and roller bearings. This highly accurate program system models the performance of large diameter bearings and ensures that the bearing meets the demanding technical requirements under the operating conditions. Figure 7 exemplarily shows the program modules used for the FE ($REBA_{FE}$) as well as for the fatigue (RE_{Life}) and contact mechanical analyses ($RE_{Contact}$) of bearing components.

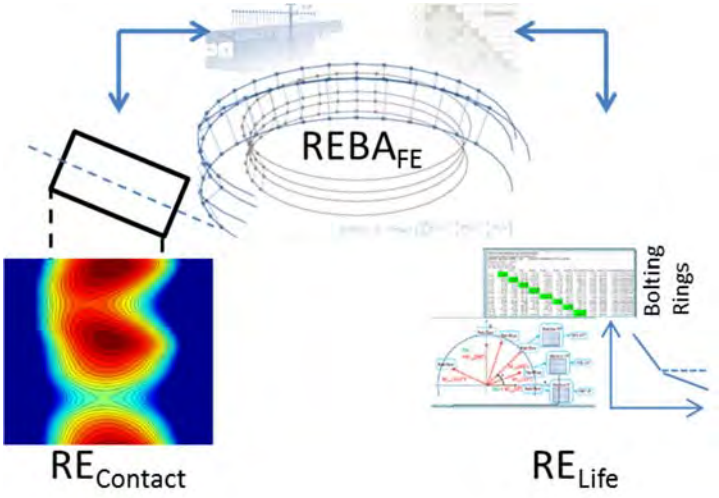

Figure 7: Program system REBA, [2]

Unlike analytical contact solutions, numerical approaches for the contact between rolling element and raceway offer a significant higher degree of discretization of the contact region. The elastic deformation due to normal load, shear load and temperature is modelled. The external contact force and the resulting pressure build-up in the load-carrying contact region are balanced [1]. Consequently, "dry" contact conditions (that means non-EHL contact conditions) have been applied. Recent investigations [1] have concluded that the loading of the contact especially in the highly stresses contact area is less influenced by elastohydrodynamic-specific effects (viscosity etc.).

For comparison purpose, Figure 8 and 9 show results of a contact simulation performed based on the commercial FE-software ABAQUS and based on the computational program system REBA.

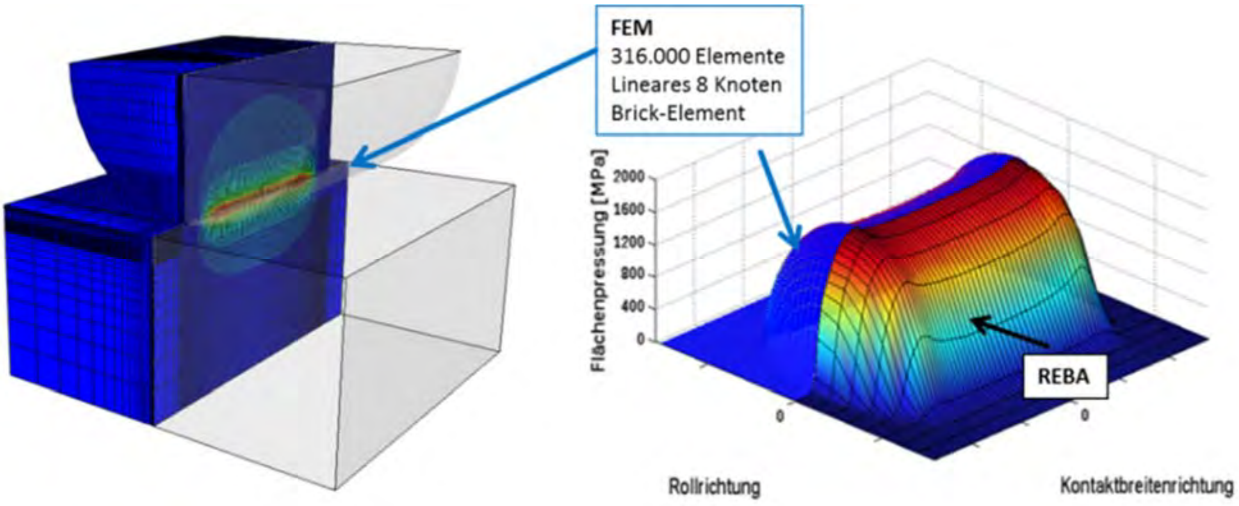

Figure 8: ABAQUS FE-model (left) and comparison of ABAQUS / REBA results (right)

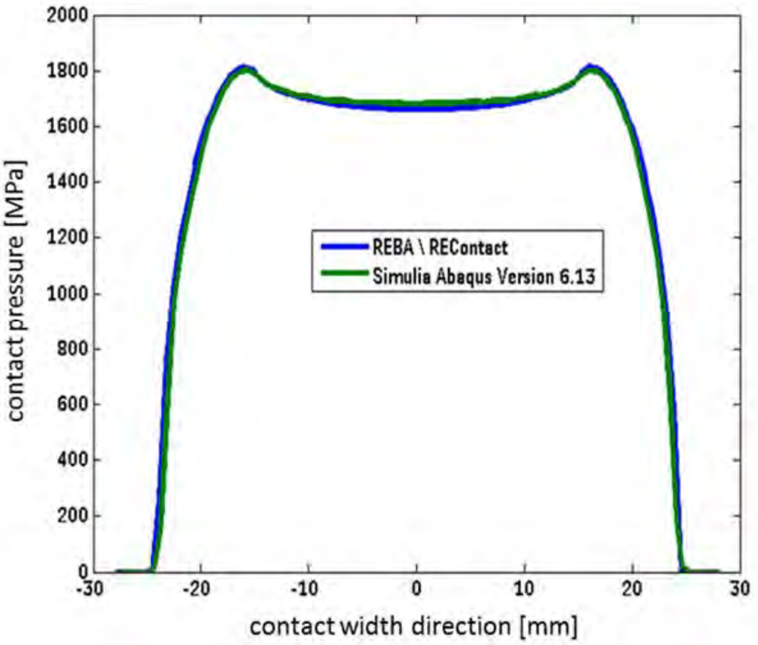

Figure 9: Comparison of ABAQUS and REBA results shown for a path in contact width direction of the rolling element

The lifetime of the raceway system is rated in accordance to DIN 26281 using the so called lamina approach [3], [12]. This includes the numerical contact analyses taking into account the individual profiling and misalignment of the rolling element. Based on DIN 26281 a number of laminas ns ≥ 30 is applied. The contact force per lamina is assessed by integrating the contact pressure in rolling direction per individual lamina. Doing so, the use of analytical stress raising functions whose application is often limited is not required.

3. Rating of the raceway system according to DIN 26281

Usually, the maximum contact pressure in the raceway system and the lifetime are used for the assessment of the performance of the raceway system of rotor main bearings. Different rating approaches are available:

- Nominal lifetime L_{10} according to DIN ISO 281 [13]
- Extended or modified lifetime L_{10nm} based on DIN ISO 281
- Nominal lifetime L_{10r} according to DIN 26281 [12]
- Extended or modified lifetime $L10_{nmr}$ based on DIN 26281

In most of the cases, the modified lifetime L_{10nmr} taking into account profiling, misalignment and lubricant conditions is used [3]. In order to get the loading of the individual lamina over the entire circumference of the raceway system, the contact area is discretized by use of a 2D- contact model [1]. Lubricant conditions are taken into account based on the a_{iso} factor.

Figure 10 exemplarily shows the loading of the upwind raceway system of a taper roller main bearing taking customer-specific boundary conditions of the companion structures into account Based on the 2D contact algorithm, a detailed view of the loading of the raceway system can be achieved. The six o'clock DOWN position of the rotor is indicated. The impact of the misalignment between rolling element and raceway system is shown.

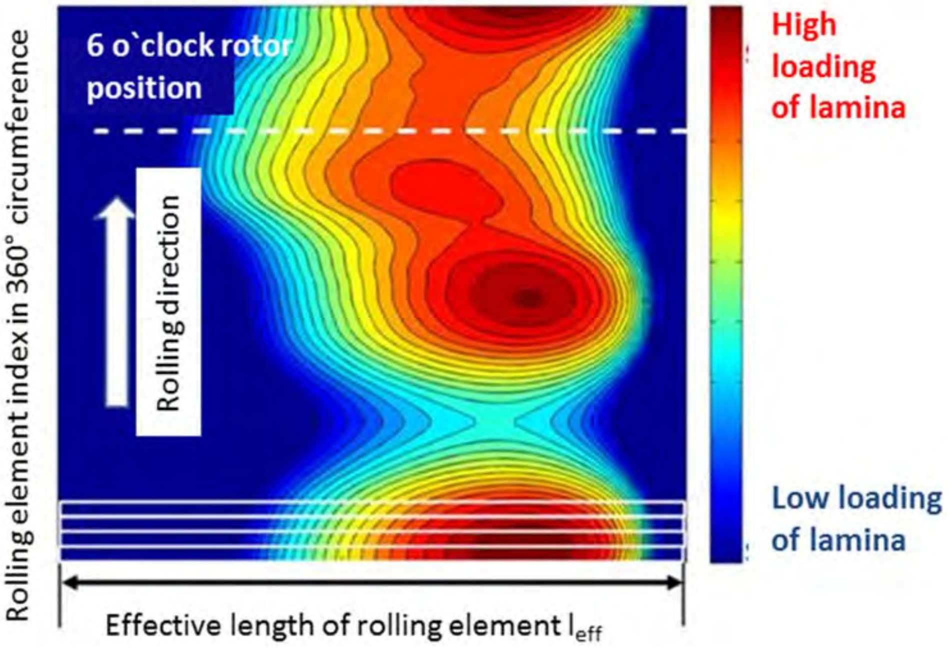

Figure 10: REBA simulation results: Loading of raceway system, upwind supporting raceway of rotor main bearing (taper roller bearing)

3.1 Stress-based fatigue endurance criteria based on Dang Van

By use of the so called Dang Van criteria [8] [9], the local cyclic loading of the rolling contact due to overrollings can be evaluated in terms of fatigue endurance. The Dang Van criterion is a stress-based fatigue endurance criteria used for multiaxial, non proportional stress situation. The Dang Van criterion defines an equivalent stress level dependent on the loading, which is finally compared with a material-dependent shear fatigue strength in order to assess the fatigue endurance.

Figure 11 schematically shows the Dang Van criterion with the boundary lines for the original and the modified model and the formula deriving the local Dang Van damage factor $n_{DV,original}$ dependent on the local hydrostatic pressure σ_{h}. For the investigations carried out within this work, the Dang Van damage factor $n_{DV,original}$ is taken into consideration. The orthogonal shear stress $\tau_{\mathrm{orthogonal}}$ is used. Table 1 gives additional explanations about the parameter of the Dang Van criteria.

Table 1: Parameter and description of Dang Van criteria

Parameter	Description
$n_{DVoriginal}$ respect. $_{modified}$	Dang Van damage factor
$\tau_{orthogonal}$	Orthogonal shear stress (in general: fluctuation of the shear stress from its mid value during a stress cycle)
α_{DV}	Material parameter
σ_h	Hydrostatic stress
τ_{endur}	Alternating shear endurance limit

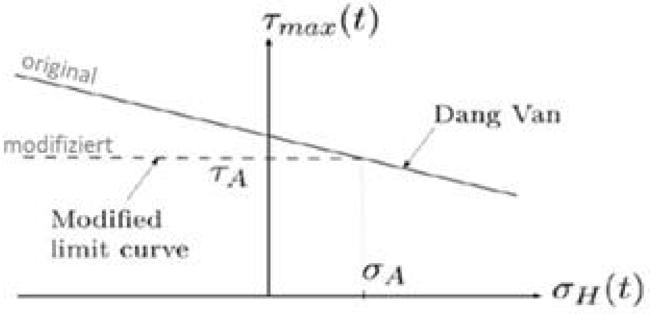

Dang Van damage factor n

$$n_{DV,original} = \frac{\tau_{orthogonal}}{\tau_{endur} - \alpha_{DV} * \sigma_h}$$

Figure 11: Dang Van criteria [8]

Figure 12 shows the endurance limit of the rolling contact dependent on the contact pressure determined based on the Dang Van criteria. The analyses are carried out for through-hardened standard bearing material without residual stresses and a shear fatigue strength of 360 MPa according to [8] and for a material with inductive surface hardening including residual stresses. Furthermore, the friction coefficient assuming friction conditions according to [1] is varied.

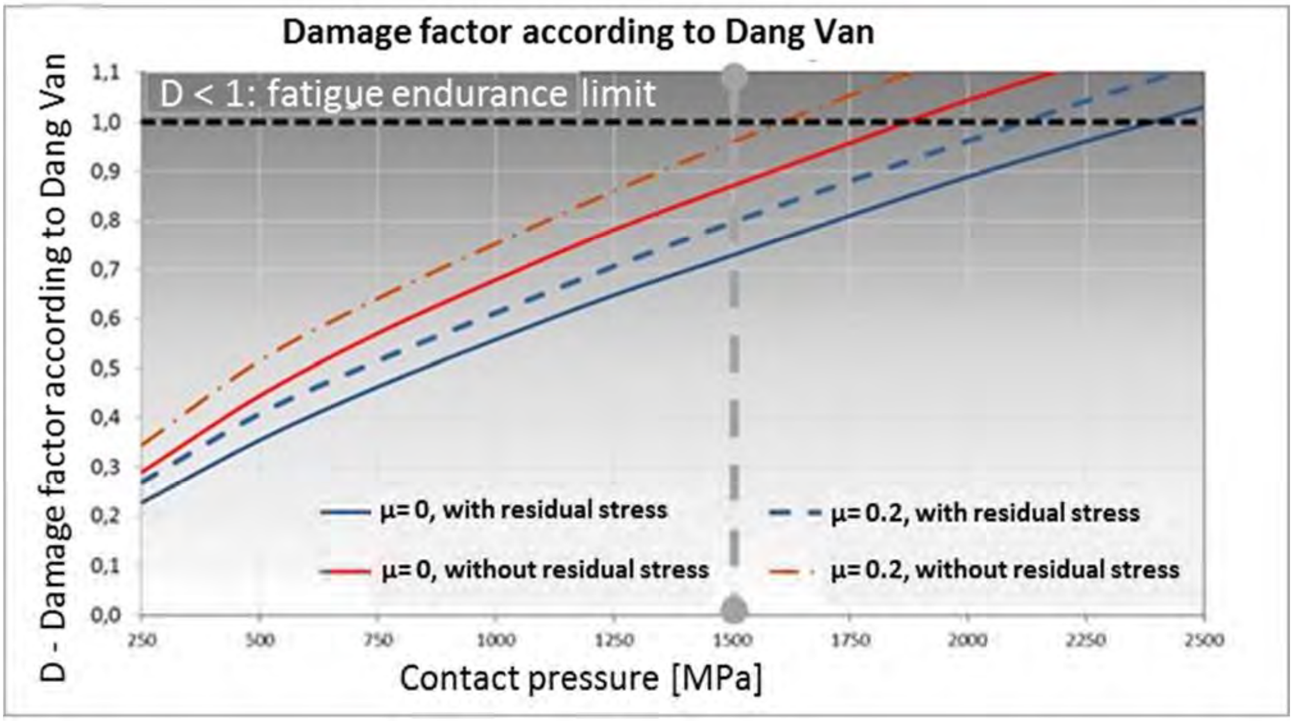

Figure 12: Calculation results based on Dang Van criterion compared with the fatigue endurance limit of approx. 1500 MPa given in DIN ISO 281

One result of these analyses is that the resistance of rolling contact towards fatigue can significantly be increased by compressive residuals stresses e.g. induced by inductive surface hardening. From this point, it can be expected that the sensitivity to imperfections such as predamage, material inclusions and wear debris inducing rolling fatigue is decreased. This finally leads to a lower probability of failure and an increase in service life of the main bearing (see also [7]). Furthermore, experiences made so far indicate that the failure / failure probability against White Etching Cracks can significantly be reduced or even avoided by use of induction hardened raceway systems.

3.2 Strain-based fatigue criteria based on Fatemi-Socie

For a quantitative evaluation of cyclic fatigue processes in rolling contact, the use of local fatigue concepts as on the basis of a Critical Plane (CP) approach is useful [1]. In case of rolling contacts, the mechanism of crack initiation is typically initiated by alternating shear stresses. Therefore, in the past the orthogonal shear stress has widely been used assessing the fatigue behavior of rolling contacts. Based on Miller and Brown's Critical Plane approach, Fatemi and Socie propose a modification to predict multiaxial life under non-proportional, out -of phase loading conditions. This model takes the maximum shear strain amplitude and the maximum normal stress on the maximum shear strain amplitude plane - correspondent to the fatigue critical slip band - into account. This approach justifies the assumption that fatigue initiation process is predominantly controlled by the maximum shear strain. The normal strain on the maximum shear plane is considered to be the second parameter involved in the fatigue damage process (crack propagation). The cyclic stress-strain curve is given based on the work of Ramberg-Osgood respectively Basquin (elastic) and Coffin, Manson and Morrow (plastic) as follows [1, 10]:

$$\varepsilon_{at} = \varepsilon_{ae} + \varepsilon_{ap} = \frac{\sigma_a}{E} + \left(\frac{\sigma_a}{K'}\right)^{\frac{1}{n'}} = \frac{\sigma'_f}{E}\left(2 \cdot N_f\right)^b + \varepsilon'_f\left(2 \cdot N_f\right)^c$$

For shear stresses, the corresponding derivation as given above leads to:

$$\gamma_{at} = \gamma_{ae} + \gamma_{ap} = \frac{\tau_a}{G} + \left(\frac{\tau_a}{K'_\gamma}\right)^{\frac{1}{n'\gamma}} = \frac{\tau'_f}{G}\left(2 \cdot N_f\right)^{b\gamma} + \gamma'_f\left(2 \cdot N_f\right)^{c\gamma}$$

Based on this approach modelling the cyclic stress resistance, Fatemi and Socie developed a so called damage parameter [10], [11] dependent on the max shear strain amplitude $\gamma_{\max}$, the corresponding max. normal stress $\sigma_{N,\max}$, the yield strength σ_y and a constant k_e found by fitting uniaxial data against the pure torsion results. Combining this approach with the strain-life respectively shear-life relation, the following equation can be found:

$$\gamma_{\max}\left(1 + k_e \cdot \frac{\sigma_{n,\max}}{\sigma_y}\right) = \frac{\tau'_f}{G}\left(2 \cdot N_f\right)^{b\gamma} + \gamma'_f\left(2 \cdot N_f\right)^{c\gamma}$$

Table 2: Parameter and description of Fatemi - Socie criteria

Parameter	Description
b	fatigue strength exponent
c	fatigue ductility exponent
N_f	cycles to failure
γ_{max}	maximum shear strain
k_e	constant (uniaxial data , pure torsion data)
$\sigma_{n,max}$	maximum normal stress during cycle
σ_y	yield strength
$\tau_f{}'$	cyclic shear strength coefficient
G	modulus of rigidity
γ'_f	coefficient of ductility

The mathematical form of this approach reflects the assumption that normal stresses only contribute to the fatigue damage if there is shear strain acting on the plane. Thus, no damage accumulation is predicted since the value of shear stress strain is zero.

The Critical Plane model proposed therefore applies to loading conditions producing shear failure mode - corresponding to the widely used assumptions in rolling contact fatigue focusing on the alternating orthogonal shear stress.

In [1] and [4] the application of this concept proposed by Fatemi-Socie is done in order to simulate the frictional contact conditions in highly loaded blade bearings of wind turbine generators. Within the framework of this work, this approach is extended taking into account the fatigue damage induced by overrolling. Here, for the cyclically stressed volume in and below the raceway surface, the damage-relevant shear strain amplitude and the maximum normal stress are evaluated on the Critical Plane.

The transient load conditions for an individual volume element in and below the contact surface of the raceway system are assessed based on the results of the steady-state 2d contact simulation [1]. Figure 13 schematically shows this approach deriving the transient load conditions.

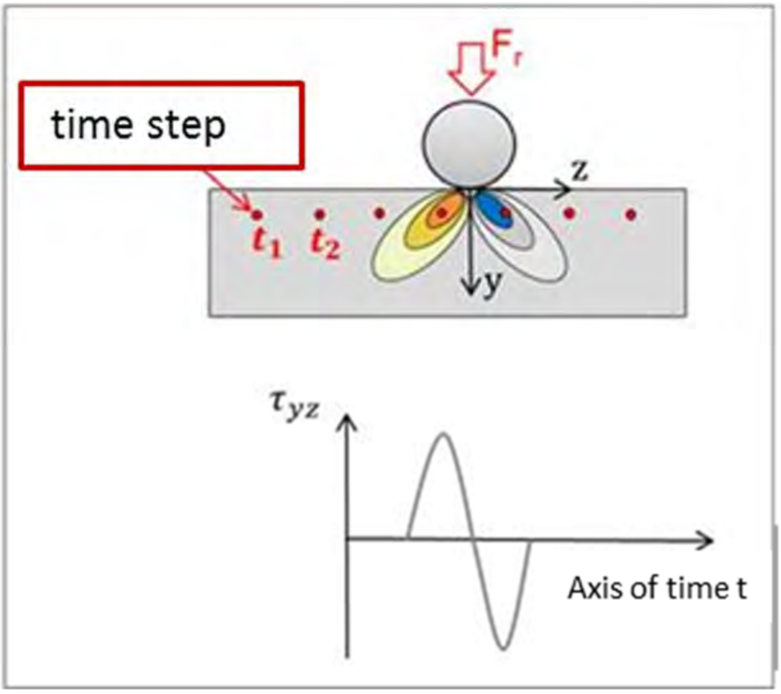

Figure 13: local modelling of the time dependent over-rolling mechanism

Figure 14 shows a comparison of calculation results between the program system REBA and the commercial FE-tool ABQUS.

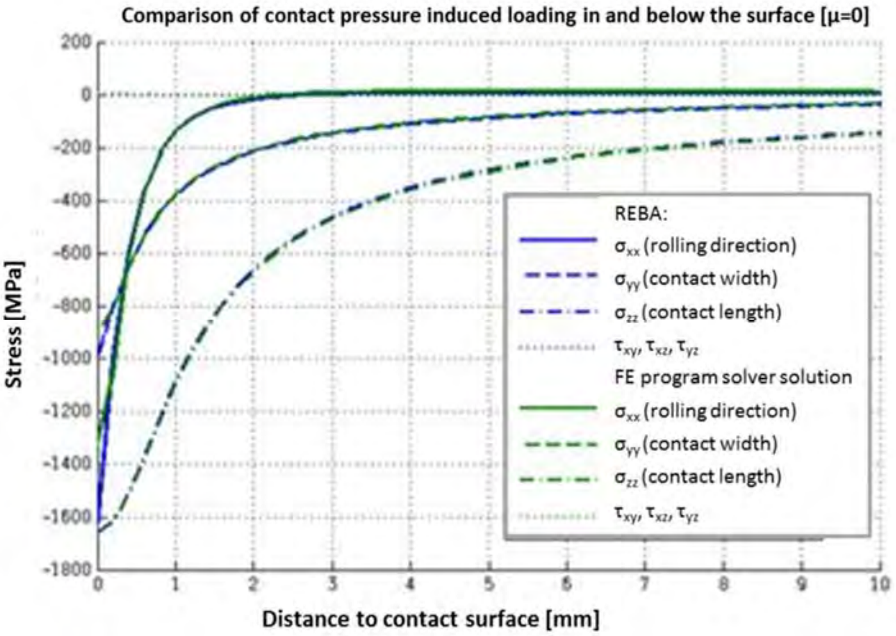

Figure 14: Comparison of calculated stresses of different procedures

Differences between REBA and the FE program solver solution on the contact surface are due to different assumptions of the numerical procedures regarding the application of shear stresses.

Figure 15 shows a comparison of S/N curves of literature, of tests and theoretically determined according to Fatemi-Socie. Experimental tests are carried out at thyssenkrupp Rothe Erde R&D with 42CrMo4 washers inductive surface hardened. The calculations have been performed taking the residual stresses as well as the core- respectively case-dependent cyclic material properties into account [6].

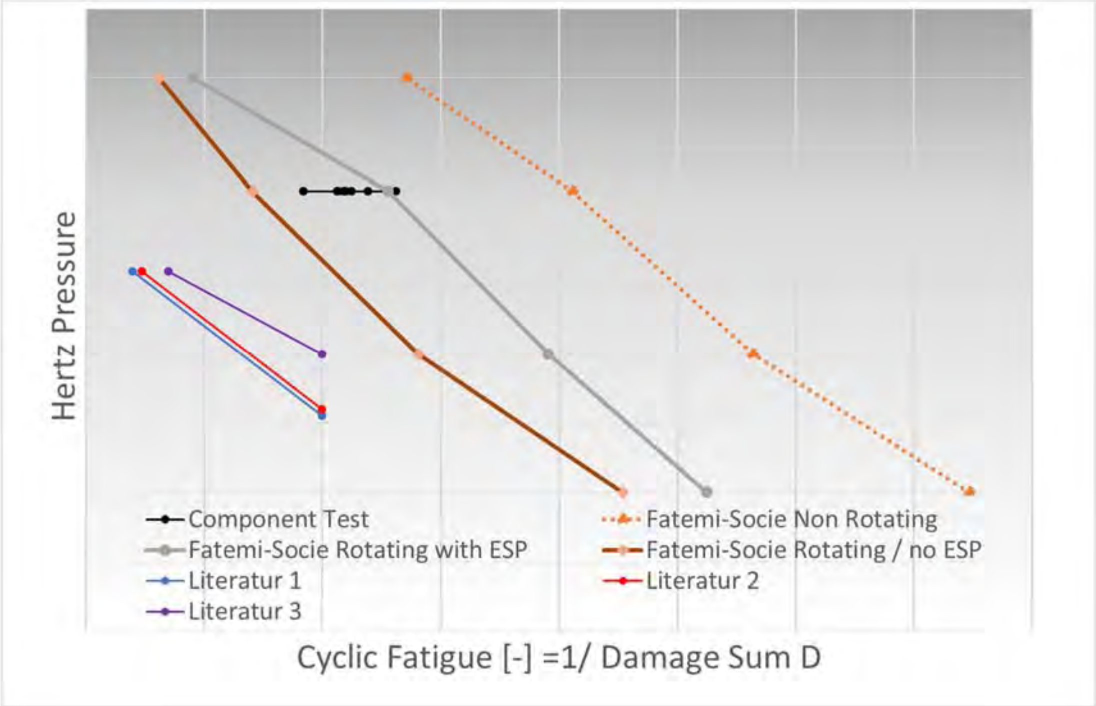

Figure 15: FE-8 test rig and literature results in comparison to simulation output based on the Fatemi-Socie approach

4 Results rotor main bearing

The theoretical analysis of the two different bearing types have been performed based on the same loads, no bearing internal play, the same number of rollers in each raceway and a stiff modelling of rings and companion structures. These assumptions allow a better comparison of the different lifetime rating procedures rather than an accurate determination of WT design specific physical phenomena. The determined load distributions are similar. However, the three row roller bearing show a lower maximum contact pressure than the taper roller bearing.

The DIN 26281 procedure taking into account a realistic set of load bins corresponding to 20 years of operation leads to a 17% lower lifetime of the three-row roller bearing. The evaluation of the lifetimes of both examined types of bearings on the basis of stress- and strain-based valuation models show a reverse result. Both, the fatigue analysis according to “Dang Van” and the lifetime rating according to “Fatemi-Socie”, show a significantly lower cyclic stress and hence a much longer service life for the three-row roller bearing. The contact pressures given in Table 3 represent the max. value of the specific load bin showing the highest duty cycle of all load bins in 20 years of operation.

	3RD DIN ISO 26281 thrust bearing theory Conform to ISO	3RD DIN ISO 26281 radial bearing theory Not conform to ISO	taper roller bearing DIN ISO 26281 radial bearing theory ISO-conform
Max. contact pressure	998 MPa (-12%)	998 MPa (-12%)	1138 MPa (100%)
L_{10r} acc. to DIN ISO	227.983 h (-17%)	632.584 h (+130%)	274.656 h (100%)

Table 3: maximum contact pressure and life time acc. to DIN 26281

An evaluation of the momentum loaded three row roller bearing based on the radial theory of the DIN 26281 lead to an increase of life time of 130% due to the 12% lower maximum contact pressure compared to the taper roller bearing. The evaluation of the bearing life time in accordance to the stress based Dang Van damaging factor also show a significantly lower cyclic fatigue of the three row roller bearing (see Table 4) due to the lower contact pressure. Table 4 summarizes the calculated Dang Van fatigue damaging factors for the highest loaded contact areas of both bearing types.

	3RD	taper roller bearing
max. contact pressure	998 MPa	1138 MPa
max. damaging factor acc. to *“Dang Van”* $n_{DV,original}$	0,60	0,66

Table 4: comparison of maximum contact pressure and fatigue

The damaging factors calculated by the Dang Van procedure are independent on the geometric angles of the bearing design. They only depend on the local contact pressure induced stress distribution and number of load cycles. The higher the induced cyclic fatigue the higher the Dang Van damaging factor is. At a level of 1.0 the fatigue endurance limit is exceeded theoretically.

The calculation procedure of “Fatemi-Socie” is based on the strain-life curve locally induced by the contacting elements determining the cyclic fatigue of the overrunning incidents. The local contact characteristics like roller to raceway misalignment and roller profile can be taken into account. This procedure also allows a simulation and evaluation of depth dependent material compressive stresses. The introduction of high compressive residual stresses by induction surface hardening increases the permissible contact pressure values significantly. Table 5 shows the calculate number of load cycles for the max loaded rolling element. Figure 16 and 17 show the distributions of the calculated local damage sum in contact depth and contact width direction.

	3RD	taper roller bearing
max. contact pressure	998 MPa	1138 MPa
max. number of load cycles N_f	$1{,}1 * 10^{12}$	$2{,}1 * 10^{11}$
damage sum D	$9{,}10 * 10^{-13}$	$4{,}68 * 10^{-12}$

Table 5: Comparison of life time according to the Fatemi-Socie calculation procedure

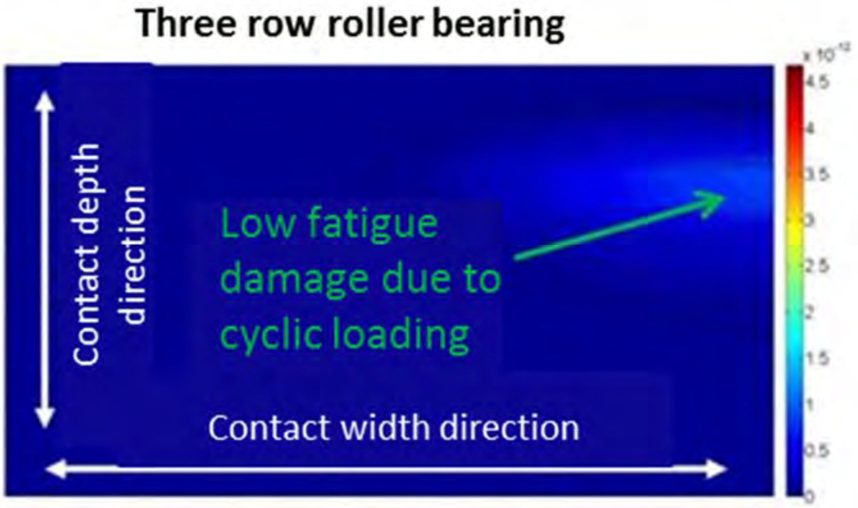

Figure 16: half of contact length - comparison of the cyclic damage sum for the three row roller bearing, see table 5

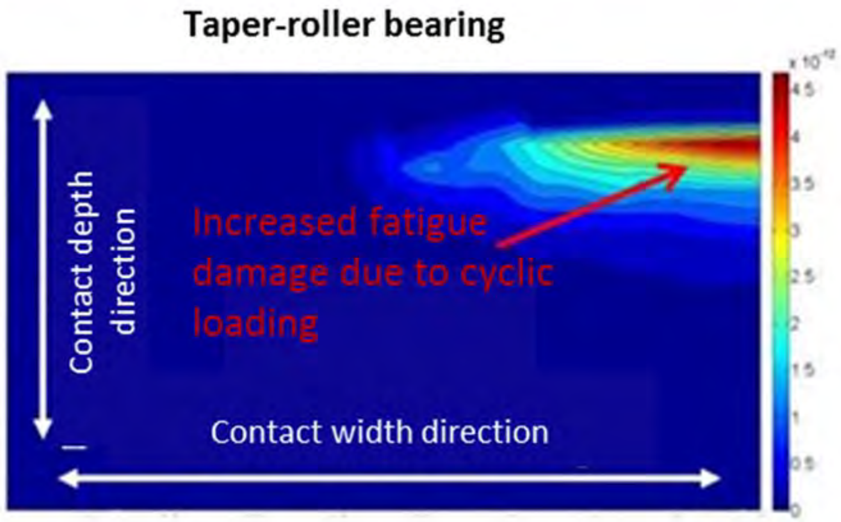

Figure 17: half of contact length - comparison of the cyclic damage sum for the taper roller bearing, see table 5

5. Summary

Within this publication a comparative study on different fatigue life time determination procedures is presented. The analyzes are carried out for a three-row roller bearing and a tapered roller bearing of same cross section. The load distributions of both bearing types are comparable whereas the three-row roller bearing reveals a significant lower maximum contact pressure in the raceway system than the taper roller bearing design. The estimated lifetime values in accordance with DIN 26281 are compared to the results of multi-axial local strain and stress based approaches based on “Fatemi-Socie” [10], [11] and “Dang-Van” [8], [9].

Strictly applying DIN 26281 respectively ISO/TS 16281 standard, which gives different calculation procedures dependent on the individual contact angle of the raceway system, the estimated lifetimes of the raceway systems are significant different for both bearing types. For the three-row roller design, the estimated lifetime is about 17% less than the corresponding value for the taper roller bearing. The review of the lifetimes based on multi-axial local and stress based approaches show a reversed picture.

Both the fatigue analysis based on Dang-Van and the concept based on Fatemi- Socie reveal a significant lower cyclic loading of the raceway system and hence an increase in service life for the three-row roller bearing. Furthermore, material and production-related influencing factors are insufficiently considered performing a lifetime rating based on DIN 26281 respectively DIN ISO 281. Especially the compressive residual stresses induced by the surface hardening process may significantly increase the strength durability of the material in and below the contact surface of the rolling contact. From this point, a decrease in sensitivity to imperfections such as pre-damage, material inclusions and wear debris induced fatigue is expected. This leads to a lower probability of failure and an increase in service lifetime.

A conclusion of the analyses performed is, that especially for large-sized diameter rotor main bearings used as “momentum bearings” a rating based on local stress respectively strain based concepts may lead to more realistic results than the standard DIN ISO 281 respectively DIN 26281 approach.

Up to now, these results achieved have not been taken in account in the above-mentioned guidelines for the certification of rotor main bearings. The intention of this paper is to form the base for a discussion about an extension of these guidelines focusing on advanced, physically based concepts rating the lifetime of raceway systems taking into account bearing-specific material properties, manufacturing processes and load situation.

6. Literature

[1] Becker, D.: Hoch belastete Großwälzlagerungen in Windenergieanlagen, Dissertation Institut für Tribologie und Energiewandlungsmaschinen ITR, TU Clausthal, 2011

[2] Handreck, T; Becker, D.; Rollmann, J.; Lüneburg, B.: Determining the characteristics of large diameter ball and roller bearings, Conference for Wind Power Drives, Aachen, 2015

[3] Becker, D.; Handreck, T.; Lüneburg, B. et al.: Gekoppelte thermische Finite Element-Analyse und Simulation der Laufbahnbeanspruchung an einem 6 MW Rotorlager, Tribologie und Schmierungstechnik, 62. Jahrgang, 01/2015, Seite 4-12

[4] Becker, D.; Schwarze, H.; Brouwer, L. Schmierfettprüfung für hochbelastete Tribosysteme unter korrosiven Umgebungsbedingungen in Windenergieanlagen und numerische Simulation der Kontaktverhältnisse, Tribologie und Schmierungstechnik, 58. Jahrgang, 01/2011, Seite 5 ff.

[5] Enhanced main bearing performance for Wind Energy Turbine (WET)- applications, M. Burtchen, U. Maschelski, B. Lüneburg, ASTM 10th International Symposium on Advances in Steel Technologies for Rolling Bearings, Toronto / Canada 2014

[6] Rollmann, J.: Wälzfestigkeitseigenschaften induktiv randschichtgehärteter bauteilähnlicher Proben und Bauteile, Dissertation, TU Darmstadt

[7] A. Pabst: Rechnerische und experimentelle Untersuchung des Einflusses von Druckeigenspannungen in Wälzlagerkomponenten und deren Auswirkung auf die Lebensdauer.

[8] Cerullo, M.: Application of Dang Van criterion to rolling contact fatigue in wind turbine roller bearings. 13th International Conference on Fracture, June 16-21, 2013, Beijing, China

[9] Cerullo, M. Proc IMechE Part C: J Engineering Tribology 228(12) (2014) 2079-89

[10] Socie, D. F., Marquis, G. B.: Multiaxial Fatigue, Society of Automotive Engineers SAE, 2000

[11] Fatemi A. and Socie D.F.: Fatigue Fract Engng. Mater. Struct. 11 (1988) 149-165

[12] DIN ISO 26281 Wälzlager – Dynamische Tragzahlen und nominelle Lebensdauer – Berechnung der modifizierten nominellen Referenz-Lebensdauer für Wälzlager

[13] DIN ISO 281 Wälzlager – Dynamische Tragzahlen und nominelle Lebensdauer

[14] Dynamische Tragfähigkeit von Rollenlagern, Lundberg, G.; Palmgren, A.; SKF Vereinigte Kugellagerfabriken Aktiengesellschaft, Schweinfurt 1950

[15] Grzybowski, R.; Steingröver, K.: Anforderungen an zukünftige Hauptgetriebe für Windenergieanlagen aus Sicht der Zertifizierung; DMK 2011; TUDpress, Dresden, 2011

[16] Germanischer Lloyd Industrial Services: Richtlinie für die Zertifizierung von Windenergieanlagen; Germanischer Lloyd, Hamburg, 2010

[17] Lüneburg, B.; Grzybowski, R.: Development and certification of rotor main bearings for multi MW wind turbine generators; International Conference Bearing World, Hannover, 2016

[18] Ristow M.: Konzept zur Lebensdauerberechnung von Rotorlagern an Windenergieanlagen. VDM Verlag, Saarbrücken, 2008

About FVA

The German Research Association for Drive Technology (Forschungsvereinigung Antriebstechnik e.V., or FVA) is an innovation network for mechanical engineering and the automotive industry. FVA members include internationally active companies, and its suppliers are among the leading research institutions of the industry. More than 200 companies, 2000 industry experts, and 100 research institutes come together under the umbrella of the FVA to collaborate on pre-competitive collective industrial research. This research forms the foundation for company-specific product innovations.

For nearly 50 years as a non-profit organisation, the FVA has promoted research and exchange of experience within the industry and the development of young academic talent. In this way, small and mid-sized companies are given the chance to work together with leading organisations on far-reaching research programs.

Rolling and plain bearings have been one of the FVA's primary focuses for many years. Topics in the areas of bearing kinematics, heat development, load carrying capacity, damage mechanisms, and friction are addressed in a large number of projects.

The FVA Workbench, the FVA's software for the design of drive systems, makes the knowledge gained from this collective research available for practical industrial application, with more than 1000 research findings easily accessible to users.

Conferences such as Bearing World are intended to promote exchange, find synergies, and create standards.

www.fva-net.de (FVA)
www.fva-service.com (FVA Workbench)
www.bearingworld.org

Bearing World Journal
Volume 1, December 2016

Published by:
Forschungsvereinigung Antriebstechnik e.V.
Lyoner Straße 18
60528 Frankfurt am Main
Germany
www.fva-net.de

ISBN 978-3-8163-0705-1